Title

Elastic and Thermal Wave Propagation based Techniques for Structural Integrity Assessment

Author

Capriotti, Margherita

Publication Date

2019

UNIVERSITY OF CALIFORNIA SAN DIEGO

Elastic and Thermal Wave Propagation based Techniques for Structural Integrity Assessment

A dissertation submitted in partial satisfaction of the
requirements for the degree
Doctor of Philosophy in

Structural Engineering

by

Margherita Capriotti

Committee in charge:

Professor Francesco Lanza di Scalea, Chair
Professor Veronica Eliasson
Professor Hyonny Kim
Professor William Kuperman
Professor Thomas Liu
Professor Kenneth Loh

2019

The dissertation of Margherita Capriotti is approved, and it is acceptable in quality and form for publication on microfilm and electronically:

Chair

University of California San Diego

2019

DEDICATION

to my parents,

who taught me love and freedom

EPIGRAPH

“ἐὰν μὴ ἔλπηται ανέλπιστον οὐκ ἐξευρήσει,

ανεξερεύνητον ἐὸν καὶ ἄπορον”

Ἡράκλειτος

TABLE OF CONTENTS

LIST OF TABLES

LIST OF FIGURES

ACKNOWLEDGEMENTS

I would like to profoundly acknowledge my advisor Prof. Lanza di Scalea, for the innumerable opportunities he gave me, the trust in me and my work and the encouraging technical and personal guidance. His enthusiasm for research, determination and honesty have always been fundamental and will always be a reference point in my future.

I am truly grateful to Prof. Kim, who has always supported me and my research and has treated me like one of his students. His positive attitude, technical expertise and wholesome person have been of great endorsement to my research years.

Thanks to my Committee, who supported my research with enthusiasm and dedication. In particular, thanks to Prof. Eliasson, who always gave a smile to my work, to Prof. Kuperman, for the stimulating discussions and wise teachings, to Prof. Liu, for the inspiring lectures and availability, to Prof. Loh, who advised me and made me feel as one of his students.

Most of my work is the result of the collaboration with Eric H. Kim, supporting each other through struggles and successes. It has been a pleasure to work and grow with him, his patience, kindness and resourceful expertise.

My gratitude goes to Antonino Spada, whose long-lasting collaboration was and is of extreme importance to my research. His precise and expert knowledge together with his understanding and kind persona supported me, even in the hardest moments.

A profound thank goes to the past and present members of the NDE/SHM Laboratory at UCSD: I am happy to have worked with all of you and your technical and personal skills. Thank you to Stefano Mariani, Thompson Nguyen, Xuan “Peter” Zhu, Simone Sternini (and the Uptown Funk times), Ranting Cui and Diptojit Datta. A special thanks goes to Albert Liang, for his honest smile and invaluable collaboration.

Thank you to the students of the Structural (and others) Deparment at UCSD: we supported and encouraged each other’s work and goals, relying on scientific and human esteem. Thanks to Sumit Gupta, Andrew Ellison, Ben Katko, Ernesto Criado Hidalgo, Francesco Fraternali.

I have been extremely lucky to meet many amazing women within UCSD: Negin Nazarian, Sohini Manna, Niki Vazou, Ivana Escobar, Nathalì Cordero, Hanna Asefaw, Valeria Leone, Anya Lefler, thank you for inspiring me and reminding me that it is not only possible but even better to be a woman, scientist and human at the same time.

A special thanks goes to another Woman, Luciana Leone, whose sensitivity, strength and truth I esteem and are beyond words: our bond is deeper and stronger than any fried parmigiana. Thank you (& Giadina & Jonathan) for always cheering for me.

Thank you to my Tourmaline family, who encouraged me to be simply myself and enjoy it, making my PhD years an intense and joyful adventure. Thank you to Marta "piuppazzachemmai" Francesconi, Maria "La Mari" Ferraro, Amedeo Minichino, Mohammed Ghonima and Ryan Hanna, who have always provided me with sincere advices, hugs and pushes, full of sweetness and spirit.

A sincere and full-of-love thank goes to my now SD family, who supported me in the toughest moments with patience, understanding, enthusiasm and flavorful adventures: Andrei Pissarenko, Lorenzo Casalino and Martina Audagnotto.

Thank you also to the Greek! friendship of "Kostas" Anagnostopoulos, "Dimo" Giamouridis, Andreas Prodromou and George Koss; and to the curiously cynic one of Lorenzo Capriotti, Alessandra Caselli, Matteo Marcozzi and Matteo Pellegri.

I would also like to acknowledge Jonathan Nussman, who, through "other sounds", understood me and helped me deeply, and Professor Bonazza, whose e-advice was key to this journey.

Thank you to my American families for always being ready to celebrate my achievements and dreams: thank you to Zia Gail & Zio Sal, Diana, Laurie & Will, Christian & Olivia, David & Kathy, Ken & Darlene, Zia Sharon, Mia & Anna, Mr. Yang. I am very happy to keep our crazy roots alive and full of smiles.

A silently loud Thank You! goes to my closest friends, now far away, who never abandoned me and constantly supported me with patience, determination and soul: Sara Spinozzi, Alessandro Buonfigli, Irene Rossi, Mattia Bernetti, Roberto Savino.

All of my work is dedicated to and made possible by my parents, Patrizia and Giuseppe, who taught me and have always given me unconditional love and unlimited freedom, understanding and supporting the research, within and outside me.

Thank you to my sisters, Susanna and Annachiara, who are with me wherever I go as infinite source and destination of pure love.

The greatest acknowledgement flies to Handa, whose gentle but firm love I never doubted of, filling every aspect of my PhD research with soulful joy, novelty and curiosity.

I am deeply thankful and extremely enjoyed all the sweat, thoughts, silences, shouts, laughs and tears we shared in these intense research years.

The research presented in Chapter 2 of this dissertation was supported by the Federal Aviation Administration (FAA), under the Cooperative Agreement 12-C-AM-UCSD. I would like to thank especially Dr. Larry Ilcewicz, who enthusiastically supported our research efforts and ideas.

The research presented in Chapter 3 was partially funded by the National Science Foundation NSF, under the research grant CMMI-20140771.

Part of the research was also supported by the US Federal Railroad Administration under grant FR-RRD-0027-11-01, with former program manager Mahmood Fateh and current program manager Robert Wilson.

Chapter 2, Section 2.3, in full, has been submitted for publication of the material as it may appear in International Journal of Solids and Structures 2019. Spada, Antonino; Capriotti, Margherita; Lanza di Scalea, Francesco. The dissertation author was the second investigator and author of this paper.

Chapter 2, Section 2.3.3, in full, is currently being prepared for submission for publication of the material. Spada, Antonino; Capriotti, Margherita; Lanza di Scalea, Francesco. The dissertation author was the second investigator and author of this material.

Chapter 2, Section 2.4.1, in part, is coauthored with Kim, Hyungsuk E. The dissertation author was the primary author of this chapter.

Chapter 2, Section 2.4.2, in full, is a reprint of the material as it appears in Materials Journals 2017. Capriotti, Margherita; Kim, Hyungsuk E.; Lanza di Scalea, Francesco; Kim, Hyonny. The dissertation author was the primary investigator and author of this paper.

Chapter 2, Section 2.4.3, in full, has been submitted for publication of the material as it may appear in Journal of Intelligent Material Systems and Structures 2019. Capriotti, Margherita; Lanza di Scalea, Francesco. The dissertation author was the primary investigator and author of this paper.

Chapter 3, Section 3.4, in part, is currently being prepared for submission for publication of the material. Capriotti, Margherita; Ellison, Andrew; Kim, Hyungsuk E.; Lanza di Scalea, Francesco; Kim, Hyonny. The dissertation author was the primary investigator and author of this material.

Chapter 4, in full, is currently being prepared for submission for publication of the material. Capriotti, Margherita; Ellison, Andrew; Kim, Hyungsuk E.; Lanza di Scalea, Francesco; Kim, Hyonny. The dissertation author was the primary investigator and author of this material.

VITA

2012 B. Sc. Mechanical Engineering, Università degli Studi di Parma, Italy

2014 M. Sc. Mechanical Engineering, Università degli Studi di Parma, Italy

2019 Ph. D. Structural Engineering, University of California San Diego

PUBLICATIONS

Spada, A., **Capriotti, M**., Lanza di Scalea, F., (in preparation). “Global-Local Model to predict scattering of multiple and dispersive guided elastic waves: 3D application on railroad tracks”, International Journal of Solids and Structures.

Capriotti, M., Ellison A., Kim H.E., Kim H., Lanza di Scalea, F., (in preparation). “Data Fusion and Correlation of Ultrasonic guided waves inspection with other conventional NDE techniques for composite aerospace structures”, Composite Structures.

Capriotti, M., Lanza di Scalea, F., (submitted). “Robust non-destructive inspection of composite aerospace structures by extraction of ultrasonic guided-wave transfer function in single-input-dual-output scanning systems”, Journal of Intelligent Material Systems and Structures.

Spada, A., **Capriotti, M**., Lanza di Scalea, F., (submitted). “Global-Local Model to predict scattering of multiple and dispersive guided elastic waves in solids”, International Journal of Solids and Structures.

Spada A., **Capriotti M**., Lanza di Scalea F., (2019). “Improved global-local model to predict guided-wave scattering patterns from discontinuities in complex parts”, Proc.SPIE SMART STRUCTURES AND MATERIALS + NONDESTRUCTIVE EVALUATION AND HEALTH MONITORING 2019, vol. 10972.

Capriotti M., Cui R., Lanza di Scalea F., (2019). “Guided wave techniques for damage detection and property characterization in composite aerospace structures”, Proc.SPIE SMART STRUCTURES AND MATERIALS + NONDESTRUCTIVE EVALUATION AND HEALTH MONITORING 2019, vol. 10972.

Lanza di Scalea F., Liang A., Sternini S., **Capriotti M**., Datta D., Zhu X., (2019). “Passive extraction of Green’s function of solids and application to high-speed rail inspection”, Proc.SPIE SMART STRUCTURES AND MATERIALS + NONDESTRUCTIVE EVALUATION AND HEALTH MONITORING 2019, vol. 10970.

Lanza di Scalea, F., Zhu, X., **Capriotti, M**., Liang, A., Mariani, S., and Sternini, S., (2018). “Passive Extraction of Dynamic Transfer Function from Arbitrary Ambient Excitations: Application to High speed Rail Inspection from Wheel-generated Waves”, ASME Journal of Nondestructive Evaluation, Diagnostics and Prognostics of Engineering Systems, 1(1), pp. 0110051- 01100512.

Capriotti M., Kim H. E., Lanza di Scalea F., Kim, H., (2017). “Non-Destructive Inspection of Impact Damage in Composite Aircraft Panels by Ultrasonic Guided Waves and Statistical Processing”, Materials Journal, Special Issue "Structural Health Monitoring for Aerospace Applications 2017", 10(6), 616; doi:10.3390/ma10060616.

Capriotti M., Cui R., Lanza di Scalea F., (2018). “Damage detection and visco-elastic property characterization of composite aerospace panels using ultrasonic guided waves”, Proceedings of the 2018 Annual Conference of Experimental and Applied Mechanics, Mechanics of Composite, Hybrid and Multifunctional Materials, vol.5.

Capriotti M., Kim H. E., Lanza di Scalea F., Kim, H., (2017). “Detection of major impact damage to composite aerospace structures by ultrasonic guided waves and statistical signal processing”, X International Conference on Structural Dynamics, EURODYN 2017.

Capriotti M., Sternini S., Lanza di Scalea F., (2017). “Passive Infrared Thermography for Defect Detection and Imaging in Structures by Correlation of Diffuse Thermal Fields”. Society for Experimental Mechanics, Annual Conference.

Capriotti M., Kim H. E., Lanza di Scalea F., Kim, H., (2017). “Development of an Ultrasonic Nondestructive Inspection Method for Impact Damage Detection in Composite Aircraft Structures”, Proc.SPIE SMART STRUCTURES AND MATERIALS + NONDESTRUCTIVE EVALUATION AND HEALTH MONITORING 2017, vol.10169, doi: 10.1117/12.2258669

Capriotti M., Sternini S., Mariani S., Lanza di Scalea F., (2016). “Extraction of thermal Green’s function using diffuse fields: a passive approach applied to thermography”, Proc.SPIE SMART STRUCTURES AND MATERIALS + NONDESTRUCTIVE EVALUATION AND HEALTH MONITORING 2016, vol. 9803, doi:10.1117/12.2218998

ABSTRACT OF THE DISSERTATION

Elastic and Thermal Wave Propagation based Techniques for Structural Integrity Assessment

by

Margherita Capriotti

Doctor of Philosophy in Structural Engineering

University of California San Diego, 2019

Professor Francesco Lanza di Scalea, Chair

Non Destructive Evaluation (NDE) is a fundamental step in several phases of the lifespan of structures. It aims at assessing the structure's state of health to guarantee its proper functioning. An added requirement of any NDE technique is to avoid any damage to the structure during the actual test.

NDE of aircraft structures, in particular, is a crucial process to guarantee passenger safety and ensure effective maintenance. Current visual inspection and lifespan estimation of aircraft are not able to properly assess the health status of structures, especially when damage is present in the

interior and is thus not visible. Composite aircrafts, in particular, are subjected to a wide variety of damages that can develop in areas that are not directly accessible from the outside.

The main application of this research comes from the need for an NDE tool that can help establishing the requirement for further inspections following a Ground-Service Equipment (GSE) impact or similar event on a composite aircraft. A successful technique for this application must be able to easily and rapidly inspect the structure, accessing it only from the outside, and detect defects in a statistically reliable manner.

This dissertation studies the physics of propagation of elastic and thermal waves and their interaction with material properties and discontinuities, combined to advanced signal processing, for the purpose of damage detection and structural integrity assessment, with particular attention to stiffened composite panels typical of modern commercial aircraft construction.

Chapter 1

Introduction

1.1 Motivation

Non Destructive Evaluation (NDE) is a fundamental step in several phases of the lifespan of structures, that aims at assessing the structure's health status and ensuring its quality. NDE includes a variety of techniques, of different physical nature and levels of complexity of operation and interpretation of the results, that all share the characteristic of not affecting the structure's function. It is often employed for damage detection and localization, but can extend to more quantitative outcomes, including property characterization and residual strength estimation.

NDE of aircraft structures, in particular, is a crucial process to ensure passenger safety, industry cost savings and technological advancements. Current visual inspection and lifespan estimation of aircraft are not able to properly assess the health status of aircraft, especially when hidden damage is present in the interior and can compromise the integrity of the overall assembly.

The vast majority of modern military and commercial aircrafts (e.g. B787, A380) is made of fiber-reinforced composite materials, owing to their high strength-to-weight and stiffness-to-weight ratios (Ashby, 1993). The complexities of the manufacturing process, for both the composite material itself and the assembly, as well as the severity of external loads, in flight and during land operations, can develop a number of structural defects that need to be detected and quantified through NDE techniques.

Composite aircraft, in particular, are subjected to a wide variety of damage that are very difficult to avoid and visually detect. The formation and propagation of damage in such materials is still open to further investigations and is unknown, especially if compared to metal. The Federal Aviation Administration (FAA), together with other agencies and companies, are very interested in understanding the causes and consequences of damages in aerospace structures and are currently devolving huge efforts in trying to develop protocols for such materials (FAA Advisory Circular, 2009; CMH-17, 2017). Damages have been categorized in 5 levels according to their severity and load carrying capacity (Ilcewitz, 2013), with 5 being the most severe. High Energy Wide Area Blunt Impacts (HEWABI), due for example to Ground Service Equipment (GSE) maneuvers, are very common during aircraft operation and can cause major damages to the structure that are often not visible from the outside (Kim et al., 2014). Such impacts are characterized by forces of large magnitudes and long time scales (DeFrancisci, 2013) and can severely affect the structural integrity of key components (e.g. damage to stiffeners and C-frames), most of which are internal, and thus challenging to access from a one-sided (external-only) NDE inspection.

1.2 Approach

Ultrasonic guided waves are an ideal candidate for this kind of inspection of composite aircraft (Staszewsky et al., 2004).

“Guided” elastic waves are widely used to probe structural components with waveguide geometries (plates, rod, pipes, etc..) in both NDE and Structural Health Monitoring (SHM) applications. Lamb waves, for example, are specific guided waves in traction-free isotropic plates. Guided waves can maximize the inspection range by exploiting the long propagation distances, while maintaining a sufficient sensitivity to small structural anomalies (e.g. defects) owing to the relatively large frequencies (~ 100’s kHz for typical plate-like structures). However, the propagation of guided waves is complicated by their multimode character (several wave modes propagating simultaneously) and dispersive character (propagation velocity is a function of frequency). Additional complications exist in the case of anisotropic layered components (e.g. laminated composites) and/or built-up structures (e.g. stiffened panels) where the guided wave crosses elements of varying thickness along its path.

Analytical solutions of guided wave propagation through multi-layered structures exist using well known global matrix or transfer matrix methods (Rose, 2014). However, purely theoretical predictions become quite challenging, or non-existent, in the presence of structural discontinuities such as defects. Datta et al. (1988) used an approximated stiffness method to study guided dispersive propagation in laminated anisotropic plates. Castaings et al. (2002) applied the modal decomposition method to analyze scattering of an incident symmetric (axial) S0 or anti-symmetric (flexural) A0 Lamb mode by an internal or an opening crack in isotropic plates, imposing velocity and stress continuity conditions at the crack section. An improved analytical approach to predict Lamb waves scattering from a step geometrical discontinuity considering a complex mode expansion with vector projection was recently proposed by Giurgiutiu and co-workers (Podder and Giurgiutiu, 2016a, 2016b; Haider et al., 2018). These studies apply to isotropic plates with thickness changes, presence of stiffeners, and horizontal cracks or disbonds. These problems can be modelled by adjacent sub-regions with rectangular geometry (sub-plates).

Numerical methods can provide more flexibility to handle more complicated geometries and defects. Guo and Cawley (1993), for example, applied the Finite Element (FE) method to investigate the interaction of the S0 Lamb mode with delaminations at different interfaces in a composite laminate. However, in order to maximize computational efficiency and maintaining accuracy at small wavelengths, it is often not optimum to carry out an FE analysis for the entire domain. When the structural details and anomalies are only a localized region of the entire “waveguide” panel, a hybrid Global-Local approach is more appropriate. Hybrid methods couple the solution available analytically in the “global” region with that available numerically (BEM or FEM) in the “local” region with the structural discontinuity. The general hybrid method to predict elastic wave scattering based on a FE discretization of the local region was utilized for axisymmetric inclusions in homogeneous isotropic media (Goetschel et al., 1982), other axially-symmetric scattering problems (Rattanawangcharoen et al., 1997), isotropic plates with notches and rivet-hole cracks (Chang and Mal, 1999; Mal and Chang, 2000; Zhou and Ichchou, 2011), defects in lap-shear joints of isotropic plates (Chang and Mal, 1995), and isotropic plates with a normal transversely isotropic weld (Al-Nassar et al., 1991). The problem of reflections of a fixed cracked edge was addressed by Karunasena et al. (1995), while the scattering from a semi-infinite plate employing the BEM method for the local part was studied by Galan and Abascal (2002), who later extended their BE-FE technique to plates with inclusions, different cracks and materials (Galan and Abascal, 2005).

Other works focused on guided wave scattering in composite plates. The use of a hybrid FE local discretization coupled with a boundary integral representation of the global part was investigated by Datta et al. (1992) for the case of a uniaxial composite plate. Boundary integral formulations were utilized to study scattering from interface cracks in a layered half-space and layered fiber—reinforced composites (Karim and Kundu, 1988; Karim et al., 1989; Karim et al., 1992). FE local-global techniques were applied to scattering in layered composite laminates with delaminations (Tian et al., 2004) and free edges (Dong and Goetschel, 1982).

The vast majority of these previous works utilized theoretical solutions (mostly normal mode expansion) to model the guided wave propagation in the global portion of the isotropic or composite plate. However, such theoretical guided wave solutions are increasingly difficult to obtain for an anisotropic composite laminate with a general number of layers. For this reason some of the authors of the present work have recently exploited the numerical efficiency of the Semi-Analytical Finite Element method (SAFE) (Hayashi et al., 2003; Bartoli et al. 2006; Marzani et al., 2008) to deal with the global portion of the GL scattering problem in composite plates of arbitrary number of layers with delamination defects (Srivastava and Lanza di Scalea, 2010). A similar use of SAFE in Global-Local scattering problems for layered composites was shown later by Ahmad et al. (2013). The SAFE method only requires the FE discretization of the cross-section of the laminate composite, and utilizes basic theoretical harmonic wave solutions in the wave propagation direction. SAFE easily deals with the particular composite lay-up by simply rotating the stiffness matrix of each layer in the wave propagation direction. In a Global-Local framework, the SAFE global solutions are matched to the FE local solutions through continuity of displacements and tractions at the local-global boundaries, as customary of hybrid approaches. Efficient wave propagation prediction, of a variety of incoming/refracted UGW modes and for several geometrical built-ups and/or defect cases, can be of great aid to the pre- and post- phases of experimental tests.

A number of studies have dealt with experimental tests of guided wave probing of components with waveguide geometries, such as aircraft fuselage and wing panels (Raghavan and Cesnik, 2007; Croxford et al., 2007; Staszewski et al., 2004; Rose, 2014; Giurgiutiu, 2015). Applications of ultrasonic guided waves to detect structural damage in composites are numerous (e.g. Karim and Kundu, 1988; Kundu and Desai, 1989; Datta et al., 1988 and 1992; Guo and Cawley, 1993; Tian et al., 2004; Kessler et al., 2002; Lowe et al., 2004; Matt et al., 2005; Banerjee et al., 2007; Ihn and Chang, 2008; Salas and Cesnik, 2009; Srivastava and Lanza di Scalea, 2010; Sohn et al., 2011; Hudson et al., 2015; He and Yuan, 2015; Murat et al., 2016; Ricci et al., 2016; Poddar and Giurgiutiu, 2016a and 2016b; Capriotti et al., 2017; Chong et al., 2017).

Generally, ultrasonic guided-wave test methods aim at detecting possible damage by identifying an "anomalous" behavior of the structure as the ultrasonic energy travels from one point A to another point B. Therefore, damage detection becomes an issue of extracting the structural "transfer function" between A and B (H_{AB}). In a practical test implementation, this transfer function is generally a frequency band-passed version of the broadband acoustic Green's function because it only applies to the useful frequency range afforded by the ultrasonic transducers used to excite and detect the wave motion.

The extraction of the transfer function of the structure (i.e. without the effect of the excitation and detection wave transduction paths) is essential to compare testing results to numerical or theoretical models aimed at characterizing the damage that is being detected. The vast majority of guided-wave tests are implemented in a "Single-Input-Single-Output" (SISO) mode, where an ultrasonic transmitter is used in conjunction with a signal ultrasonic receiver. The extraction of the structure's transfer function in this case requires a deconvolution of the excitation from the reception - as well known since the 70's in equivalent electrical engineering applications (Roth, 1971). However, the precise excitation spectrum into the structure is difficult to determine because it results from a convolution of the excitation signal, the transmitting transducer frequency response, and the transducer-to-structure coupling frequency response (which is generally unknown).

In addition, guided-wave inspection of structural components often requires some kind of scanning of either the test part or the ultrasonic transducers to spatially map potential damage. Scanning can be most efficiently performed by non-contact means of wave transduction (e.g. laser-based, air-coupled, water-based). In these cases, extracting the pure transfer function of the structure without biases from the excitation and detection response spectra is even more challenging because of the possible transduction variations through the scan.

In light of the above requirements, a more robust guided-wave inspection test compared to the SISO approach is to utilize a "dual-output" approach where the transfer function is extracted between two receiving points. This is the approach used, for example, in "passive" structural monitoring utilizing random excitations (e.g. operational loads on the structure), where it becomes essential to eliminate the effects of the acoustic excitation source because generally uncontrolled (Farrar and James, 1997; Lobkis and Weaver, 2001; Michaels and Michaels, 2005; Salvermoser et al., 2015; Snieder and Safak, 2006; Sabra et al., 2007 and 2008; Duroux et al., 2010; Tippmann et al., 2015; Tippmann and Lanza di Scalea, 2015 and 2016; Lanza di Scalea et al., 2018a and 2018b). The "dual-output" approach has the best chance of minimizing the effect of the energy transductions paths and isolating the true structural transfer function that is the only metric affected by the presence of possible damage. It was recently shown in a couple of different inspection scenarios (Snieder and Safak, 2006; Lanza di Scalea et al., 2018a and 2018b) how the transfer function extraction in a dual-output approach is best conducted by performing a deconvolution operation between the two receivers.

For remote inspection and 2D field imaging, NDE has relied also on InfraRed (IR) thermography. A quite exhaustive review of the technique can be found in Shull (2002). IR Thermography allows for ease and practicality in the experimental set-up and implementation, especially when large structures such as aircrafts need to be inspected, and visualization of the results, providing a ready to use heat map of the entire specimen, with no further need of interpretation. Especially when involving thin wide structures, such as composite airplane fuselages or wings, IR thermography offers the possibility to inspect and image subsurfaces, exploiting heat diffusion, detecting typical crucial damages as disbonds, delaminations and cracks.

Theoretically, heat propagation has been studied for centuries. Cole and Beck et al., (2010) thoroughly describe heat propagation in terms of Green's Functions, relying on the fundamental theoretical work by Morse & Feshback (1953) and Carslaw & Jaeger (1959). The interpretation of heat diffusion as thermal waves has been investigated by numerous scientists (Marin, 2002; Marin et al., 2010, Ozisik and Tzou, 1994). Mostly, Mandelis (Mandelis, 1995; Mandelis, 2013) and his co-workers (Nicolaideis et al., 2000; Kaiplavil et al., 2012; Kaiplavil et al., 2014) think about the thermal field as the result of the "propagation" of waves of fluctuating temperature, formulate the mathematical expression and apply it for imaging in a variety of fields, according to specific signal processing techniques (Tabatabaei et al., 2009; Tabatabaei et al., 2012).

While the passive GF retrieval by cross-correlation of diffuse fields has been fully demonstrated (Lobkis and Weaver, 2001) and applied by numerous scientists in seismology, civil engineering (Snieder and Safak, 2006), oceanography (Sabra et al., 2005) and SHM (Tippman et al., 2015; Lanza di Scalea et al., 2018), as mentioned above, no experimental relevance has still been reported for thermal waves. Snieder has extended the approach to other physics, including electromagnetics, optics and non-elastic fields, and has generalized the formulation in terms of energy principles.

The exploitation of heat propagation and temperature evolution for inspection and imaging translates into the IR thermography technique. Meola and Carlomagno in 2004 presented an exhaustive review on the principles of IR thermogaphy and the recent advances in its main implementation techniques (i.e. pulse thermography PT and lock in thermography). Servais et al. in 2008 used IR thermography for the characterization of manufacturing and maintenance of aerospace composite discontinuities, relying on on time and frequency methods. Ibarra-Castanedo et al. in 2007 and Lopez et al. in 2014 applied PT to aerospace structures for a qualitative and quantitative assessment, exploiting and comparing three different processing methods. In particular Flash Thermography processed according to the Thermal Signal Reconstruction (TSR) method, proposed by Sheperd (2004), established an effective and more quantitative approach of adopting IR thermography in NDE inspections. Shepard (2007) and his co-workers (Lhota, 2014; Frendberg, 2014; Oswald-Tranta, 2017), explain and discuss the method; many scientists and applications adopted it, as in Roche et al., 2014. All of the above literature exploits temporal discontinuities in the cooling evolution of temperature, after Lau et al in 1991 and Vavilov et al. in 1992 understood the potential of the huge database offered by a video of 2D temperature maps, which constituted the recording of the propagation of thermal waves.

Spatial discontinuities can also be exploited, in particular if spot or linear heat sources are applied: Varis et al. (1995) discuss the evolution of heat in space in layered anisotropic carbon fiber composites, Grinzato et al. (1998) apply it for NDE of frescoes, while Siakavellas et al. (2012) use line heating thermography for the detection of cracks at fastener holes. The actual spatial deviation of thermal images is proposed and used by Li et al. (2011) for crack imaging by laser-line and laser-spot thermography.

1.3 Outline of the dissertation

In this work, both elastic and thermal waves are discussed and investigated with the common application to the NDE of composite structures used in modern commercial aircraft construction.

Chapter 2 describes elastic wave propagation.

In Section 2.1, the theory of ultrasonic guided waves introduces this propagation phenomenon and NDE technique in aluminum and composite plates are reviewed.

In Section 2.2, a numerical approach (Global Local method) is presented. Predicting the scattering behaviour of ultrasonic waves in the presence of specific structural defects is essential to (a) properly guide the experimental implementation of an NDT/SHM test through proper selection of mode-frequency combinations, and (b) provide quantitative, rather than qualitative information on a defect from knowledge of the given defect’s scattering pattern. Such wave propagation predictions are very challenging in fuselage and wing aircraft components that are anisotropic, multi-layered, and stiffened by built-up stringers.

Experiments using guided wave inspection of composite aerospace panels are presented in Section

2.3. This section describes a method that utilizes Ultrasonic Guided Waves (UGWs), non-contact transducers and statistical processing to achieve the above-mentioned goals. The need for rapid inspection of the structure points to UGWs as suitable candidates. The focus is on the detection of impact damage in the aircraft (FAA, Composite aircraft structures, 2009), and on the development of a field-applicable method. To do so, non-contact air-coupled ultrasonic transducers are employed in a scanning mode.

Section 2.4 discusses the “dual-output” approach of extracting the structural transfer function as applied to a UGW test scenario, and implements this method in two scanning systems that are utilized for damage detection in composite aircraft panels. This work is part of a larger research effort (Capriotti et al., 2017) aimed at developing inspection systems for detecting impact-caused damage in parts representative of commercial aircraft construction (e.g. B787 and A380). The work focuses on stiffened fuselage panels consisting of a composite skin and co-cured composite stringers. Results are first shown for a composite plate (skin-only) to compare the experimentally determined guided-wave transfer functions to that predicted by a Semi-Analytical Finite Element (SAFE) method. The section then discusses the results of two scanning systems utilizing the “dual-output” scheme, one based on a total air-coupled approach and the other one based on a hybrid impact/air-coupled approach.

Chapter 3 describes thermal wave propagation.

In Section 3.1, the basic principles of IR thermography are explained.

This is followed by a theoretical investigation of heat diffusion in Section 3.2. The latter is composed of a first introduction of heat propagation as thermal waves and its solution by the Green’s function (GF) method. The formulation of temperature distribution in terms of GF solutions is exploited for the theoretical derivation of thermal Green’s function retrieval, in a passive manner. Most of the theoretical derivation for the thermal field in Section 3.2 relies on the analogies and differences between the hyperbolic wave equation and parabolic heat diffusion equation and is derived from Snieder’s work on the GF extraction for the diffusion equation (Snieder, 2006).

Section 3.3 presents numerical analyses of heat propagation in plates, for pristine and defective cases. The simulations involve processing of temperature time histories for the retrieval of active thermal Green’s functions, in time domain and spatial domain. In particular, the exploitation of the spatial domain employs spot size and linear heat sources.

Lastly, the application of IR thermography to the NDE of composite aerospace structures and damage detection is presented in Section 3.4. Flashed Thermography combined with the Thermographic Signal Reconstruction (TSR) method, as proposed by Sheperd (2004), are employed on impacted composite panels where different impact energies and types have generated damage on the flange and cap of the stiffeners. The beneficial effect of the TSR processing on this experimental NDE approach is shown and damage information can be inferred, besides detection only. The work relies also on the interpretation of the defect as a virtual (or secondary) heat source, as observed by Manohar in his PhD thesis and related works (Manohar et al., 2013).

Chapter 4 correlates UGWs measurements for quantitative damage characterization, gathering the findings from elastic and thermal waves techniques. Section 4.1 motivates the work and describes the datasets. In Section 4.2 features are extracted from the UGW measurements to understand their sensitivity to specific damage modes. In Section 4.3, such features are correlated to ultrasonic C-scan, X-ray computed tomography scan and IR thermography to detect and characterize specific damage modes.

In the last chapter (Chapter 5), the overall conclusions and future recommendations are provided.

Chapter 2

Techniques of Elastic Wave Propagation

The propagation of ultrasonic waves in a not infinite medium (semi-infinite or bounded) generates a specific type of waves, named ultrasonic guided waves. The boundaries of the medium, as those given by a half-space or a finite geometry, interact with the travelling wave so that boundary conditions can be satisfied.

When ultrasonic longitudinal and shear waves propagate into waveguides as rods, tubes, thin plates or multi-layered structures, they reflect back and forth inside the waveguide at certain angles, due to the high mismatch in acoustic impedance at the boundaries, leading to interference phenomena (Figure 1). For the particular incident angle and frequency chosen, the interference phenomena could be constructive, destructive or intermediate.

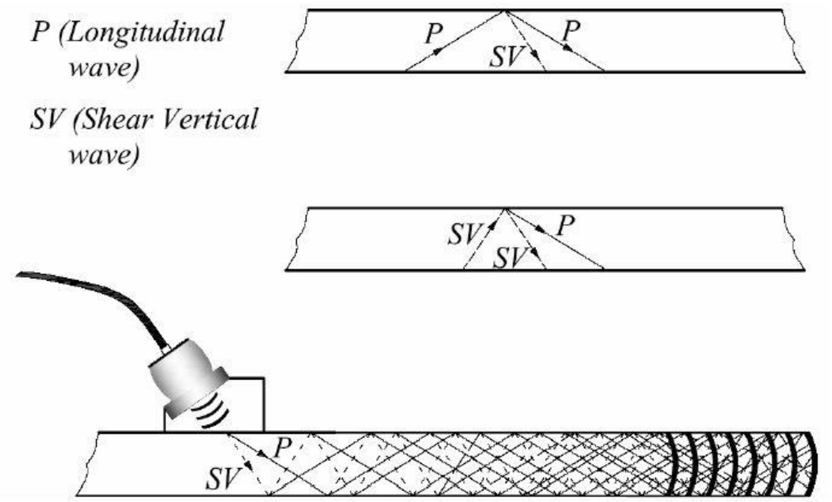

Figure 1 - Guided waves formation in plate

The solutions of constructive interference that satisfy the wave propagation equation for those boundary conditions lead to a set of propagating guided wave modes. Waves propagating on the surface of a semi-infinite solid have to satisfy zero tractions at the boundary (Rayleigh waves). They decay with depth and have an elliptical particle displacement. Lamb waves propagate in a free plate, satisfying the zero tractions condition at the top and bottom surfaces of the plate. This work focuses on this particular type of wave and their generation, propagation and interaction will be better illustrated in the next paragraphs. Stoneley waves propagate at the interface between two media, where the continuity of tractions and displacements is satisfied. When one of the two media is a liquid, Sholte waves propagate.

2.1 Theory of Ultrasonic Guided Waves

Combining theory of elasticity, specifically the constitutive equations and the compatibility relations, to the equations of motion, we obtain the governing equation for particle displacement (Rose, 2004; Lowe, 1992). In the derivation, we will assume the materials to be elastic (no damping) so that the waves will be free propagating waves that travel with no input or loss of energy.

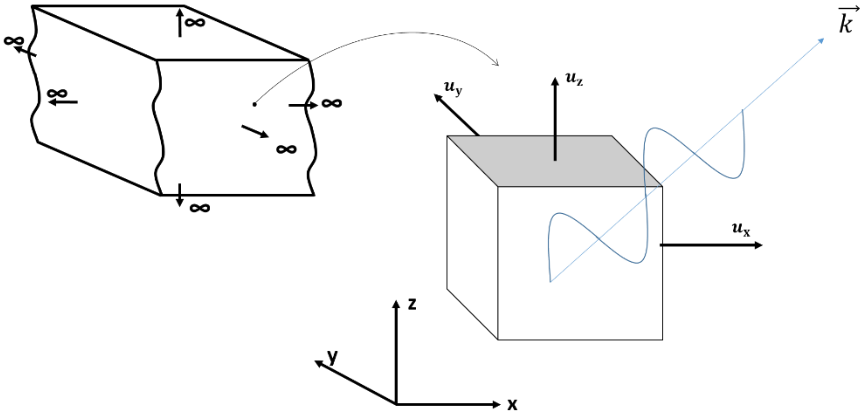

Figure 2 - Wave propagation and particle displacement in bulk isotropic medium.

Referring to the reference system in
Figure 2, we write the three equations of motions corresponding to the three directions x, y, z in terms of stresses, where u_x, u_y, u_z are the displacements:

$$\begin{cases} \rho \dfrac{\partial^2 u_x}{\partial t^2} = \dfrac{\partial \sigma_{xx}}{\partial x} + \dfrac{\partial \sigma_{xy}}{\partial y} + \dfrac{\partial \sigma_{xz}}{\partial z} \\ \rho \dfrac{\partial^2 u_y}{\partial t^2} = \dfrac{\partial \sigma_{yx}}{\partial x} + \dfrac{\partial \sigma_{yy}}{\partial y} + \dfrac{\partial \sigma_{yz}}{\partial z} \\ \rho \dfrac{\partial^2 u_z}{\partial t^2} = \dfrac{\partial \sigma_{zx}}{\partial x} + \dfrac{\partial \sigma_{zy}}{\partial y} + \dfrac{\partial \sigma_{zz}}{\partial z} \end{cases}$$

2.1-1

Introducing the constitutive equations for stresses and strains:

$$\sigma_{xx} = \lambda(\varepsilon_{xx} + \varepsilon_{yy} + \varepsilon_{zz}) + 2\mu\varepsilon_{xx}, \qquad \sigma_{yy} = \lambda(\varepsilon_{xx} + \varepsilon_{yy} + \varepsilon_{zz}) + 2\mu\varepsilon_{yy}\,,$$

$$\sigma_{zz} = \lambda(\varepsilon_{xx} + \varepsilon_{yy} + \varepsilon_{zz}) + 2\mu\varepsilon_{zz}$$

2.1-2

$$\sigma_{xy} = \mu\varepsilon_{xy}, \qquad \sigma_{yz} = \mu\varepsilon_{yz}\,, \qquad \sigma_{xz} = \mu\varepsilon_{xz}$$

where the Lamè elastic stiffness constants are $\lambda = \frac{E\nu}{(1+\nu)(1-2\nu)}$ and $\mu = \frac{E}{2(1+\nu)} = G$, and strain-displacements compatibility equations:

$$\varepsilon_{xx} = \frac{\partial u_x}{\partial x}, \qquad \varepsilon_{yy} = \frac{\partial u_y}{\partial y}, \qquad \varepsilon_{zz} = \frac{\partial u_z}{\partial z}$$

$$\varepsilon_{xy} = \frac{\partial u_x}{\partial y} + \frac{\partial u_y}{\partial x}, \qquad \varepsilon_{yz} = \frac{\partial u_y}{\partial z} + \frac{\partial u_x}{\partial y}, \qquad \varepsilon_{xz} = \frac{\partial u_x}{\partial z} + \frac{\partial u_z}{\partial x}$$

2.1-3

we obtain the equations of motion in 3D (eqs. **2.1-4**) in terms of displacements, also known as the governing wave equations:

$$\begin{cases} \rho \dfrac{\partial^2 u_x}{\partial t^2} = (\lambda + \mu) \dfrac{\partial}{\partial x}\left(\dfrac{\partial u_x}{\partial x} + \dfrac{\partial u_y}{\partial y} + \dfrac{\partial u_z}{\partial z}\right) + \mu \nabla^2 u_x \\ \rho \dfrac{\partial^2 u_y}{\partial t^2} = (\lambda + \mu) \dfrac{\partial}{\partial y}\left(\dfrac{\partial u_x}{\partial x} + \dfrac{\partial u_y}{\partial y} + \dfrac{\partial u_z}{\partial z}\right) + \mu \nabla^2 u_y \\ \rho \dfrac{\partial^2 u_z}{\partial t^2} = (\lambda + \mu) \dfrac{\partial}{\partial z}\left(\dfrac{\partial u_x}{\partial x} + \dfrac{\partial u_y}{\partial y} + \dfrac{\partial u_z}{\partial z}\right) + \mu \nabla^2 u_z \end{cases}$$

2.1-4

For an isotropic medium, we can consider the x direction of wave propagation only. Assuming a harmonic solution of the type:

$$\boldsymbol{u} = \left(u_x, u_y, u_z\right) = Ae^{i(\frac{2\pi \boldsymbol{x}}{\lambda} - \omega t)} + Be^{i(\frac{2\pi \boldsymbol{x}}{\lambda} + \omega t)}$$

2.1-5

where the wavefront is an infinite plane perpendicular to the direction of wave propagation, and rewriting it for the wavenumber $k = \frac{\omega}{c}$ as:

$$\boldsymbol{u} = \left(u_x, u_y, u_z\right) = Ae^{i(\boldsymbol{kx} - \omega t)} + Be^{i(\boldsymbol{kx} + \omega t)}$$

2.1-6

we can recognize waves travelling in the positive x direction in the first term and in the negative direction in the second term. The particle motion is a combination of the displacements in the three directions. Using this solution in eq. (2.1-4), we can solve for two modes: a dilatational wave motion, where the particles move parallel to the direction of wave propagation, with a speed dependent on both extensional and shear behavior (longitudinal waves):

$$c_L = \frac{\omega}{k} = \sqrt{\frac{E(1-\nu)}{\rho(1+\nu)(1-\nu)}}$$

2.1-7

and a rotational motion, where the particles move perpendicular to the direction of wave propagation, with a speed c_T (shear waves):

$$c_T = \frac{\omega}{k} = \sqrt{\frac{G}{\rho}}$$

2.1-8

To separate the fields in eqs. (**2.1-4**), we can use Helmoltz method, where we define the longitudinal wave potential $L = \nabla\phi$ and shear wave potential $S = \nabla$ x ψ. The total displacement field is given by the superposition of the two potentials and the solution to the separated eqs. (**2.1-9**)

$$\begin{cases} \frac{1}{c_L^2}\frac{\partial^2\phi}{\partial t^2} = \nabla^2\phi \\ \frac{1}{c_T^2}\frac{\partial^2\boldsymbol{\psi}}{\partial t^2} = \nabla^2\boldsymbol{\psi} \end{cases}$$

2.1-9

becomes:

$$\phi = A_L e^{i\omega(\frac{\boldsymbol{Nx}}{c_L}-t)} = A_L e^{i(\boldsymbol{kx}-\omega t)}$$

$$\boldsymbol{\psi} = A_S e^{i\omega(\frac{\boldsymbol{Nx}}{c_T}-t)} = A_S e^{i(\boldsymbol{kx}-\omega t)}$$

2.1-10

where $\boldsymbol{n}$ is the wave propagation direction vector, A_L and A_S are the complex amplitudes and $c = \frac{\omega}{|\boldsymbol{k}|}$ is the wave speed (Lowe, 1992).

Considering that the medium extends infinitely in the y direction, we can reduce the problem to a 2D infinite space (x-z), and simplify the derivation considering plane strain ($\frac{\partial}{\partial y} = 0$) and in-plane motion ($u_y = 0$). The displacements u_x and u_z can be found as:

$$\boldsymbol{u} = \nabla\phi = \quad \begin{cases} u_x = n_x A_L e^{i\omega(\frac{N_x x}{c_L} + \frac{N_z z}{c_L} - t)} \\ u_z = n_z A_L e^{i\omega(\frac{N_x x}{c_L} + \frac{N_z z}{c_L} - t)} \end{cases}$$

2.1-11

for longitudinal waves and

$$\boldsymbol{s} = \nabla \text{ x } \boldsymbol{\psi} = \begin{cases} u_x = n_z A_S e^{i\omega(\frac{N_x x}{c_T} + \frac{N_z z}{c_T} - t)} \\ u_z = n_x A_S e^{i\omega(\frac{N_x x}{c_T} + \frac{N_z z}{c_T} - t)} \end{cases}$$

2.1-12

for shear waves.

Through the combination of these wave solutions to a set of boundary conditions for stress and displacement, on the finite domain, as

$$\begin{gathered} u(x, y, z, t) = u_0(x, y, z, t) \\ t_i = \sigma_{ji} n_j \end{gathered}$$

2.1-13

a relationship in terms of wave velocity versus frequency can be established (Rose, 2004). This so-called dispersion relation governs the propagation of each guided wave mode in space and time and the dependency of the wave phase velocity to frequency. The relationship between the incident angle and phase velocity is expressed by the Snell's Law, so that each waveguide has its unique set of dispersion curves.

Starting from the particular case of waves at the boundary between two semi-infinite half spaces, for an incident longitudinal wave, the frequency of the incident shear wave and the two reflected longitudinal and shear wave has to be the same. Together with Snell's Law, where the wavenumber k_x in the *x* wave propagation direction has to be the same at the interface, the waves have to travel with the same phase velocity $c_p = \frac{\omega}{k_x}$.

The latter expresses a fundamental dependence of the frequency from the wavenumber and it establishes that wave velocity is a function of frequency, hence wave distorsion must occur (Rose, 2004). Also, the real solutions of k represent right and left propagating waves. While the individual harmonics travel with different phase velocities c_p, the superimposed packet travels with the group velocity c_g. For this group of waves to be maintained, the changes in phase for all the components should be the same, leading to $c_g = \frac{d\omega}{dk}$ and due to the dependence of the phase velocity on frequency, we also have that $c_g = c_p + k\frac{dc_p}{dk}$.

Many structures can be considered as waveguides themselves, naturally supporting the propagation of guided waves, provided that the wavelengths are large enough compared to some key dimensions of the waveguide. The energy of such waves is carried along the waveguide, with no leakage, as long as the mismatch in acoustic impedance between the layers is significant.

For thin plates, the discussion seen about wave propagation at the interface of two media is extended to an additional interface, where traction free conditions have to be satisfied at both interfaces constituting the top and bottom of the plate. Moreover, the amplitudes of the displacements traveling out of such interfaces have to equal zero, to satisfy conservation of energy (guided waves).

Relying again on the methods of potentials combined to a harmonic plane wave solution assumption of the type of equations (2.1-10), which, for a plain strain case become:

$$\phi = \boldsymbol{\Phi}(\boldsymbol{z})e^{i(kx-\omega t)}$$

$$\boldsymbol{\psi} = \boldsymbol{\Psi}(\boldsymbol{z})e^{i(kx-\omega t)}$$

2.1-14

It is possible to notice how they represent a solution of waves travelling along x (longitudinal direction of the plate) and having a fixed distribution along z (transverse direction of the plate) as standing waves. The displacements and stresses in terms of potentials are:

$$u_x = u = \frac{\partial \phi}{\partial x} + \frac{\partial \psi}{\partial z}$$

$$u_y = v = 0$$

$$u_z = w = \frac{\partial \phi}{\partial z} + \frac{\partial \psi}{\partial x}$$

$$\sigma_{zx} = \mu\left(\frac{\partial w}{\partial x} + \frac{\partial u}{\partial z}\right)$$

$$\sigma_{zz} = \lambda\left(\frac{\partial u}{\partial x} + \frac{\partial w}{\partial z}\right) + 2\mu\frac{\partial w}{\partial z}$$

2.1-15

Substituting equations (**2.1-14**) into the governing decoupled wave equations, we can solve as:

$$\phi = \boldsymbol{\Phi}(z)e^{i(kx-\omega t)} = [A_1\sin(pz) + A_2\cos(pz)]e^{i(kx-\omega t)}$$

$$\boldsymbol{\psi} = \boldsymbol{\Psi}(z)e^{i(kx-\omega t)} = [B_1\sin(qz) + B_2\cos(qz)]e^{i(kx-\omega t)}$$

2.1-16

where $p^2 = \frac{\omega^2}{c_L^2} - k^2$ and $q^2 = \frac{\omega^2}{c_T^2} - k^2$.

We substitute these solutions into the displacements and stresses in equations (**2.1-16**) and separate variables that are even or odd with respect to z=0 (Bartoli, 2007).

$$\boldsymbol{u_x} = [(\boldsymbol{A_2 ik\, cos}(\boldsymbol{pz}) + \boldsymbol{B_1 q}\,\mathbf{cos}(\boldsymbol{qz})) + (\boldsymbol{A_1 ik\, sin}(\boldsymbol{pz}) - \boldsymbol{B_2 q\, sin}(\boldsymbol{qz}))]\boldsymbol{e^{i(kx-\omega t)}}$$

$$\boldsymbol{u_z} = [-(\boldsymbol{A_2 p\, sin}(\boldsymbol{pz}) + \boldsymbol{B_1 ik}\,\mathbf{sin}(\boldsymbol{qz})) + (\boldsymbol{A_1 p\, cos}(\boldsymbol{pz}) - \boldsymbol{B_2 ik\, cos}(\boldsymbol{qz}))]\boldsymbol{e^{i(kx-\omega t)}}$$

2.1-17

In particular, thanks to the symmetry of the plate geometry, waves, whose displacement in the propagation direction x is odd with respect to z=0, hence proportional to a sinusoidal function, constitute the anti-symmetric modes (second terms of the above equations). Their in-plane particle displacement ($u = u_x$) is asymmetric and their out-of-plane displacement ($w = u_z$) is instead symmetric, as it will be shown in Figure 8. For waves whose u_x is even with respect to z=0, hence proportional to a cosinusoidal function (first terms in the above equations), the in-plane particle displacement $u = u_x$ is symmetric and their out-of-plane displacement ($w = u_z$) is instead asymmetric, as shown in Figure 8. They constitute the symmetric modes. The overall displacement generates a flexural behavior in the anti-symmetric mode and an extensional one for the symmetric mode (see Figure 3).

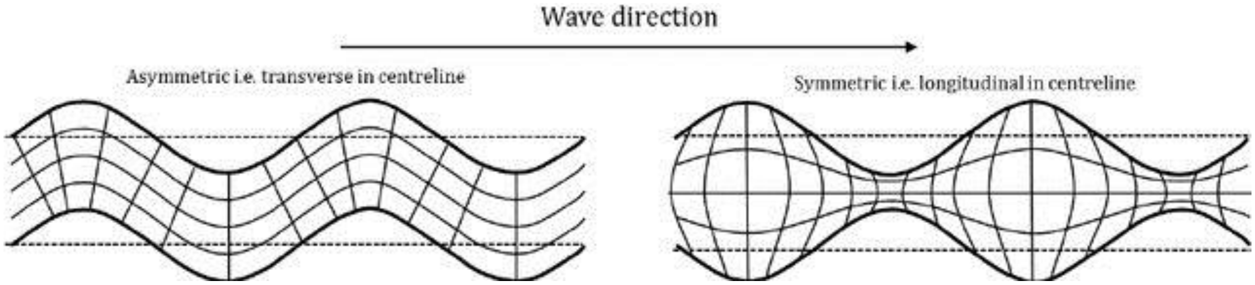

Figure 3 - Displacement in anti-symmetric and symmetric modes

The amplitudes of potentials, displacements and stresses can be found imposing the traction-free boundary conditions:

$$\sigma_{zx} = \sigma_{zz} = 0 \; at \; z = \pm\frac{d}{2} = \pm h$$

2.1-18

where d is the thickness of the plate.

After some manipulations and substitutions into two homogenous equations, imposing the determinant equal to zero to find a non-trivial solution to what is called the characteristic equation, we obtain a transcendental equation for symmetric modes:

$$\frac{\tan(qh)}{\tan(ph)} = -\frac{4k^2pq}{(q^2-k^2)^2}$$

2.1-19

and for antisymmetric modes:

$$\frac{\tan(qh)}{\tan(ph)} = -\frac{(q^2-k^2)^2}{4k^2pq}$$

2.1-20

The solutions to the above equation can be found numerically for k, for a given ω, hence we obtain the wave velocity for every <frequency*thickness> product.

2.2 Analytical and Semi-analytical investigation

For an isotropic Aluminum plate, whose properties are reported in Table 1, the solution of the transcendental equations is shown in Figure 4: a root-finding algorithm searches for the wavenumber that would verify the transcendental equation for given <frequency x thickness> values; the dispersion curves are then computed in terms of phase and group velocities according to eqs.(**2.1-19**) and (**2.1-20**) for both symmetric (blue) and anti-symmetric (red) modes.

Table 1 - Aluminum plate: Material properties

Property Name	Thickness (mm)	Density (kg/m^3)	E_y (GPa)	G_{xy} (GPa)	ν	C_L (m/s)	C_T (m/s)
Property Value	2.688	2700	72.08	26.96	0.3368	6370	3160

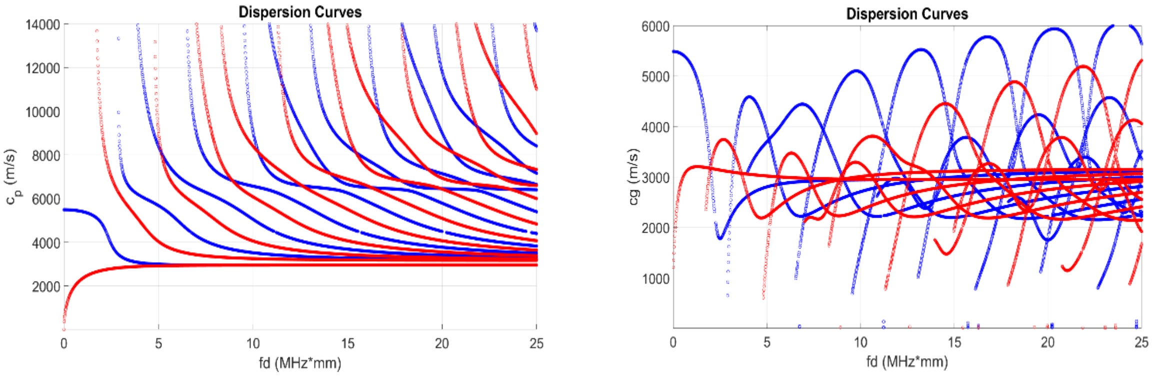

Figure 4 - Analytical Dispersion curves for Aluminum plate in Table 1: (left) phase velocity, (right) group velocity; anti-symmetric modes in red, symmetric modes in blue.

It is possible to notice the dispersive behavior of the propagating modes, especially for the first anti-symmetric mode at low frequencies: the velocity changes rapidly causing higher frequencies to travel faster than the lower ones, until reaching an asymptotic behavior.

To estimate dispersion curves analytically for a multi-layered plate, equivalent properties have to be used. Each ply's local stiffness modulus, shear modulus and Poisson ratio can be reduced into global properties (Fung Y.C., 1965; Jones, 1999), thanks to the transformation below, with respect to the wave propagation system of reference (see Figure 5).

$$C^g = T_\varepsilon^T C\, T_\varepsilon$$

2.2-1

Where C is the stiffness matrix in the lamina local (1-2) coordinates, C^g is the stiffness matrix in the lamina global (x-y-z) coordinates and T_ε is a transformation matrix with respect to ϑ, the angle of rotation of the local system with respect to the global.

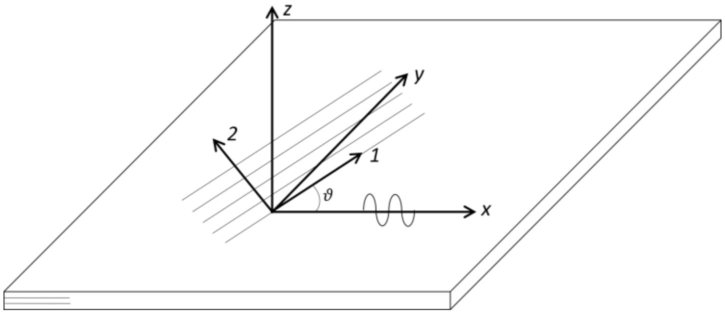

Figure 5 - Local-Global reference system for multi-layered anisotropic plate.

Following the classic laminate plate theory, the global properties at the lamina level are then "weighted" and integrated over the thickness of the laminate to constitute the A, B, D matrices. Such matrices (3x3 for plane stress assumption) establish the relationship between curvatures κ and strains ε, and Forces and Moments, for the whole laminate (Jones, 1999). In particular, A_{ij} establishes the relationship between extensional/shear in-plane loads and deformations, B_{ij} the coupling between out-of-plane and in-plane loads/deformations and D_{ij} the one for bending and twist, as follows:

$$\begin{Bmatrix} N_x \\ N_y \\ N_{xy} \\ M_x \\ M_y \\ M_{xy} \end{Bmatrix} = \begin{bmatrix} A_{ij} & B_{ij} \\ B_{ij} & D_{ij} \end{bmatrix} \begin{Bmatrix} \varepsilon_x \\ \varepsilon_y \\ \gamma_{xy} \\ \kappa_x \\ \kappa_y \\ \kappa_{xy} \end{Bmatrix}$$

2.2-2

From these relationships, the equivalent properties at the laminate level can then be extracted, so that they describe the multi-layered laminate as a homogeneous isotropic plate of the same thickness. If the plate in study is a fiber reinforced polymer, wave propagation phenomena due to fiber/matrix and ply-to-ply interaction, anisotropy given by the fibers' orientation and 3D effects are neglected. Moreover, the reduction of anisotropic laminates to homogeneous isotropic plates doesn't account for skewness and allows decoupling between the Lamb modes and the SH0 mode, which is not true and can only be described by other models (i.e. SAFE) and observed experimentally. As an example, the CFRP laminate with properties described in Table 2 and Table 3 (old panel properties and layup) presents the dispersive behavior shown in Figure 6, when reduced to an equivalent plate (Table 4). From the values corresponding to specific elements in the ABD matrices, it is possible to predict coupling between stresses and strains in different directions and planes:

$$A_{ij} = \begin{bmatrix} 195.70 & 49.73 & 0 \\ 49.73 & 195.70 & 0 \\ 0 & 0 & 59.99 \end{bmatrix}; \;\; B_{ij} = [0]; \;\; D_{ij} = \begin{bmatrix} 140.98 & 20.28 & 6.36 \\ 20.28 & 108.28 & 6.36 \\ 6.36 & 6.36 & 25.47 \end{bmatrix}.$$

For example, being the laminate in analysis quasi-isotropic, it shows the same in-plane stiffness, so that wave propagation along x or y direction should exhibit the same characteristics. Also, matrix B is empty, so mode conversion from an A0 (dominated by out-of-plane displacement) into an S0 (dominated by in-plane displacement) should be reduced. Lastly, being the coefficients A_{16} and A_{26} basically 0, very little coupling should happen between SH0 and S0, and viceversa.

Table 2 - Composite plate: Layup

Material Name	Layup (°)	Thickness Ply (mm)	Density (kg/m^3)
Cytec X840/Z60 6k Weave Fabric	0	0.208	1600
Cytec X840/Z60 12k Tape	[0/45/0/45/90/-45/0/45/90/-45]$_S$	0.142	1600
Cytec X840/Z60 6k Weave Fabric	0	0.208	1600

Table 3 - Composite plate: Material properties

Material Name	E_1 (GPa)	E_2 (GPa)	E_3 (GPa)	G_{12} (GPa)	G_{23} (GPa)	G_{13} (GPa)	ν_{12}	ν_{23}	ν_{13}
Cytec X840/Z60 6k Weave Fabric	80	80	13.8	6.5	4.1	5.1	0.06	0.37	0.50
Cytec X840/Z60 12k Tape	168.2	10.3	10.3	7.0	3.7	7.0	0.27	0.54	0.27

Table 4 - Composite plate: Equivalent material properties

Property Name	Thickness (mm)	E_x (GPa)	E_y (GPa)	G_{xy} (GPa)	ν	C_L (m/s)	C_T (m/s)
Property Value	2.688	48.895	48.895	16.023	0.254	6079	3165

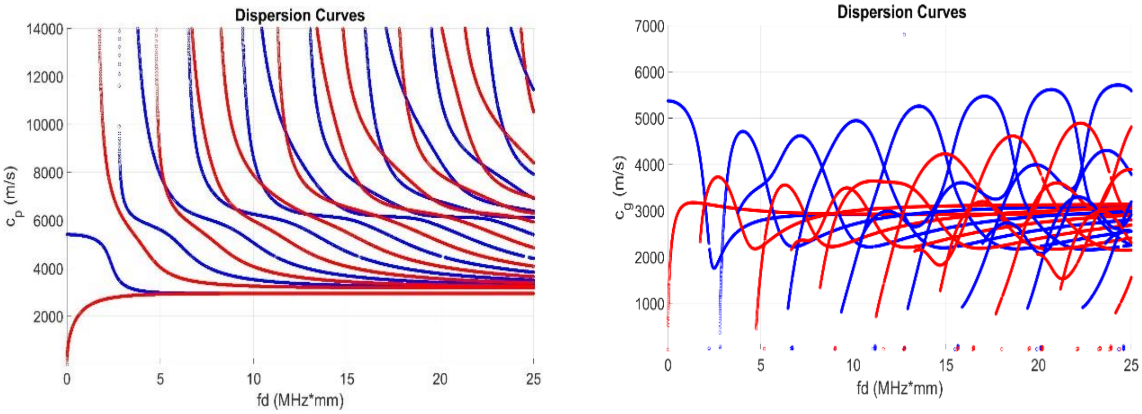

Figure 6 - Analytical Dispersion curves for Composite plate in Table 4Table 1: (left) phase velocity, (right) group velocity; anti-symmetric modes in red, symmetric modes in blue.

Other methods can take into account the anisotropy of these materials. The analytical solution presented above is a simplification and cannot fully capture the entire properties, especially in the transverse plane xz. In fact, the classic laminate theory assumes the Euler Bernoulli theorem and plane stress (Jones, 1999), which is not correct for wave propagation in multi-layered anisotropic plates. In the case of multi-layered plates, more advanced methods need to be employed to compute solutions (dispersion curves and wave amplitudes), as presented in Lowe, where the wave components in each layer have to satisfy coupling at all interfaces. Two main methods have been used: the transfer matrix method, developed by Thompson in 1950, which relates the stresses and displacements at the bottom with those at the top, and transfers them to each layer, and the global matrix method, developed by Knopoff in 1964, that formulates a matrix for the whole layup. The limiting case of three layers reduces the analysis to the wave propagation solution for a thin plate.

UGWs have been described so far by exact solutions based on the superposition of partial bulk waves method, which requires the solution to the differential equations of motions. For waveguides of a generic cross-section or multi-layered structure, numerical methods are more suitable.

Following this approach, wave propagation into single or multi-layered anisotropic plates, as well as in other prismatic waveguides, is also formulated and solved by an eigenvalue problem, but in this case, the solution is approximate, depending on the degrees of freedom/number of modes included in the problem. Semi Analytical methods follow this formulation.

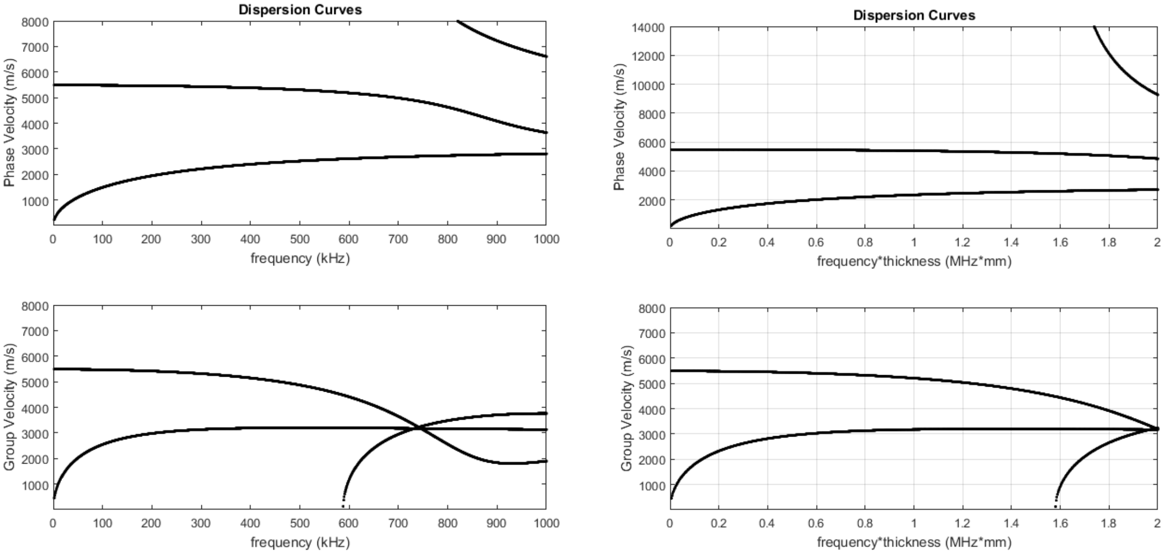

Figure 7 - SAFE Dispersion curves for Aluminum plate: (top) phase velocity, (bottom) group velocity.

A detailed description of the Semi Analytical Finite Element (SAFE) method can be found in Hayashi and Rose (2003) and Bartoli (Bartoli et al., 2005; Bartoli, 2007), for an unforced solution, and in Marzani, for the forced one. We report in Section 2.4.3 the fundamental steps. The main idea behind this method is to discretize only the cross-section of the waveguide by the well-known Finite Element (FE) method, to relate mass and stiffness properties to displacements and forces for node and elements in a defined geometry. The eigenvalue problem can be then formulated to express harmonic wave propagation in one direction, analytically, following the normal mode decomposition approach. The dispersion relation is found as wavenumbers for a range of frequencies and as wavemodes along the thickness of the waveguide. We report here the solution for an Aluminum plate of the same properties as above, in terms of dispersion curves (Figure 7) and modeshapes (Figure 8), for elastic wave propagation.

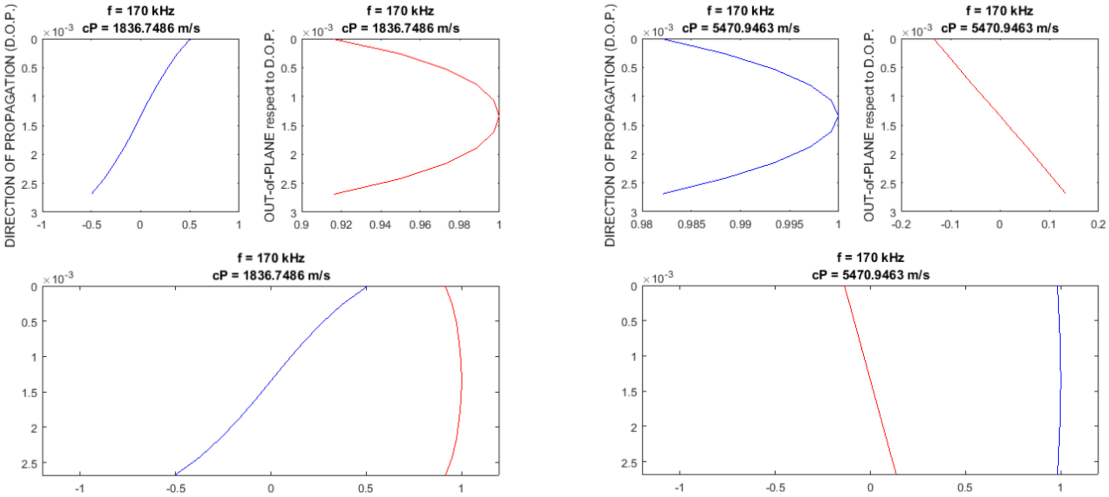

Figure 8 - In-plane (blue) and out-of-plane (red) displacements for modeshapes of A0 (left) and S0 (right) at 170 kHz for Aluminum plate.

It is worth noting here the typical in-plane and out-of-plane displacement distribution along the thickness of the plate, described above, for the first modes: Figure 8 shows the modeshapes at 170 kHz for the first antisymmetric mode A0 (left) and symmetric mode S0 (right). The antisymmetric mode is dominated by the out of plane displacement, that forces the particles to move in the same direction with respect to the midplane, establishing a flexural behavior. The symmetric modeshapes instead is mainly dominated by a symmetric in-plane displacement, generating a mode of the extensional type. The higher the order of the mode, the more complex will be the distribution of the displacements along the thickness, besides the frequency also affecting them. The modeshapes influence the interaction of the propagating wave with the geometrical features of the plate (or waveguide in general), hence their particle motion can be used to aim at specific interactions (i.e. surfaces or internal) and their excitation and reception has to be maximized accounting for their distribution. These observations will be used along this work to design and interpret experiments.

SAFE can accommodate anisotropic and multilayered plates and offers the advantage of easily accessing the laminae stiffness properties to study guided wave propagation for a variety of cases.

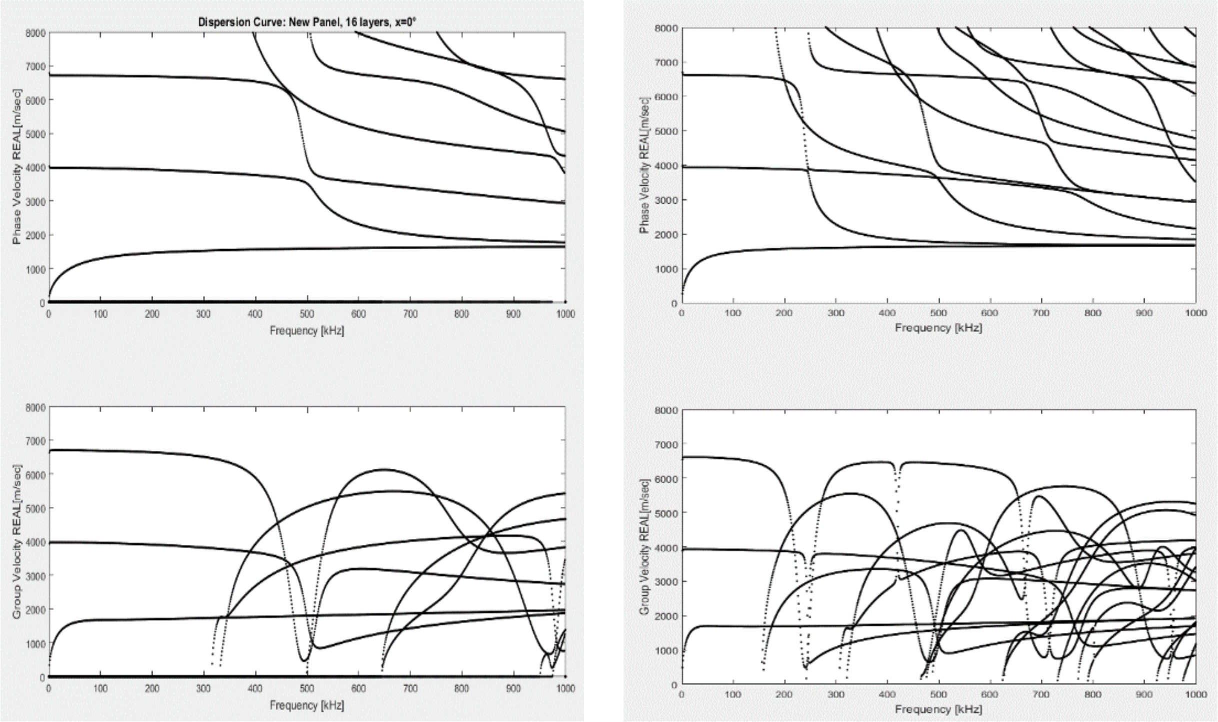

Figure 9 - SAFE Dispersion curves for Composite plate in Table 2: (top) phase velocity, (bottom) group velocity; (left) single laminate thickness, (right) double laminate thickness.

Parametric studies and/or inversion with respect to the experimental data can be performed to solve for laminate thickness, ply orientation and elastic constants, together with different wave propagation directions and frequency ranges. The left plot in Figure 9 shows the dispersion curves obtained with SAFE for the composite laminate in Table 2, along with its modeshapes in Figure 10, where we can observe the distribution of the displacements along the thickness of the laminate.

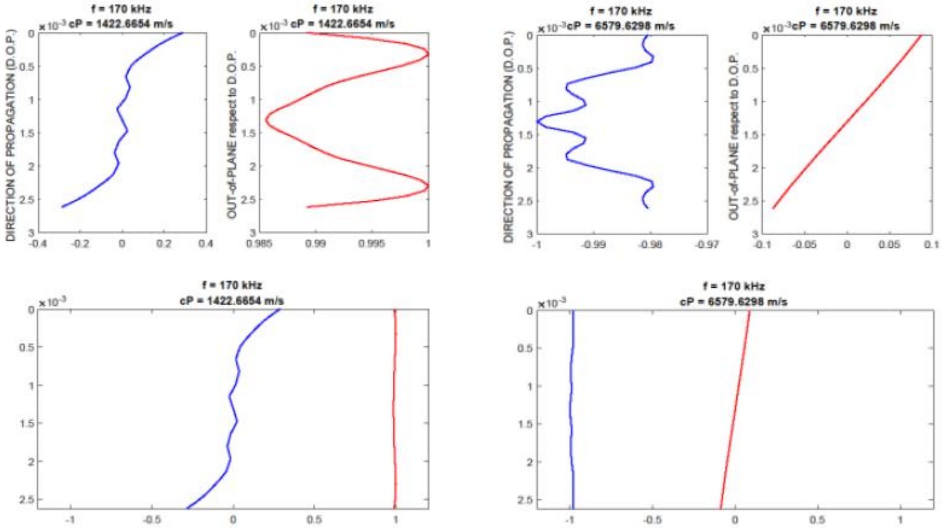

Figure 10 - In-plane (blue) and out-of-plane (red) displacements for modeshapes of A0 (left) and S0 (right) at 170 kHz for Composite plate.

The thickness of the plate affects the dispersion behavior, as it can be appreciated in Figure 9: the right plots belong to the same laminate in the left, in terms of material properties and orientation of the plies, but the specimen is now composed of two laminates, so that the thickness is twice the one in the left plots. The modes “shift” to the left, appearing at lower frequencies. The shift of the cut-off frequencies of modes can be used to infer plate thickness or the presence of defects/disbonds.

To be noted is also the presence of an additional mode type, the shear horizontal mode SH0: we are showing it in here for completeness, since it is not correct to decouple the in-plane displacements (x and y directions) due to the ply orientation and anisotropic behavior of the CFRP. Also, the skewness effect is neglected here and in the experimental tests presented in the next sections, thanks to the quasi-isotropic layup of the composite laminate in consideration and the observation of wave propagation in the direction corresponding to one of the principle directions of material symmetry.

The modeshapes are shown in Figure 10 and maintain the same antisymmetric/symmetric properties of those shown for an isotropic material (Aluminum). The discontinuity in the elastic properties along the thickness, due to the different ply orientation, though, can be appreciated in the deviation of both in-plane and out-of-plane displacements from low order polynomial trends.

An interesting study can be done when altering the stiffness properties at different plies and at different locations along the thickness of the laminate. For example, Figure 11 and Figure 12 show the results for the same CFRP laminate, when the stiffness matrix C is reduced to 5% at the first three top plies.

The reduction in the superficial stiffness manifests itself in the modeshape, where a discontinuity along the displacement distribution appears for both in plane and out of plane displacements, when the structure is excited by either the antisymmetric (left) or symmetric (right) mode.

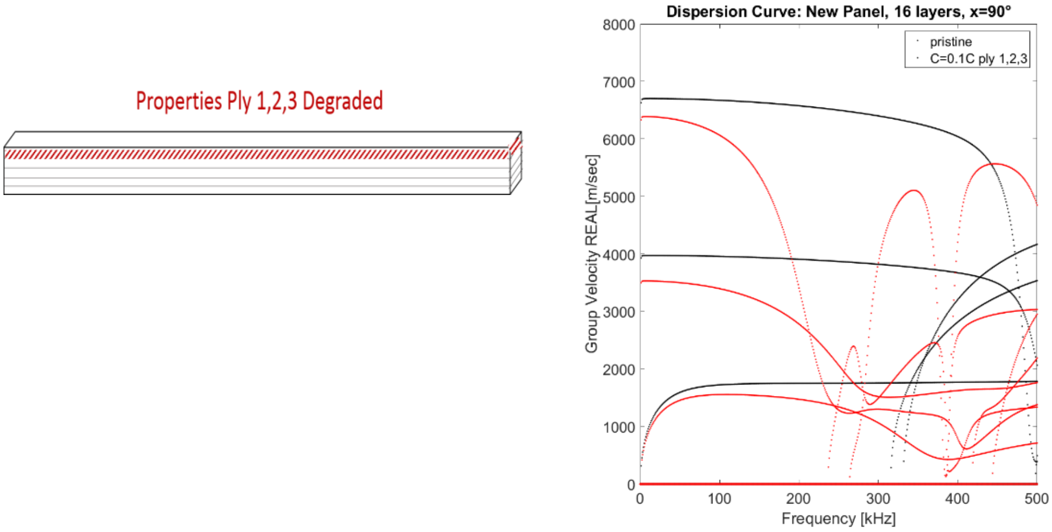

Figure 11 - SAFE Dispersion curves for Composite plate (group velocity): comparison pristine (black) and altered top surface layers (red).

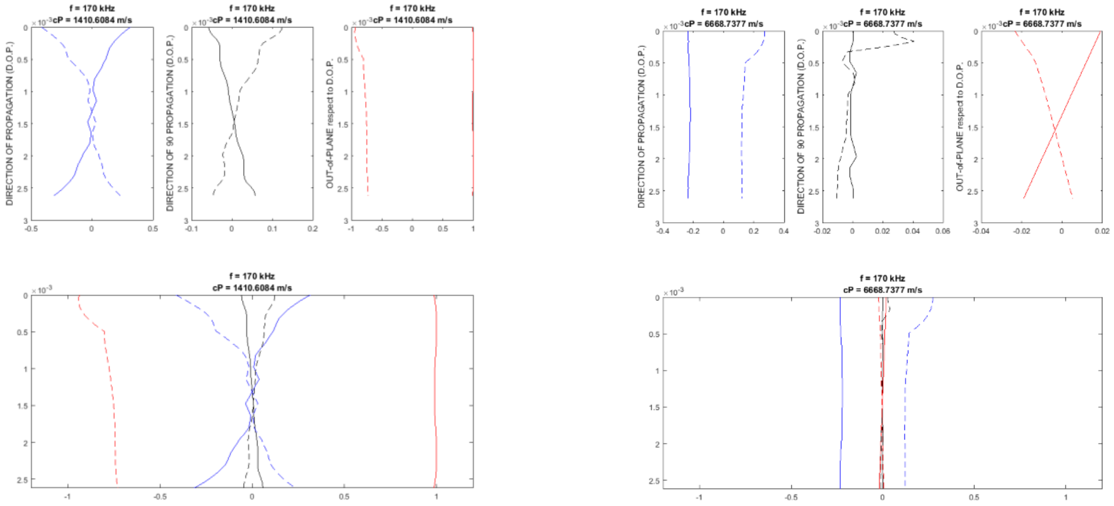

Figure 12 - In-plane (blue and black) and out-of-plane (red) displacements for modeshapes of A0 (left) and S0 (right) modes for Composite plates: comparison pristine (solid) and altered surface layers (dashed).

The case of a 95% reduction in stiffness at the central plies is instead studied in Figure 13:

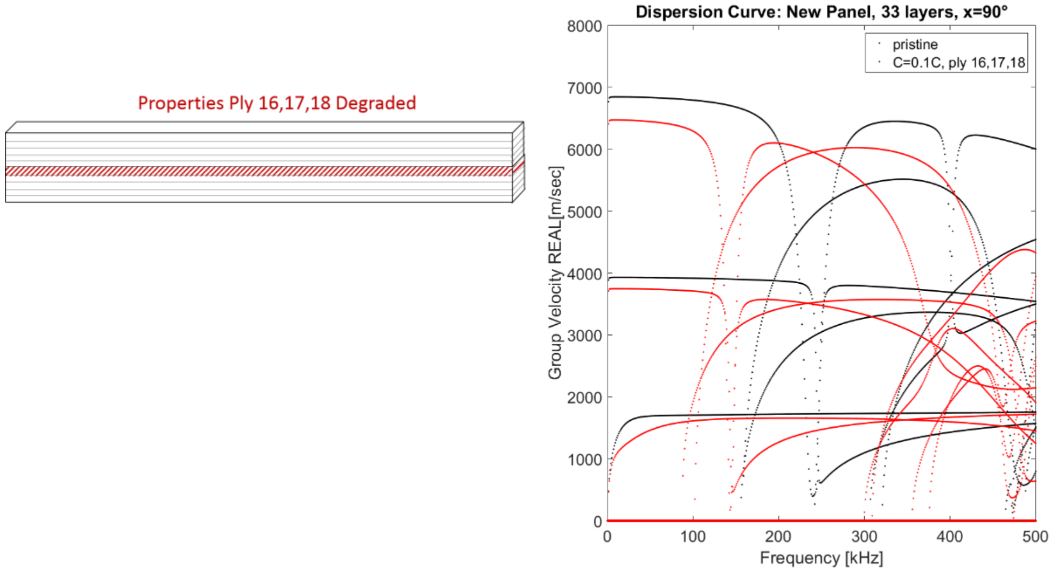

Figure 13 - SAFE Dispersion curves for Composite plate (group velocity): comparison pristine (black) and altered middle layers (red).

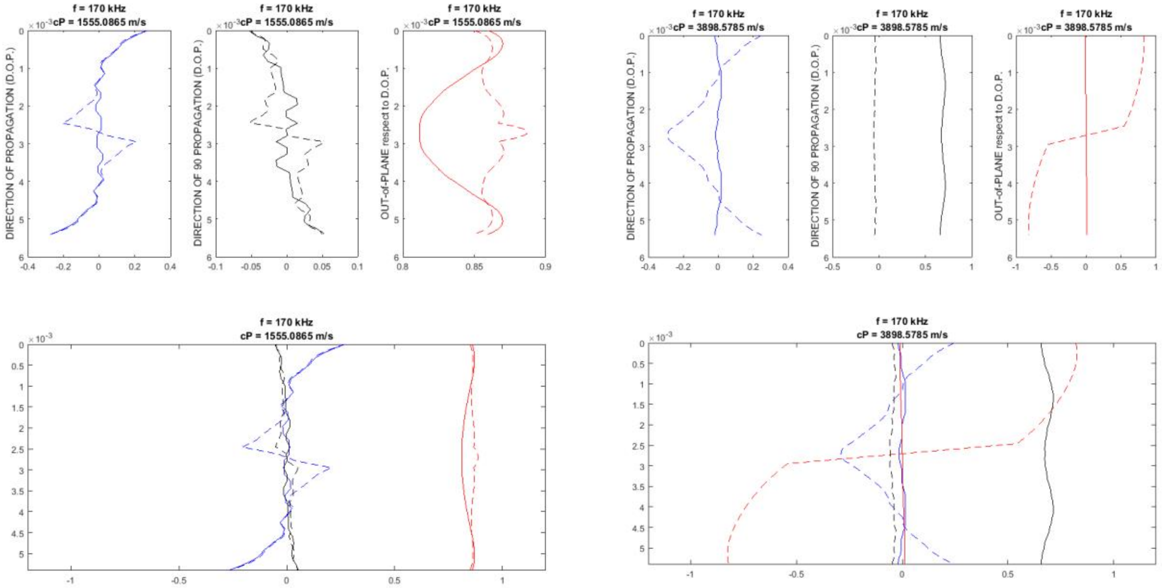

Figure 14 - In-plane (blue and black) and Out-of-plane (red) displacements for modeshapes A0 (left) and SH0 (right) modes for Composite plates: comparison pristine (solid) and altered middle layers (dashed).

The sensitivity of the wave propagation behavior to the lamina's elastic properties can be particularly observed in the modeshapes (Figure 14), where a strong discontinuity in the displacements can be again noticed in correspondence of the plies with reduced stiffness. The SH0 mode in particular excites this kind of defect, due to its shear in-plane nature, that couples very well with this "disbond-like" case study.

These observations show the importance of wave propagation understanding and prediction and the potential of Ultrasonic Guided Waves (UGWs) to inspect structures, infer structural changes and quantitatively inform, beyond qualitative visual inspection.

2.3 Global-Local model to predict scattering of guided elastic waves

2.3.1 Problem formulation

The present paper builds on the work by Srivastava and Lanza di Scalea (2010) to unify the global (SAFE) -local (FE) formulation and implement it in a computationally efficient code able to solve extremely complex scattering problems such as layered composite laminates with built-up geometries. The method is applied to studying guided wave scattering in a composite skin-to-stringer assembly that is widely used in modern aircraft construction. The Global-Local method formulated here allows to efficiently predict reflection and transmission spectra of the relevant guided wave modes that can be utilized for an optimized NDE or SHM test of the structure. Despite the criticality of skin-to-stinger assemblies in aircraft and the consequent high need for inspections (Capriotti et al., 2017), the authors are not aware of any previous quantitative study aimed at predicting wave scattering from defects in these components. The reason is the material and geometrical complexity of this assembly, that instead presents a great opportunity for the proposed Global-Local formulation.

Let us consider the general scattering case shown in Figure 15. An incident time harmonic guided wave travelling along the *x* positive direction in a prismatic region (global region) is scattered into reflected and transmitted waves after interacting with a (local) region with geometrical discontinuities (e.g. build-ups) and/or structural defects (e.g. cracks, delaminations, etc..).

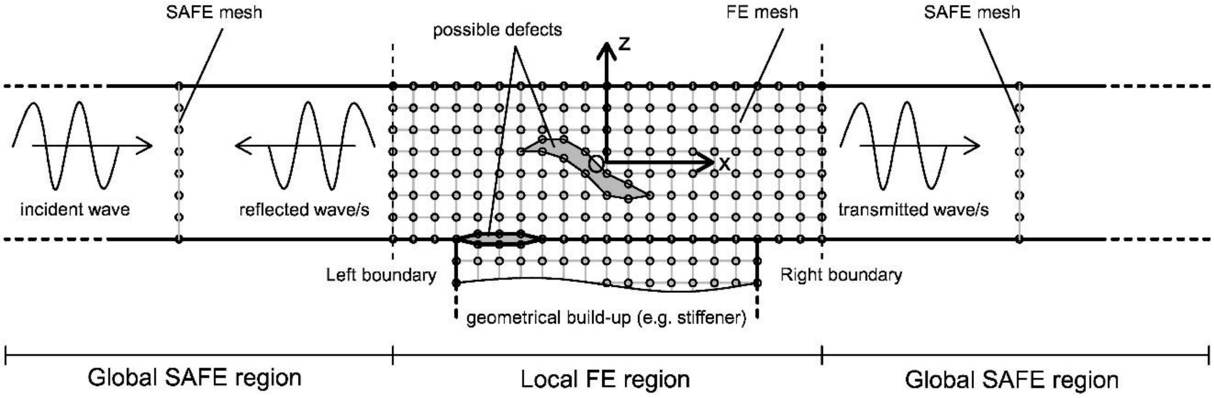

Figure 15 - Geometrical representation of the scattering of an incident wave in a waveguide prismatic structure in reflected and transmitted waves from a local region with geometrical and/or material discontinuities.

The equilibrium of each part of the problem is guaranteed by the Principle of Virtual Work (PVW). The general weak form for the harmonic elasto-dynamic case, written considering virtual displacements and strains, is (in Voigt’s notation):

$$\int_{\Omega} \delta\bar{\boldsymbol{\varepsilon}}^T \boldsymbol{\sigma}\, d\Omega = \int_{\Gamma_t} \delta\bar{\mathbf{u}}^T \mathbf{t}\, d\Gamma - \int_{\Omega} \delta\bar{\mathbf{u}}^T \left(\rho\, \ddot{\mathbf{u}}\right) d\Omega \tag{1}$$

where $\mathbf{u} = \begin{bmatrix} u_x & u_y & u_z \end{bmatrix}^T$, $\mathbf{t} = \begin{bmatrix} t_x & t_y & t_z \end{bmatrix}^T$, $\boldsymbol{\varepsilon} = \begin{bmatrix} \varepsilon_x & \varepsilon_y & \varepsilon_z & \gamma_{yz} & \gamma_{xz} & \gamma_{xy} \end{bmatrix}^T$, and $\boldsymbol{\sigma} = \begin{bmatrix} \sigma_x & \sigma_y & \sigma_z & \tau_{yz} & \tau_{xz} & \tau_{xy} \end{bmatrix}^T$ are displacement, traction, strain and stress vectors respectively. All these variables are space and time dependent. In Eq. (1) the bar above a letter stands for complex conjugate, while $\ddot{\mathbf{u}}$ is the acceleration, ρ the density, Ω the volume of the medium and Γ_t the medium's loaded external surface. In this work, body forces and damping effects are neglected.

In order to model both reflections and transmissions, the entire domain Ω is subdivided into one "local" region in the center and two "global" regions on either side. Figure 15 shows a plain strain case (that is assumed in the application problem studied in this paper), where the cross-sectional SAFE discretization of the global waveguide reduces to a 1D mesh along *z*, and a full FE mesh is instead used in 2D domain (*x*-*z* plane) for the local region. The extension of the concept to a general 3D case is trivial (2D SAFE discretization in the global region and 3D FE discretization in the local region). The GL formulation as written here applies to a general 3D case.

Let us imagine separating the local region from the global region at their left and right boundaries of Figure 15. Since equilibrium must continue to hold, internal tractions arise at each boundary due to the internal stress caused by the application of external actions. Using the PVW for each region, the traction vector **t** in Eq. (1) consists of the internal tractions at the boundaries, which behave as new external forces. The vector **t** could be evaluated as $\mathbf{t} = \boldsymbol{\sigma}\,\mathbf{n}$, with **n** the unit vector normal to the Γ_t surface and $\boldsymbol{\sigma}$ the stress second-order tensor. Alternatively, using Voigt notation:

$$\mathbf{t} = \mathbf{L}_n^T\, \boldsymbol{\sigma} \tag{2}$$

where

$$\mathbf{L}_n = \begin{bmatrix} n_x & 0 & 0 \\ 0 & n_y & 0 \\ 0 & 0 & n_z \\ 0 & n_z & n_y \\ n_z & 0 & n_x \\ n_y & n_x & 0 \end{bmatrix} \tag{3}$$

with n_x, n_y, n_z the direction cosines of the normal $\mathbf{n}$. In what follows, a superscript 'ℓ' or 'g' is adopted to identify quantities referring to the "local" region or the "global" region, respectively.

The local region is discretized by 2D or 3D finite elements. Accordingly, the approximate displacement $\mathbf{u}_h^{\ell-e}$ at a point inside the local e-th element is obtained from the nodal values $\mathbf{d}^{\ell-e}$ through the shape functions $\mathbf{N}^{\ell}$ using known FE concepts:

$$\mathbf{u}_h^{\ell-e}\left(x,y,z,t\right)=\mathbf{N}^{\ell}\left(x,y,z\right)\mathbf{d}^{\ell-e}\,e^{-i\omega t} \tag{4}$$

where ω is the circular frequency.

The corresponding approximate strains and stresses are

$$\boldsymbol{\varepsilon}_h^{\ell-e}=\mathbf{L}\,\mathbf{u}_h^{\ell-e} \tag{5}$$

$$\boldsymbol{\sigma}_h^{\ell-e}=\mathbf{C}^{\ell-e}\,\boldsymbol{\varepsilon}_h^{\ell-e} \tag{6}$$

where $\mathbf{L}$ and $\mathbf{C}^{\ell-e}$ are the compatibility and constitutive matrices respectively, with $\mathbf{C}^{\ell-e}$ a real matrix for purely elastic cases, and a complex matrix for viscoelastic cases.

Including all the approximate variables in Eq. (1) and defining the vector $\mathbf{U}^{\ell}$ for the entire nodal local displacements, the dynamic undamped equilibrium equations for the local region are obtained as:

$$\left(\mathbf{K}^{\ell}-\omega^{2}\,\mathbf{M}^{\ell}\right)\mathbf{U}^{\ell}=\mathbf{F}^{\ell}, \tag{7}$$

with $\mathbf{K}^{\ell}$, $\mathbf{M}^{\ell}$ and $\mathbf{F}^{\ell}$ the classic FE stiffness matrix, mass matrix and force vector.

To interpolate the displacements of the global region, the same procedure is followed, but in a simplified manner. The SAFE method adopts a harmonic exponential term, $e^{i(\xi x-\omega t)}$, to describe analytically the wave behaviour in the wave propagation direction, *x*, where ξ represents the wave number. By combining the analytical solution along the wave propagation with an FE cross-sectional (*y*-*z*) discretization, the approximate displacement $\mathbf{u}_{h}^{\mathrm{g}-e}$ within a single SAFE element of the global region can be written as:

$$\mathbf{u}_{h}^{\mathrm{g}-e}\left(x,y,z,t\right)=\mathbf{N}^{\mathrm{g}}\left(y,z\right)\,\mathbf{d}^{\mathrm{g}-e}\,e^{i\left(\xi x-\omega t\right)} \tag{8}$$

with $\mathbf{d}^{\mathrm{g}-e}$ the nodal displacements and $\mathbf{N}^{\mathrm{g}}$ the shape functions of the global cross-sectional mesh.

Following the same steps discussed in Bartoli et al. (2006) or in Rose (2014), the expression of the approximate strain vector in SAFE is derived as:

$$\boldsymbol{\varepsilon}_{h}^{\mathrm{g}-e}=\left(\mathbf{B}_{1}+i\,\xi\,\mathbf{B}_{2}\right)\mathbf{d}^{\mathrm{g}-e}e^{i\left(\xi x-\omega t\right)} \tag{9}$$

where

$$\mathbf{B}_{1}=\mathbf{L}_{y}\mathbf{N}_{,y}^{g}+\mathbf{L}_{z}\mathbf{N}_{,z}^{g}\qquad\text{and}\qquad\mathbf{B}_{2}=\mathbf{L}_{x}\mathbf{N}^{g} \tag{10}$$

are two compatibility matrices.

In Eq. (10) $\mathbf{L}_{x}$, $\mathbf{L}_{y}$ and $\mathbf{L}_{z}$ are particularized expressions of $\mathbf{L}_{n}$ given in Eq. (3) for a unit normal vector aligned to the *x*, *y* or *z* axis respectively, while $\mathbf{N}_{,y}^{\mathrm{g}}$ and $\mathbf{N}_{,z}^{\mathrm{g}}$ are the derivatives of the global shape function matrix with respect to the *y* or *z* coordinates. Approximate strains are then transformed into approximate stresses by applying the constitutive laws

$$\boldsymbol{\sigma}_h^{\mathrm{g}-e} = \mathbf{C}^{\mathrm{g}-e}\,\boldsymbol{\varepsilon}_h^{\mathrm{g}-e} \tag{11}$$

with $\mathbf{C}^{\mathrm{g}-e}$ the element constitutive matrix for the global region.

It is worth noting that in Eqs. (6) and (11) the constitutive matrices must refer to the (O, *x*, *y*, *z*) reference system. Therefore, for anisotropic materials, any local stiffness matrix $\tilde{\mathbf{C}}$ (e.g. lamina in the principal directions of material symmetry) needs to be transformed to the general (O, *x*, *y*, *z*) system **C** according to

$$\mathbf{C} = \mathbf{R}^T \tilde{\mathbf{C}}\,\mathbf{R} \tag{12}$$

with **R** the transformation matrix.

For the particular case of a laminated composite whose lamina is oriented at an angle ϑ with respect to the *x* direction, the transformation matrix is:

$$\mathbf{R} = \begin{bmatrix} m^2 & n^2 & 0 & 0 & 0 & mn \\ n^2 & m^2 & 0 & 0 & 0 & -mn \\ 0 & 0 & 1 & 0 & 0 & 0 \\ 0 & 0 & 0 & m & -n & 0 \\ 0 & 0 & 0 & n & m & 0 \\ -2mn & 2mn & 0 & 0 & 0 & m^2 - n^2 \end{bmatrix} \tag{13}$$

with $m = \cos\vartheta$ and $n = \sin\vartheta$.

With Eqs. (8)-(11) and (2) at hand, the PVW applied to the semi-infinite global region gives:

$$\left(\mathbf{K}^{\mathrm{g}} - \omega^2 \mathbf{M}^{\mathrm{g}}\right)\mathbf{U}^{\mathrm{g}} = \mathbf{F}^{\mathrm{g}} \tag{14}$$

where $\mathbf{U}^{\mathrm{g}}$ is the vector collecting the displacements of all the nodes of the global region mesh. Furthermore:

$$\mathbf{K}^{\mathrm{g}} = \mathop{\mathrm{A}}_{e=1}^{n_{el}} \int_{\Omega^{\mathrm{g}-e}} \left(\mathbf{B}_1 - i\,\xi\,\mathbf{B}_2\right)^T \mathbf{C}^{\mathrm{g}-e} \left(\mathbf{B}_1 + i\,\xi\,\mathbf{B}_2\right) d\Omega \tag{15}$$

$$\mathbf{M}^{\mathrm{g}} = \mathop{\mathrm{A}}_{e=1}^{n_{el}} \int_{\Omega^{\mathrm{g}-e}} \left(\mathbf{N}^{\mathrm{g}}\right)^T \rho^e\, \mathbf{N}^{\mathrm{g}}\, d\Omega \tag{16}$$

$$\mathbf{F}^{\mathrm{g}} = \left[\mathop{\mathrm{A}}_{e=1}^{n_{el}} \int_{\Gamma_t^{\mathrm{g}-e}} \left(\mathbf{N}^{\mathrm{g}}\right)^T \mathbf{L}_n^T\, \mathbf{C}^{\mathrm{g}-e} \left(\mathbf{B}_1 + i\,\xi\,\mathbf{B}_2\right) d\Gamma\right] \mathbf{U}^{\mathrm{g}} \tag{17}$$

are the stiffness matrix, mass matrix and force vector, respectively.

In Eqs. (15)-(17) $\mathop{\mathrm{A}}_{e=1}^{n_{el}}$ symbolizes the assembly operator, with n_{el} the total number of elements.

Referring again to the scattering case of Figure 15, it can be assumed that the nodal displacements $\mathbf{q}_{l\,B}$ recorded at the left boundary is a combination of the incident wave and the reflected waves. The nodal displacements $\mathbf{q}_{r\,B}$ at the right boundary, instead, are those of the transmitted waves. Hence:

$$\begin{gathered}\mathbf{q}_{l\,B} = \mathbf{q}_{incident} + \mathbf{q}_{reflected}\,, \\ \mathbf{q}_{r\,B} = \mathbf{q}_{transmitted}\,.\end{gathered} \tag{18}$$

In the subject case of multimode guided waves, the incident, reflected and transmitted waves can be thought of as the superimposition of a finite number N_M of global cross-sectional mode shapes, each amplified by a participation coefficient having the physical meaning of the amplitude of the single wave mode.

The incident mode can be modelled by imposed displacements or forces at the source. In the present paper, a pure incident mode is generated by imposing the unique cross-sectional displacement shapes at the relevant frequencies for the chosen mode. The evaluation of the unique mode shapes is performed by solving an eigenproblem, that is shown in the next section. If the symbol $\mathbf{\Phi}$ is used to represent the generic mode shape, and the factor $e^{-i\omega t}$ is omitted for simplicity, Eqs. (18) are explicitly rewritten as:

$$\mathbf{q}_{l\,B} = \mathbf{\Phi}_{in}^{+} e^{i\left[\xi_{in}^{+}\left(d_s - x_{l\,B}\right)\right]} + \sum_{j=1}^{N_M} A_j^{-} \mathbf{\Phi}^{(j)^{-}} e^{i\left(-\xi_j^{-} x_{l\,B}\right)} \tag{19}$$

$$\mathbf{q}_{r\,B} = \sum_{j=1}^{N_M} A_j^{+} \mathbf{\Phi}^{(j)^{+}} e^{i\left(\xi_j^{+} x_{r\,B}\right)} \tag{20}$$

where the superscript “+” represents a wave travelling in the right and the superscript “-” a wave travelling in the left direction. Therefore: $\mathbf{\Phi}_{in}^{+}$ and ξ_{in}^{+} are mode shape and wavenumber of the incident wave (assumed at unity amplitude); A_j^{-}, $\mathbf{\Phi}^{(j)^{-}}$ and ξ_j^{-} are amplitude, mode shape and wavenumber of the *j*-th reflected mode; and A_j^{+}, $\mathbf{\Phi}^{(j)^{+}}$ and ξ_j^{+} amplitude, mode shape and wavenumber of the *j*-th transmitted mode. d_s, $x_{l\,B}$ and $x_{r\,B}$ measure the distances of the source, left boundary and right boundary, respectively, from the origin of the reference system that is set at the center of the local region (see Figure 15).

Eqs. (19) and (20) can be rewritten in a compact form:

$$\mathbf{q}_{l\,B} = \mathbf{\Phi}_{in}^{+} e^{i\left[\xi_{in}^{+}\left(d_s - x_{l\,B}\right)\right]} + \mathbf{G}^{-} \mathbf{D}^{-} \tag{21}$$

$$\mathbf{q}_{r\,B} = \mathbf{G}^{+} \mathbf{D}^{+} \tag{22}$$

where

$$\mathbf{G}^{\pm} = \begin{bmatrix} \mathbf{\Phi}^{(1)^{\pm}} & \mathbf{\Phi}^{(2)^{\pm}} & \cdots & \mathbf{\Phi}^{(j)^{\pm}} & \cdots & \mathbf{\Phi}^{(N_M)^{\pm}} \end{bmatrix} \tag{23}$$

$$\mathbf{D}^{\pm} = \left[D_1^{\pm} \quad D_2^{\pm} \quad \cdots \quad D_j^{\pm} \quad \cdots \quad D_{N_M}^{\pm} \right]^T , \tag{24}$$

with

$$D_j^{+} = A_j^{+} \, e^{i\left(\xi_j^{+} x_{r\,B}\right)} \tag{25}$$

$$D_j^{-} = A_j^{-} \, e^{i\left(-\xi_j^{-} x_{l\,B}\right)} . \tag{26}$$

Eqs. (21) and (22) are entirely composed of known terms, except for the $A_j^{\pm}$ amplitudes. These equations also guarantee the continuity of displacements between the global and the local regions. The evaluation of $A_j^{\pm}$ is therefore performed in order to also guarantee the continuity of tractions at the left and the right boundaries.

Let us recall the equilibrium Eq. (7) for the local region. A partition of Eq. (7) can be performed in order to separate the contribution of the inner (I) and boundary (B) degrees of freedom, obtaining:

$$\begin{bmatrix} \mathbf{S}_{II} & \mathbf{S}_{IB} \\ \mathbf{S}_{BI} & \mathbf{S}_{BB} \end{bmatrix} \begin{bmatrix} \mathbf{U}_I^{\ell} \\ \mathbf{U}_B^{\ell} \end{bmatrix} = \begin{bmatrix} \mathbf{0} \\ \mathbf{F}_B^{\ell} \end{bmatrix} \tag{27}$$

where

$$\mathbf{S} = \mathbf{K}^{\ell} - \omega^2 \mathbf{M}^{\ell} , \tag{28}$$

$$\mathbf{U}_B^{\ell} = \left[\mathbf{q}_{l\,B}^{T} \quad \mathbf{q}_{r\,B}^{T} \right]^T , \tag{29}$$

$$\mathbf{F}_B^{\ell} = \left[\left(\mathbf{f}_{l\,B}^{\ell}\right)^T \quad \left(\mathbf{f}_{r\,B}^{\ell}\right)^T \right]^T . \tag{30}$$

In Eq. (30) $\mathbf{f}_{l\,B}^{\ell}$ and $\mathbf{f}_{r\,B}^{\ell}$ are the force vectors at the left and right boundaries. They are obtained as the opposites of the consistent nodal force vectors at the same boundaries but considered as belonging to the global regions.

From Eq. (17), for a unit normal vector **n** identifying the positive or negative directions of the *x* axis ($\mathbf{n}=\begin{bmatrix}\pm 1 & 0\end{bmatrix}^T$), the consistent nodal force vectors for the two global regions are equal to:

$$\mathbf{F}_{lB}^{\mathrm{g}}=\mathbf{F}_{in}^{+}\,e^{i\left[\xi_{in}^{+}\left(d_s-x_{lB}\right)\right]}+\mathbf{F}^{-}\,\mathbf{D}^{-} \tag{31}$$

$$\mathbf{F}_{rB}^{\mathrm{g}}=\mathbf{F}^{+}\,\mathbf{D}^{+} \tag{32}$$

where

$$\mathbf{F}^{\pm}=\begin{bmatrix}\mathbf{F}^{(1)^{\pm}} & \mathbf{F}^{(2)^{\pm}} & \cdots & \mathbf{F}^{(j)^{\pm}} & \cdots & \mathbf{F}^{(N_M)^{\pm}}\end{bmatrix} \tag{33}$$

and

$$\mathbf{F}_{in}^{+}=\left[\mathop{\mathrm{A}}_{e=1}^{n_{el}}\int_{\Gamma_{t_B}^{\mathrm{g}-e}}\left(\mathbf{N}^{\mathrm{g}}\right)^{T}\mathbf{L}_x^{T}\,\mathbf{C}^{\mathrm{g}-e}\left(\mathbf{B}_1+i\,\xi_{in}^{+}\,\mathbf{B}_2\right)d\Gamma\right]\mathbf{\Phi}_{in}^{+}\,, \tag{34}$$

with

$$\mathbf{F}^{(j)^{\pm}}=\mp\left[\mathop{\mathrm{A}}_{e=1}^{n_{el}}\int_{\Gamma_{t_B}^{\mathrm{g}-e}}\left(\mathbf{N}^{\mathrm{g}}\right)^{T}\mathbf{L}_x^{T}\,\mathbf{C}^{\mathrm{g}-e}\left(\mathbf{B}_1+i\,\xi_{j}^{\pm}\,\mathbf{B}_2\right)d\Gamma\right]\mathbf{\Phi}^{(j)^{\pm}}\,. \tag{35}$$

From Eqs. (31) and (32) $\mathbf{f}_{lB}^{\ell}$ and $\mathbf{f}_{rB}^{\ell}$ are obtained as:

$$\mathbf{f}_{lB}^{\ell}=-\mathbf{F}_{lB}^{\mathrm{g}},\qquad \mathbf{f}_{rB}^{\ell}=-\mathbf{F}_{rB}^{\mathrm{g}}. \tag{36}$$

A static condensation procedure applied to Eq. (27) leads to the following final equations:

$$\left(\mathbf{S}_{BB}^{*}\begin{bmatrix}\mathbf{G}^{-} & \mathbf{0}\\ \mathbf{0} & \mathbf{G}^{+}\end{bmatrix}+\begin{bmatrix}\mathbf{F}^{-} & \mathbf{0}\\ \mathbf{0} & \mathbf{F}^{+}\end{bmatrix}\right)\begin{bmatrix}\mathbf{D}^{-}\\ \mathbf{D}^{+}\end{bmatrix}=-\left(\mathbf{S}_{BB}^{*}\begin{bmatrix}\mathbf{\Phi}_{in}^{+}\\ \mathbf{0}\end{bmatrix}+\begin{bmatrix}\mathbf{F}_{in}^{+}\\ \mathbf{0}\end{bmatrix}\right)e^{i\left[\xi_{in}^{+}\left(d_s-x_{l\mathbf{B}}\right)\right]} \tag{37}$$

where $\mathbf{S}_{BB}^{*} = \mathbf{S}_{BB} - \mathbf{S}_{BI}\,\mathbf{S}_{II}^{-1}\,\mathbf{S}_{IB}$ is the condensed matrix of **S**.

Eq. (37) is solved to find $\mathbf{D}^{-}$ and $\mathbf{D}^{+}$. Since the coefficient matrix is not square, the least squares method should be applied. Once the $\mathbf{D}^{-}$ and $\mathbf{D}^{+}$ coefficients are known, the unknown A_j^{-} and A_j^{+} reflected and transmitted amplitudes can be finally determined.

As seen in the previous section, the GL method exploits the knowledge of at least N_M mode shapes of the guided waves. These are derived as the (unforced) solutions of the equilibrium Eqs. (14) for the global region, which can be particularized as

$$\left[\mathbf{K}_1 + i\,\xi\,\mathbf{K}_2 + \xi^2\mathbf{K}_3 - \omega^2\mathbf{M}^{g}\right]_M \boldsymbol{\Phi} = \mathbf{0} \tag{38}$$

with M the number of total degrees of freedom for the global region mesh.

The stiffness matrices $\mathbf{K}_j\ \left(j = 1, 2, 3\right)$ are derived from Eq. (15) and explicitly given by Bartoli et al. (2006). Eq. (38) constitutes a generalized eigenproblem in □ and □. It is a common practice to reduce Eq. (38) to a linear eigenproblem in □ by doubling the size of the problem:

$$\left[\mathbf{A} - \xi\,\mathbf{B}\right]_{2M} \mathbf{Q} = \mathbf{0} \tag{39}$$

where $\mathbf{Q} = \begin{bmatrix} \boldsymbol{\Phi} \\ \xi\,\boldsymbol{\Phi} \end{bmatrix}$. **A** and **B** are known matrices for fixed values of the circular frequency □. Their explicit expression is:

$$\mathbf{A} = \begin{bmatrix} \mathbf{0} & \mathbf{K}_1 - \omega^2\,\mathbf{M}^{g} \\ \mathbf{K}_1 - \omega^2\,\mathbf{M}^{g} & i\,\mathbf{K}_2 \end{bmatrix}, \qquad B = \begin{bmatrix} \mathbf{K}_1 - \omega^2\,\mathbf{M}^{g} & \mathbf{0} \\ \mathbf{0} & -\mathbf{K}_3 \end{bmatrix}. \tag{40}$$

The solution of Eq. (39) is given in terms of eigenvalues ξ and eigenvectors **Q**. While the eigenvectors are complex, the eigenvalues can be pairs of real numbers ($\pm\xi_{Re}$) representing propagating waves in the ± x directions, pairs of complex conjugate numbers ($\pm\xi_{Re} \pm i\,\xi_{\mathrm{Im}}$) representing evanescent waves decaying in the ± x directions, or pairs of purely imaginary numbers ($\pm i\,\xi_{\mathrm{Im}}$) representing non oscillating evanescent waves in the ± x directions (Hayashi et al. 2003).

The corresponding mode shape $\mathbf{\Phi}$ can be extracted as the upper part of vector **Q**, while the associated attenuation, phase (c_p) and group (c_g) velocities can be obtained as

$$att = \xi_{\mathrm{Im}} \tag{41}$$

$$c_p = \omega / \xi_{Re} \tag{42}$$

$$c_g = \frac{\partial\omega}{\partial\xi} = \frac{\mathbf{\Phi}_L^T\left(i\,\mathbf{K}_2 + 2\,\xi\,\mathbf{K}_3\right)\mathbf{\Phi}_R}{2\omega\;\mathbf{\Phi}_L^T\mathbf{M}^{\mathrm{g}}\mathbf{\Phi}_R} \tag{43}$$

with $\mathbf{\Phi}_L$ and $\mathbf{\Phi}_R$ indicating the left and right mode shapes respectively.

The knowledge of the velocities for each $\xi - \omega$ pair allows to build the dispersion curves. It is also important for the purposes of this topic to "follow" a given wave mode at varying frequencies. In order to do that, the results in this paper adopt the B-orthogonality wave mode sorting algorithm originally proposed by Loveday and Long (2007). Since at the same frequency ω, two eigenvectors r and s obtained from Eq. (39) must respect the orthogonality condition with the **B** matrix, the same condition can be assumed for the next frequency step $\left(\omega + \Delta\omega\right)$, allowing to "follow" or "track" the mode during frequency sweeping according to:

$$\mathbf{Q}_r^T(\omega)\mathbf{B}\mathbf{Q}_s(\omega+\Delta\omega)\cong\begin{cases}0 & if\ r\neq s\\ \neq 0 & if\ r=s\end{cases}. \tag{44}$$

The soundness of the proposed GL method can be validated by verifying the conservation of energy between the incident mode and the scattered (reflected and transmitted) modes:

$$E_{in}=\sum_{j=1}^{N_M}\left(E_{\mathrm{Refl}}^{(j)}+E_{Transm}^{(j)}\right) \tag{45}$$

where E_{in}, $E_{\mathrm{Refl}}^{(j)}$, $E_{Transm}^{(j)}$ are the energy fluxes of the incident wave and of the *j*-th reflected and transmitted waves, respectively.

The energy flux carried by the propagating mode *j* in the **n** direction over a unit period of time through the cross-sectional area □□can be evaluated as:

$$E^{(j)}=\int_{\Gamma}\mathbf{P}^{(j)}\square\mathbf{n}\,d\Gamma, \tag{46}$$

where

$$\mathbf{P}^{(j)}=-\frac{1}{2}\mathrm{Re}\left[\boldsymbol{\sigma}^{(j)}\,\bar{\dot{\mathbf{u}}}^{(j)}\right] \tag{47}$$

is the Poynting vector, with $\boldsymbol{\sigma}$ the stress tensor in matrix form notation and $\bar{\dot{\mathbf{u}}}$ the complex conjugate velocity vector.

Substitution of Eq. (47) into Eq. (46) allows to rewrite Eq. (46) in Voigt notation as

$$E^{(j)}=-\frac{1}{2}\int_{\Gamma}\mathrm{Re}\left[\left(\mathbf{L}_n^T\,\boldsymbol{\sigma}\right)^T\bar{\dot{\mathbf{u}}}\right]d\Gamma\cdot \tag{48}$$

By taking into account the harmonic time dependence of $\boldsymbol{\sigma}$ and $\mathbf{u}$ and considering the particular case of waves travelling in the x direction, the energy term for the j-th mode becomes:

$$E^{(j)} = -\frac{\left|A_j\right|^2}{2}\,\mathrm{Re}\left[i\,\omega\,\mathbf{F}^{(j)^T}\,\bar{\boldsymbol{\Phi}}^{(j)} \right] \tag{49}$$

where $\boldsymbol{\Phi}^{(j)}$ and $\mathbf{F}^{(j)}$ are the nodal displacements and correspondent consistent forces for mode j according to the adopted FE discretization.

2.3.2 2D Case study: scattering of guided waves in skin-to-stringer assembly of composite aircraft panels

The GL formulation described above was implemented in a Matlab© code. The code was designed to calculate the response within a fixed frequency range of the incoming wave and for a fixed number of frequency steps. The general numerical procedure is schematized in Figure 16.

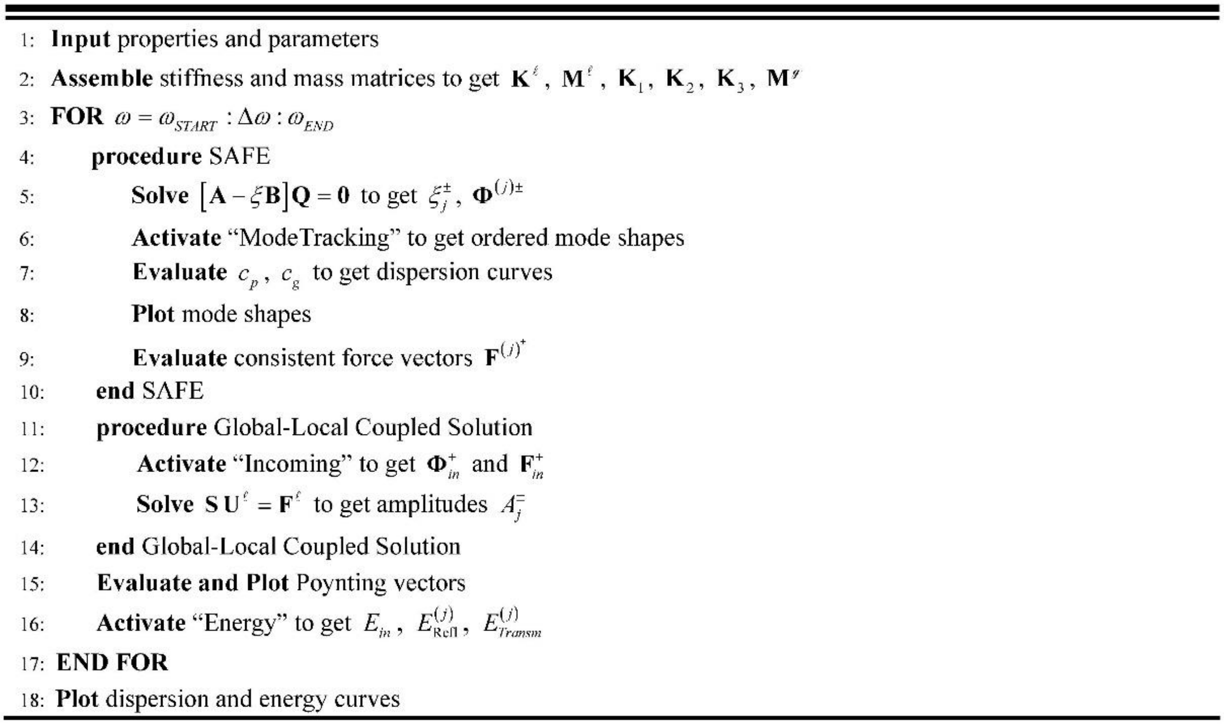

```
Input properties and parameters
Assemble stiffness and mass matrices to get $\mathbf{K}^{\ell}$, $\mathbf{M}^{\ell}$, $\mathbf{K}_1$, $\mathbf{K}_2$, $\mathbf{K}_3$, $\mathbf{M}^{g}$
FOR $\omega = \omega_{START} : \Delta\omega : \omega_{END}$
    procedure SAFE
        Solve $[\mathbf{A} - \xi\mathbf{B}]\mathbf{Q} = \mathbf{0}$ to get $\xi_j^{\pm}$, $\mathbf{\Phi}^{(j)\pm}$
        Activate "ModeTracking" to get ordered mode shapes
        Evaluate $c_p$, $c_g$ to get dispersion curves
        Plot mode shapes
        Evaluate consistent force vectors $\mathbf{F}^{(j)^{+}}$
    end SAFE
    procedure Global-Local Coupled Solution
        Activate "Incoming" to get $\mathbf{\Phi}_{in}^{+}$ and $\mathbf{F}_{in}^{+}$
        Solve $\mathbf{S}\,\mathbf{U}^{\ell} = \mathbf{F}^{\ell}$ to get amplitudes $A_j^{=}$
    end Global-Local Coupled Solution
    Evaluate and Plot Poynting vectors
    Activate "Energy" to get $E_{in}$, $E_{\mathrm{Refl}}^{(j)}$, $E_{Transm}^{(j)}$
END FOR
Plot dispersion and energy curves
```

Figure 16 - Key steps of the Matlab GL code.

The geometry of the case study is shown in Figure 17, and represents a scaled version of a skin-to-stringer assembly found in commercial aircraft construction. This structure is being considered for ultrasonic guided-wave inspection (Capriotti et al., 2017). Scattering results for typical incoming wave modes were obtained for a “pristine” case and for four “damage” cases representing relevant defects in this structure. These predictions can allow to best target the inspection to a particular defect and/or to quantitatively relate a measured scattering behavior to a particular defect.

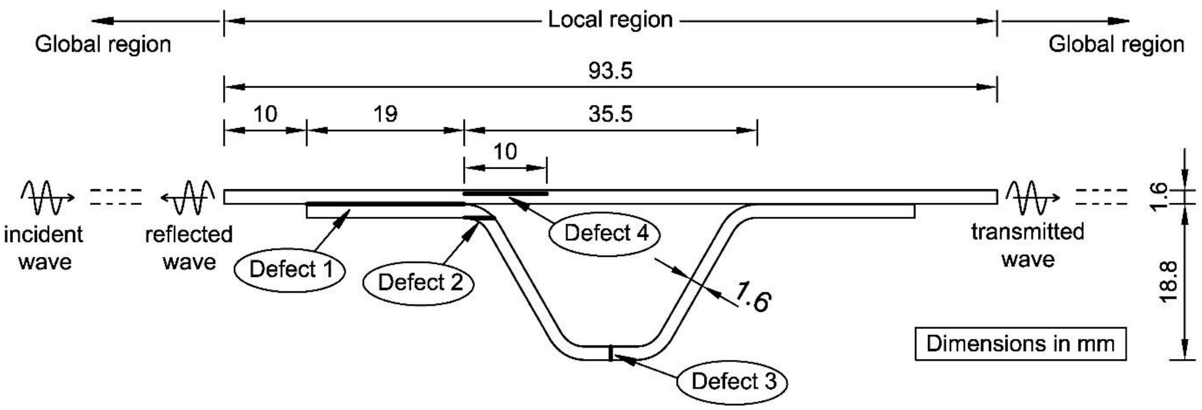

Figure 17 - Global-Local model of the composite skin-to-stringer assembly, with the four "defected" configurations: delamination between skin and stringer (Defect 1), horizontal fracture in the stringer heel (Defect 2), vertical fracture in the stringer cap (Defect 3), and delamination between 2nd and 3rd laminae in the skin (Defect 4).

In the model, the skin and the hat-shaped stringer are both 8-layers of $\left[0/+45/-45/0\right]_S$ carbon-epoxy unidirectional laminae with a total thickness of 1.6 mm. An additional 0° lamina is placed at the interface between skin and stringer. The zero-degree lamina direction corresponds to the out-of-plane direction of the 2D drawing in Figure 17. The density of each lamina is 1530 kg/m^3 and the elastic properties in the principal direction of material symmetry are given in Table 5 (assuming transverse isotropy), where *1* is the fiber direction, *2* is the direction perpendicular to the fibers in the lamina plane, and *3* the through-thickness direction.

Table 5 - Elastic properties for the CFRP lamina

Property	C_{11}	C_{12}	C_{13}	C_{22}	C_{23}	C_{33}	C_{44}	C_{55}	C_{66}
GPa	135	5.70	5.70	14.20	8.51	14.20	2.87	4.55	4.55

Shown in Figure 17, the "local" region was extended to include 10 mm on either side of the stringer, in order to limit any role of evanescent modes when computing reflection and transmission spectra. A total of 12376 quadrilateral 2-D isoparametric linear elements (5952 for the skin and 6424 for the stringer) were used for the local discretization, for a total number of local FE nodes of 13022. On the "global" side, for computational consistency, two 1D isoparametric linear elements were used for each lamina, for a total of 16 elements and 17 nodes. Four Gauss points were used for the quadrature of the 2D elements, and 2 Gauss points for the 1D elements. The maximum size of the elements was $L = 0.26\ \mathrm{mm}$, in order to satisfy the following customary meshing criterion:

$$\lambda_T > \beta L \tag{50}$$

where $\lambda_T = 2\pi c_T / \omega$ is the wavelength of transverse waves at frequency ω traveling at bulk shear velocity c_T. With linear elements, values of $\beta = 10$ (Chang and Mal, 1995) or $\beta = 20$ (Bartoli et al., 2005; Galan and Abascal, 2005) are customary. For the case of quadratic elements, a value of $\beta = 4$ was utilized. All analyses were run using a Core i7 CPU with 64 GB of RAM, in the frequency range of DC-500 kHz, with steps of 5 kHz. The incident wave source distance was $d_s = 0.25\ \mathrm{m}$ from the middle of the stringer (origin of the reference system) on the left side of the drawing in Figure 17.

An initial validation of the accuracy of the proposed GL algorithm was conducted on a simpler geometry of a pristine multi-layered composite plate corresponding to the skin only of Figure 17. This analysis was done to check the generation of the dispersion curves and wave energy conservation in the scattering process.

From the SAFE portion of the GL code, the results in terms of phase velocity and group velocity dispersion curves in the DC-500 kHz frequency range are presented in Figure 18a and Figure 18b, respectively. Four modes appear in this range, including three fundamental modes (m_1, m_2 and m_3) and a higher-order mode (m_4) with cut-off frequency ~450 kHz. As expected, the curves are generally similar to the Rayleigh-Lamb dispersion curves of isotropic plates, with m_1 corresponding to the zero-order flexural (A_0) Lamb mode, m_2 corresponding to the zero-order axial (S_0) Lamb mode, m_3 to the zero-order shear horizontal (SH_0) Lamb mode, and m_4 to the first-order flexural (A_1) Lamb mode.

For the remainder of the paper, the attention will be focused on the flexural and the axial modes since they are the ones most commonly utilized in guided-wave testing of composite or metal plates.

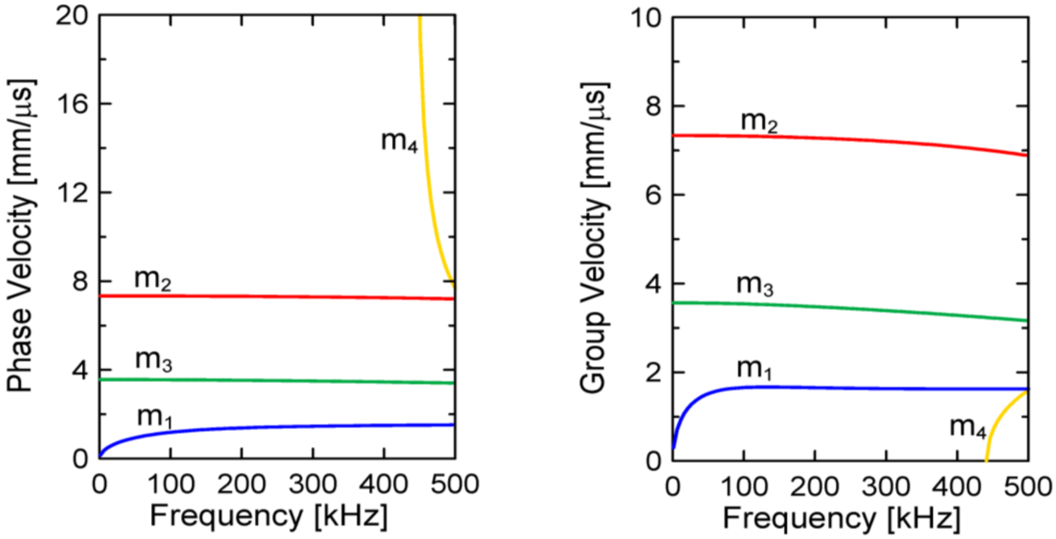

Figure 18 - (left) Phase velocity dispersion curves and (right) group velocity dispersion curves for the CFRP composite laminate (skin only) from the SAFE portion of the GL code.

The energy conservation check for the transmission (Transm) and reflection (Refl) scattering processes was performed for the two cases of incident m_1 (flexural) mode and incident m_2 (axial) mode according to Eq. (45) of the GL formulation. In particular, the left boundary of the local region in the schematic of Figure 17 was used for the computation of the reflected waves, and the right boundary of the local region in Figure 17 was used for the computation of the transmitted waves.

Figure 19a shows the scattering spectra for the case of m_1 incident. As expected, due to the absence of discontinuities or geometrical asymmetries in the pristine composite skin, the same mode m_1 is entirely transmitted and no mode is reflected (total transmission) throughout the frequency range. The same result is obtained for the case of m_2 incident, shown in Figure 19(c), that again shows the total m_2 transmission with no reflections. In addition, the scattering spectra in both cases have a constant unity amplitude that corresponds to the incident energy, demonstrating energy conservation. These results give confidence on the accuracy of the GL model for the skin structure. The fact that no spurious reflections are seen at the higher frequency values also gives reassurance on the level of mesh discretization adopted.

The energy distribution for the incident modes across the laminate thickness is shown in Figure 19(b) for the m_1 mode and in Figure 19(d) for the m_2 mode. These figures plot the values of the Poynting vector along the wave propagation direction, *x*, at the Gauss points. Energy distributions recorded at the left and the right boundaries coincide with those of the incoming mode, as expected in pristine conditions. These cross-sectional energy plots shine light on the different “nature” of the incident modes, with the m_1 (flexural) mode focusing its energy on the outer plies of the laminate, and the m_2 (axial) mode affecting both outer plies and inner plies of the laminate. It is known (e.g. Matt et al. 2005) that these distributions control how different modes interact with adjacent components (e.g. the stringer) and with skin defects located at different depths.

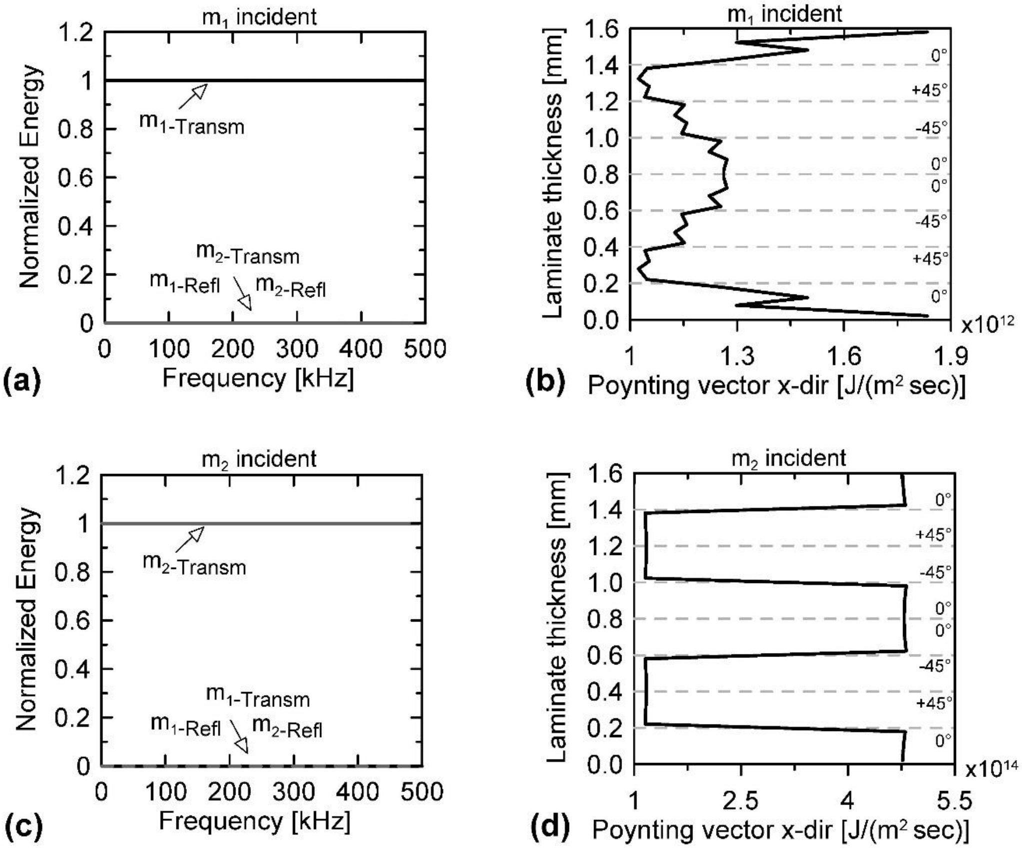

Figure 19 - Skin laminate: (a) Transmission and reflection energy spectra and (b) cross-sectional energy (Poynting vector) in the case of an m1 incident mode. (c) Transmission and reflection energy spectra and (d) cross-sectional Poynting vector in the case of an m_2 incident mode.

The next Global-Local analysis was conducted on the full skin-to-stringer assembly of Figure 17. The goal was to predict scattering spectra in this system for the case of a pristine assembly, and four different defects as shown in Figure 17. These defects consisted of: delamination between skin and stringer

(Defect 1), horizontal fracture in the stringer (Defect 2), vertical fracture in the stringer (Defect 3), and delamination between 2nd and 3rd laminae in the skin (Defect 4). Defects 1, 2 and 3 were modelled by removing some of the elements from the mesh; Defect 4 was modelled by doubling the nodes and physically separating the elements between the second and third layer for the length specified in Figure 17.

The addition of the hat-shaped stringer to the skin laminate significantly increases the complexity of the scattering problem. Key results from the GL model of the pristine assembly are shown in Figure 20 and Figure 21 for the cases of incident m_1 (flexural) mode and incident m_2 (axial) mode.

Figure 20a shows the scattering spectra (reflections and transmission) in the DC-500 kHz frequency range for an incident m_1 mode. As for the skin-only results, the reflection spectra are computed at the left boundary of the local region and the transmission spectra are computed at the right boundary of the local region. As before, the total energy is computed adding up the transmitted and reflected energy for all the modes, considering a unity incoming mode. Figure 20a shows a computed total energy spectrum flat and close to 1, which satisfies conservation of energy to within very small numerical errors caused by the FE discretization and the normal mode decomposition. The same figure also shows that, when m_1 is incident, the majority of the energy is transmitted through the skin-to-stringer assembly and reflected back into the skin as the same mode m_1, with very little mode conversion into m_2. This is true at most frequencies, except for specific frequencies such as 105 kHz, 200 kHz, 260-320 kHz and 450-470 kHz, where the mode-converted m_2 is transmitted through the overall structure more than m_1. The lower frequency range (up to 200 kHz) is very sensitive to m_1, reaching more than an 80% of transmission, with transmission peaks at ~ 50 kHz and ~ 135 kHz. These values could therefore be ideal excitation frequencies for a pitch-catch guided-wave inspection that uses m_1 in transmission. Conversely, 90% of the m_1 energy is reflected in the high frequency range (~360-460 kHz) that can instead be considered for a pulse-echo guided-wave test using reflection measurements. The spectra in Figure 20a also reveal interesting m_1-m_2 mode-conversion bands, such as the m_2 transmission in the ~ 260-320 kHz range and the m_2 reflection around 200 kHz. The mode conversion information can also be extremely useful in a practical guided-wave test. The higher-order mode m_4 appears with a very small contribution above its cut-off frequency of 450 kHz.

The corresponding case of an m_2 incident mode is shown in Figure 20b. The spectra identify specific frequency ranges for predominant transmission or reflection behaviour, as well as m_2-m_1 mode conversion opportunities. For example, significant mode conversion into both transmitted m_1 and reflected m_1 occur in the 150-350 kHz range, as well as at some other individual frequencies revealed by the energy peaks. The plot also shows the small contribution of the higher-order mode m_4 above 450 kHz.

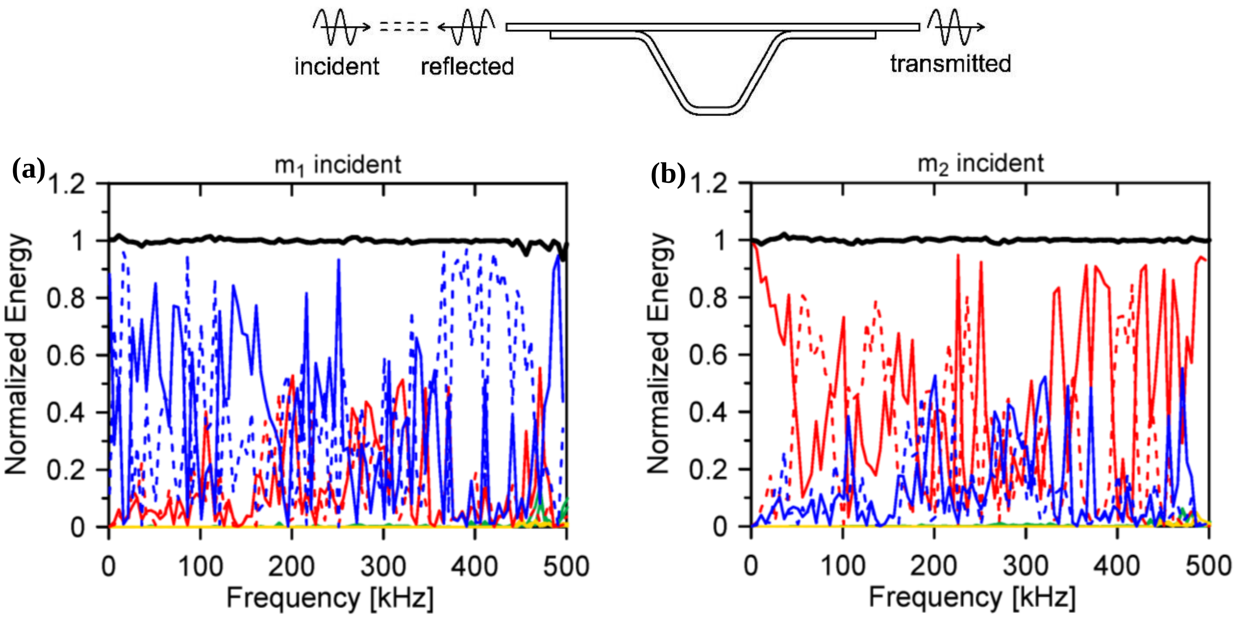

Figure 20 - Reflection and transmission energy spectra for (a) m1 incident mode and (b) m2 incident mode in the skin-to-stringer pristine assembly.

In order to shine additional light on these behaviours, Figure 21 shows results obtained when zooming into the two salient frequency values of 150 kHz and 200 kHz. For an m_1 incident mode, for example, the spectra in Figure 21a shows that at 150 kHz most of the energy is transmitted as the same mode m_1. This result is best explained by the cross-sectional energy distribution (Poynting vector along x) shown in Figure 21b that confirms the same energy shapes at the left boundary and at the right boundary, i.e. little or no disturbance to the nature of the m_1 mode as it crosses through the stringer at this frequency. Conversely, at a 200 kHz frequency, the spectra for the incident m_1 mode in Figure 21a shows considerable (50%) mode conversion into an m_2. This different behaviour is again explained by the cross-sectional energy plots of Figure 21c that show how the m_1 cross-sectional shape at the left boundary changes into an m_2 shape at the right boundary after traveling through the stringer (see also Figure 19).

If m_2 is used as the incoming mode, at 150 kHz Figure 21d shows a 50-50 split between transmission and reflection. The Poynting vector plots of Figure 21e at 150 kHz confirms this behaviour, showing a split of incoming energy into the left boundary and the right boundary. At 200 kHz, instead, significant $m_2 - m_1$ mode conversion takes place (as seen in the previous m_1 incoming case), as confirmed by the Poynting vectors of Figure 21f showing a change from m_2 distribution at the left boundary into an m_1 distribution at the right boundary after travelling through the stringer.

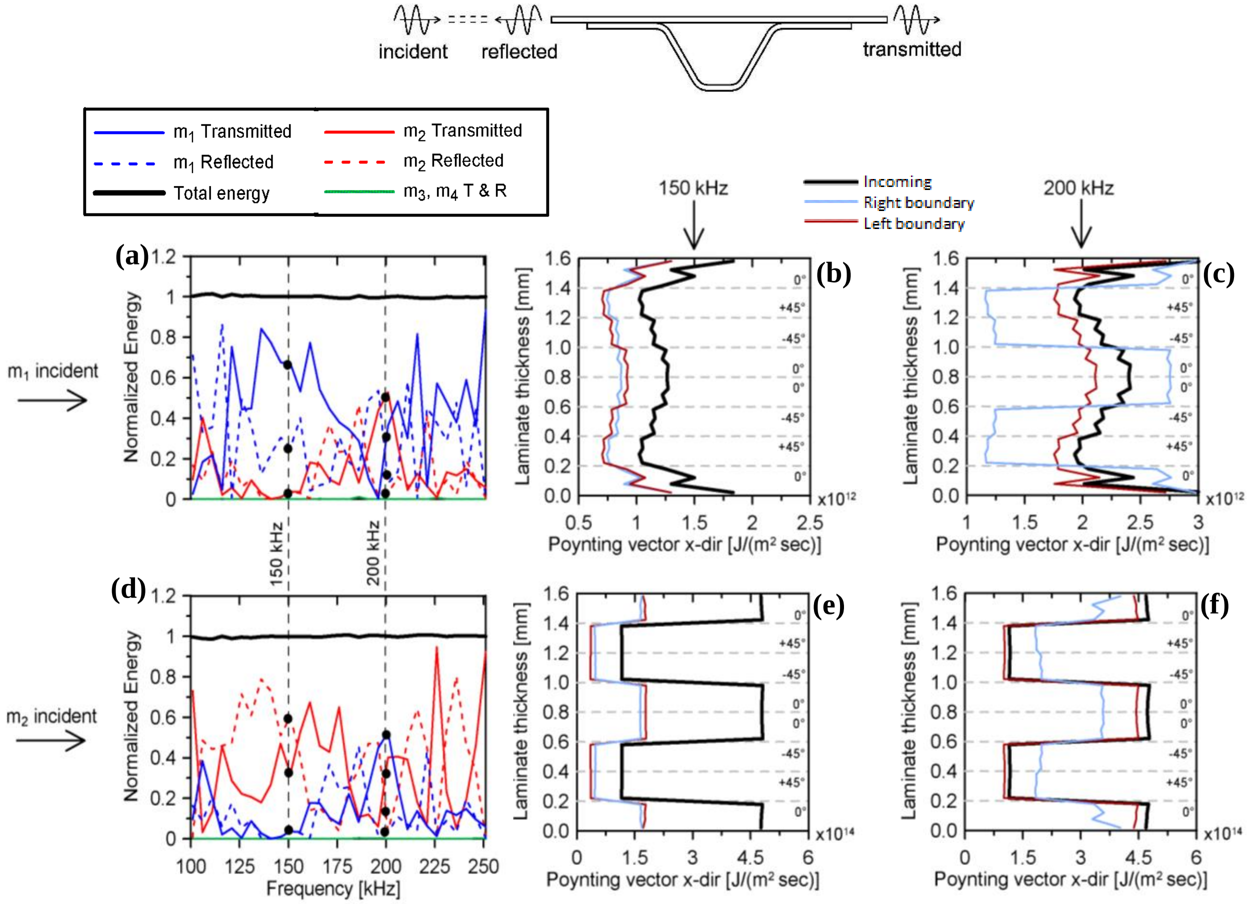

Figure 21 - Scattering behaviour at specific frequencies (pristine skin-to-stringer assembly). (a) Zoomed scattering spectra for the m1 incident mode with cross-sectional energy (Poynting vector) at 150 kHz (b) and at 200 kHz (c). Corresponding results for the m2 incident mode in (d), (e) and (f).

The interest in the GL scattering modeling of the “damaged” skin-to-stinger assembly is to explore defect-mode sensitivities in specific frequency ranges in ways that cannot be obtained from theoretical considerations due to the material and geometrical complexity of the scattering problem. In this section scattering spectra from the GL method are shown for the various defects considered. For the sake of compactness, the results are shown for the transmission behaviour only and considering possible mode conversions. This is done in analogy with a pitch-catch guided-wave testing approach of the type experimentally utilized for a similar structure by Capriotti et al. (2017). In order to better isolate the role of each defect, the calculations are shown in terms of <defect - pristine> “difference” spectra. Negative values in the difference spectra correspond to wave energy absorptions caused by the defect, whereas positive values in the difference spectra correspond to enhanced wave transmission caused by the defect.

The results for Defect 1 (skin-to-stringer delamination) are shown in Figure 22. This delamination was simulated by eliminating the transition lamina at the left side of the interface. If the flexural m_1 is used as the incoming mode (Figure 22a), frequencies in the 85-420 kHz range show a good sensitivity to this defect. In particular, for example, significant m_1 wave energy absorption (negative peaks in the difference spectrum) can be expected at 160 kHz (70% absorption), 250 kHz and 350 kHz. Conversely, increased m_1 energy transmission (as high as 70% increase) can be expected at 90 kHz and 290 kHz. The transmission of the axial mode m_2, Figure 20d, is also found quite sensitive to this defect. The figure for m_2 transmission shows significant absorption peaks (up to 90%) in the higher frequency range 250-450 kHz, and significant transmission peaks (up to 85%) in the lower frequency range of 50-250 kHz. The stronger transmission at certain frequencies can be intuitively explained by the fact that skin-stringer delamination eliminates wave energy leakage into the stringer and thus confines the wave transmission to the skin only. The mode conversion transmission spectra are also shown in Figure 20b and Figure 22c. These plots reveal specific ranges of opportunity for detecting the damage through mode conversion, such as the 200-400 kHz range where several absorption peaks are present. In an actual test, these mode-frequency ranges can be exploited to optimally detect this kind of defect.

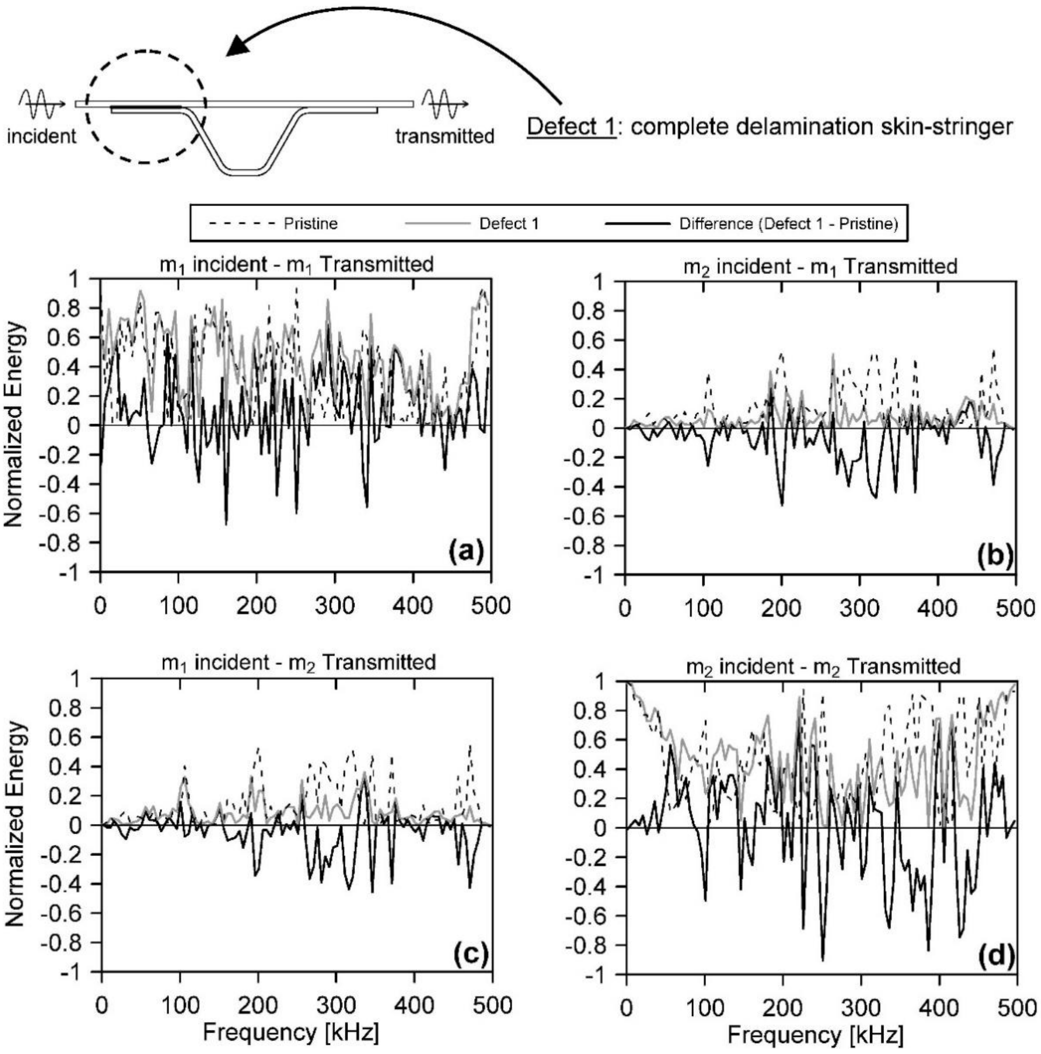

Figure 22 - Defect 1 case (skin-stringer delamination). Wave transmission spectra for pristine, defect and (defect-pristine) difference for (a) m1 incident - m1 transmitted; (b) m2 incident - m1 transmitted (mode conversion); (c) m1 incident – m2 transmitted (mode conversion), and (d) m_2 incident – m_2 transmitted.

The case of the stringer heel crack defect (Defect 2) is shown in Figure 23, where the schematic depicts the simulated fracture at the top-left corner of the stringer. The transmitted flexural m_1 energy for the same m_1 incoming mode (Figure 23a) shows good sensitivity particularly in the lower frequency range DC-250 kHz as well as around 350 kHz, where the negative difference spectrum indicates energy absorption (up to 90% at 250 kHz) induced by this defect. Increased transmission (positive difference spectrum) on the order of 50% is instead predicted at specific frequency values such as 115 kHz and 195 kHz. The transmitted axial m_2 mode under the same incoming m_2 mode (Figure 23d) is also quite sensitive to this defect, with wave energy absorption as high as 90% in the 350 – 450 kHz range, and increased transmissions up to 50% in other frequency ranges. The mode conversion spectra of m_2 incident-m_1 transmitted (Figure 23b) and m_1 incident-m_2 transmitted (Figure 23c) generally show less sensitivity to this defect than the same-mode spectra, with maximum ~40% energy absorption in the 200 – 350 kHz range.

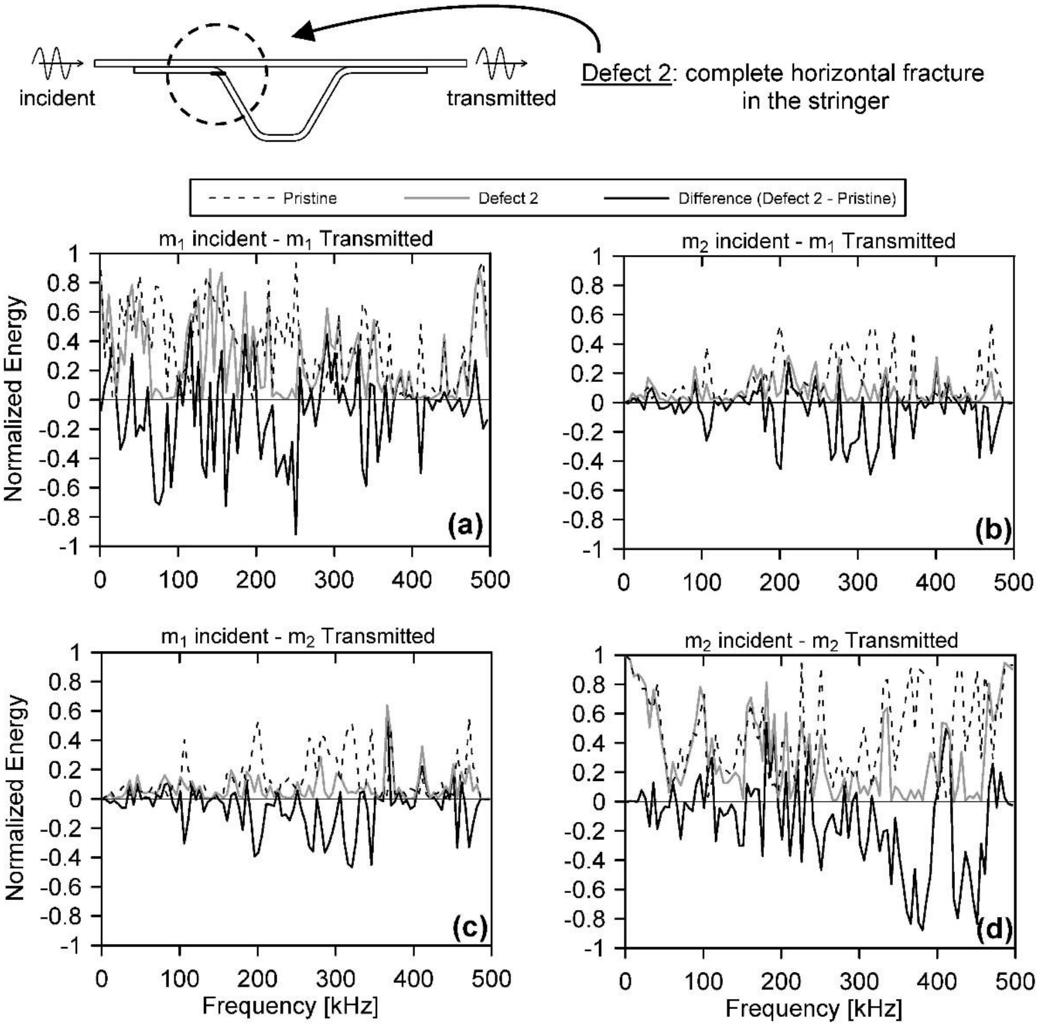

Figure 23 - Defect 2 case (stringer heel crack). Wave transmission spectra for pristine, defect and (defect-pristine) difference for (a) m1 incident - m1 transmitted; (b) m2 incident - m1 transmitted (mode conversion); (c) m1 incident – m2 transmitted (mode conversion), and (d) m_2 incident – m_2 transmitted.

The case of the stringer cap crack (Defect 3) is shown in Figure 24. The transmission spectra are similar to those obtained for the Defect 2 case: the flexural m_1 - m_1 combination (Figure 24a) is most sensitive in the low frequency range DC-200 kHz, while the axial m_2 – m_2 combination (Figure 24d) is mostly sensitive in the higher frequency range of 250-450 kHz. In these ranges, both combinations show significant energy absorption (as high as ~ 90%) caused by the defect. The mode-converted spectra of m_2 – m_1 (Figure 24b) and m_1 – m_2 (Figure 24c) for Defect 3 are also similar to those of Defect 2, with smaller sensitivity compared to the same-mode spectra. One notable difference between the two stringer damage cases is the same-mode transmission spectrum around 250 kHz, where the stringer heel crack Defect 2 causes 90% absorption for the m_1 - m_1 combination (Figure 23a) that does not occur for the stringer cap crack Defect 3 (Figure 24a); the opposite occurs for the m_2 – m_2 combination at 250 kHz, where the stringer cap crack Defect 3 produces 90% absorption (Figure 24d) that is much reduced for the stringer heel crack Defect 2 (Figure 23d). These kinds of considerations can help selecting specific mode-frequency combinations and/or interpreting results of guided-wave measurements in these structures.

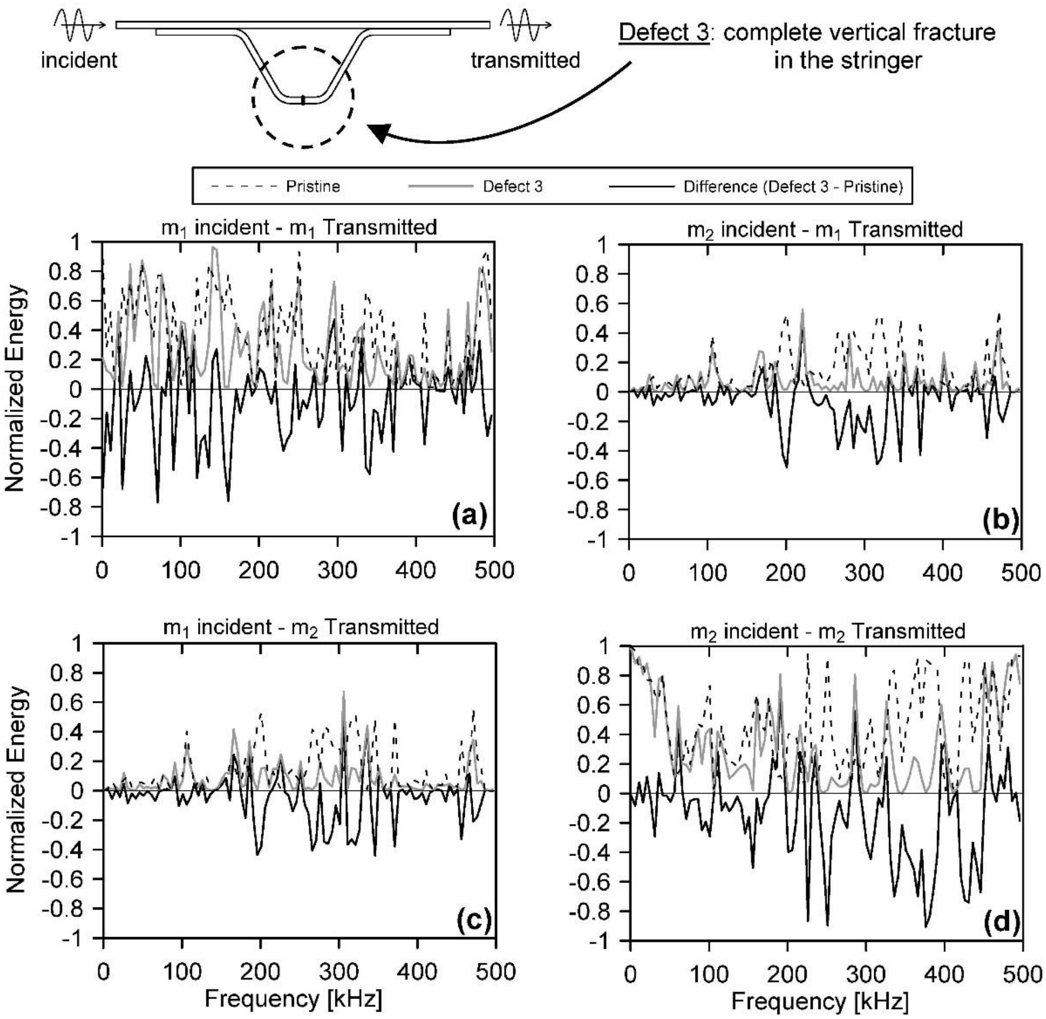

Figure 24 - Defect 3 case (stringer cap crack). Wave transmission spectra for pristine, defect and (defect-pristine) difference for (a) m1 incident - m1 transmitted; (b) m2 incident - m1 transmitted (mode conversion); (c) m1 incident – m2 transmitted (mode conversion), and (d) m_2 incident – m_2 transmitted.

The last defect that was considered is the skin delamination (Defect 4), that was inserted between the 2nd and the 3rd layer of the composite skin laminate as schematized in Figure 25. In this case, a very sensitive combination is the same mode flexural m_1 - m_1 (Figure 25a), with significant energy absorption throughout the entire frequency range and absorption peaks of 70% at 80 kHz and 210 kHz. Interestingly, the axial m_2 – m_2 combination (Figure 25d) is only sensitive to this delamination in the high frequency range above 400 kHz, with a peak 80% absorption at 425 kHz. This result is expected by the rule of thumb consideration of ultrasonic testing where higher frequencies are more sensitive due to the smaller wavelength-to-defect size ratios. However, the full GL analysis presented here reveals a much more complete picture of mode sensitivities, with specific “sensitive” mode-frequency combinations also at the lower frequencies (e.g. in the aforementioned m_1 - m_1 combination). Since the skin delamination breaks the geometrical symmetry of the skin, it creates some $m_2 – m_1$ and $m_1 – m_2$ mode conversions, shown in Figure 25b and Figure 25c, particularly in the 250-350 kHz range. The mode conversions in this frequency range could also be utilized to detect this kind of defect in an actual inspection test.

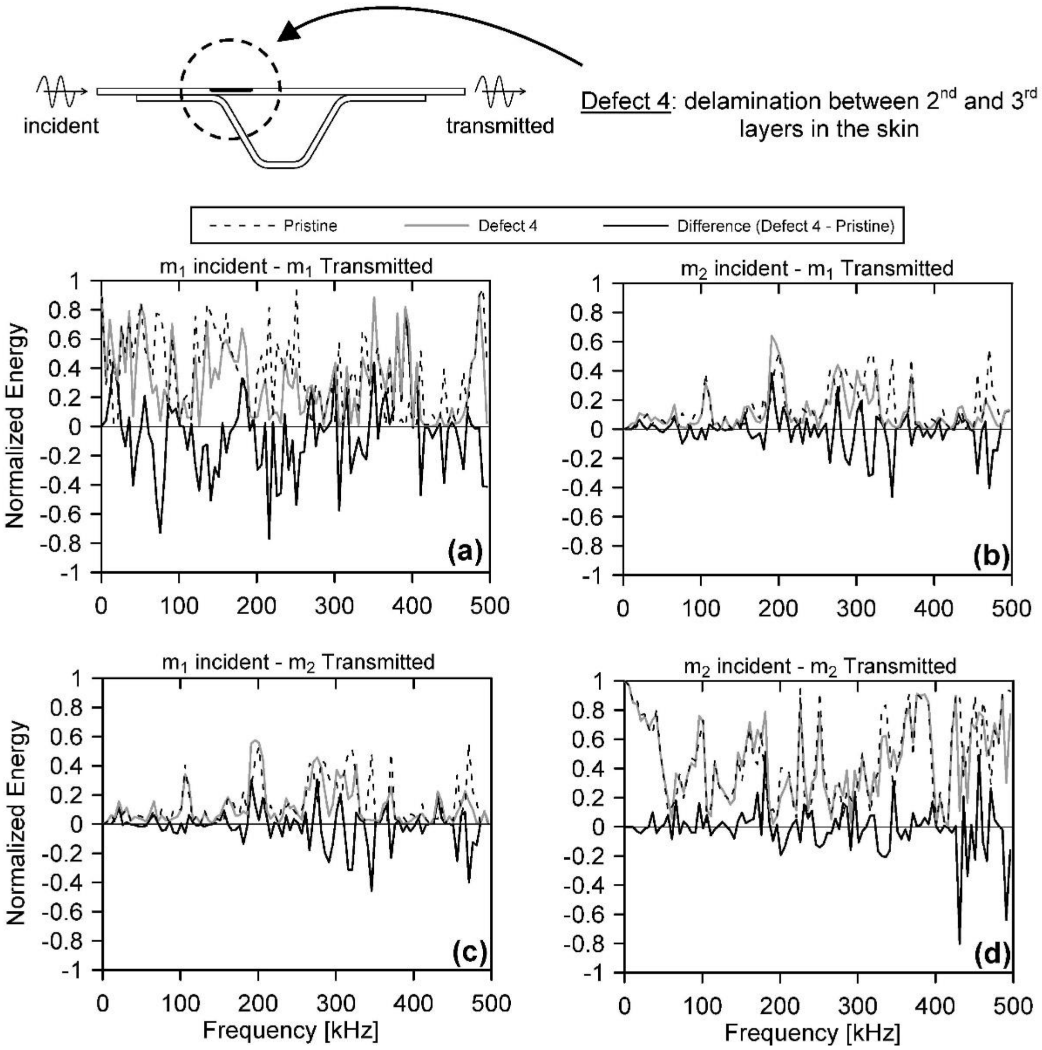

Figure 25 - Defect 4 case (skin delamination). Wave transmission spectra for pristine, defect and (defect-pristine) difference for (a) m1 incident - m1 transmitted; (b) m2 incident - m1 transmitted (mode conversion); (c) m1 incident – m2 transmitted (mode conversion), and (d) m_2 incident – m_2 transmitted

This work has addressed the problem of scattering of multimode and dispersive elastic waves propagating in waveguide geometries. Among other applications, this topic is of great interest to ultrasonic guided-wave NDT or SHM of structural components where defects are detected by recording transmission or reflection scattering of a generated incoming wave mode. Predictions of these scattering patterns for a given defect can allow to select optimum mode-frequency combinations for the incoming mode, and/or to identify the type of defect being detected by a specific scattering observation.

For general cases that are complex in terms of either geometry or material properties (or both), this problem requires a numerical solution. A unified Global – Local (GL) approach has been presented here, exploiting the computational efficiency of the Semi-Analytical Finite Element (SAFE) technique for a cross-sectional discretization of the "global" portion, coupled with a full Finite Element discretization of the "local" portion containing the scatterer. Compared to previous GL studies, this contribution adds: (a) a general and consistent formulation for the evaluation of the nodal tractions at the global-local boundaries; (b) the implementation of a robust mode tracking control, based on B-orthogonality, for the automatic selection of incoming and scattered modes; (c) the possibility to model a wide frequency range also including higher-order modes; (d) the automatic inclusion of an energy balance check in the results; and (e) the unification of SAFE and FE in a stand-alone numerical Matlab code that is readily extendable to more general cases (e.g. independent treatment of the two global regions, explicitly given theoretical formulation such as consistent nodal forces at the boundaries, or extension to 3D cases).

The proposed GL algorithm was applied to a composite skin-to-stringer assembly typical of commercial aircraft construction. Various relevant defects were modelled, and scattering spectra were obtained for guided-wave frequencies as high as 500 kHz under incoming flexural (A_0-type) or axial (S_0-type) modes that are typically employed as excitations in guided-wave testing of these components. The results reveal quite interesting transmission spectra, same-mode or mode-converted, that are peculiar to each of the defects considered. These predictions can be extremely useful to guide and interpret guided-wave inspection tests conducted on these components.

The results shown for the skin-to-stringer case study only apply to the specific geometry and material properties considered. However, the cross-sectional mode shapes mostly control the partition of energy between the incoming mode and the scattered modes. Consequently, some scalability of the results to components of different thicknesses can be qualitatively predicted on the basis of the well-known invariance of the guided-wave cross-sectional mode shapes with the <frequency × thickness> product (Rose 2014). In other words, for the same mode shape to be generated, frequency and thickness must be inversely proportional. As a result, for example, specific frequency values of interest in the scattering spectra predicted for a given thickness of the skin could be scaled to a different skin thickness, provided that the <frequency × thickness> product is the same.

The section has considered elastic waves with no viscoelastic damping. Damping could be included by considering complex stiffness matrices in the analysis resulting in complex wavenumbers as discussed, for example, by Bartoli et al. (2006). The inclusion of damping would affect the predicted scattering spectra mostly in amplitude, with presumably small shifts in peak frequency positions since those are mostly controlled by cross-sectional mode shapes (that should not change significantly with damping).

2.3.3 3D Case study: scattering of guided waves from internal cracks in railroad tracks

Although the GL formulation presented applies to a general 3D case, the case study considered in the previous section was a 2D (plain strain) analysis that is quite applicable to a scanning-type guided-wave system of the type utilized by Capriotti et al. (2017). An extension to a 3D scattering case for internal flaws in railroad tracks using this algorithm has also been studied by the authors and is presented below.

Even though, railroad tracks are usually inspected by ultrasonic bulk waves, they can be considered as waveguides themselves, since their own geometry supports the propagation of elastic guided waves. The scattering in this structure is of particular interest to the authors both from a theoretical point of view, as an extension of the GL method to a 3D case, and for a practical use to aid the work described in (Lanza di Scalea et al., 2018). The extension of the GL method to the 3D case requires the use of 3D elements in the

FE local region and of 2D elements in the SAFE global region; also, the assumption of plain strain is removed. Wave propagation in the x-direction only is still considered.

The geometry of the 3D case study is shown in Figure 26, and represents a real size version of a 136 lbs track, as the one found in regular railways. Scattering results for typical incoming wave modes were obtained for a “pristine” case and for four “damage” cases representing different percentages of damage in the rail head, in presence of a transverse defect (as similarly done in Bartoli et al., 2005), one of the most relevant cause of failure of this structure, due to fatigue. The material properties and dimensions of the rail are described in Table 6. The defect is modeled as a missing slice of the head of the rail, perpendicular to the wave propagation direction, where a column of element has been removed for 15%, 50%, 85% or 100% of the cross-section in the head.

A total of 22884 wedge 3-D isoparametric linear elements, arranged in 81 columns, were used for the local discretization, for a total number of local FE nodes of 13022. On the “global” side, for computational consistency, 284 triangular linear elements were used to discretize the cross-section for a total of 182 nodes. Six Gauss points were used for the quadrature of the 3D elements, and three Gauss points for the 2D elements. The maximum size of the elements was L=0.25 mm, in order to satisfy the meshing criterion:

$$\lambda_T > \beta L \tag{1}$$

where λ_T is the wavelength of transverse waves Due to computational limitation in the RAM, a value of $\beta = 20$ satisfies the meshing criterion up to 33 kHz, while a $\beta = 10$ is satisfied up to 66 kHz. The performance degrades as frequencies increase and will be better discussed in the following paragraphs. All analyses were run using the same Core i7 CPU with 64 GB of RAM, in the frequency range of DC-200 kHz, with steps of 1 kHz, to capture the highly populated dispersion behavior of this kind of waveguide. The incident wave source distance was $d_s = 1$ m from the center of the geometry (origin of the reference system) on the left side.

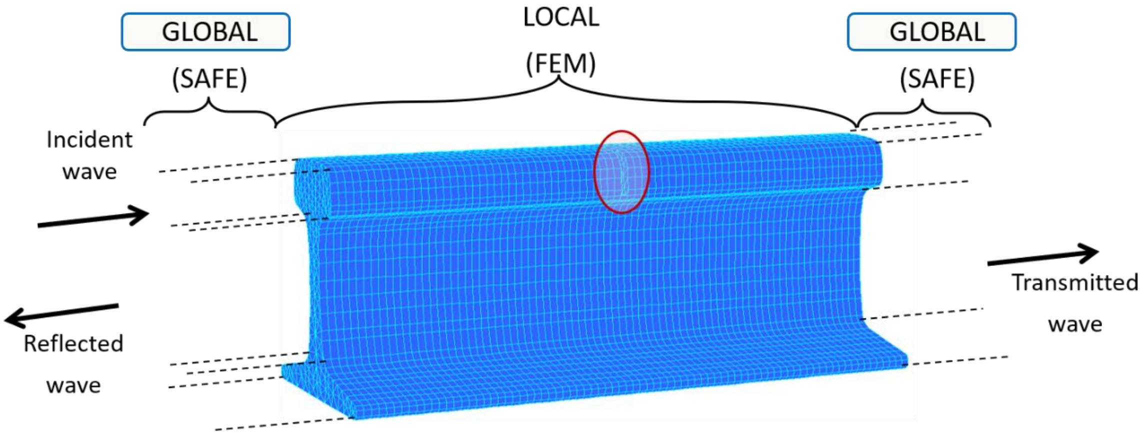

Figure 26 - Global-local model for 3D application on rail track.

Table 6 - Rail AREMA 136 lbs Properties

Property	ρ kg/m^3	c_L m/s	c_T m/s	Height x Width mm
Property Value	7932	5960	3260	186 x 152

An initial validation of the accuracy of the proposed GL algorithm was conducted on a pristine geometry. This analysis was done to check the generation of the dispersion curves and wave energy conservation in the scattering process, after the method was extended to the 3D case in its code implementation.

From the SAFE portion of the GL code, the results in terms of phase velocity and group velocity dispersion curves in the DC-200 kHz frequency range are presented in Figure 27a and Figure 27b, respectively.

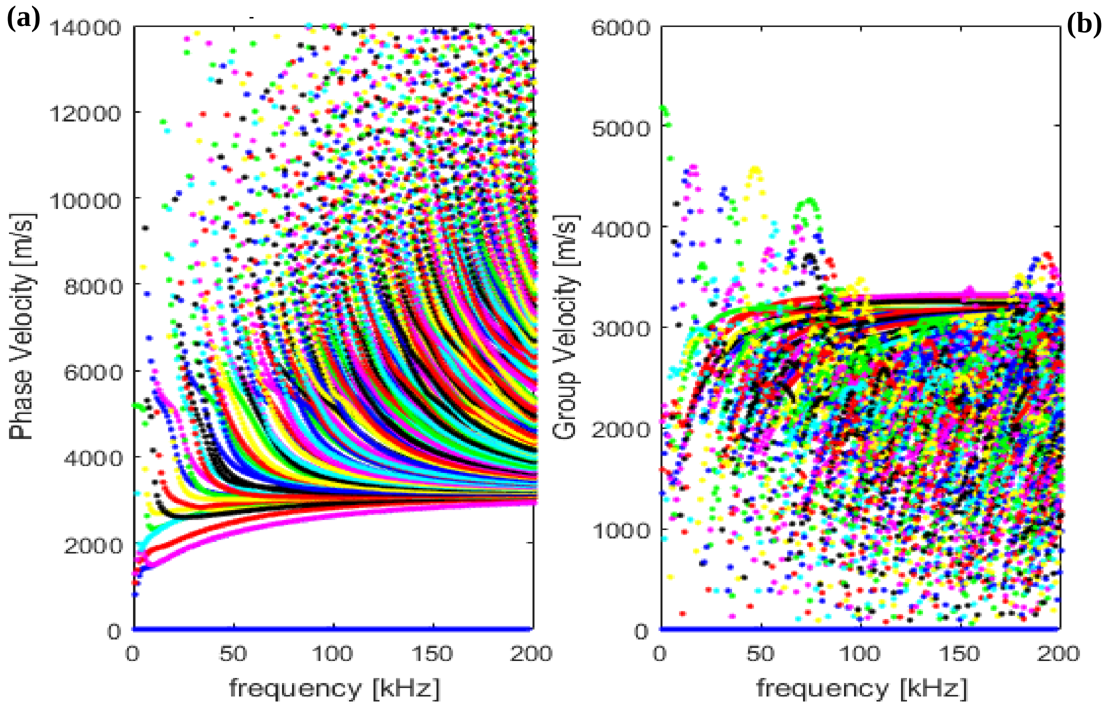

Figure 27 - GL dispersion curves for railroad track: (left) phase velocity, (right) group velocity.

A large number of modes populate the dispersion curve in this case (e.g. 10 modes in the first 10 kHz only), due to the size of the waveguide and its complex cross-section.

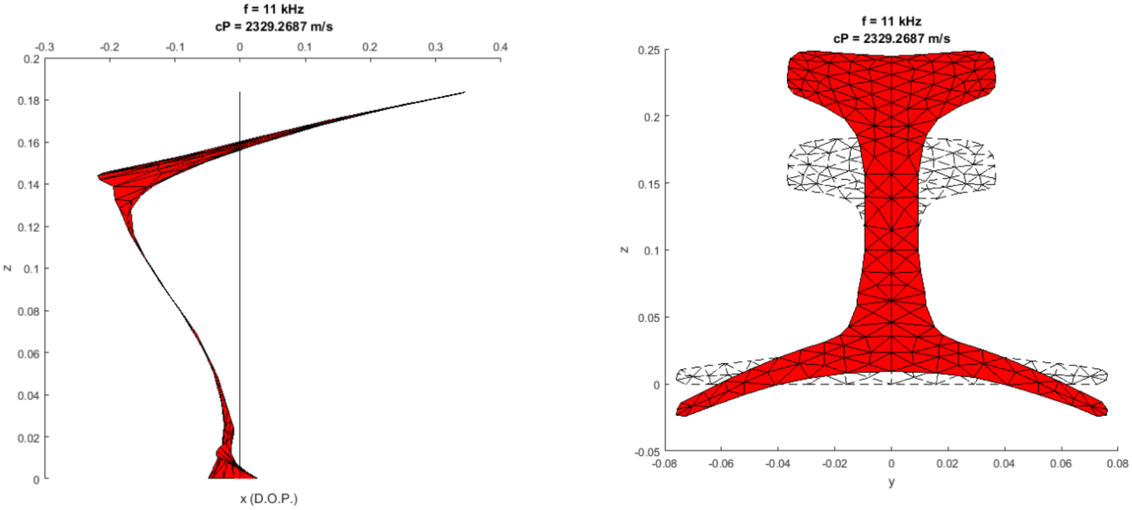

Figure 28 - Mode 5: modeshapes side view for in-plane displacement (left), front-view for out-of-plane displacement (right).

Several modeshapes were analyzed to select the modes that had a strong interaction with the head of the rail: experimental excitability of such modes together with high group velocity for ease of reception and interpretation of the experimental signals (i.e. early time of arrival) has been accounted for in the selection of the incoming modes. Figure 28 reports the side and front view of mode 5 at 10 kHz, to emphasize the in-plane displacement (left) and out-of-plane displacement (right). The same is done in for mode 8.

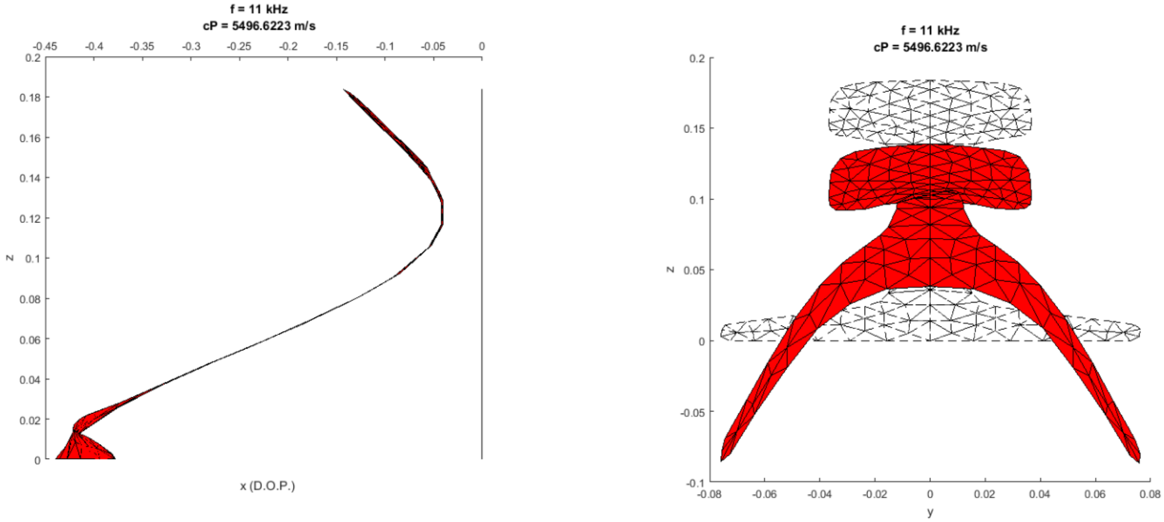

Figure 29 - Mode 9: modeshapes side view for in-plane displacement (left), front-view for out-of-plane displacement (right)

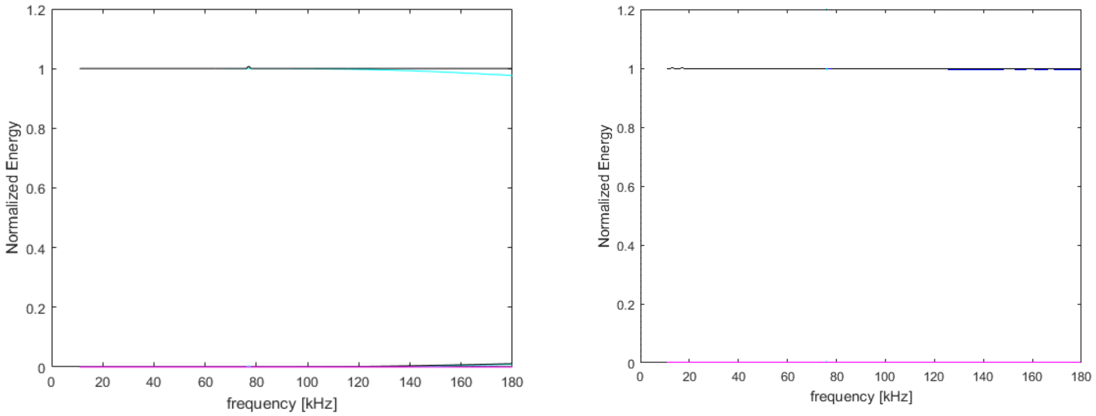

Figure 30 - Reflection and transmission energy spectra for (left) m5 incident mode and (rigth) m8 incident mode in the pristine rail.

Figure 30 shows the Normalized Energy for a pristine rail, when mode 5 (left) or mode 8 (right) are incident in the range 10-180 kHz. Both plots validate the 3D GL method, showing conservation of energy for the entire frequency range, when the pristine rail is analyzed. A slight mode conversion takes place above 130 kHz when mode 5 is incident.

Figure 31 shows the same mode 5 interacting with a transverse defect in the rail, of an increasing percentage.

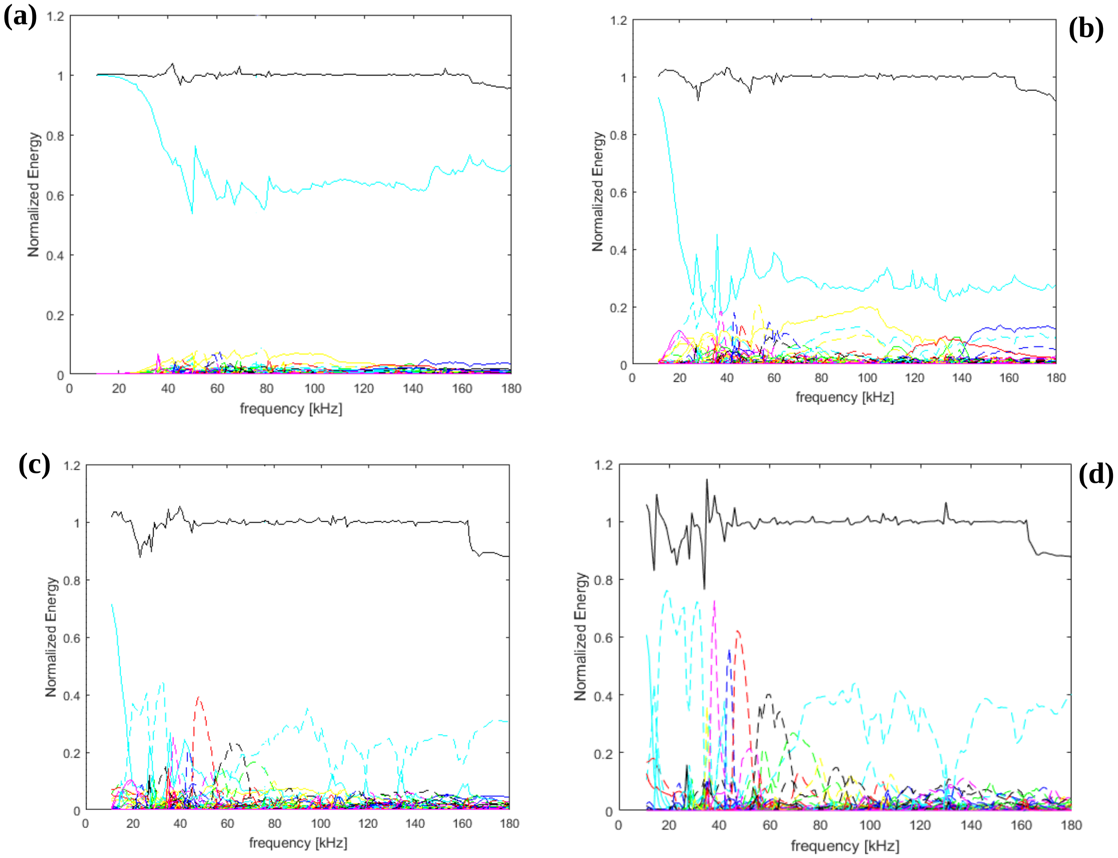

Figure 31 - Reflection and transmission energy spectra for m5 incident mode in the defected head of the rail by (a) 15%, (b) 50%, (c) 85% and (d) 100%.

It is clear how the discontinuity creates mode conversion, reducing the transmitted energy: the larger the defect size (15% to 50%), the stronger the mode conversion (30% to 75% of the total energy), and the lower the frequency at which mode conversion occurs (50 kHz to 20 kHz). The latter phenomena can be explained by the physical interaction and hence alteration of waves of increasing wavelength with larger defects. Moreover, when the defect involves 85% and more of the rail head, most of the wave is reflected back (dashed lines). At 50 kHz, mode 5 couples with mode 29 in particular, where up to 60% of the latter is reflected back when the whole head of the rail is damaged. This effect could be exploited for example when using a pulse-echo approach in an experimental set-up to detect and characterize the percentage of defected rail. It also highlights how, for frequencies higher than 160 kHz, the conservation of energy is not respected, with an effect that is clearer as the defect size increases. This is related with the leakage of energy absorption from modes included in the analysis towards modes that are not.

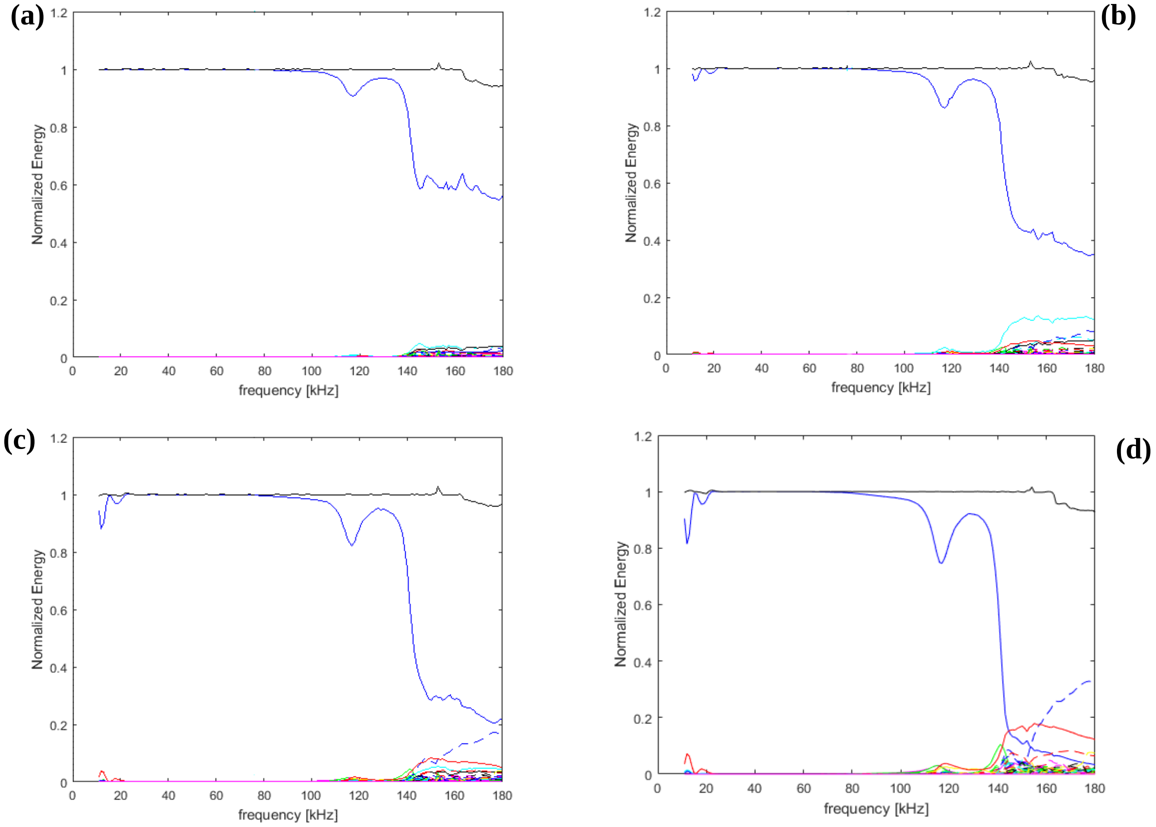

Figure 32 - Reflection and transmission energy spectra for m8 incident mode in the defected head of the rail by (a) 15%, (b) 50%, (c) 85% and (d) 100%.

When exciting the structure with mode 8 (Figure 32), the inspecting wave starts interacting with the head of the rail only at the higher frequencies: above 110 kHz the transmitted energy decays due to the defect. Again, the more the defect size increases, the higher the mode conversion of the incoming mode in other modes. Moreover, when the defect size is at least 50% of the rail head, scattering happens also at lower frequencies (below 20 kHz) and the effect increases with the defect. This interaction might be due to the intrinsic character of the modeshape.

In this formulation, only propagating modes are considered and evanescent modes are neglected, assuming their energy vanishes away from the scatterer (geometrical discontinuity or defect). At lower frequencies, though, this assumption is not fully satisfied as Figure 33 and Figure 34 show: the total energy has a higher error in its convergence to 1, showing that the boundaries at which the reflected/transmitted energy is computed are not far enough for the evanescent modes to have decayed. To confirm this assumption, a study on the distance of the boundaries from the scatterer has been performed, as discussed below.

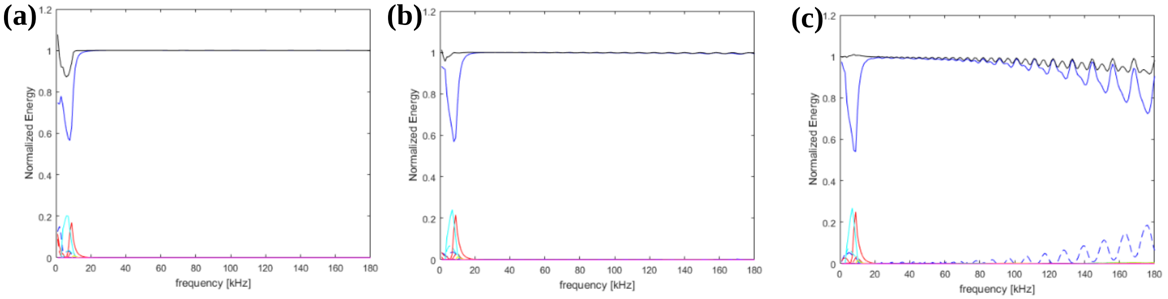

Figure 33 - Size of the Local region and element size study on mode 1 incident: (a) 10cm, (b) 20cm, (c) 40cm.

Mode 1 is chosen as the incoming mode and Figure 33 shows its interaction with a 100% H.A. defect in the head, for a rail having a local region length of 10cm (a), 20cm (b) and 40cm (c). It can be noted how the dimension of the local region affects the results, due to the effect of the evanescent modes: as the distance of the boundary is placed further from the discontinuity, the total energy converges to 1, even at higher wavelengths. From a solid mechanics point of view, this effect is similar to a sort of De Saint Venant principle: as the stress in a beam at a distance higher than the height of the cross-section is not dependent on the shape of the traction distribution applied at boundaries, here if the distance from the boundary is smaller than the height of the cross-section, energy is not conserved.

In the same analysis, it is evident how the meshing refinement affects the performance of the method. Due to computational limitations, the size of the elements used to discretize the geometry is augmented as the distance to be modeled increases, namely dx=1.25mm for the 10cm case, dx=2.5mm for the 20cm case, dx=5mm for the 40cm case. Depending on the phase velocity of the mode, the criterion is not satisfied above a certain frequency, and convergence errors become larger as the frequency increases. A trade-off between the element size and the dimension of the local problem needs to be found to optimize the results and computational expense. In addition, scalability can be exploited for isotropic and symmetric cases, exploiting the dispersion relationship between phase velocity and <frequency x thickness> product, so that a real sized problem, very computationally expensive, can be scaled down to a smaller and faster study.

Finally, the number of scattered modes to be included in the analysis was investigated. Particularly for large and complex waveguides as railroad tracks, the number of modes populating the dispersion curves is very high, hence the dimension of the problem is quite big, both in terms of theoretical complexity and computational effort. A condition on the inclusion of the maximum number of scattered modes can be imposed, as long as the error in the total energy remains within an acceptable threshold (i.e. less than 10%). Figure 34 shows the improvement in the total energy result as the number of modes is increased, for an incoming mode 5 on the 100% defect case.

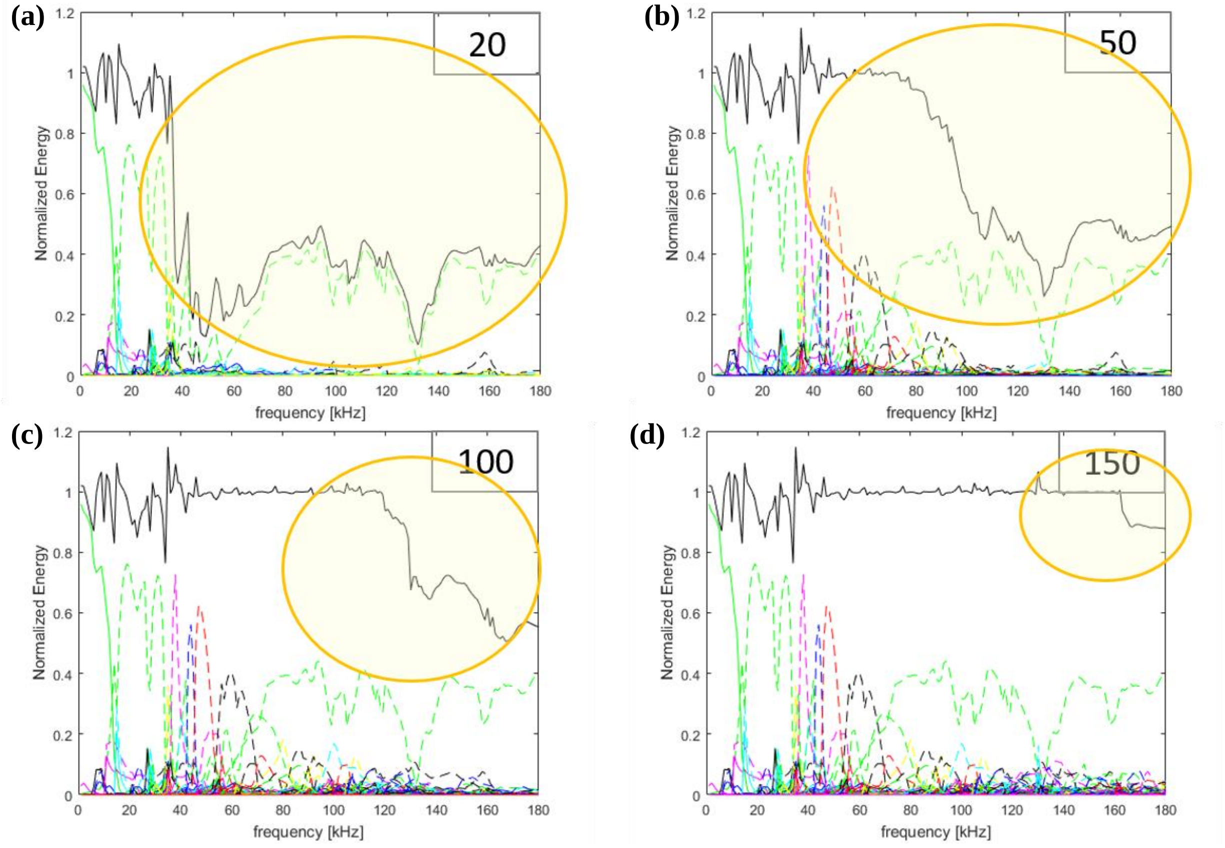

Figure 34 - Reflection/transmission energy spectra for m5 incident: study on number of max scattered mode included in the analysis: (a) 20 modes, (b) 50 modes, (c) 100 modes, (d) 150 modes.

In light of the results and considerations in terms of meshing criterion, evanescent modes and number of modes scattered, a new analysis on a 40cm rail geometry, element size 2.5mm instead of 5mm (2.5mm is the element size of the 20cm rail), 150 modes scattered, has been run with the 3D GL method, for the 100% H.A. defect case study. These results are compared with those obtained for the 20cm rail and shown in the following Figure 35.

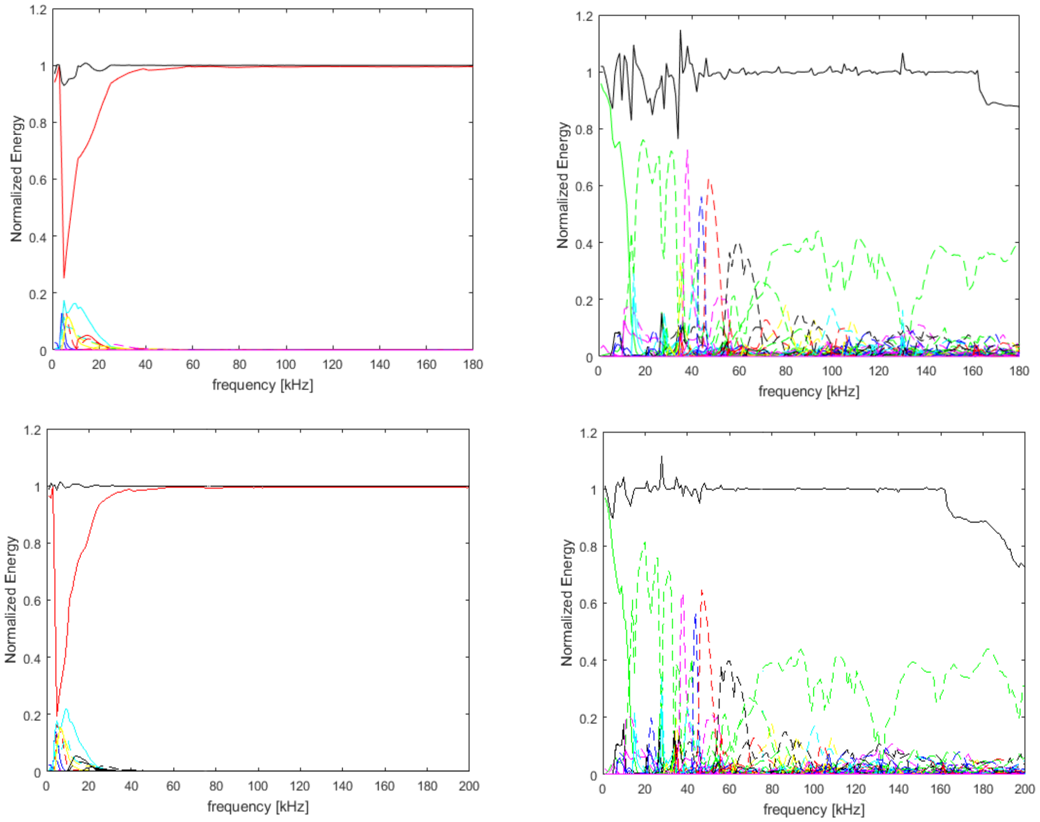

Figure 35 - Reflection/transmission energy spectra for m2 (left) and m5 (right) incident on 100% H.A. defect in a 20cm (top) vs a 40cm (bottom) rail.

For both modes, it can be noticed how the distance damage-boundaries affects the result, confirming the influence of the evanescent modes to achieve conservation of energy. The error with respect to a total normalized energy converging to 1 reduces as the distance from the boundaries increases and exceeds twice the cross-section of the waveguide (see Table 7).

Table 7 - Error of total energy: distance from boundary effect

Size Local Region (cm)	**Error (%)**			
	Mode 1	*Mode 2*	*Mode 3*	*Mode 4*
20	12.8	7.2	11.9	23.6
40	2.4	1.4	4.0	11.4

In this work, the 136lbs rail track and transverse defect have been studied only, but the proposed GL method can be extended to any waveguide geometry and type of defect.

In addition, the homogeneous solution presented here can be extended to the forced solution, where a spatial and temporal distribution of forces can more closely simulate a real test scenario. The implementation of such solution requires a precise frequency step and frequency range to satisfy sampling criteria and to provide a minimum time range to observe wave propagation for the modeled distance. The author is currently running a variety of cases for both isotropic and anisotropic materials, 2D and 3D problems, to extract a time-domain response representing the structural behavior of the specimen with and without defects, given certain loading set-ups.

2.4 Application

The theoretical and numerical studies performed in the previous sections provide insights in ultrasonic guided wave propagation and enables experimental tests and NDE inspections on composite panels. Three major sets of composite panels were fabricated in the Advanced Composite Laboratory at UCSD for the High Energy Wide Area Blunt Impact (HEWABI) project, followed by the NDE HEWABI project and a later NASA project. Details on the specimens fabrication and impact damage formation are provided in Section 2.4.1. UGWs were chosen as the NDE technique to inspect the damaged panels. An inspection prototype was developed, as shown in Section 2.4.2, after some preliminary investigations, described in the section below.

2.4.1 Test specimen and previous studies

In the first place, composite panels from a previous FAA HEWABI project (De Francisci, 2013) developed many major internal damage modes of interest from impact tests. These previously tested composite panels made ideal test specimens for damage-detection studies in the NDE project because they contained large hidden damage to critical elements. The panels were designed and fabricated by University of California San Diego with supportive guidance from industry experts and were impacted with rubber bumper indenters (see Figure 36) to investigate damage modes induced from a GSE impact scenario.

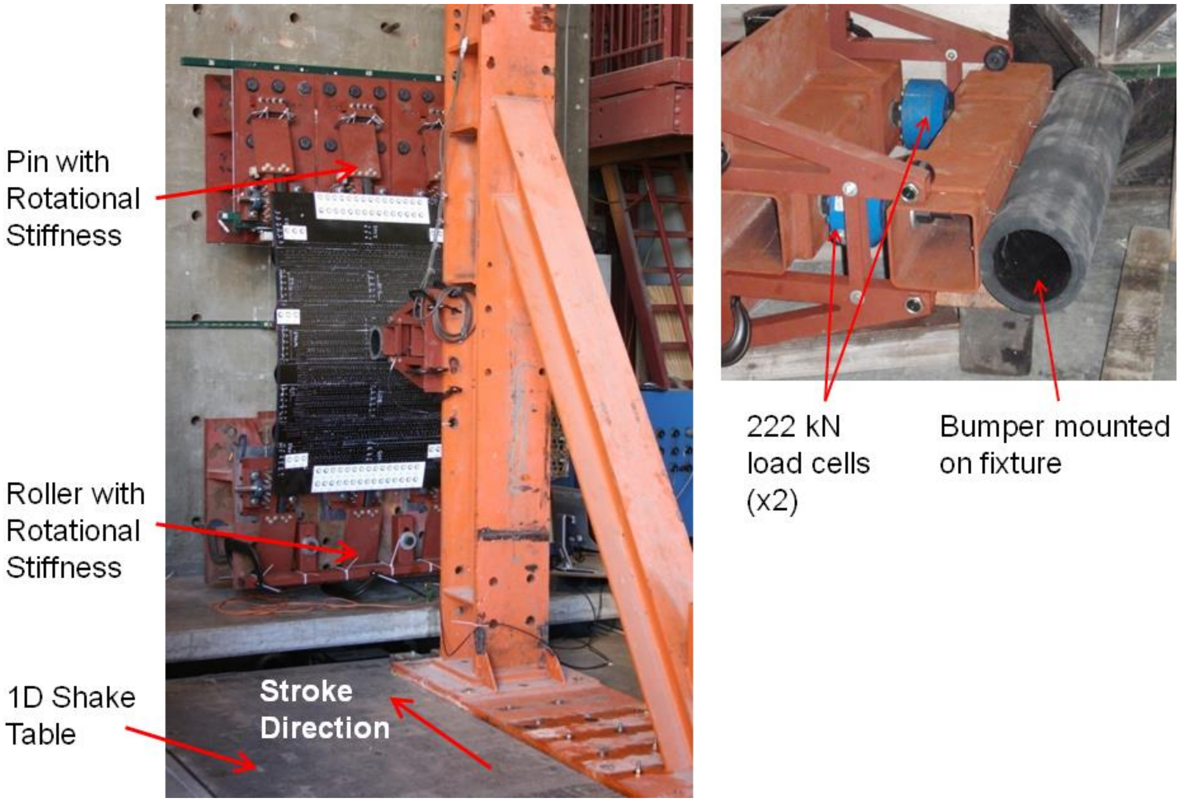

Figure 36 - HEWABI project phase I: damage formation with 1D impact on panel (experimental setup).

The composite panels were fabricated using Cytec X840/Z60 12k unidirectional tape and X840/Z60 6k weave fabric prepreg materials with ply layups, as listed in

Table 8. All parts were laid up by hand at UC San Diego and were autoclave-cured at San Diego Composites under a 176.7ºC cure temperature. The panels were quasi-statically or dynamically loaded to induce different types of damage from various impact cases. The major damage modes generated are: cracked fames, crushed shear ties, stringer heel cracks, skin cracks, skin-to-stringer disbonds.

Table 8 - Composite parts layup sequences

Part	Layup	Thickness (mm)	Material
Skin	[**0**/[0/45/90/-45]$_{2S}$/**0**]*	2.7	Tape
Stringer	[[0/45/-45/90/45/-45/0]$_{S}$/**0**]**	2.4	Tape
Shear Tie	[45/0]$_{3S}$	2.9	Fabric
C-frame	[45/0]$_{3S}$***	2.9	Fabric

* First and last 0° plies are woven fabric

** Last 0° ply is woven fabric

*** Two additional 0° fabric were added to both sides of flange

Skin and stiffening internal components have their own unique wave path and share a common wave path only at the mechanically fastened region every 12 inches, where the shear-ties, bolted to the skin, connect the C-frames to the whole assembly, as shown in Figure 38a. Although wave propagation through each individual internal component was studied, differentiating between stiffened internal structure wave transmission versus skin wave transmission remained challenging. The complex assembly and depth of the internal components affects the wave propagation scattering pattern and travel through multiple wave paths. It is very important to understand how much of the wave transmitted/received through the skin penetrates the internal components and is affected by it. Therefore, various levels of assembly and aspects of joining were further investigated to establish their influence on UGW transmission.

The tests performed on the panel, with subcomponent parts assembled and disassembled, helped to understand wave energy leakage into the internal structural components versus transmission within the skin only. UGW tests were performed first on the full assembly (skin with C-frame bolt joined by shear ties), then again after removal of the C-frame, and, finally, after the removal of the shear ties (see Figure 38). The transducers were consistently fixed in place throughout these assembly and disassembly procedures, using a 3D-printed hold-down mount, as seen in Figure 37, to avoid variations in amplitude due to coupling thickness and sensors pressure. Figure 39 shows UGW test results at 150 kHz and the intensity increase for each disassembled part: a 43% increase when only the C-frame was disassembled, and a 633% increase when the shear ties were disassembled for skin-only wave propagation. Test results could be related to how much energy was drawn into the internal composite stiffening components. It was noted that 86% of the energy leaked into the internal structure when the skin-only wave energy was compared to the fully assembled panel. These tests proved the possibility to inspect the internal components of the aircraft fuselage through UGWs in a pitch-catch mode, up to the shear-ties level of penetration.

Figure 37 - 3D-printed hold-down mounts for transducers on outer skin

(a) Full assembly with C-frame and shear ties

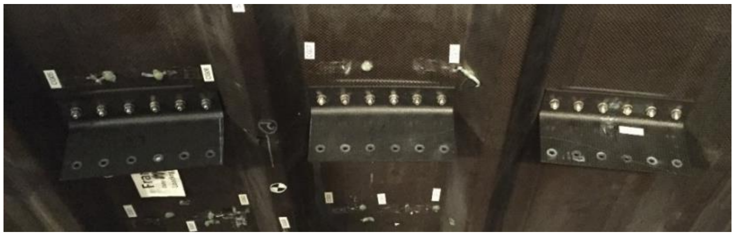

(b) C-frame only removed (shear ties mounted)

(c) C-frame and shear ties removed (co-cured shims visible on skin)

Figure 38 - Different levels of disassembly for UGW tests: (a) full assembly with C-frame and shear ties, (b) C-frame only removed, (c) C-frame and shear ties removed.

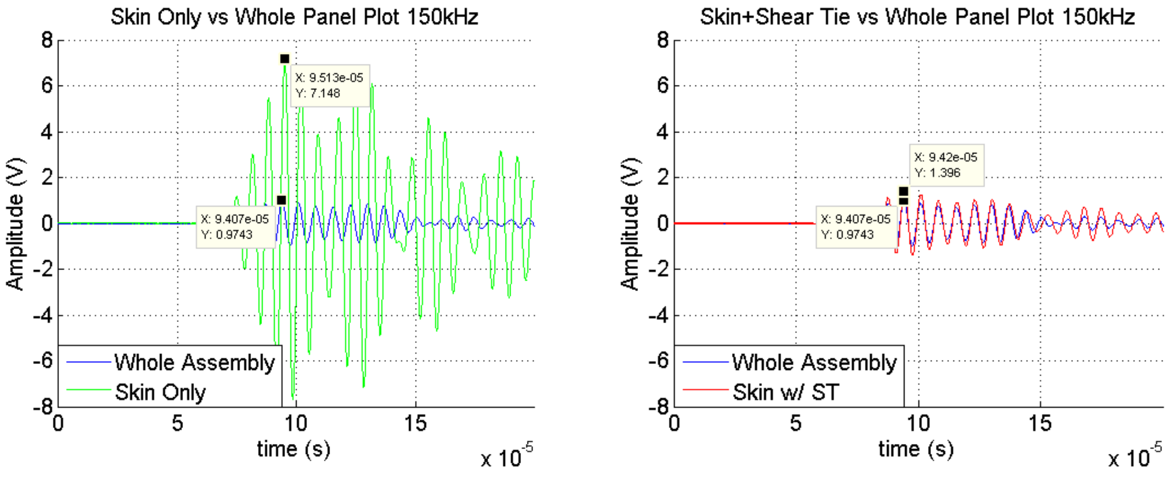

(a) Skin-only vs. entire assembly

(b) Skin and shear ties vs. entire assembly

Figure 39 - Assembling/disassembling test results: (a) skin-only vs. entire assembly and (b) skin and shear ties vs. entire assembly.

Although the assembly and disassembly test showed that a significant amount of energy leaks into the internal structure, it was still unclear how much of the internally transmitted waves is able to transfer out, back to the skin side. To investigate wave transmission through the internal structure only, two smaller stringer panels were joined by a single C-frame, leaving a break in the skin (see figure 14). By conjoining two panels, skin discontinuity exists and only the waves transmitted through the internal components (and in particular through the C-frame) arrive at the receiver transducer. As seen in Figure 40, the transmitter and receiver are attached to the skin on each panel at the center of each shear tie. For a better comparison of the internally transmitted UGW behavior at different frequencies, UGW test results from Pico Sensors (the transmitter and the receiver) were investigated instead of the narrowband frequency R15s sensors. Figure 41 shows that the UGWs transmitted through the internal structure at 50 kHz had much higher energy than the UGWs at 150 kHz. Similarly, additional frequency sweep test results show that frequencies lower than 80 kHz give a strong internal wave energy transmission. Therefore, it would be best to use an excitation frequency lower than 80 kHz to better investigate UGW propagation through the internal components as shear-ties and C-frames, which is a necessary condition for detecting damage in those components.

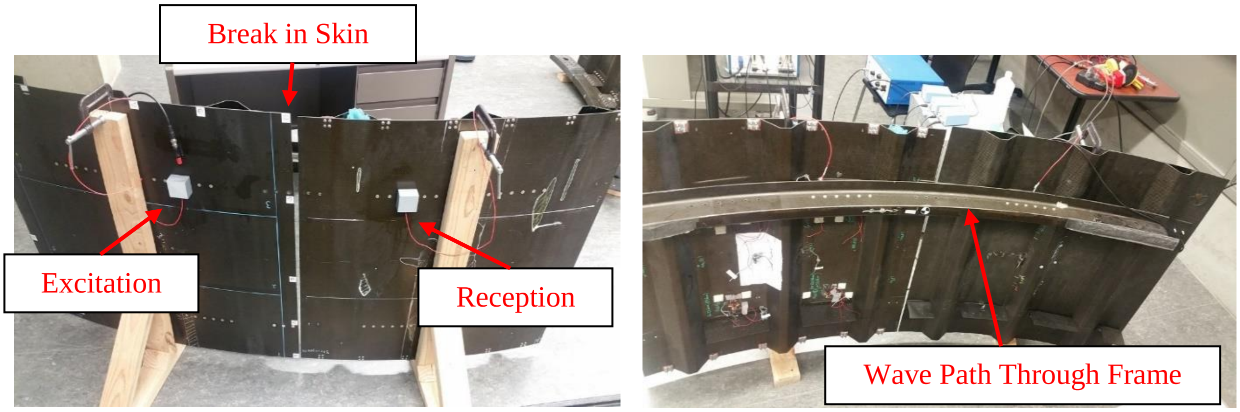

Figure 40 - Conjoined panels by C-frame to study wave propagation in C-frame only: (left) outside skin view, (right) inside skin view.

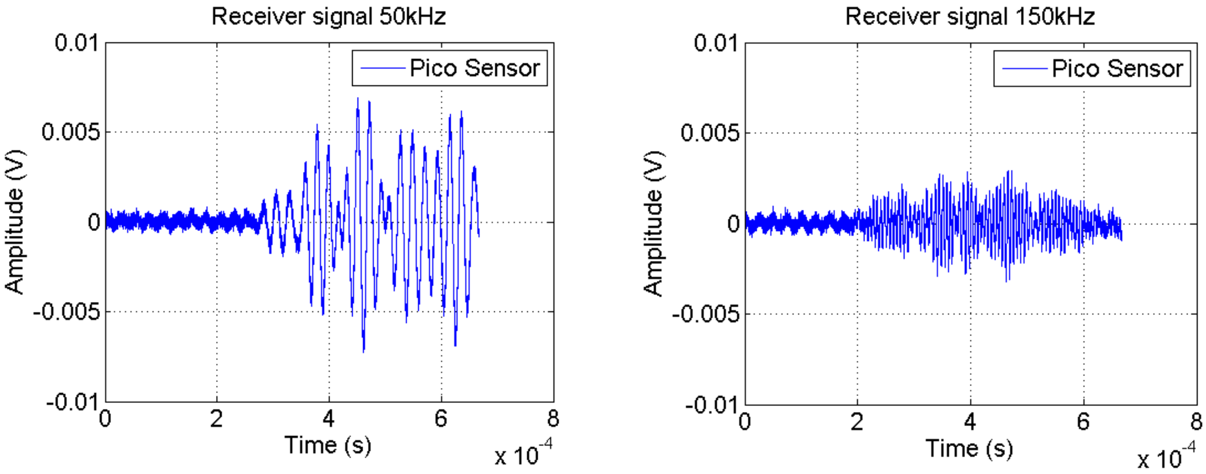

Figure 41 - Conjoined panels tests result: (left) 50kHz, (right) 150kHz received waveform.

The use of UGWs and the analysis employed in the development of the technique rely on the wave propagation as it is determined by the given material, geometry, assembly, and finally health condition of the specimen. The characterization of the wave-propagation properties becomes important to understand and better exploit the feature changes, and validate the assumption made to perform the experimental tests. As discussed in the previous section, the analytical solution cannot account for the wave propagation through many interfaces (mainly the higher attenuation), into different angles, and for geometries that are more complex. This can be accounted for using numerical FE simulations and experimental investigation. The characterization of the assembly is achieved here by the extraction of experimental dispersion curves.

A 2D FFT can be used to extract phase-velocity dispersion curves for a given structure, assuming that the velocity does not change with direction, i.e. neglecting anisotropy. Exploiting the dispersive and multimode character of UGWs when generated by a broadband excitation, the 2D-FFT method, as explained by Cawley in (ref), can extract amplitude and velocities information of multiple modes, for the whole frequency range as:

$$U(k,f) = \int_{-\infty}^{+\infty}\int_{-\infty}^{+\infty} u(x,t)e^{-i(kx-\omega t)}dx\,dt$$

provided a sufficient spatial and temporal sampling.

To do so experimentally, a multiple input, single output (or single input, multiple output) configuration is needed, using fixed broadband capacitive air-coupled transducers (BAT, from Microacoustics) for reception and a pulsed laser excitation (Q-switched ND:Yag, 1064 nm, 9 ns duration). Test results for a laser impulse sent along a line of 64 points (nodes) with a 1-mm resolution, as shown in Figure 43, are discussed below. The two transducers focus on receiving mostly a specific mode. Mode selection is achieved tuning the angle of the transducers, following Snell’s law, that relates phase velocity and incidence/reflection angle:

$$\frac{sin\vartheta_1}{c_1} = \frac{sin\vartheta_2}{c_2}$$

In this case 1 is the composite material and 2 is air, since the wave has to travel through the composite, it hits the boundary with a $\vartheta_1 = 90°$ and exits in air before reaching the transducer. The latter has to be angled at a $\vartheta_2 = \sin^{-1}(c_{air}/c_{p_{mode}})$, where $c_{air} = 340\, m/s$. For an estimated $c_{P_{A0}} = 1500\, m/s$ and $c_{P_{S0}} = 4500\, m/s$, transducer 1 was angled at $\vartheta_2 = 13°$ to better capture the first anti-symmetric mode, while transducer 2 was angled at $\vartheta_2 = 0°$ to better capture the first symmetric mode. The figure below explains the angle tuning for mode selection when using non-contact transducers.

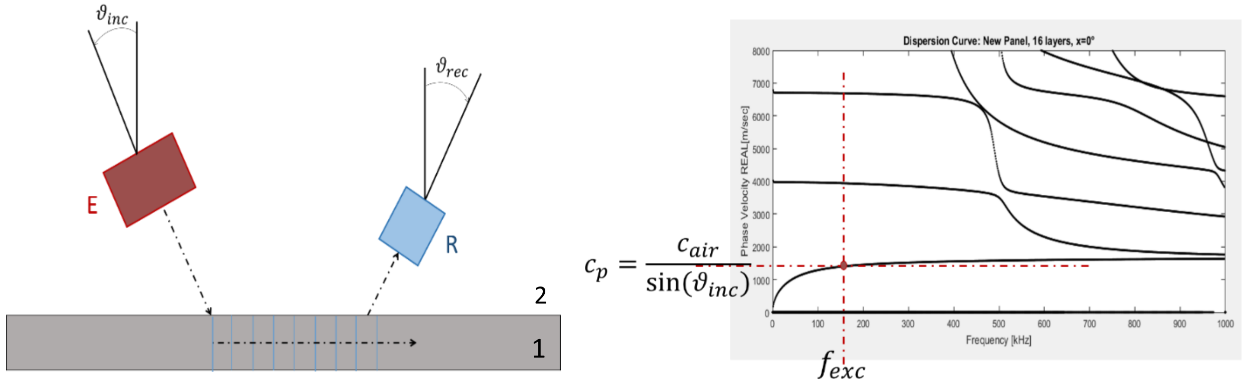

Figure 42 - Angle tuning for mode selection in air-coupled transducer excitation/reception: (left) orientation of the sensors, (right) phase velocity selection.

Similar tests repeated on an aluminum plate are shown for purposes of comparison. The time signal on the first point of the line scan, node 1, appear in Figure 44 for two receivers. The respective FFT for one receiver for the A_0 and S_0 modes, as gated in Figure 44, appears in Figure 45.

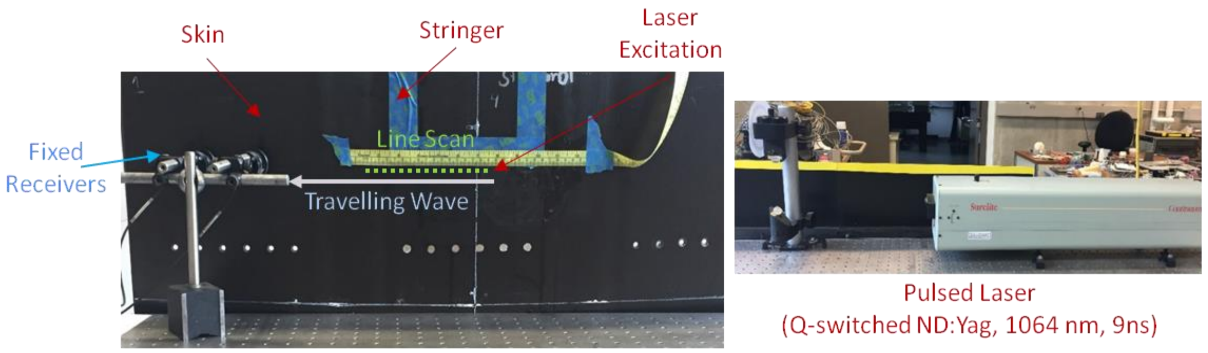

Figure 43 - Laser scanning test setup on composite panel: (left) fixed air-coupled receivers and scanned region on specimen, (right) laser and optics used for excitation.

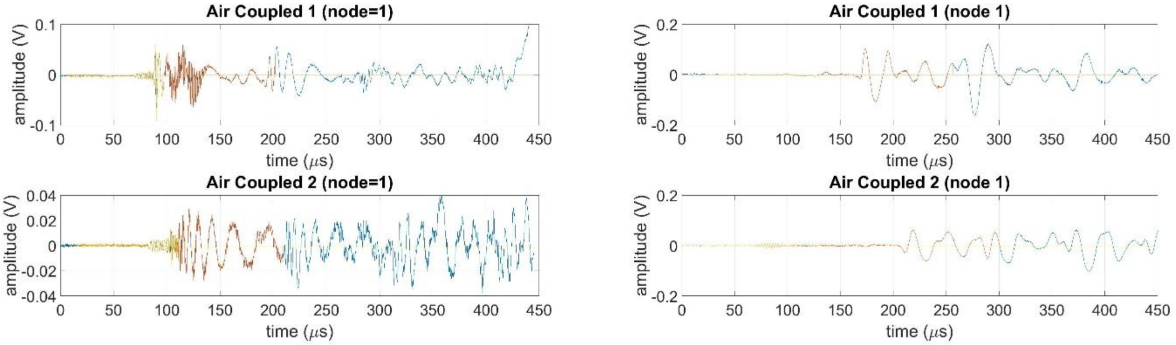

(a) Aluminum plate (b) Composite plate

Figure 44 - Time signal at node 1 for two air-coupled receivers (top and bottom): (a) aluminum plate and (b) composite plate.

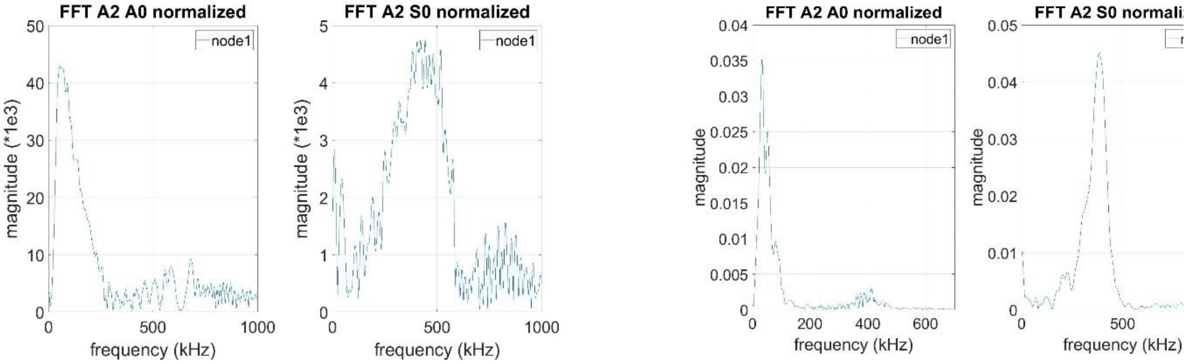

(a) Aluminum plate (b) Composite plate

Figure 45 - FFT of signal at node 1 for A0 and S0 modes: (a) aluminum plate and (b) composite plate.

The composite material attenuates the higher frequencies and higher order modes, and the curved and complex (multiple components) structure disturbs the dispersion of the wave packets and interferes within them. By applying a 2D FFT, it is possible to visualize the phase velocity dispersion curves in terms of frequency wavenumber for the multiple modes plotted in Figure 46.

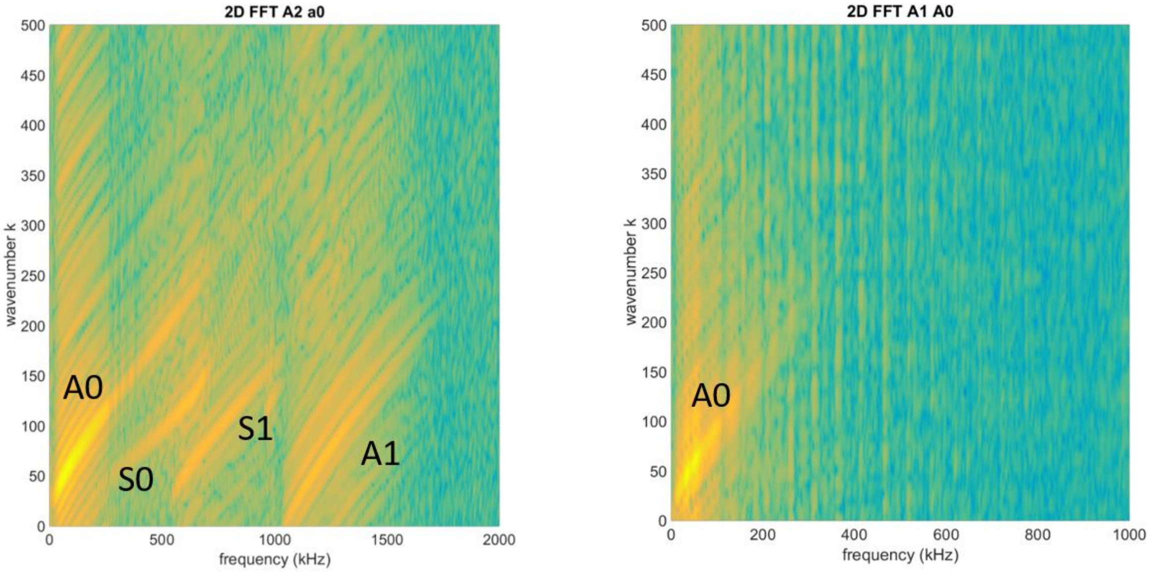

(a) Aluminum plate (b) Composite plate

Figure 46 -2D FFT for experimental extraction of dispersion curves: (a) aluminum plate and (b) composite plate.

The composite panel filters out most of the modes, especially at the higher frequencies. Plotting this information in a phase velocity vector, the following dispersion curves appear in Figure 47.

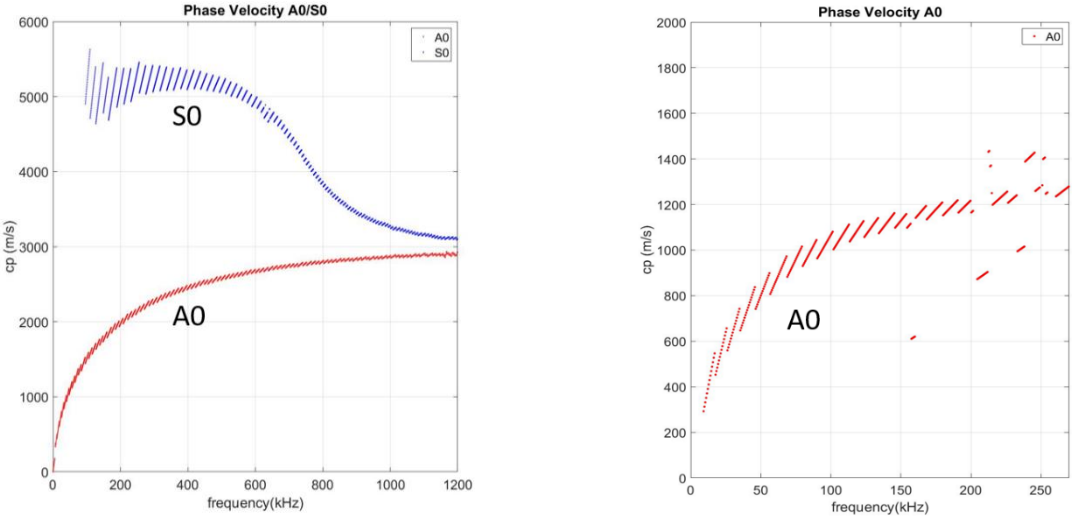

(a) Aluminum plate (b) Composite plate

Figure 47 - Experimental dispersion curves (phase velocity): (a) aluminum plate and (b) composite plate

Group velocity dispersion curves retrieval has also been studied using Continuous Wavelet Transform (CWT). Energy information in amplitude and time of arrival can be extracted through CWT, as shown in Figure 48c. Knowing the distance between excitation and reception, group velocity can be extracted for the whole frequency range and multiple modes. A preliminary result confirms the use of the A_0 mode group velocity as 1600 m/s for 170 kHz in the gating of the defect-detection analysis performed and shown in Figure 48d.

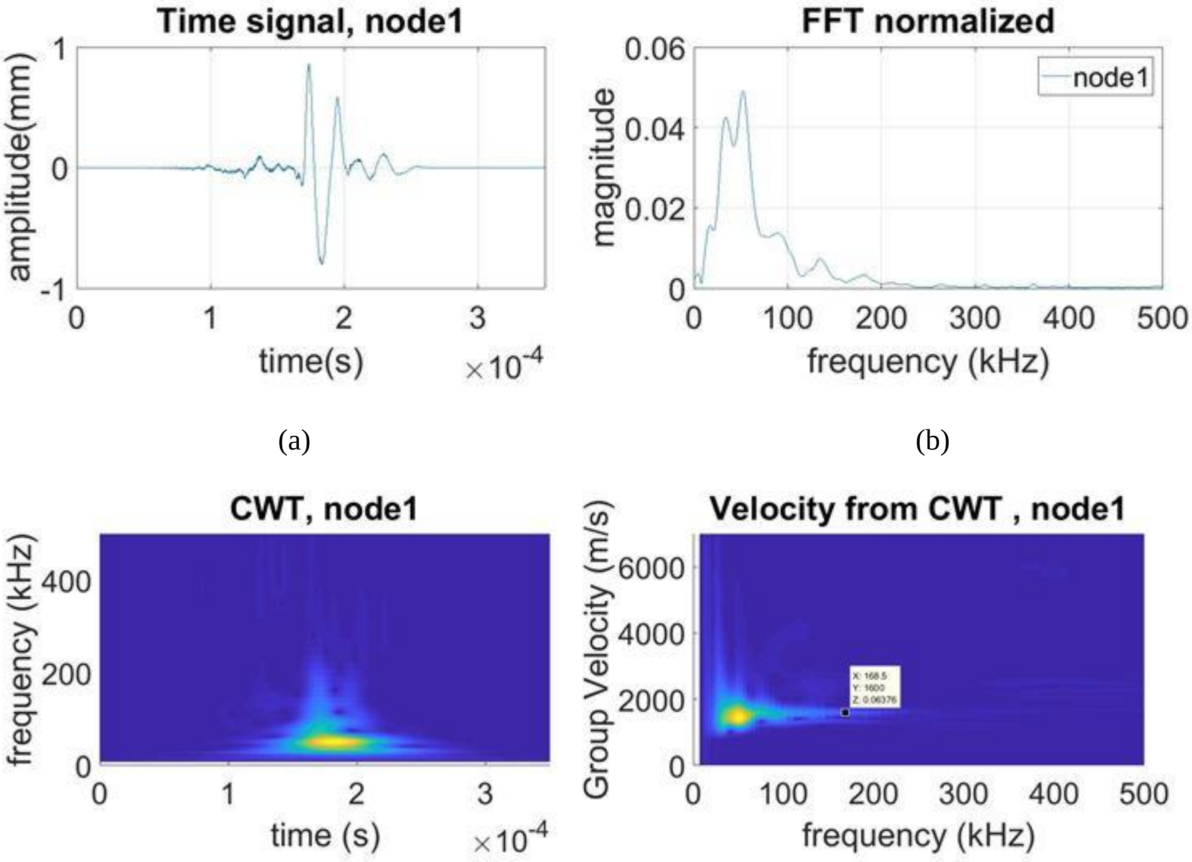

(a) (b)

(c) (d)

Figure 48 – Data from experimental extraction of dispersion curves. Composite plate at node 1: (a) gated time signal, (b) FFT of A0 mode, (c) time-frequency CWT, and (d) experimental dispersion curve (group velocity) for A0 mode.

2.4.2 Nondestructive Inspection of Composite Aircraft Panels by Ultrasonic Guided Waves and Statistical Processing

The same carbon/epoxy composite panels representative of commercial aircraft construction (e.g. wide-body fuselage), manufactured and tested at UCSD from a previous FAA sponsored HEWABI project, (De Francisci, 2013) were used to develop and test the NDE technique. The panels were designed and manufactured following industry procedures and dedicated fabrication processes to achieve comparable aerospace characteristics and quality. While the test specimens varied in size, they were manufactured with the same material and overall structural design. Each test panel (Figure 49) was composed of a curved skin, stiffened by co-cured stringers along longitudinal direction, and by C-frames (bolted to the skin by shear-ties) along the radial direction. The lay-up of the skin was as in Table 8. All parts were cured via the autoclave process.

These panels were subjected to wide area blunt impacts by using a rubber impactor driven by a one degree of freedom actuator table to simulate a GSE in-service contact and resulting damage formation. Different damage types and severities at various locations were generated and surveyed by visual inspection and hand-held ultrasonic scanning. Detected damage included, from the outside skin into the C-frames: skin cracks, stringer-skin disbonds or detachments, stringer cracks, shear tie cracks, and C-frame cracks. Some of these are highlighted in Figure 49.

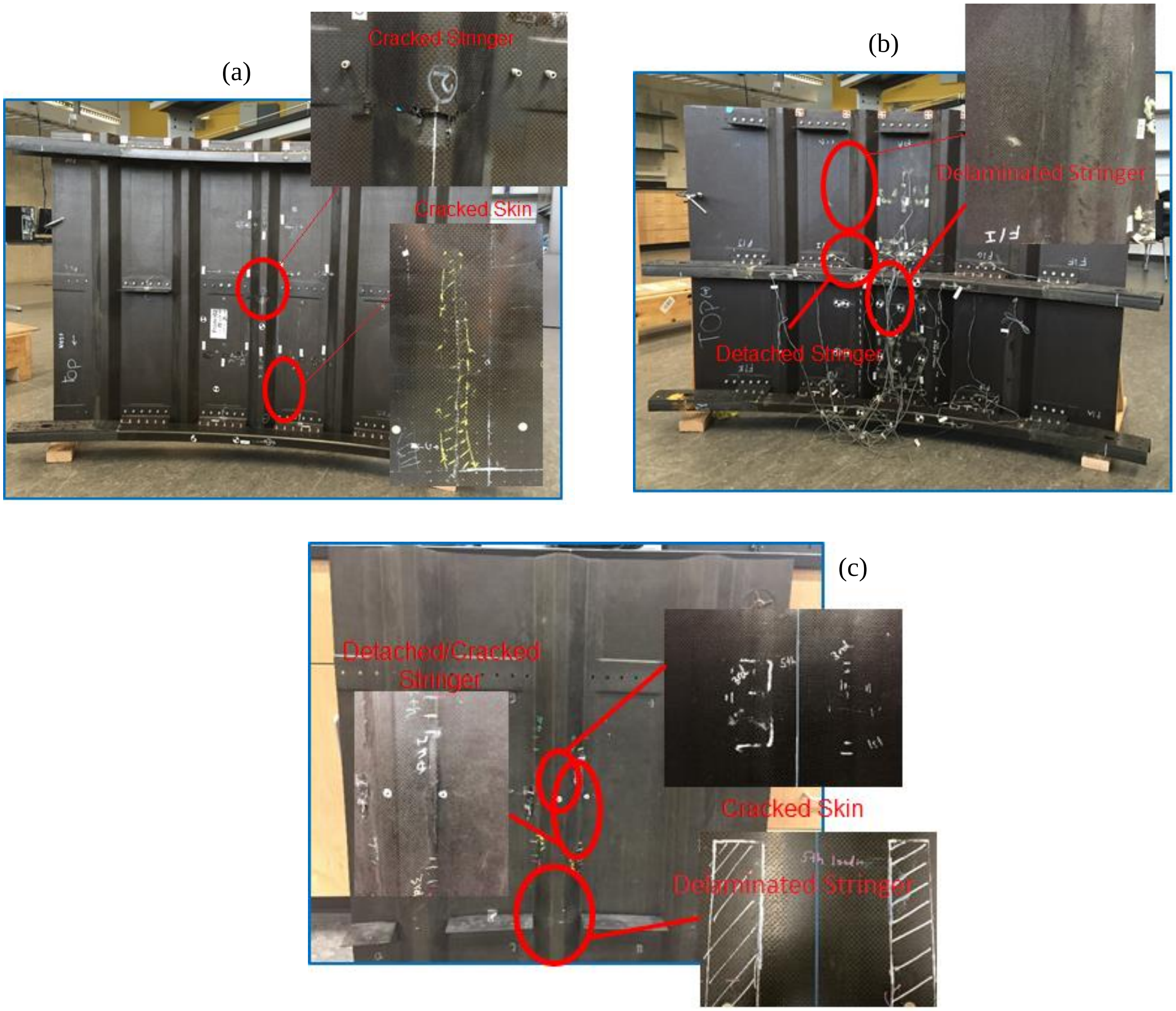

Figure 49 - Test specimens: (a) Panel 1: five stringers, three C-frames panel with cracked skin and cracked stringer; (b) Panel 2: four stringers, three C-frames panel with disbonded/detached stringer; (c) Panel 3: three stringers, two C-frames panel with cracked skin, detached/cracked stringer and disbonded stringer.

The nature of the structure suggested the use of UGW: the ultrasonic waves can travel inside the different components of the assembly that behave as natural waveguides. Moreover, the complexity of the panels, in terms of size, curvature, material and number of interfaces and travelling paths, require wide area coverage and low attenuation, properties that can be satisfied by UGW. The schematic below (Figure 50(a)) shows the adopted inspection approach: the excitation is sent from the outside skin, the wave penetrates into the stringers and shear ties, travels into the C-frames and, after interacting with defects if present, can be collected again from receivers placed on the outer skin.

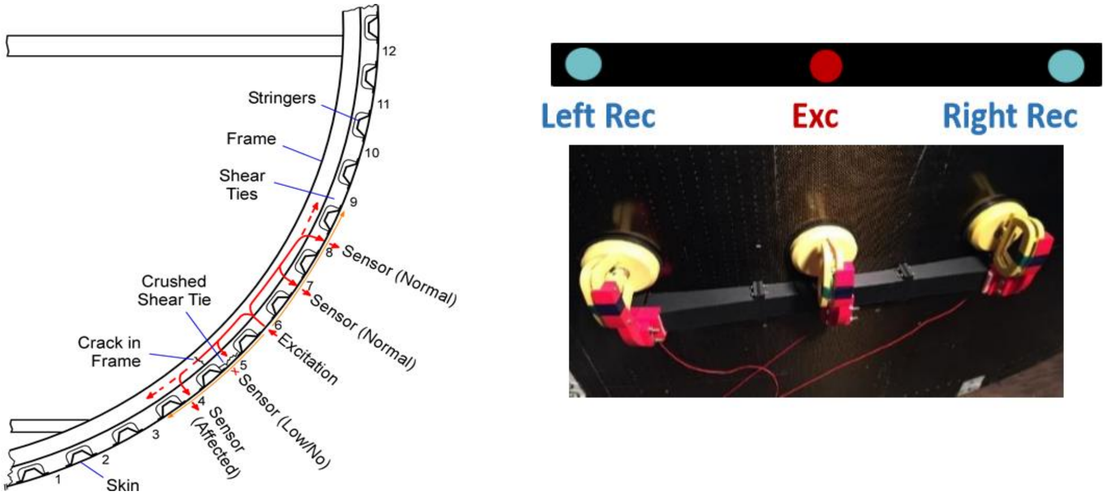

(a) (b)

Figure 50 - (a) Schematic of the UGW approach for the aerospace panel inspection. (b) Differential scheme for contact inspection.

Numerical Finite Element studies of UGW propagation in this kind of stiffened panel were previously conducted in Nucera et al. (2015), in the context of real-time impact force identification. Those simulations also supported the idea of exploiting the multiple wave modes simultaneously present in this structure. Figure 51 shows some results from FE simulations conducted using the procedure detailed in Nucera et al. (2015), where it is possible to notice the presence of the two fundamental modes (anti-symmetric A_0 and symmetric S_0) and their propagation into the different components. The specific excitation used in this figure was an impulsive force of duration of 0.1 μs, and therefore generating a usable frequency bandwidth up to 10 kHz. These kinds of simulations aided the time gating of the various wave modes measured in the experimental tests that are discussed in the next sections.

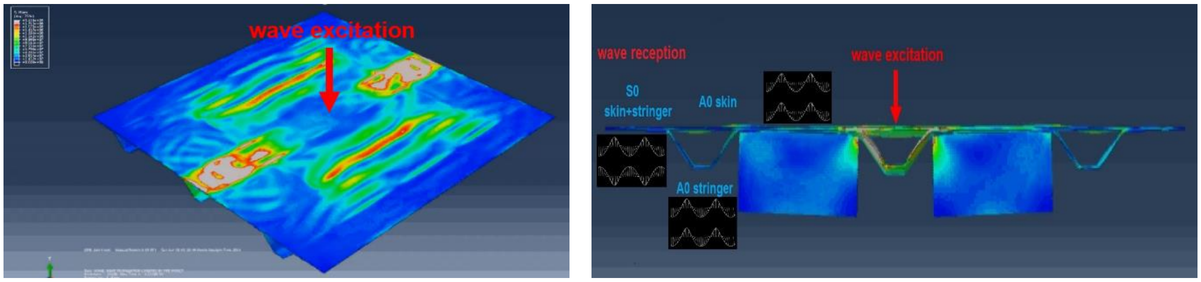

(a) (b)

Figure 51 - FE model of a stiffened composite panel: (a) 3D view; (b) cross-sectional view showing multi-mode wave propagation and acoustic inter-talk between the skin, stringer and shear ties.

Due to the requirement for rapid inspection, a line scanning approach of UGW testing was taken. Accordingly, the test panels were scanned along a stringer direction as shown in Figure 52.

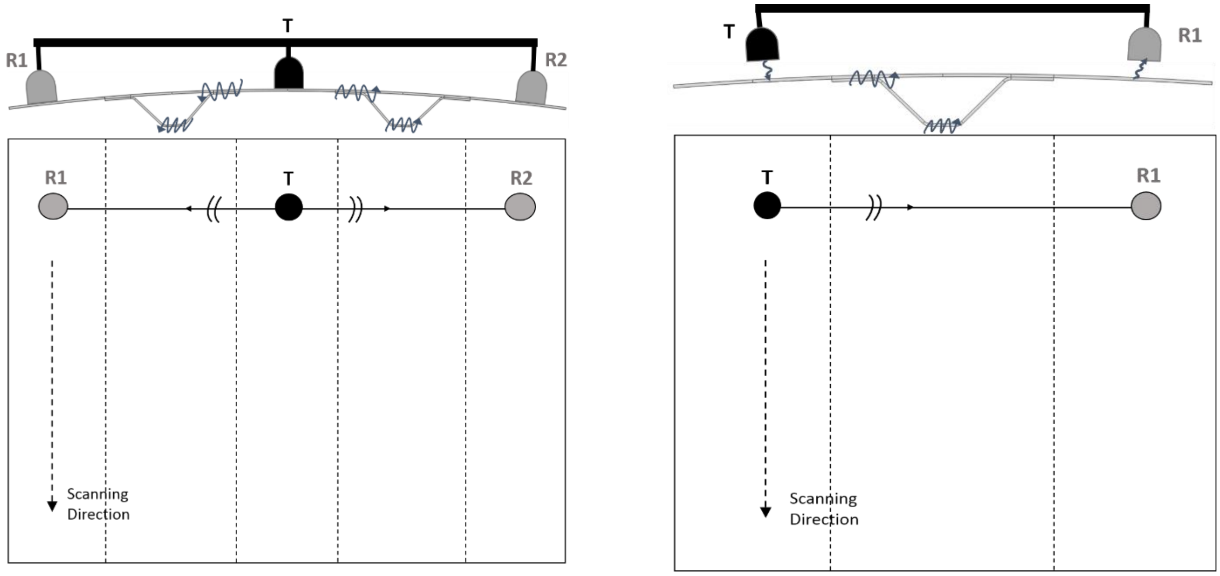

(**a**) (**b**)

Figure 52 - Line scanning approach for (a) contact system and (b) non-contact system; cross-sectional view (top drawings) and front view (bottom drawings).

This scanning process also lends itself to a statistical analysis aimed at minimizing signal behavior due to normal operational variability across a scan (specimen inhomogeneities, etc.) and maximizing signal variations due to true structural defects. Following the general statistical Multivariate Outlier Analysis (MOA) for novelty detection (Worden et al., 2000; Rizzo et al., 2007), the test scans were normalized by their normal statistical distribution ("baseline"). A baseline is built relying on signals collected from a known pristine area of the impacted specimen; every test scan is then compared to its baseline through a MOA processor. Relying on the physics of wave propagation, the latter extracts specific features from each UGW signal, and feeds them into a feature vector. A Damage Index (DI) is computed according to the Mahalanobis Squared Distance metric:

$$DI = (x - \bar{x}) * C^{-1} * (x - \bar{x})^T, \tag{1}$$

where x is the feature vector, $\bar{x}$ is the baseline average vector and C is the baseline covariance matrix. A large value of DI represents a deviation from the normal statistics of the signals, hence an outlier in the distribution or, in a damage detection perspective, a defect.

The feature extraction process is performed on selected time-gated wave packets, corresponding to different wave modes propagating in the stiffened panel structure. This selection relies on velocity information about the various propagating modes and enhances the sensitivity of the technique to specific defects.

The initial experimental implementation of the NDE technique used contact PZT transducers to excite and detect the UGWs in the test panels. Conventional ultrasonic gel couplant was used. Moreover, the contact approach utilized a differential detection scheme that relies on the "imbalance" of the signal received on two opposite sides of the transmitter to detect a possible defect. The contact prototype with differential scheme is shown in Figure 50b. The differential scheme, which UCSD has used effectively in another NDE project that required scanning across a test structure (Mariani et al., 2013), is robust against coupling variations of the transmitter and several other changes not associated to damage. A narrowband PZT transmitter centered at 150 kHz was used in conjunction with two receivers centered at the same frequency (Mistras R15S). A five-cycle toneburst with Hanning modulation at 150 kHz was used as the excitation signal. A National Instruments PXI unit running under LabVIEW was used as the signal generation and acquisition instrument. At each scan line, the UGWs were collected by the two receivers, gated in time, and processed to extract features related to the imbalance between the two (e.g. ratios of amplitudes). The specific features used are listed in Table 9 ($x_{1/2}$ refers to the signal from receiver 1 and 2, respectively).

Table 9 - Contact technique features list.

Feature #	Feature Name	Feature Extraction
1	RMS Ratio	$\frac{RMS(x_1)}{RMS(x_2)}$
2	Maximum Value Ratio	$Max(\frac{Max\lvert x_1\rvert}{Max\lvert x_2\rvert}, \frac{Max\lvert x_2\rvert}{Max\lvert x_1\rvert})$
3	Area under Packet Ratio	$\frac{Area(x_1)}{Area(x_2)}$
4	Peak to Peak Normalized Difference	$\frac{\lvert Ppk(x_1) - Ppk(x_2)\rvert}{\sqrt{Ppk(x_1) * Ppk(x_2)}}$
5	Area under FFT Normalized Difference	$\frac{\lvert AreaFFT(x_1) - AreaFFT(x_2)\rvert}{\sqrt{AreaFFT(x_1) * AreaFFT(x_2)}}$
6	Maximum Value Cross-Correlation Normalized Difference	$\frac{\max\left(xcorr(x_1, x_2)\right)}{\sqrt{\max\left(xcorr(x_1)\right) * \max\left(xcorr(x_2)\right)}}$
7	Variance Normalized Difference	$\frac{\lvert Var(x_1) - Var(x_2)\rvert}{\sqrt{Var(x_1) * Var(x_2)}}$
8	RMS Normalized Difference	$\frac{\lvert RMS(x_1) - RMS(x_2)\rvert}{\sqrt{RMS(x_1) * RMS(x_2)}}$

These features were then fed into the feature vector and used to compute the DI metric according to eq. (1). The scan resolution across the damaged areas was approximately 1 cm.

Representative results are shown in Figure 53(a) and (b) for Panel 1 and Panel 2, respectively. The vertical lines represent known positions of defects from the prior visual surveys and ultrasonic scans. It can be noticed how the DI increases noticeably in known damaged areas, with very low noise levels, owing to the statistical Outlier Analysis. As expected from a skin probing technique, the sensitivity to damage is higher for the skin defects than for the stringer defects, although the latter are also clearly visible over the very low noise floor of the pristine structure.

Using a traditional B-scan that simply relies on the maximum amplitude of the signal with no statistical processing, no reliable detection of damage could be achieved. As shown in Figure 55(a) and (b), the ratio between the maximum amplitude of the signals collected at receivers 1 and 2 is a highly variable metric, with poor robustness of defect detection. The statistical analysis improves the reliability of the result, since it normalizes the metric by the "normal" statistics of the structure.

These promising results led to the development of the next-generation prototype that does not require contact with the test structure as described in the next section.

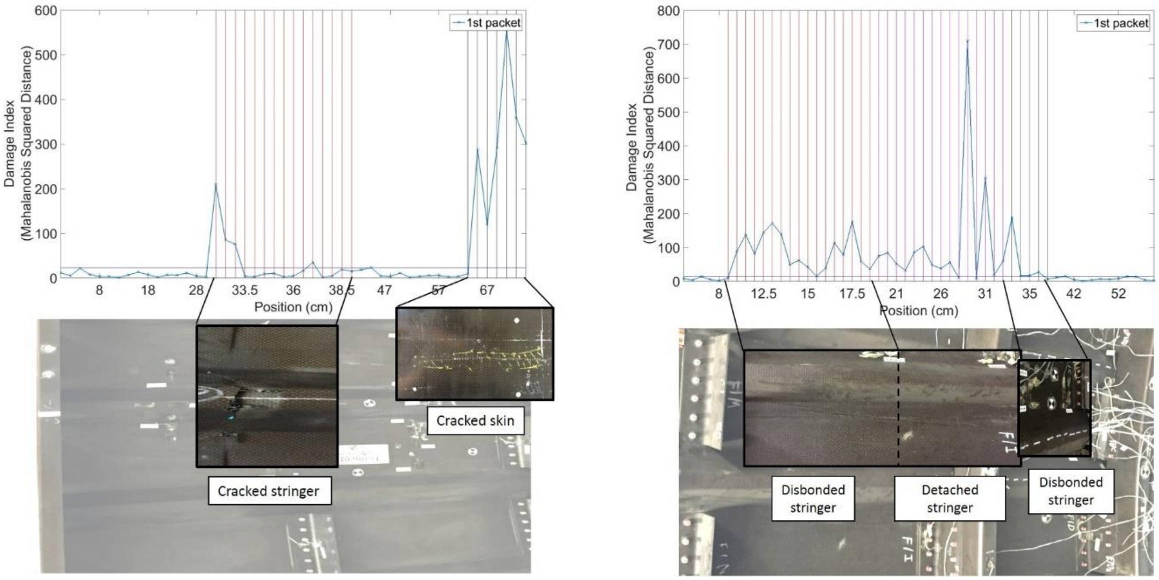

(a) (b)

Figure 53 - Representative results from contact UGW scans: (a) Panel 1, (b) Panel 2.

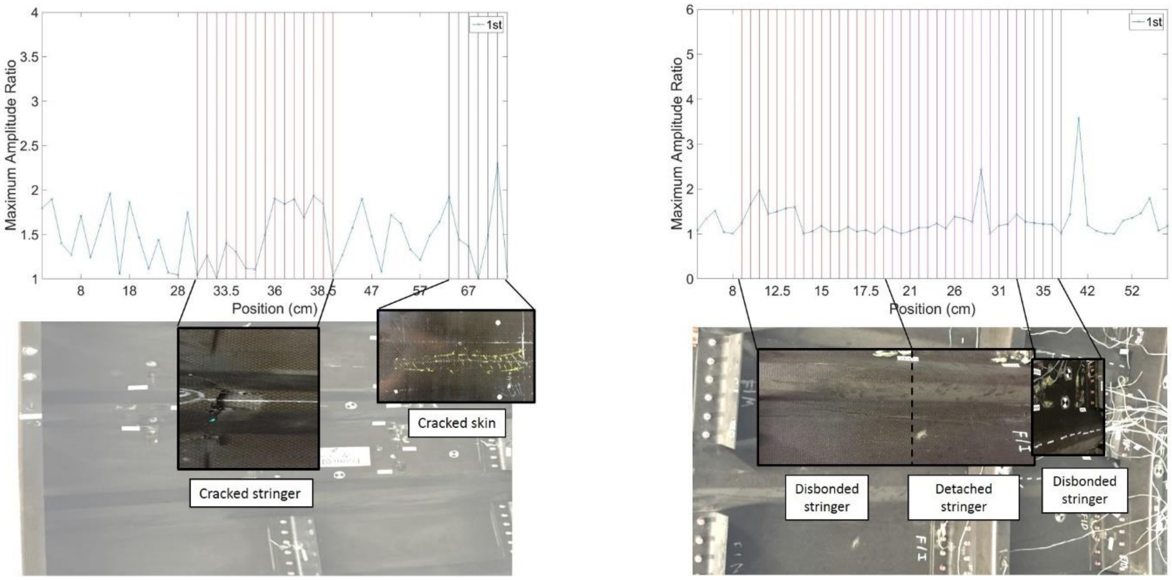

(a) (b)

Figure 54 - Amplitude Ratio from contact UGW scans: (a) Panel 1, (b) Panel 2

To ease the applicability of a rapid scanning technique for an actual field application, a non-contact version of the UGW system was designed, constructed and tested, which omits the need of couplant application per scan. Shown in Figure 55, the non-contact scanning prototype consists of a cylindrically focused air-coupled transmitter (Ultran NCG200-S50-C76-EP-X) (right-hand side in Figure 55) and an unfocused air-coupled receiver (Ultran NCG200-S19) operated in a pitch-catch mode. The transducers (both narrowband with a central frequency of 170 kHz) are mounted on a moving cart that allows the rapid and consistent scanning of the test structure. The stability of the non-contact coupling removes the need for the differential approach such that a simple pitch-catch test scheme is appropriate. The transducers are also oriented at angles that maximize the transduction of the dominant flexural mode in the panel's skin (Rose, 2004; Tuzzeo et al., 2007). Both transducers are piezocomposite devices that minimize the acoustic impedance mismatch with air for maximum ultrasonic signal transmission and reception. The excitation signal is a five-cycle toneburst with Hanning modulation centered at 170 kHz. The same NI PXI unit used in the contact setup was used for signal excitation and acquisition.

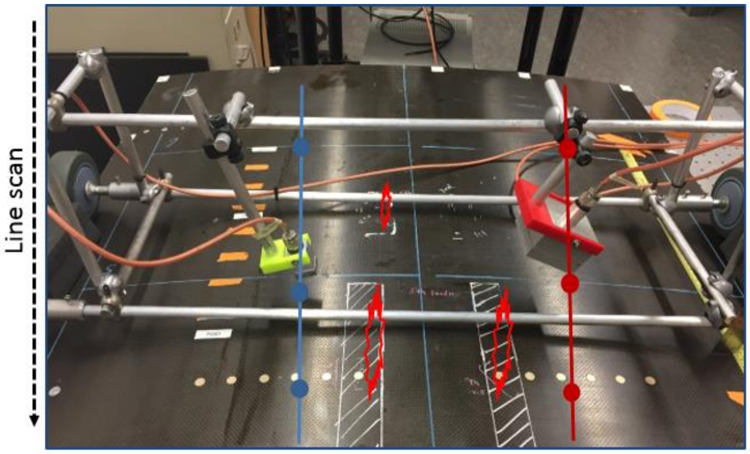

Figure 55 - Non-contact air-coupled scanning prototype experimental setup on Panel 3.

The previously-mentioned multi-mode wave propagation was exploited in the non-contact technique. A typical received RF waveform from Panel 3 is shown in Figure 56. It is possible to notice different arrivals. Measurements from contact PZT transducers mounted at specific locations of the panel, as well as group velocity information from the FE analysis, allowed to separate the dominant flexural mode traveling primarily in the panel skin from that leaking from the skin into the co-cured stringers.

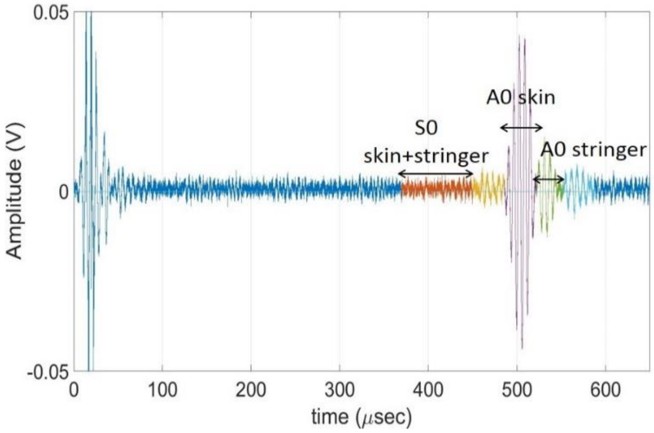

Figure 56 - Typical RF waveform measured by the air-coupled pitch-catch prototype from Panel 3.

The multivariate outlier analysis allows to select individual modes (from time gating) to build the feature vector. The features chosen are related to the signal strength and velocity, and are listed in Table 10, where x_p refers to the signal and p identifies each wave mode packet used.

Table 10 - Non-contact technique features list

Feature #	Feature Name	Feature Extraction
1	Maximum Value	$Max\|x_p\|$
2	Index of Maximum Value	$Ind(Max\|x_p\|)$
3	Variance	$Var(x_p)$
4	Kurtosis	$Kurt(x_p)$

The figure below presents the DI trace obtained from the line scan of test panel 3 and using (a) only skin modes, and (b) skin and stringer modes. It can be noticed how adding the stringer modes results into an enhanced defect detection sensitivity, especially for the stringer defects.

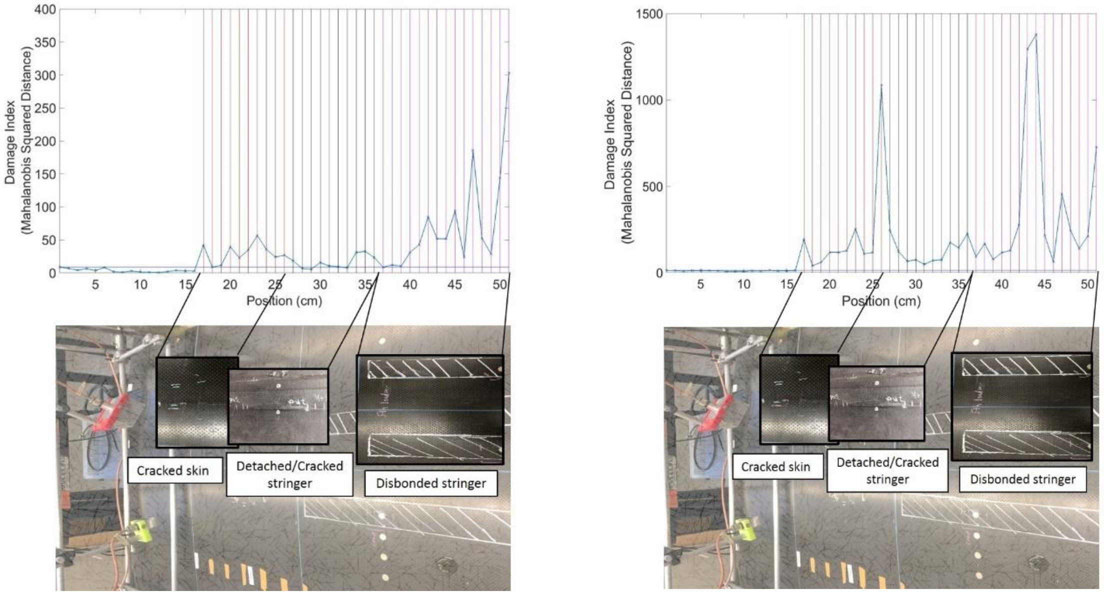

(a) **(b)**

Figure 57 - Representative results from noncontact (air-coupled) UGW scans of Panel 3: (a) skin modes only; (b) skin modes plus stringer modes

Again, the B-scan for the maximum amplitude value is reported in Figure 58, to show the benefit of the statistical analysis.

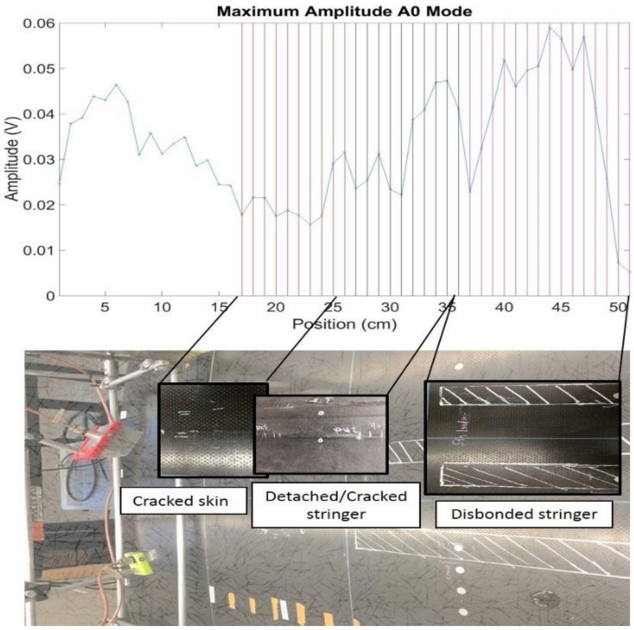

Figure 58 - Maximum Amplitude from non-contact UGW scans: Panel 3

In order to properly assess the performance of the tests, Receiver Operating Characteristic (ROC) curves were computed (Mariani S., PhD Thesis 2007). These plots compare the Probability of Detection (POD) to the Probability of False Alarm (PFA) for different threshold levels applied to the DI traces.

ROC curves were computed for each defect type at varying DI thresholds: a curve located in the upper left corner of the plot indicates a good defection performance (high POD and low PFA). The Area Under the Curve (AUC) is a metric that summarizes this goodness in performance. The dashed straight line represents the 50-50 guess.

Figure 59 shows the ROC curves for the contact NDE prototype on Test Panel 1 and Test Panel 2 for the disbonded stringer, the detached stringer and the cracked skin types of defects. Each symbol in the curves represents a threshold level applied to the DI traces from the line scans. These results indicate, for example, that the cracked skin defect can be detected with an 86% POD and 0% PFA or, alternatively, with a 100% POD and 26% PFA. Similarly, the disbonded stringer defect can be detected with a 94% POD and 0% PFA or, alternatively, with a 100% POD and 29% PFA. A somewhat worse performance was found for the detached stringer defect, where an 80% POD affords a 0% PFA (and a 100% POD results into a 47% PFA).

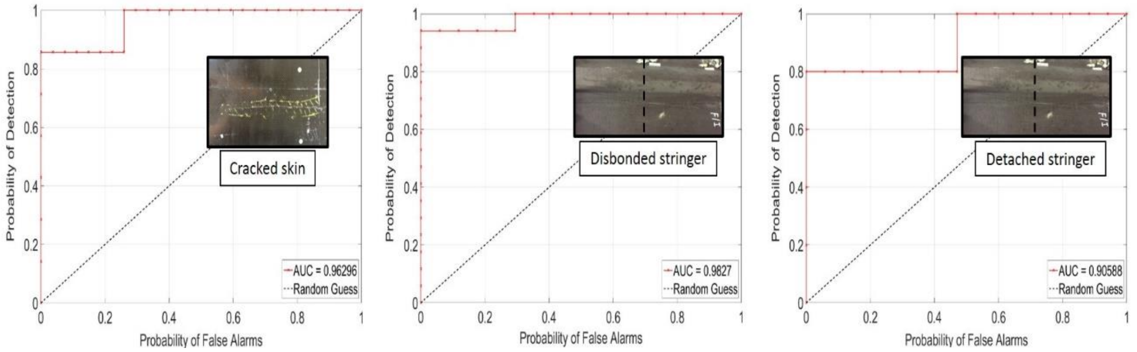

Figure 59 - ROC curves for the contact NDE technique: cracked skin, disbonded stringer and detached stringer defects (Panel 1 and Panel 2).

Figure 60 and Figure 61 show the ROC curves for the non-contact NDE technique applied to Test Panel 3. Figure 60 shows the results obtained using the skin modes only. The detection performance is excellent, especially considering the non-contact nature of the coupling. The best detection performance was found for the cracked skin and the disbonded stringer defect (e.g. 100% POD with less than 10% PFA), with somewhat worse performance for the detached/cracked stringer defect (e.g. 100% POD with 25% PFA, or 70% POD with 0% PFA).

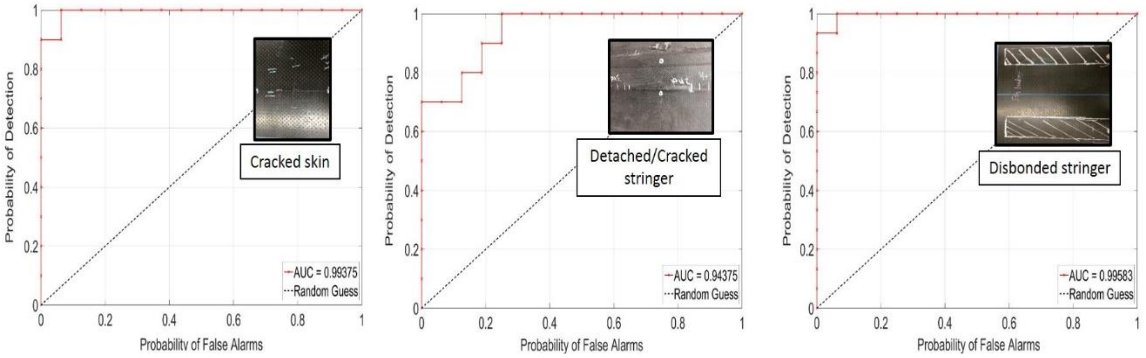

Figure 60 - ROC curves for the non-contact NDE technique (skin modes only): cracked skin, detached stringer and disbonded stringer defects (Panel 3).

In Figure 61, the stringer modes are added to the skin modes in the feature vector. This combination results in a perfect detection performance for all defects considered, i.e. a 100% POD with 0% PFA. The reason for this improvement is that the acoustic cross-talk between skin and stringer is such that modes primarily propagating into one of the two components are sensitive to defects in the other component, in addition to defects in the same component.

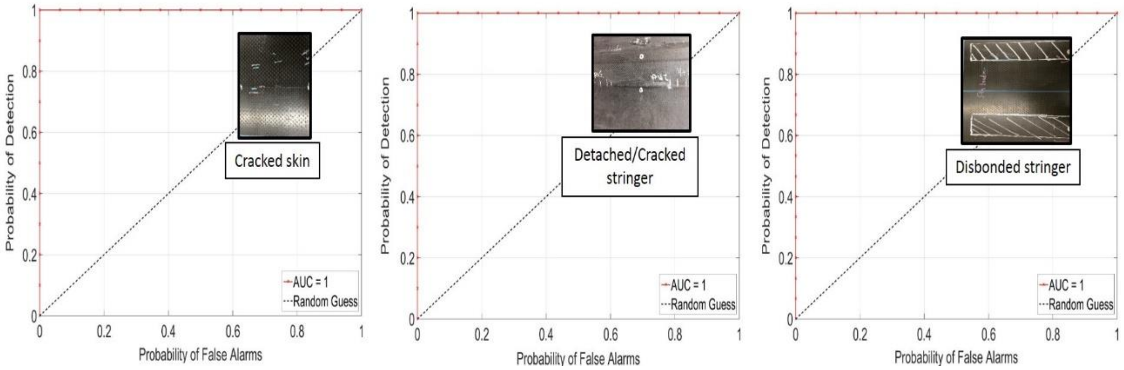

Figure 61 - ROC curves for the non-contact NDE technique (skin and stringer modes): cracked skin, detached stringer and disbonded stringer defects (Panel 3).

This section summarizes a rapid NDE technique for the detection of structural defects in composite aircraft structures subjected to Ground Service Equipment (GSE) impacts. The approach taken utilizes the waveguide geometry of the structure by means of ultrasonic guided waves. Two laboratory prototypes for line scanning have been developed, one using contact PZT transducers with a differential approach, and one using non-contact (air-coupled) transducers in a pitch-catch approach. The inspection utilizes a statistical outlier analysis that compensates each measurement for the normal (baseline) variation during a scan, thereby increasing the POD (true detections) and decreasing the PFA (false positive). Tests conducted on previously impacted test panels representative of commercial aircraft construction indicated an excellent detection performance (in terms of POD vs. PFA tradeoffs) for skin and stringer defects. A perfect detection for these defects was actually obtained by the non-contact system once both skin wave modes and stringer wave modes were combined in the statistical feature vector.

The prototypes discussed here are early-stage laboratory systems that do not include automatic data processing of the scan. Ongoing work is aimed at adding a tachometer to track the position of the inspection head, and implementing automatic signal processing to generate the scan output in quasi-real time.

The defects tested in this study were limited to the panel skin and stringers. Defects located in the deeper structure, specifically shear ties and C-frames, were not targeted because the frequencies used were found too high to penetrate these regions. Ongoing work is aimed at testing lower UGW frequencies in an effort to penetrate into the C-frames to provide comprehensive coverage of the structure.

2.4.3 Inspection of composite aerospace structures by extraction of UGW transfer function

To increase the level of damage/structural characterization, as explained in the introduction, and to reduce the equipment bulkiness, towards portability and automation for in situ inspection, the UGW NDE technique moved to a new design and more advanced approach.

The motivation to an improved scanning and signal processing can be well understood observing Figure 62, where three defected condition of the panel show very low SNR, when using a linear (less powerful) amplifier:

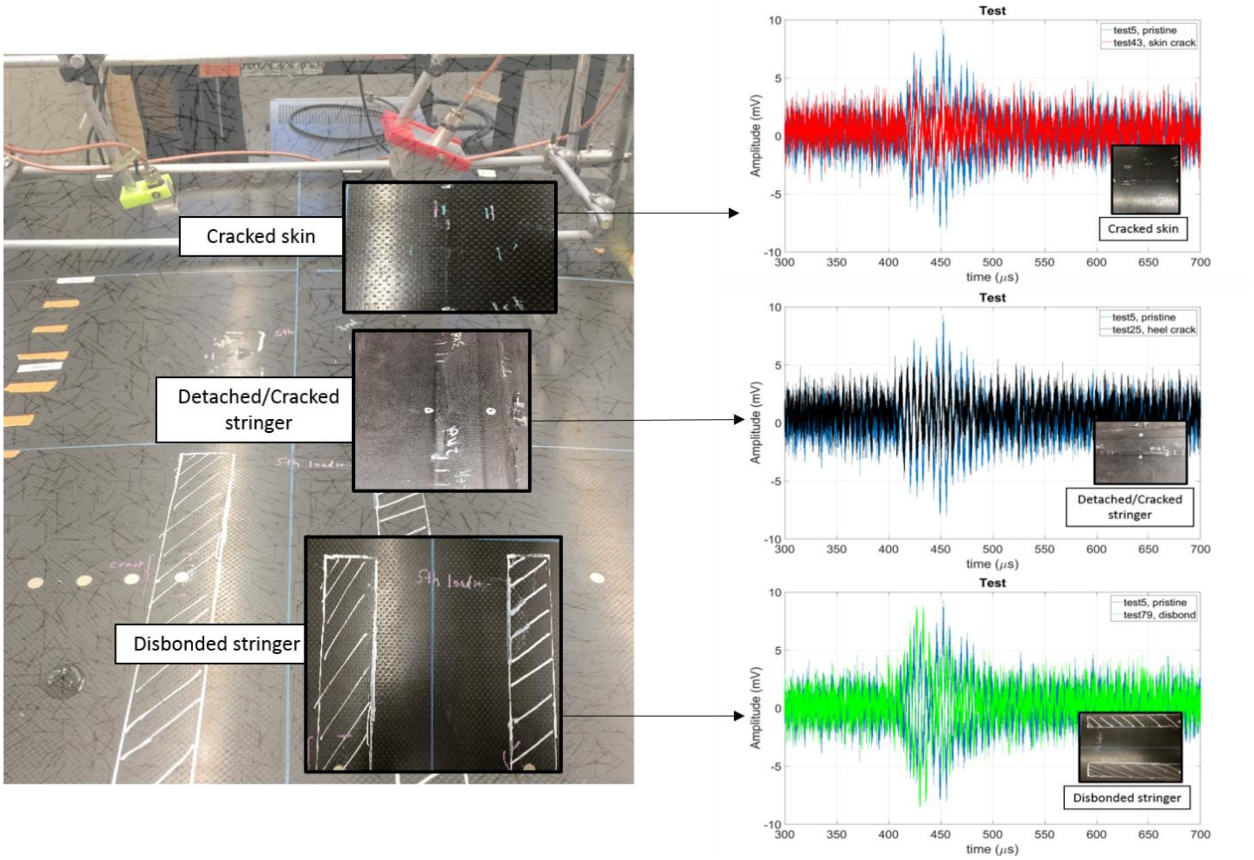

Figure 62 - Portable cart-scan set-up (left) with corresponding typical low SNR RF waveforms at specific defective locations (right): cracked skin (top, red), detached/cracked stringer (center, black), disbonded stringer (bottom, green), with respect to pristine location (blue).

It can be noticed how the quality of the signal degraded and the wavemodes are less clear. Also, the data obtained in Figure 62 are the result of an averaging processing where 100 averages per scan have been used.

To better investigate and isolate wave propagation in the stiffening structure skin-to-stringer and its interaction with different damage modes, a third set of composite panels was fabricated at UCSD under a NASA project.

The theory of the dual-output extraction of the transfer function is illustrated below. The problem at hand is schematized in the block diagram of Figure 63. The first goal is to isolate the transfer function of the waveguide structure between two points A and B, H_{AB}. The second goal is to associate any changes in the extracted H_{AB} to the presence of structural damage between A and B. The technique shown in Figure 63 uses one transmitter of ultrasonic guided waves (e.g. an air-coupled transmitter or an impactor in a scanning system) in combination with two receivers positioned at points A and B (e.g. a pair of air-coupled receivers) – hence a single-input-dual-output (SIDO) scheme.

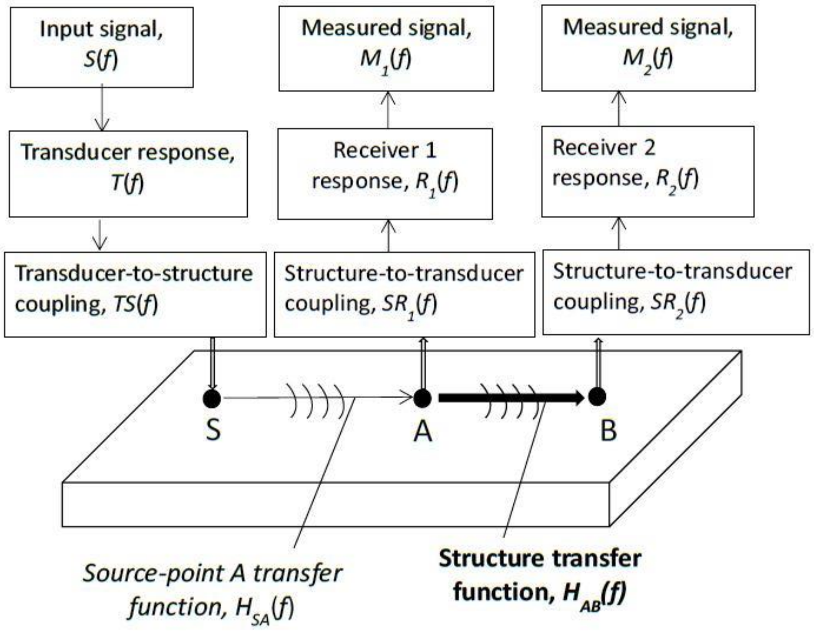

Figure 63 - Extraction of the structural transfer function between two points A and B by a single-input-dual-output (SIDO) scheme.

The formulation is more easily presented in the frequency domain. By using the convolution theorem and assuming linearity, the signal measured by receiver 1 can be written as:

$$M_1(f) = S(f) \cdot T(f) \cdot TS(f) \cdot H_{SA}(f) \cdot SR_1(f) \cdot R_1(f) \qquad (1)$$

In eq. (1), $S(f)$ is the input signal, $T(f)$ is the transmitting transducer frequency response, $TS(f)$ is the transducer-to-structure coupling frequency response, $H_{SA}(f)$ is the structure transfer function between source and point A, $SR_1(f)$ is the structure-to-receiver 1 coupling response, and $R_1(f)$ is the receiver 1 frequency response.

Similarly, the signal measured by receiver 2 can be written as:

$$M_2(f) = S(f) \cdot T(f) \cdot TS(f) \cdot H_{SA}(f) \cdot H_{AB}(f) \cdot SR_2(f) \cdot R_2(f) \tag{2}$$

where $H_{AB}(f)$ is the desired structure transfer function between A and B, $SR_2(f)$ is the structure-to-receiver 2 coupling response, and $R_2(f)$ is the receiver 2 frequency response.

The deconvolution operation between the two receivers leads to:

$$Deconv = \frac{M_2(f)}{M_1(f)} = H_{AB}(f) \cdot \frac{SR_2(f)}{SR_1(f)} \cdot \frac{R_2(f)}{R_1(f)} \tag{3}$$

If the two receivers are the same device (e.g. two air-coupled receivers), their frequency response and structure-to-transducer coupling can be reasonably assumed equal, hence: $R_1(f)= R_2(f)$ and $SR_1(f)= SR_2(f)$. In this case,

$$Deconv = \frac{M_2(f)}{M_1(f)} = H_{AB}(f) \tag{4}$$

The time-domain transfer function can be simply computed from the frequency domain by an inverse Fourier Transform operation:

$$H_{AB}(t) = \int_{-\infty}^{\infty} H_{AB}(f) \mathrm{e}^{i2\pi ft}\, df \tag{5}$$

Hence the deconvolution operation between the two receivers can isolate the desired structure transfer function without the influence of spurious factors, primarily the excitation signal that can be highly variable (e.g. an impactor) and could lead to false positive indications of damage.

If the response of the two receivers is different, the deconvolution operation of eq. (3) can still be an effective structural monitoring metric because it leads to a scaled version of the pure H_{AB} where the scale factor does not change during the scanning process. Hence any changes in this metric can be reasonably attributed to changes in the structure (e.g. damage) between A and B.

In an effort to validate the transfer function extraction by the above SIDO scheme, the paper presents comparable results obtained from a Semi-Analytical Finite Element (SAFE) method on a fiber-reinforced laminate corresponding to the skin portion of the aircraft skin-to-stringer assembly.

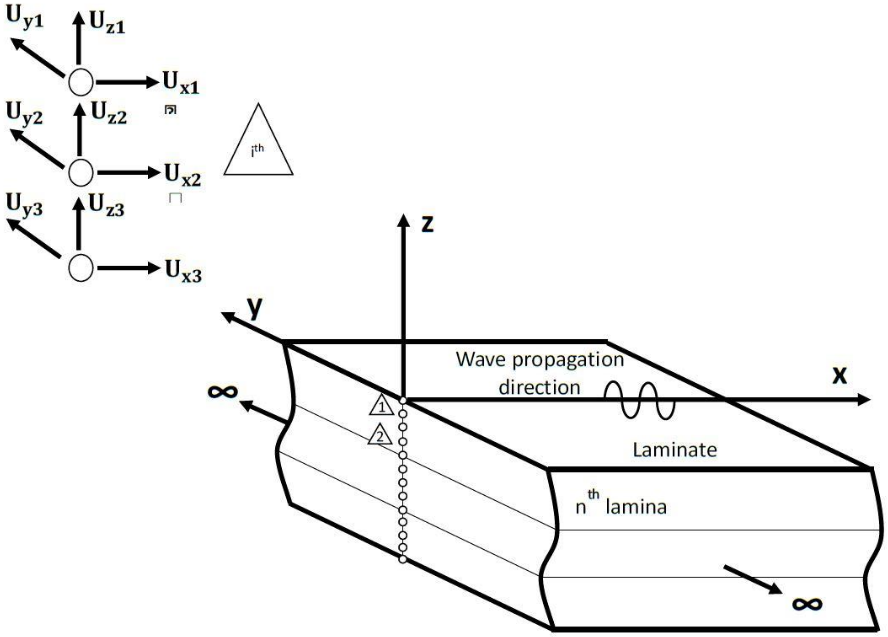

Figure 64 - Schematic of the SAFE method for modeling ultrasonic guided wave propagation in laminated composites.

The SAFE method (Hayashi et al., 2003; Bartoli et al., 2006; Marzani et al., 2008), schematized in Figure 64, can efficiently predict dispersive guided wave solutions by discretizing only the cross-section (*y*, *z*) of the laminate waveguide by finite elements, and imposing analytical (harmonic) wave propagation solutions along the wave propagation, *x*. The displacement field for each finite element is expressed as

$$u^{(e)}(x,y,z,t) = \begin{bmatrix} \sum_{j=1}^{n} N_j(y,z)U_{xj} \\ \sum_{j=1}^{n} N_j(y,z)U_{yj} \\ \sum_{j=1}^{n} N_j(y,z)U_{zj} \end{bmatrix}^{(e)} e^{i(kx-\omega t)} \qquad (6)$$

where $N_j(y,z)$ are finite element shape functions, *U* is the nodal displacement vector, *k* is the wavenumber, ω is the frequency, and *t* is time.

In the case of a multilayered composite laminate, the local lamina stiffness matrix **C** can be rotated onto the global (*x*, *y*, *z*) reference system of the laminate using the following transformation relation (Bartoli et al., 2006):

$$\mathbf{C}_\theta = \mathbf{R}_1 \mathbf{C}\ \mathbf{R}_2^{-1} \tag{7}$$

The global stiffness matrix $\mathbf{C}_\theta$ is then assembled to describe the entire laminate.

Using energy balance from Hamilton's principle, the SAFE formulation leads to the following eigenvalue problem for an M-degree of freedom system:

$$\left[\mathbf{A} - k\,\mathbf{B}\right]_{2M} \mathbf{Q} = 0 \tag{8}$$

where the matrices **A** and **B** contain mass and stiffness terms and the vector $\mathbf{Q} = [\mathbf{U} \quad k\mathbf{U}]^{\mathrm{T}}$ contains the nodal displacements (Hayashi et al., 2003).

The eigenproblem of eq. (7) can be solved by finding the eigenvalues k_{m} (*m*-th mode wavenumber) and the eigenvectors $\mathbf{U}_{\mathrm{m}}$ (*m*-th mode cross-sectional mode shapes) for each frequency ω. Considering propagative modes only, the phase velocity dispersion curves for the waveguide are then calculated as $c_{\mathrm{ph}}(\omega) = \omega / k$, and the group velocity as $c_{\mathrm{gr}}(\omega) = \partial \omega / \partial k$ following well known relations (Rose, 2014).

These eigensolutions represent the unforced vibrating modes of the waveguide. From these, a transfer function for the structure can be calculated by computing the "forced" solution of the waveguide, i.e. the waveguide's response at point x_{R} to a given forcing excitation at point x_{S}. The forced response can be calculated from SAFE in a normal mode expansion sense by summing the contributions of the unforced modes, each weighted by a "participation factor" that represents the degree of similarity between the excitation shape and the mode shape (Hayashi et al., 2003). Using the notation by (Marzani et al., 2008), the forced response in the frequency domain can be written as:

$$\overline{\mathbf{U}}(x_R) = -i \sum_{m=1}^{M} \frac{k^m}{D_m} \left(\mathbf{U}_L^m\right)^T \overline{\mathbf{F}}\ \mathbf{U}_R^m\, e^{ik_m(x_R - x_S)} \tag{9}$$

where $D_m = \left(\mathbf{Q}_L^m\right)^T \mathbf{B}\ \mathbf{Q}_R^m$, m is the individual mode, M is the total number of forward propagating modes, the subscripts L and R represent left and right eigenvectors, the superscript T is transpose, and the vector $\overline{\mathbf{F}}$ contains the applied nodal forces in frequency (Fourier coefficients). Eq. (9) is solved at each frequency value (Fourier series expansion). The forced response can be converted to the time domain by the following inverse Fourier Transform:

$$\mathbf{U}(x_R, t) = \int_{-\infty}^{\infty} \overline{\mathbf{U}}(x_R, f)\, \mathrm{e}^{\boldsymbol{i2\pi f t}}\, df \tag{10}$$

For purposes of comparison with the experimental transfer function, the SAFE predicted response is computed by considering a forcing function signal that best matches the frequency content of the experimental signals. For example, for a (narrowband) air-coupled transducer excitation, the model uses a Hanning modulated toneburst forcing function with a similar frequency bandwidth; for a (broadband) hammer impact excitation, the model uses an impulse-type forcing function.

This section presents a comparison between experimental and predicted transfer functions for guided waves propagating in a Carbon-Fiber-Reinforced Composite (CFRP) laminate representative of the skin of a B787 aircraft fuselage panel. The laminate was a 30 cm × 30 cm plate, composed of 16 plies, each with a thickness of 0.164 mm, with a quasi-isotropic and symmetric layup $[45/\text{-}45/0/45/90/\text{-}45/0/90]_s$. Material's constants from the manufacturer (unidirectional prepreg tape) are shown in Table 11.

Table 11- Layup and Lamina Elastic constants for the CFRP material.

Skin	[0/45/-45/90/45/-45/0]$_S$	2.624mm	Tape (0.164mm x ply)
Skin to Stringer	[0/45/-45/90/45/-45/0]$_S$ /90/[0/45/-45/90/45/-45/0]$_S$	5.412mm	Tape (0.164mm x ply)

E_{11} (GPa)	E_{22} (GPa)	G_{12} (GPa)	G_{23} (GPa)	ν_{12}	ν_{23}	ρ (kg/m^3)
160.08	8.97	6.21	3.45	0.28	0.36	1550

The guided-wave transfer functions for the laminate (Figure 65) were experimentally extracted using the dual-output scheme of Section 2 and numerically predicted using the SAFE model of Section 3.

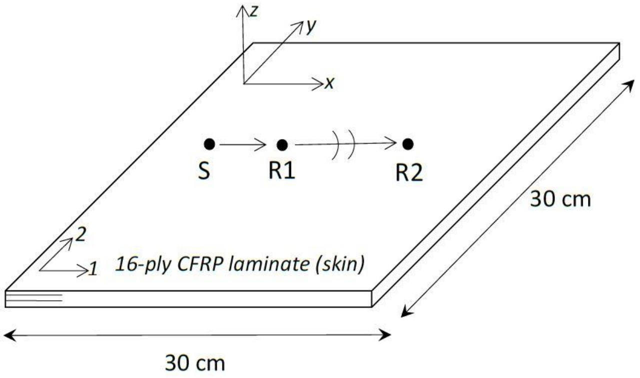

Figure 65 – Extraction of transfer function in composite laminate "skin".

The wave excitation and the two wave receptions were performed by piezoelectric transducers (PICO sensors, Mistras Corporation) attached to the plate by wax to ensure good acoustic coupling. The two receivers were positioned at a distance of 25.4 mm (1") from one another. The transmitting transducer was excited with a center frequency of 170 kHz.

The experimental transfer function was extracted by first time-gating the responses from the two receivers to eliminate wave reflections from the plate's boundaries (Figure 66(a) and (b)). After transforming to the frequency domain, the deconvolution operation between the receivers was performed according to eq. (4), followed by a band-pass filtering in the 50 kHz – 270 kHz range that contained the signal energy from the measurements - Figure 66(c). An inverse Fourier Transform lead to the time-domain experimental transfer function that is shown in Figure 66(d). The final trace in Figure 66(d) shows a clear wave packet arriving at around 20 □sec. This corresponds to a flexural guided wave mode for the composite laminate that would be produced by an excitation located at R_1 and detected by a receiver located at R_2 in Fig. 3, and is exactly the type of result that was expected by the dual-output deconvolution operation in this case. If a structural defect were to be present between R_1 and R_2, this trace would be affected due to wave scattering at the discontinuity.

The corresponding transfer function predicted by the SAFE model for this case is also shown in Figure 66(e) and overlapped to the experimental trace. Amplitudes are scaled to 1 since attenuation effects were not considered in the numerical analysis. The match is quite favorable, in terms of both arrival times and overall shape of the wave packet. This result confirms the applicability of the deconvolution operation between the two receivers to extract the structure's transfer function.

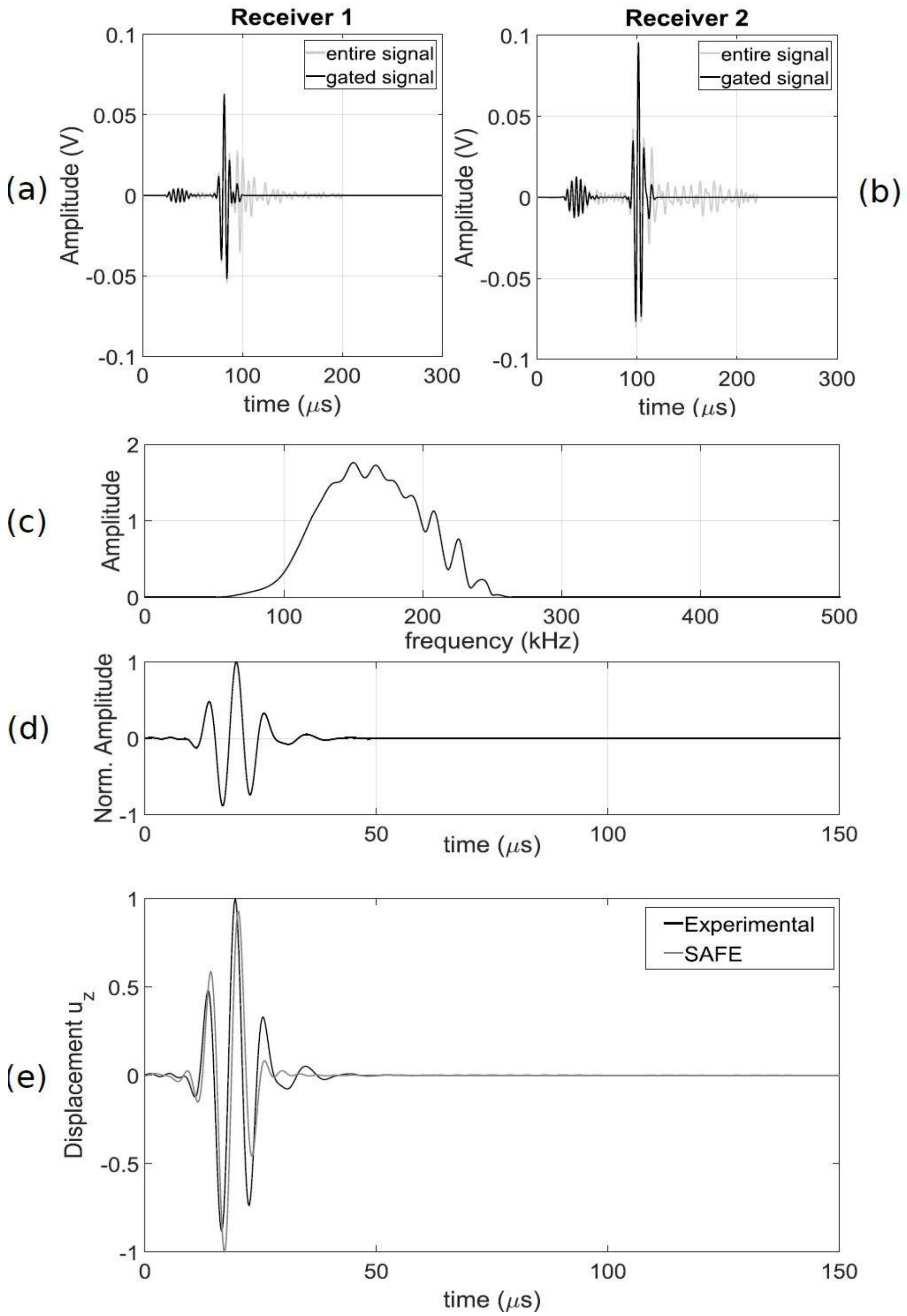

Figure 66 – CFRP laminate skin: (a) response measured by receiver 1; (b) response measured by receiver 2; (c) experimental transfer function in the frequency domain; (d) experimental transfer function in the time domain; (e) comparison between experimental and numerical (SAFE) transfer functions.

To calculate the predicted response, the SAFE model was run for the given laminate lay-up using the properties in Table 11 and rotating the stiffness matrix of each ply according to eq. (7). The wave propagation direction was along the fibers in the top ply of the laminate. The FE cross-sectional discretization used quadratic mono-dimensional elements with 2 elements per ply, 3 nodes per element and three degrees of freedom per node. The analysis started with the computation of the unforced guided-wave modes of the laminate as the solutions of the eigenproblem in eq. (8). Figure 67 shows the results of the unforced solutions from SAFE in terms of phase velocity dispersion curves –Figure 67(a), group velocity dispersion curves – Figure 67(b), and cross-sectional displacement mode shapes at 170 kHz for the three fundamental wave modes of axial (S_0) – Figure 67(c), flexural (A_0) – Figure 67(e), and shear horizontal (SH_0) – Figure 67(d). Some of the profiles show the typical “jumpy” behavior that is due to the different ply orientations. For the computation of the transfer function shown in Figure 66(e), eq. (10) was employed at the two receiver positions R_1 and R_2 using a forcing function at S consisting of an out-of-plane force (direction *z*) applied to the top node of the cross-section as a toneburst of 50 -270 kHz, consistently with the experimental bandwidth.

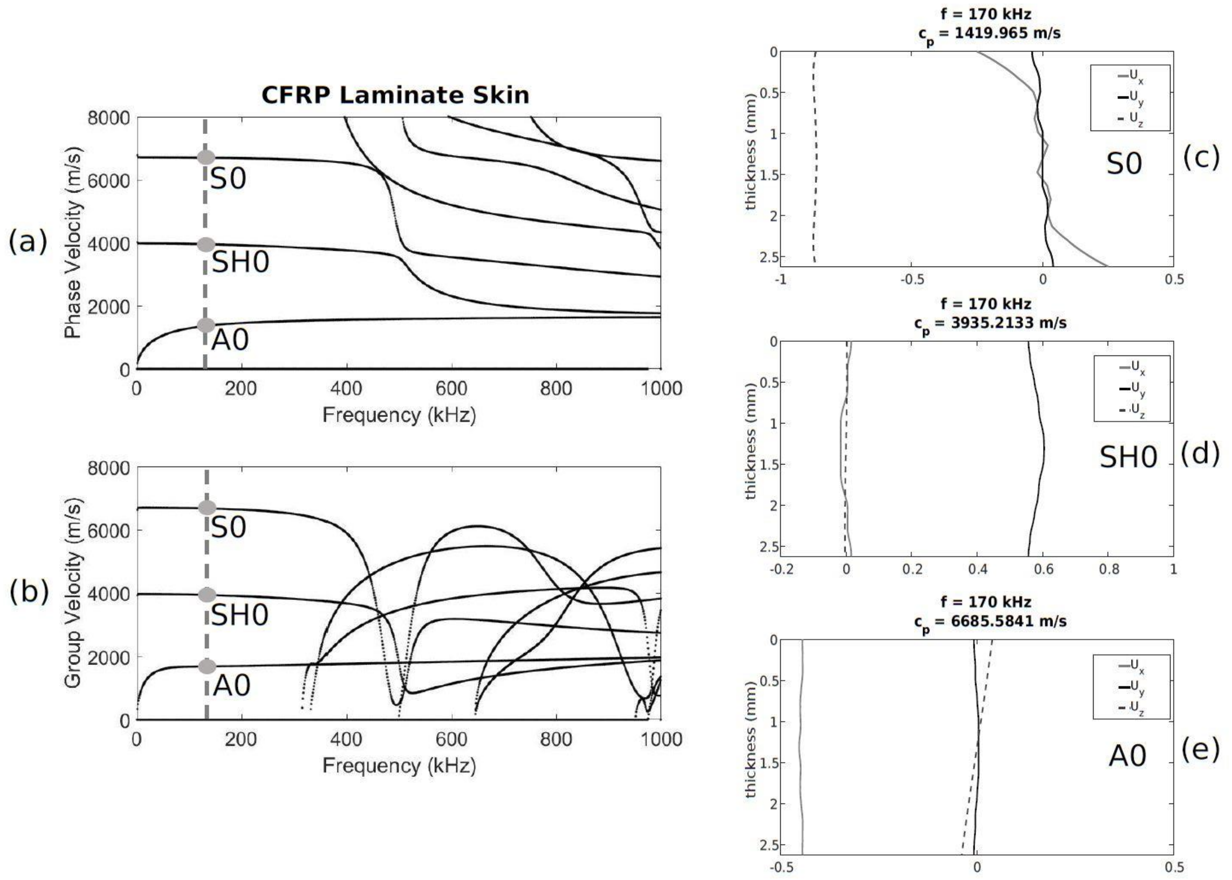

Figure 67 – SAFE solutions for the CFRP laminate skin for 0 deg wave propagation direction: (a) phase velocity dispersion curves; (b) group velocity dispersion curves; (c)-(e) cross-sectional displacement profiles for modes S_0, SH_0 and A_0 at 170 kHz.

Two test panels (herein referred to as "panel A" and "panel B") were used for the follow-up experimental work. Pictures of the test articles are shown in Figure 68 and Figure 69, respectively. The panels represented skin-to-stringer assemblies found in composite aircraft such as the B787 (Capriotti et al., 2017). The articles consisted of 1.35 m × 1.10 m (panel A) and 1.08 m × 1.10 m (panel B) parts made of a CFRP skin with five (panel A) and four (panel B) co-cured, hat shaped CFRP stringers. The skin material was the same as the laminate described in the previous Section 4. The stringers were co-cured on the skin along the skin surface's fiber direction and had the same lay-up as the skin, with an additional 90 deg ply at the co-cured interface.

The two panels contained a series of defects that were of interest to this study. Shown in Figure 68, panel A contained two slits (one on the stringer cap and the other one on the stringer heel), and an impact damage site on the stringer flange (at impact energy of ~80 J). Shown in Figure 69, panel B contained three impact damage sites on the stringer cap (at impact energies of ~30 J, ~50 J and ~70 J, respectively). The interest was to develop an expedite method to detect these defects that are representative of common impact-caused structural damage found in these structures. A requirement of the method was to access the panels on the skin side, since access to the interior aircraft structure is generally not allowed in a practical inspection at an airport depot.

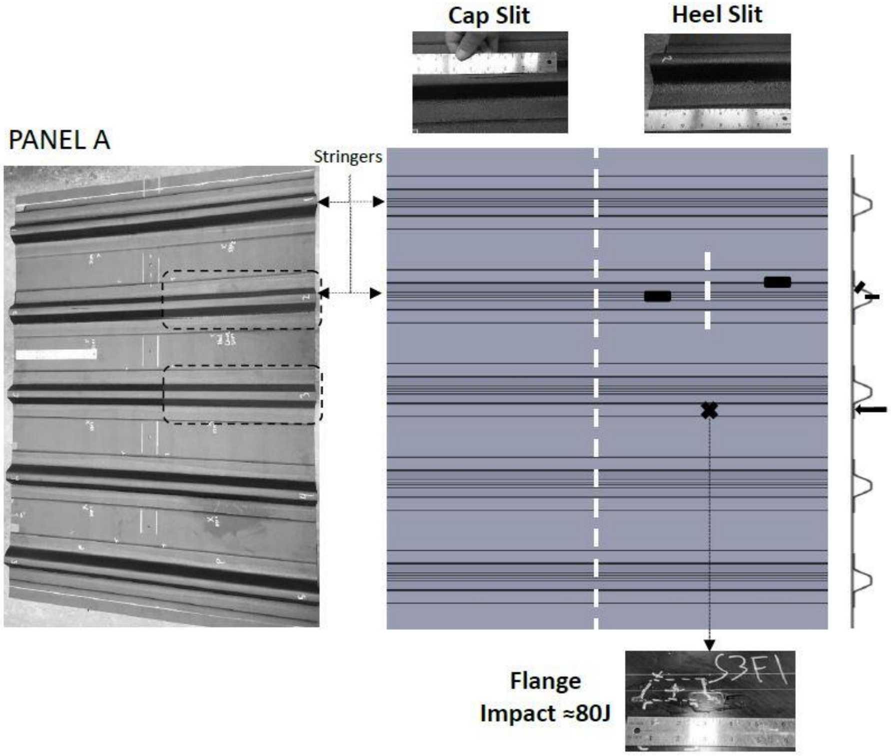

Figure 68 – The CFRP stiffened panel “A” with defects.

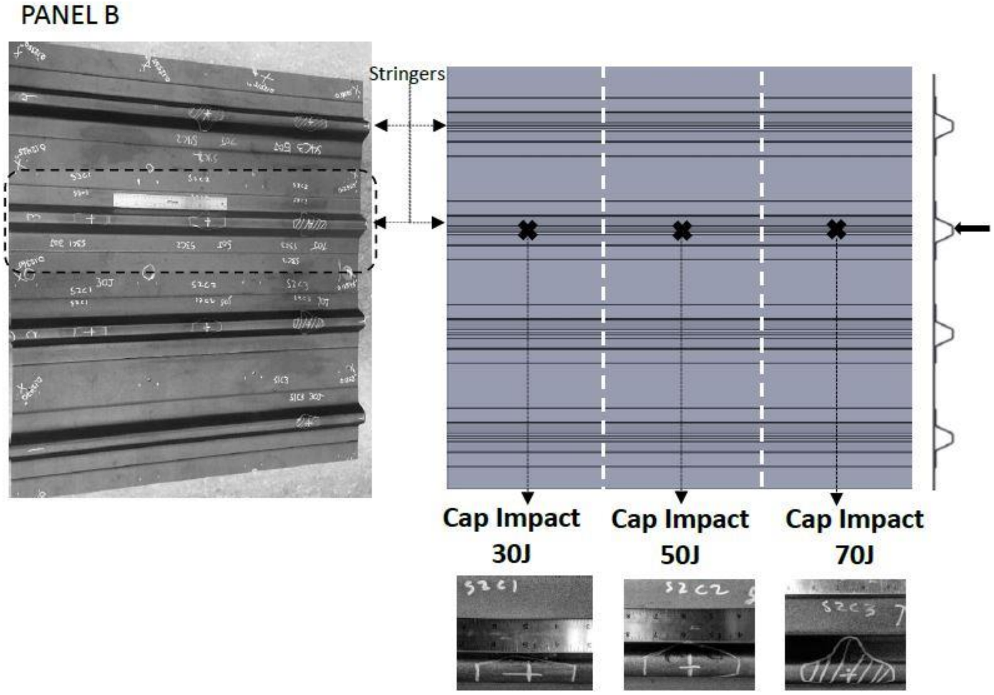

Figure 69 - The CFRP stiffened panel "B" with defects.

The experimental approach chosen for this task was to exploit the guided-wave transfer function across each stringer as the metric to detect the damage of interest. According to the SIDO scheme discussed above, this required two receivers placed on either side of the stringer, in combination with a wave transmitter. The deconvolution operation, filtered in the useful frequency band of the waves, yielded time-domain transfer functions characterizing the wave path between the two receivers.

Damage sensitive features were extracted from the transfer function traces and processed by an Outlier Analysis (OA) (Barnett and Lewis, 1994; Worden et al., 2000). The waveforms were gated according to expected time of arrival of the main flexural "skin" mode, but also including an earlier higher-order flexural mode due to the flanges, axial modes propagating into the skin and later flexural and/or converted modes propagating into the stringer. The gate window also avoided reflections from the outer boundaries of the panels and from adjacent stringers' flanges. A multivariate OA was used, where a

Damage Index was computed from the Mahalanobis Squared Distance (MSD) operation, where the transfer function at each scanned position along the panel was compared to the mean and the covariance of a set of transfer functions from known pristine areas of the panel (baseline). Root Mean Square (related to the signal magnitude or strength) and Skewness (related to the signal shape or phase distribution) were computed from the gated time-domain transfer functions and combined into the Feature Vector for the computation of the MSD discordancy metric (Damage Index). These features are among those previously used in ultrasonic guided-wave testing studies (e.g. Rizzo et al., 2007).

The tests were implemented in a line scanning mode to generate the Damage Index trace along the stringer (similarly to an ultrasonic B-scan display). A high Damage Index corresponded to points where the transfer function was a statistical outlier relative to the pristine region, hence indicative of a defect location.

Two scanning systems were designed for this purpose. The first system ("air-coupled system", Figure 70) was based on air-coupled ultrasonic excitation and detection and operated in a relatively high and narrow frequency bandwidth of 110 – 210 kHz. This frequency was expected to be sensitive to damage affecting primarily the skin and the skin-to-stringer interface, such as the stringer flange impact damage. The transmitter was a cylindrically-focused, 50 mm x 50 mm, piezocomposite air-coupled transducer (NCG200-S50-C76-EP-X from Ultran Corporation) with a center frequency 200 kHz. The two receivers were unfocused piezocomposite air-coupled transducers (NCG200-S19 also from Ultran Corporation) with a center frequency of 200 kHz.

The second system (hybrid "impact/air-coupled system", Figure 71) replaced the air-coupled excitation with a custom impactor to lower and broaden the frequency bandwidth to 40 – 275 kHz. The lower frequency was expected to better penetrate the stringers for detection of the stringer cap impact damage. The impactor was a specially built, ultralight CFRP laminated strip with an aluminum tip with a proven performance of a DC-350 kHz frequency range. Since the deconvolution operation is independent of the exact shape of the forcing function, there was no need to instrument the impactor with a piezoelectric sensor. The receivers in this hybrid system were broadband, micro-machined capacitive air-coupled transducers (BAT-1© from Microacoustics Corporation) with a frequency response of 20 kHz – 2 MHz.

In both scanning systems, the air-coupled transducers were oriented at an angle of ~ 13 deg from the normal to the surface in order to maximize the detection of flexural-type modes primarily excited in the panel, according to Snell's law of refraction. Both systems were mounted on a wheeled cart that also had a spring-loaded encoder to track the cart's position during a scan.

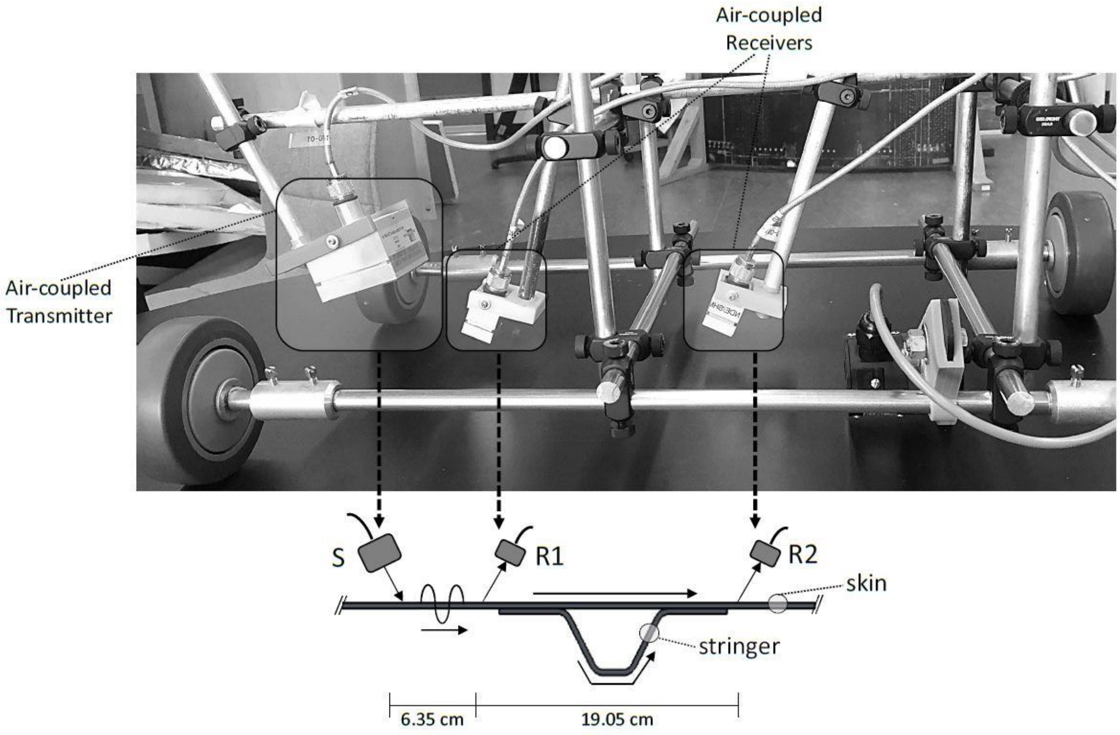

Figure 70 -The SIDO air-coupled scanning system for defect detection in the stiffened panels.

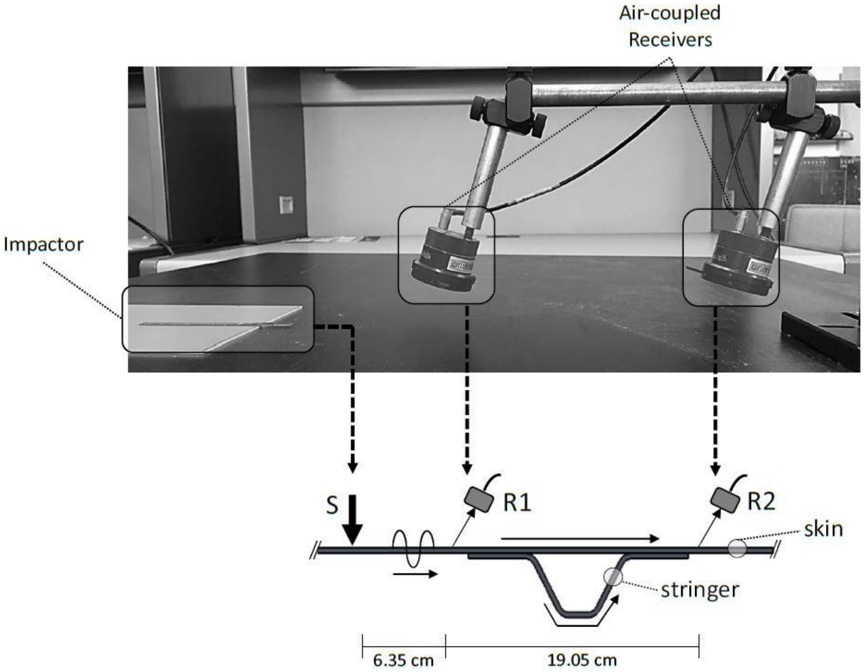

Figure 71 - The SIDO hybrid impact/air-coupled scanning system for defect detection in the stiffened panels.

Typical waveforms recorded in the air-coupled system by the two receivers under air-coupled excitation across the stringer of one of the test panels are shown in Figure 72(a) and (b). The signals are characterized by a main A_0 skin mode, according to the time of arrival and the nature of the test set up, followed by reflections from the edges of the panel and from the skin-to-stringer overlap. Notice the large attenuation affecting the signal at receiver 2 due to the significant wave leakage and scattering as it travels across the skin-to-stringer assembly. The transfer function extracted from these measurements, shown in Figure 72(c), has a much improved signal-to-noise ratio with clearer waveform features in terms of both magnitudes and arrival times. This transfer function is less dependent on transduction responses and highlights the coherent contributions between the two receivers. As such, the full transfer function allows to detect other modes arriving prior to and after the dominant skin flexural mode, caused by the complex wave path across the assembly.

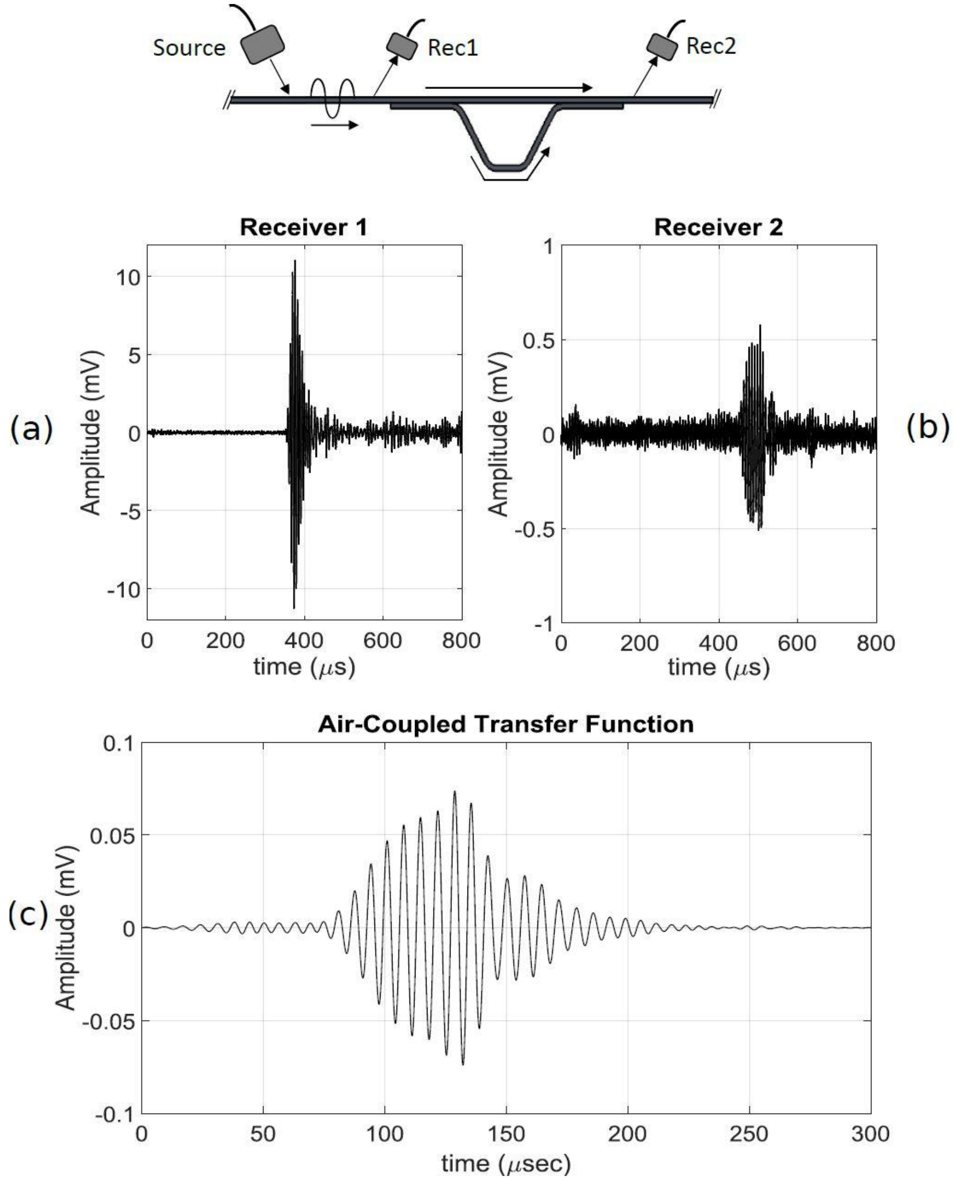

Figure 72 - Air-coupled system: (a), (b) raw waveforms received by the two receivers; (c) reconstructed transfer function.

Typical waveforms recorded in the hybrid impact/air-coupled system by the two receivers are shown in Figure 73(a) and (b). The broadband nature of these signals can be noticed. The reconstructed transfer function is shown in Figure 73(c). As discussed for the air-coupled system, the signal-to-noise ratio of the transfer function greatly improves relative to the raw air-coupled waveforms. The trace shows the main flexural mode along with additional modes arriving later due to the additional penetration of the wave energy into the stringer. The various modes can be identified more clearly than in the raw waveforms. Figure 73(d) and (e) shows the filtered versions of the transfer function in the bands of 1-115 kHz and 115-275 kHz, respectively. Again, wave arrivals and shapes are very clear in the transfer function results.

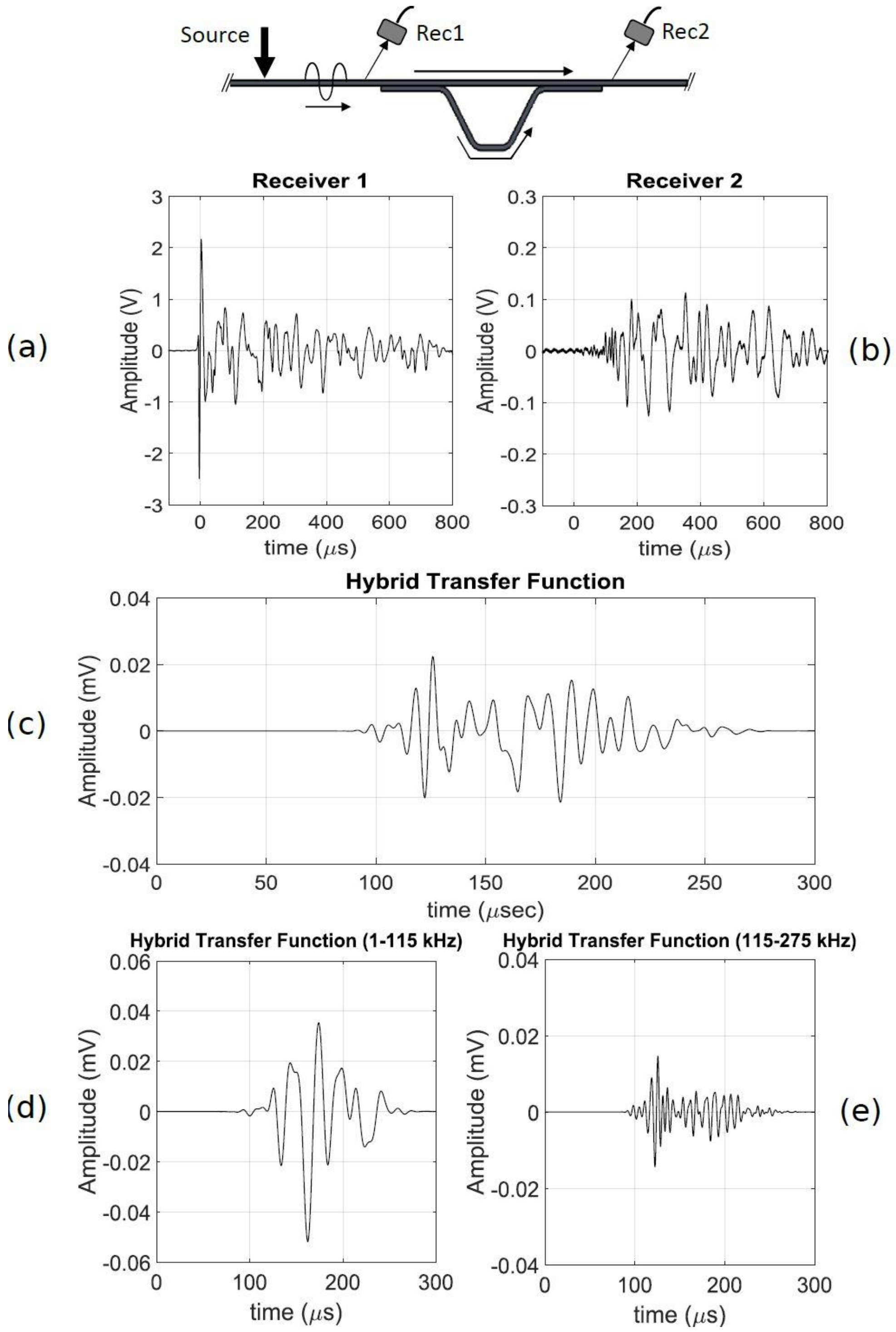

Figure 73 - Hybrid impact/air-coupled system: (a), (b) raw waveforms received by the two receivers; (c) reconstructed transfer function; (d) filtered transfer function (low frequency range); (e) filtered transfer function (high frequency range).

The next two figures show the effect of damage on the time-domain transfer function of the two systems. Figure 74 includes representative results from the stringer flange impact damage in panel A. The main effect of this type of damage is an attenuation and phase shift of the transfer function signatures. This is seen in both the air-coupled transfer function of Figure 74(a), and the hybrid transfer function of Figure 74(b). This result can be explained by the increased scattering experienced by the guided wave as it travels through the damaged portions of the skin-to-stinger overlap that was impacted. The fact that the attenuation is as evident in the air-coupled trace of Figure 74(a) as in the impact/air-coupled trace of Figure 74(b) suggests that this type of damage affects directly the skin, either by damage extending through the skin or by damage at the skin-to-stringer overlap region. The results for the high-frequency band and the low-frequency band of the hybrid system confirm this observation. The transfer function attenuation is more evident in the high-frequency range of Figure 74(d) compared to the low-frequency range of Figure 74(c), as the low frequency range has a higher propensity to penetrate from the skin into the stringer.

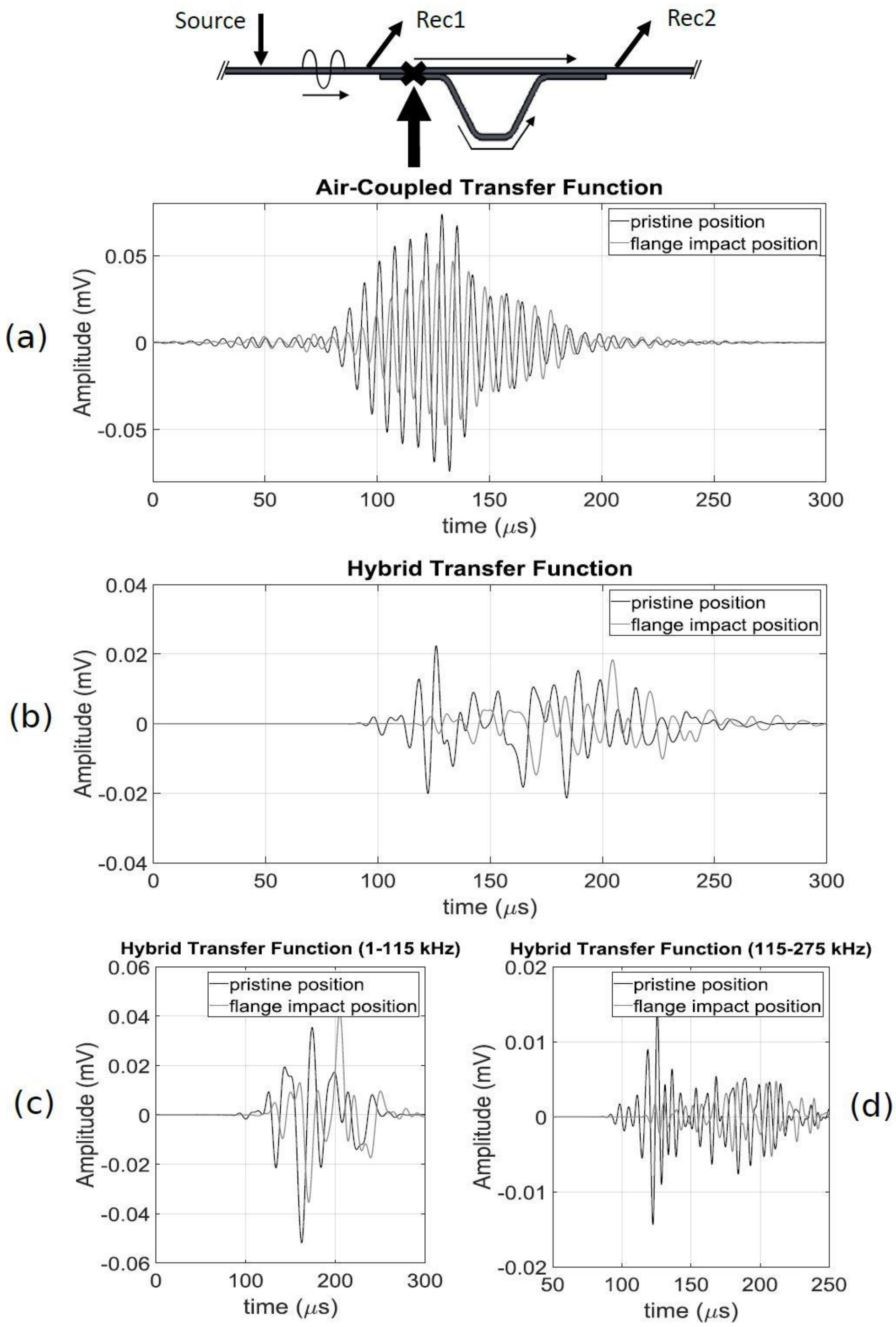

Figure 74 - Effect of the stringer flange impact damage on the time-domain transfer functions: (a) air-coupled system; (b) hybrid impact/air-coupled system (full bandwidth); (c) hybrid impact/air-coupled system (low frequency range); (d) hybrid impact/air-coupled system (high frequency range).

Figure 75 shows representative results from one of the stringer cap impact damages (50 J) in panel B. Differently from the flange impact case shown in the previous figure, the effect of this type of damage is an increase in magnitude of the reconstructed transfer function, seen both in the air-coupled system of Figure 75(a) and in the hybrid impact/air-coupled system in Figure 75(b). This observation can be explained by the fact that damage present in the stringer but not affecting the skin may cause a decrease in skin-to-stringer acoustic leakage. The decrease in leakage, in turn, results in additional channeling of the ultrasonic energy within the skin producing a stronger energy transmission. The transfer function increase is as marked in the low frequency range shown in Figure 75(c) as in the high frequency range shown in Figure 75(d).

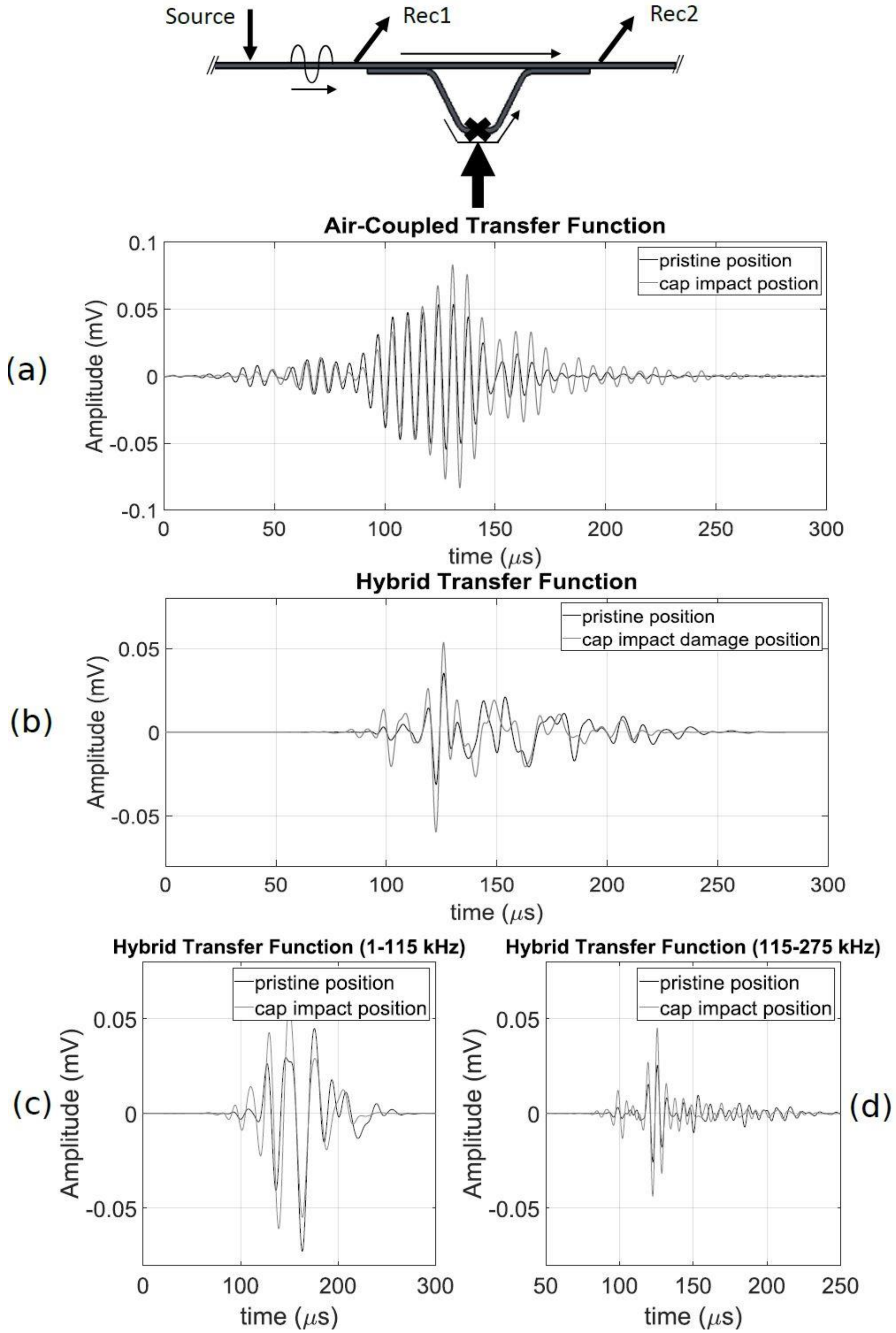

Figure 75 - Effect of the stringer cap impact damage on the time-domain transfer functions: (a) air-coupled system; (b) hybrid impact/air-coupled system (full bandwidth); (c) hybrid impact/air-coupled system (low frequency range); (d) hybrid impact/air-coupled system (high frequency range).

The transfer function results of the type shown in the previous section were time gated and processed through the Outlier Analysis as discussed in Section 5a for the generation of the Damage Index scans. The analysis tracked the two metrics of Root Mean Square (related to the magnitude or strength of the time-domain transfer function) and the Skewness (related to the shape of phase distribution of the time-domain transfer function) in a two-variable Feature Vector that was compared to the baseline distribution of feature vectors (pristine locations). The following three figures show the Damage Index traces obtained in one pass by the two scanning systems when moving over the defects discussed in Figure 68 and Figure 69 for the two test panels.

The result for the stringer (artificial) cap slit and the stringer (artificial) heel slit in panel A are shown in Figure 76. The air-coupled system, Figure 76(a), shows a good detection of the artificial slit in the stringer heel, that is sufficiently aligned with the actual location of this damage indicated by the horizontal thick line. The Damage Index is mostly activated at the center of the slit, with less sensitivity at the slit's edges. As for the second defect in the same trace, the artificial slit in the stringer cap, the air-coupled system shows very poor sensitivity due to the fact that the high frequency content utilized by this system is not able to sufficiently penetrate from the skin into the stringer for probing the stringer cap. The results from the hybrid impact/air-coupled system for the same two defects are shown in Figure 76(b) (full bandwidth of 1-275 kHz) and Figure 76(c) where the low frequency range (1-115 kHz) is shown separated from the high-frequency range (115-275 kHz). It is evident that the hybrid system provides an excellent detection of both the stringer heel slit and the stringer cap slit, owing to the lower frequency range coupled with the increased energy from the impact that enables the wave penetration into the stringer. Interestingly, the high-frequency range in Figure 76(c) shows particular sensitivity to the heel slit edges probably due to the particular wave scattering at these locations. Overall, the detection of both defects by the hybrid system shows a reasonable match with the known defect extensions (horizontal thick lines).

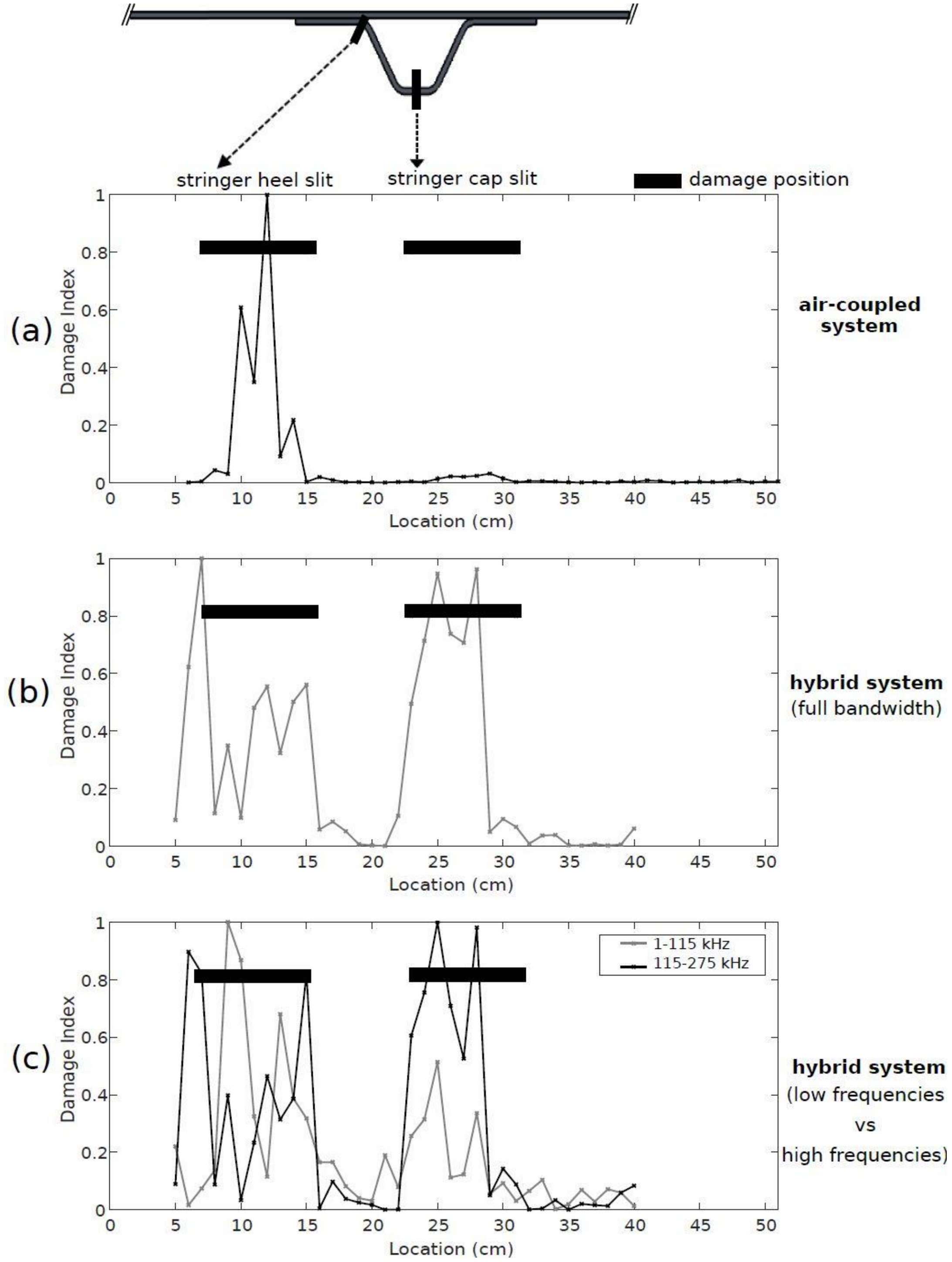

Figure 76 - Damage Index traces from one scan through the stringer heel slit and the stringer cap slit in panel A: (a) result from the air-coupled system; (b) result from the hybrid impact/air-coupled system (full bandwidth); (c) result from the hybrid impact/air-coupled system (low frequencies vs. high frequencies).

The scan results over the flange impact defect of panel A are shown in Figure 77. Figure 77(a) shows a very good detection of the impacted flange by the air-coupled system, with maximum sensitivity at the center of the suspected damage (as reported by an ultrasonic A-scan). Hence it is confirmed that the high-frequency range of the air-coupled system is sufficiently sensitive to the overlap between the skin and the stringer that is likely affected by the flange impact. Very good detection of this damage is also shown by the hybrid system in Figure 77(b) (full bandwidth) and Figure 77(c) where the low frequency range and the high frequency range are separated. In particular, the high frequency range seems to be mostly sensitive to the center of the damage, whereas the low frequency range is also activated by the wave absorption in the wider delaminated area around the impact location.

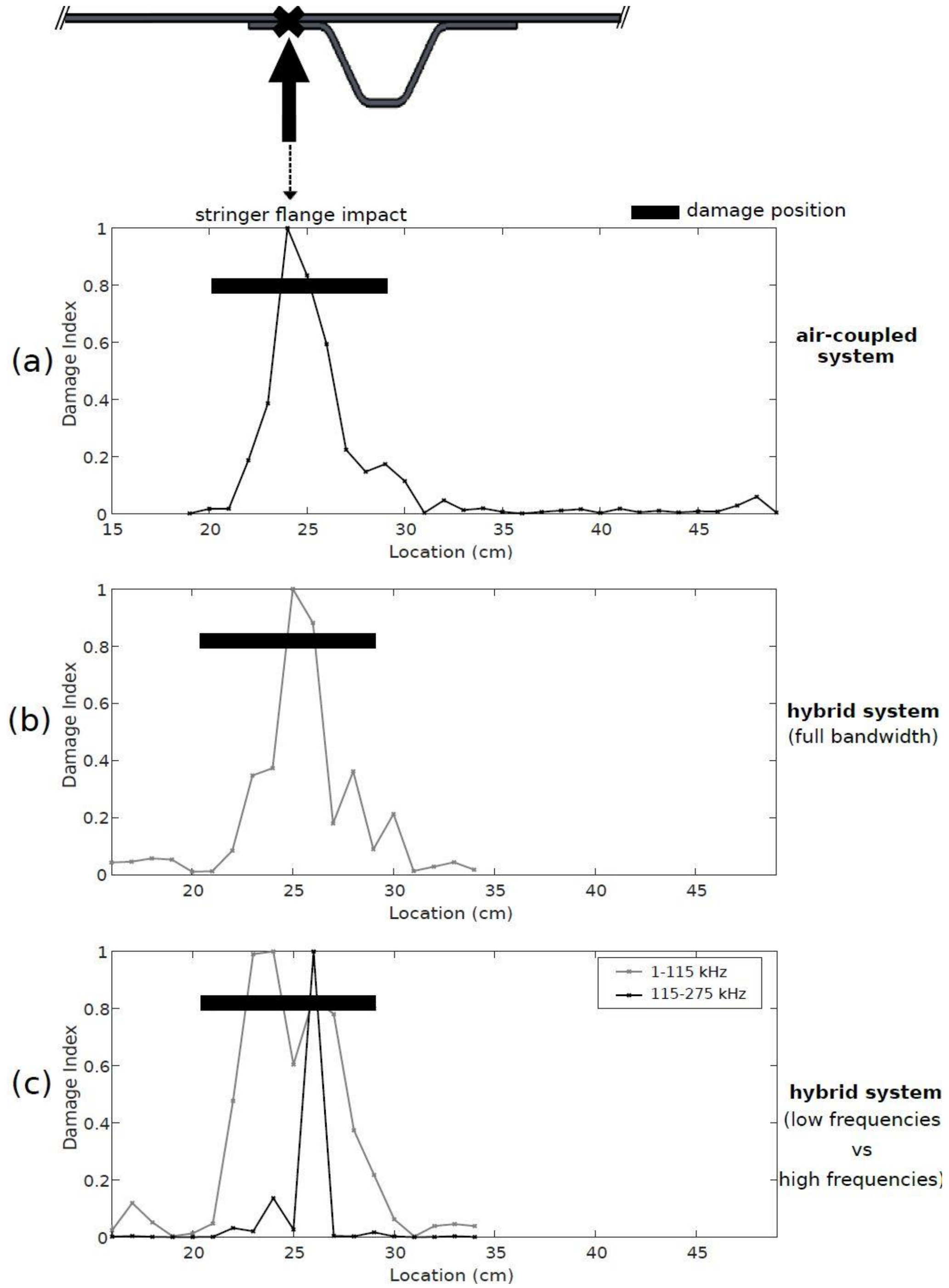

Figure 77 - Damage Index traces from one scan through the stringer flange impact in panel A: (a) result from the air-coupled system; (b) result from the hybrid impact/air-coupled system (full bandwidth); (c) result from the hybrid impact/air-coupled system (low frequencies vs. high frequencies).

The results from the stringer cap impacts at 70 J, 50 J, and 30 J energy levels in panel B are shown in Figure 78. The Damage Index trace for the air-coupled system, Figure 78(a), shows a very poor signal-to-noise ratio, indicating that this system did not perform well for these defects, as expected due to the inability of high frequency waves to penetrate deep into the stringer. Although individual points of elevated Damage Index values can be seen in this trace at the center of the impacts, it is very difficult to make any conclusions on the extension of damage from the noisy traces of Figure 78(a).

A much better result is obtained by the hybrid system in Figure 78(b) and (c). This was expected due to the lower frequency range and increased energy enabling the wave penetration into the stringer. The trace in Figure 78(b) shows very good indication of the damage extension, reasonably matching the suspected extension as determined by ultrasonic A-scans of the impacted areas (thick horizontal lines). For the 70 J and 30 J impact damage, the behavior of the low frequency band and the high frequency band, Figure 78(c), is quite comparable. For the 50 J damage, the high-frequency signal tends to be mostly sensitive to the central locations of the damaged area, with the low-frequency signal affected by a wider area. This is the results of the complex scattering caused by the specific damage shape and morphology generated by this particular impact.

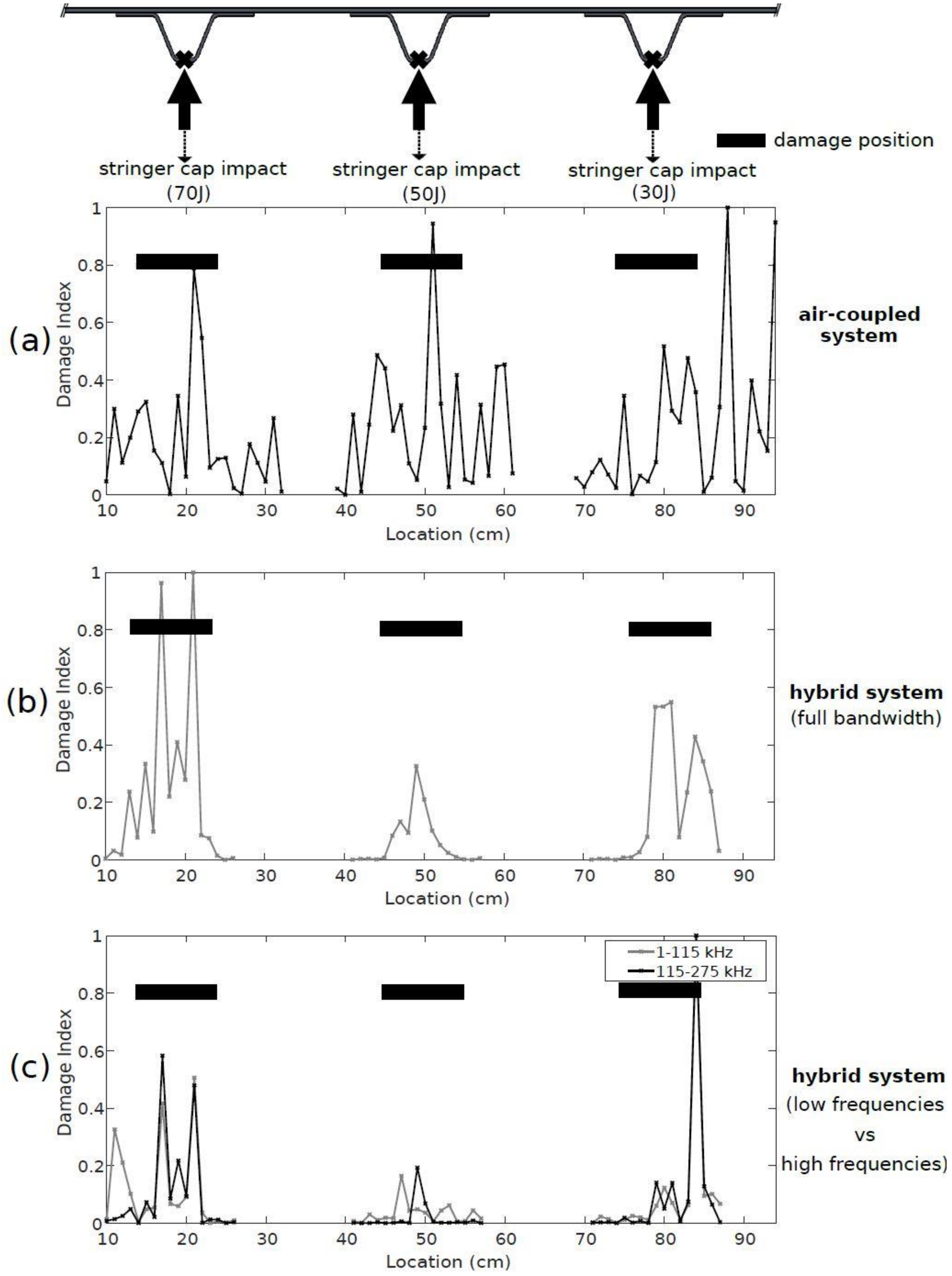

Figure 78 - Damage Index traces from scans through the stringer cap impacts (30 J, 50 J and 70 J) in panel B: (a) result from the air-coupled system; (b) result from the hybrid impact/air-coupled system (full bandwidth); (c) result from the hybrid impact/air-coupled system (low frequencies vs. high frequencies).

Concluding, a transfer function approach for ultrasonic guided-wave testing is presented for damage detection purposes. The method is based on a single-input-dual-output (SIDO) scheme that minimizes the effects of the transducers' response and the transducers-to-structure coupling effects compared to a traditional single-input-single-output (SISO) guided-wave testing. For example, the SIDO method enables the use of excitation sources with unknown spectra (e.g. non-instrumented impactors). By utilizing a deconvolution operation, the SIDO approach additionally brings out the coherent wave paths between the two receivers and minimizes the incoherent contributions. These performances are particularly relevant to scanning systems where the acoustic transduction can be variable.

This method, combined with a statistical Outlier Analysis, was utilized to design two scanning systems applied to the rapid inspection of representative composite aircraft panels subjected to various types of impact-caused damage. The two systems explore, respectively, the narrow/high frequency range (~110-210 kHz) offered by non-contact air-coupled piezocomposite transducers and the broad/low frequency range (~ 40-270 kHz) offered by the combination of an ultralight impactor and air-coupled capacitive transducers. The results show how stringer flange impacts affect the skin and the skin-to-stringer interface, generally producing a decrease in wave transmission strength that is detectable by the high frequency wave content excited by both the air-coupled system and the hybrid system. Stringer cap impacts, instead, generally produce an increase in wave transmission strength (through decreased acoustic leakage) that mostly affects the low frequency and high magnitude wave content that are excited by the hybrid system.

ACKNOWLEDGEMENTS

Chapter 2, Section 2.3, in full, has been submitted for publication of the material as it may appear in International Journal of Solids and Structures 2019. Spada, Antonino; Capriotti, Margherita; Lanza di Scalea, Francesco. The dissertation author was the second investigator and author of this paper.

Chapter 2, Section 2.3.3, in full, is currently being prepared for submission for publication of the material. Spada, Antonino; Capriotti, Margherita; Lanza di Scalea, Francesco. The dissertation author was the second investigator and author of this material.

Chapter 2, Section 2.4.1, in part, is coauthored with Kim, Hyungsuk E. The dissertation author was the primary author of this chapter.

Chapter 2, Section 2.4.2, in full, is a reprint of the material as it appears in Materials Journals 2017. Capriotti, Margherita; Kim, Hyungsuk E.; Lanza di Scalea, Francesco; Kim, Hyonny. The dissertation author was the primary investigator and author of this paper.

Chapter 2, Section 2.4.3, in full, has been submitted for publication of the material as it may appear in Journal of Intelligent Material Systems and Structures 2019. Capriotti, Margherita; Lanza di Scalea, Francesco. The dissertation author was the primary investigator and author of this paper.

Chapter 3

Techniques of Thermal Wave Propagation

3.1 Background of Infrared Thermography: principles

Infrared Thermography is one of the most common NDE techniques for the inspection of the subsurface of structures in several applications. The possibility to cover a wide area and to simply interpret and visualize the results makes it very powerful and easy to apply. Moreover, the technique is non-contact and allows in-situ inspection, avoiding the need to disassemble the structure for dedicated testing. It is usually operated in an active manner, where an external heat source (usually consisting in powerful light sources, emitted in a very short time period) “excites” the thermal field in the specimen and temperature differences can be appreciated, both spatially and temporally. Both theory and applications will be shown. The drawback of the need of an external heat source could be overcome with passive thermography, avoiding additional costs and set-up effort, preserving the thermal status of the specimens and offering additional resolution and imaging enhancement. Moreover, the nature of the technique itself supports this alternative approach, since the output of a common thermographic test (thermal image) constitutes a huge temperature database of the specimen. This latter approach will be illustrated theoretically.

IR thermography evolved from photothermal radiometry (PTR), where an IR detector monitors the surface temperature variation in the sample, measured as a change in the infrared emission according to Stefan-Boltzmann’s law:

$$W = \int \varepsilon W_{\lambda} d\lambda = \varepsilon \sigma T^{4}$$

3.1-1

The law establishes the important dependence of total flux W radiated into a hemisphere from a body at temperature T. σ is the Stefan-Boltzmann constant and ε is the emissivity, which is integrated over all wavelengths λ to eliminate the dependence and is fixed for different materials. The emissivity is the ratio of the capacity of a body to emit/absorb energy in the form of radiation with respect to the one of a black body ($\varepsilon = 1$).

The spectral radiant emittance, (W_{λ} flux radiated into a hemisphere per wavelength interval $d\lambda$) is determined by Planck's law:

$$W_{\lambda} = \frac{c_1}{\lambda^5} \frac{1}{e^{\left(\frac{c_2}{\lambda T}\right)} - 1}$$

3.1-2

where c_1 and c_2 are constants. Hence, the amount of radiation emitted depends on temperature and wavelength, as Figure 79 shows:

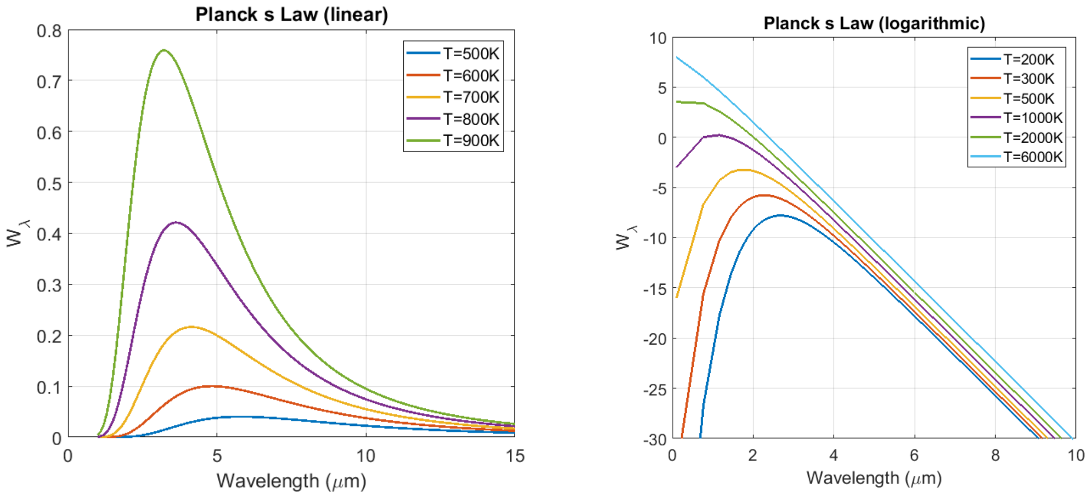

Figure 79 - Planck's Law (left: linear scale; right: logarithmic scale): spectral radiant emission versus wavelength

Also, at each temperature, the emission peaks at certain wavelengths λ_m, as described by Wien's law:

$$\lambda_m T = a = 2897.8\ \mu m\ K$$

At room temperature, the emission peaks at around 10 μm . It is important to choose the correct infrared detector that is most sensitive to the wavelength corresponding to the maximum emittance for the studied temperature range.

3.2 Theoretical Investigation

3.2.1 Theory of TW and Green's function method

The output of IR thermography is a 2D temperature field, resulting from the energy exchanges inside a body governed by heat conduction and its interaction with the structural and thermal properties.

Given a body in a cartesian reference system *(x, y, z)*, we can write the energy balance as:

$$-\nabla \boldsymbol{q} + n(\boldsymbol{r}, t) = \rho c \frac{\partial T}{\partial t}$$

3.1-3

where n (W/m^3) is the rate of energy generation, q (W/m^2) is the heat flux, ρ is the density and c is the specific heat. The right-hand side term contains the heat flowing into/out of the body and the internal heat sources, while the right-hand side term expresses the rate of storage of energy or the change in specific internal energy. Introducing Fourier's Law,

$$\boldsymbol{q} = -k\ \nabla T$$

3.1-4

Eq. (**3.1-3**) can be rearranged in terms of temperature as:

$$\boldsymbol{\nabla^2 T} + \frac{1}{k}\ n = \frac{1}{\alpha}\ \frac{\partial T}{\partial t}$$

3.1-5

Where the material dependence of the temperature distribution is expressed by the diffusivity $\alpha = \frac{k}{\rho c} = [\frac{m^2}{s}]$. Eq. (**3.1-5**) is the governing heat diffusion equation.

The same result can be achieved starting from a more generalized heat wave equation:

$$\boldsymbol{\nabla}^2\boldsymbol{T} + \frac{1}{k}\bar{n}(\boldsymbol{r},t) = \frac{1}{\alpha}\frac{\partial \boldsymbol{T}}{\partial t} + \frac{1}{s^2}\frac{\partial^2 \boldsymbol{T}}{\partial t^2}$$

3.1-6

where $\bar{n}(r,t) = n(r,t) + \frac{\alpha}{s^2}\frac{\partial n(r,t)}{\partial t}$ and s is the thermal wave speed. For speeds that are very high (in metals s=10^5 m/s) and thermal time constants $\tau_c = \frac{R^2}{\alpha}$ very small (in metals, τ_c =10^{-14} s), but larger than the material's relaxation time τ (Ozisik et al., 1994; Marin, 2010), the above equation can be simplified to a Fourier type heat conduction, expressed by eq.(3.1-5). To be noticed, the neglection of the propagating term in eq. (3.1-6) makes heat propagation a parabolic diffusion equation. Although the scientific community is divided on this controversial definition, we will refer to this kind of propagation as thermal wave (TW).

The solution to eq. (**3.1-5**) can be found in terms of Green's function. This method is very useful when dealing with analogies with propagating fields and when defects or inhomogeneities can be viewed as secondary sources (Cole et al., 2010). The formal definition of Green's function has itself very powerful consequences in manipulating wave fields and interpreting them. The Green's function is the solution to an auxiliary equation:

$$\nabla^2\boldsymbol{g} + \frac{1}{\alpha}\delta(\boldsymbol{r} - \boldsymbol{r}_0)\delta(t-\tau) = \frac{1}{\alpha}\frac{\partial \boldsymbol{g}}{\partial t}$$

3.1-7

for an excitation of the delta Dirac type in time and space and homogenous initial and boundary conditions. It is the transfer function of the path between the source and any space coordinate and it is here reported in 1-D as:

$$g(x,t \mid \xi,\tau) = \frac{1}{\sqrt{4\pi\alpha(t-\tau)}} e^{-\frac{(x-\xi)^2}{4\alpha(t-\tau)}}$$

3.1-8

The GF itself contains the structural and material information needed to characterize the specimen. In an NDE perspective, any alteration to the Green's function of a path can represent the presence of a defect: Figure 80 shows the spatial effect of the alteration of diffusivity in the 1D GF, for various instants of time.

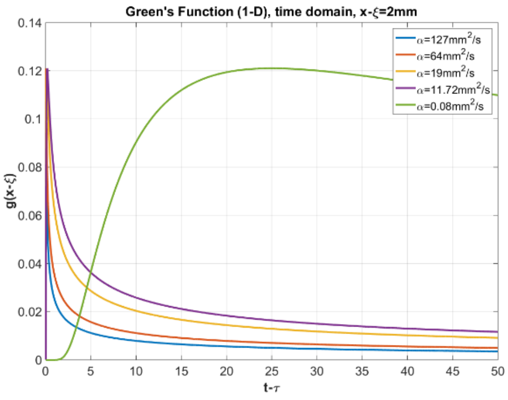

Figure 80 - Green's function in space domain for different time instants: (left) diffusivity of PVC; (right) diffusivity of Steel

Figure 81 shows the Green's function evolution in time, as evaluated at two different locations, 2mm and 4mm from the source respectively: the trend changes due to diffusivity, where a highly diffusive material as Gold (α = 127 mm^2/s) dissipates heat much faster than PVC (α = 0.08 mm^2/s).

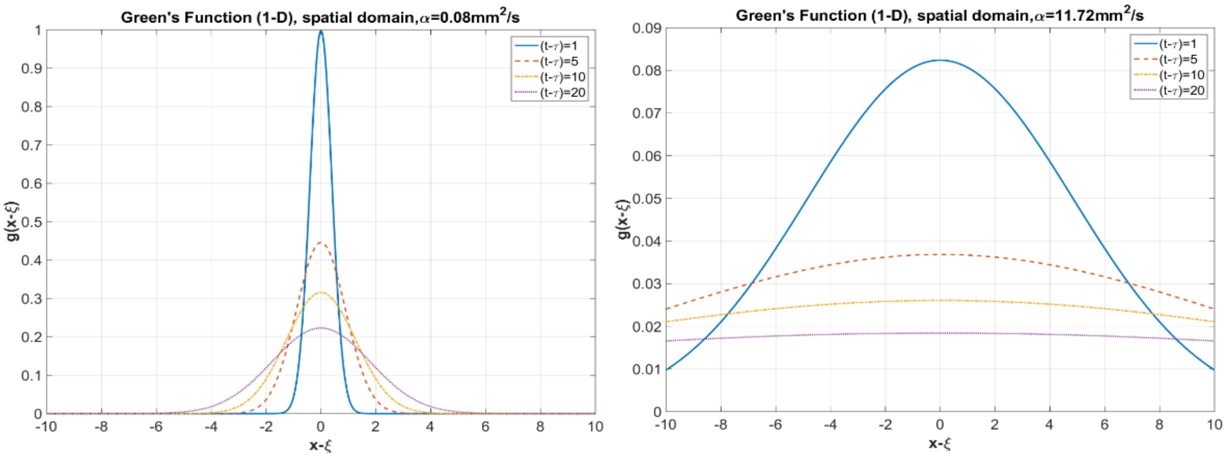

Figure 81 - Green's function in time domain for varying diffusivity values: (left) at x=2mm; (right) at x=4mm

The retrieval of the GF in a thermal field could be used for defect detection and material characterization.

Transforming the equation of heat diffusion in the frequency domain, it becomes:

$$\boldsymbol{\nabla}^2\boldsymbol{T}(\boldsymbol{r},\boldsymbol{\omega})-\frac{1}{k}N(\boldsymbol{r},\omega)=\sigma^2T(\boldsymbol{r},\omega)$$

3.1-9

where $\sigma(\omega)=\sqrt{\frac{i\omega}{\alpha}}=(1+i)\sqrt{\frac{\omega}{2\alpha}}$ is a type of a wavenumber. To be noted, $\sigma(\omega)$ is the complex counterpart of a real wavenumber, using the analogy with the elastic wave equation (Mandelis, 1995). It contains a material dependency as the inverse relationship with diffusivity, and expresses a dispersive relationship, between time and space (or frequency and wavenumber) governed by an analogous velocity term (diffusivity).

The TW solution in terms of Green's function is:

$$T(r,\omega)=\left(\frac{\alpha}{k}\right)\iiint_{V_0}Q(r_0,\omega)G(r|r_0;\omega)dV_0$$
$$+\ \alpha\oint_{S_0}[G(r|r_0^s;\omega)\nabla_0T(r_0^s,\omega)-T(r_0^s,\omega)\nabla_0G(r|r_0^s;\omega)]dS_0$$

3.1-10

it can be expressed as the result of two contributions: the transfer function of a certain path convoluted with a source $Q(r_0,\omega)$ or the temperature distribution due to initial temperature boundary conditions. We can think about G as the building block for more complex solutions, where the source is arbitrary and the initial and boundary conditions are inhomogeneous.

Exploiting the concepts above and following Mandelis (2013), the first case study is a simple plate, considered as a semi-infinite and then finite medium.

In the first case, the Green's function associated to the homogeneous problem is:

$$G(R|R';\omega) = \frac{1}{4\pi\alpha}(\frac{e^{-\sigma R}}{R} + \frac{e^{-\sigma R\prime}}{R'})$$

3.1-11

where R'=$|r - r'_0|$is the source location. The problem is formulated as 3D heat diffusion, where Neumann adiabatic boundary conditions are applied. The heat source is simulated as a Gaussian Laser beam, of width W, with time harmonic flux, and it is imposed as an initial boundary condition as:

$$k\nabla_0 T(r_o^s,\omega) = \frac{F_0}{2}(1 + e^{i\omega t})e^{-\frac{x^2+y^2}{W^2}}$$

3.1-12

so that the resulting thermal wave field is:

$$T(x,y,z;\omega) = \frac{F_0}{2k}e^{-\frac{(x^2+y^2)}{W^2}}\left(\int_0^\infty \frac{e^{-\sigma\sqrt{\rho^2+z^2}-\left(\frac{\rho}{W}\right)^2}}{\sqrt{\rho^2+z^2}}\, I_0\left(\frac{2\rho}{W^2}\sqrt{x^2+y^2}\right)\rho d\rho\right)$$

3.1-13

When reducing the source to a very focused beam located in (x_0^s, y_0^s), on top of the plate (z=0), the TW simplifies to:

$$T(x,y,z;\omega) = \frac{\alpha F_0}{2k}G(x,y,z|x_0^s,y_0^s,0;\omega) = (\frac{F_0}{4\pi k})\frac{e^{-\sigma\sqrt{(x-x_0)^2+(y-y_0)^2+z^2}}}{\sqrt{(x-x_0^s)^2+(y-y_0^S)^2+z^2}}$$

3.1-14

When considering the plate as a medium bounded by two infinite parallel planes at z=0 and z=L, where L is the thickness of the plate, we can schematize the problem as follows (see Figure 82):

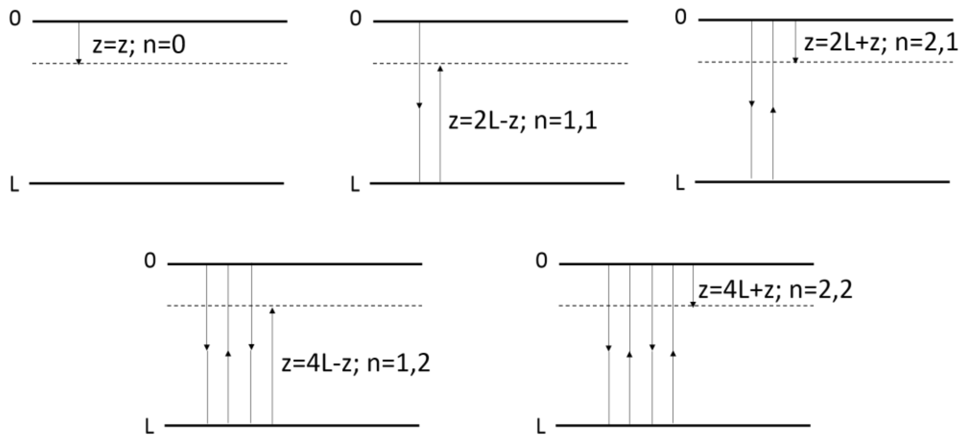

Figure 82 - Heat propagation within a finite medium as a reflecting thermal wave

The problem is formulated again as 3D heat diffusion, with the same initial and boundary conditions as above. Also the same source (a Gaussian laser beam) is applied as initial boundary condition, so that we can exploit the GF solution as in eq. (3.1-13).

The Green's function associated to the problem is:

$$G(x,y,z|x_0,y_0,z_0;\omega) = \frac{1}{4\pi\alpha}\sum_{n=-\infty}^{\infty}[\frac{e^{-\sigma|r-r_{0n}|}}{|r-r_{0n}|} + \frac{e^{-\sigma|r-r'_{0n}|}}{|r-r'_{0n}|}]$$

3.1-15

where $|r-r_{0n}| = \sqrt{(x-x_0)^2+(y-y_0)^2+(z-(2nL-z_0))^2}$ and $|r-r'_{0n}| = \sqrt{(x-x_0)^2+(y-y_0)^2+(z-(2nL+z_0))^2}$; $2nL \pm z_0$ are the rays travelling from the top of the plate to the back and vice versa.

The resulting Thermal Wave is:

$$T(x,y,x;\omega) = \frac{F_0}{2k}e^{-\frac{x^2+y^2}{W^2}}\left\{\Im_0(x,y,z;\omega) + \sum_{n=1}^{\infty}\Im_n(x,y,2nL-z;\omega) + \Im_n(x,y,2nL+z;\omega)\right\}$$

3.1-16

where $\Im_n(x,y,2nL\pm z;\omega) = \int_0^\infty \frac{e^{-\sigma\sqrt{\rho^2+(2nL\pm z)^2}-(\frac{\rho}{W})^2}}{\sqrt{\rho^2+(2nL\pm z)^2}} * I_0\left(\frac{2\rho}{W^2}\sqrt{x^2+y^2}\right) * \rho d\rho$, I_0 is the modified

Bessel function of 1st kind and order 0 and $\rho = \sqrt{(x-x_0)^2+(y-y_0)^2}$.

Heat propagation is treated as a thermal wave bouncing back and forth off the surfaces of the plate, treated as half-spaces, so that the resulting thermal field is the sum of all the contributions given by the reflections within the thickness of the plate. This interpretation is valid for thin structures and has been implemented in Matlab for an Aluminum plate of 10mm x 10mm x 6mm, n=4 backwall reflections. It can be noticed how the Temperature diffuses from the location of the source outwards and through the depth (Figure 83). Also, the different frequency components of the field behave differently, showing a higher diffusion for higher frequencies.

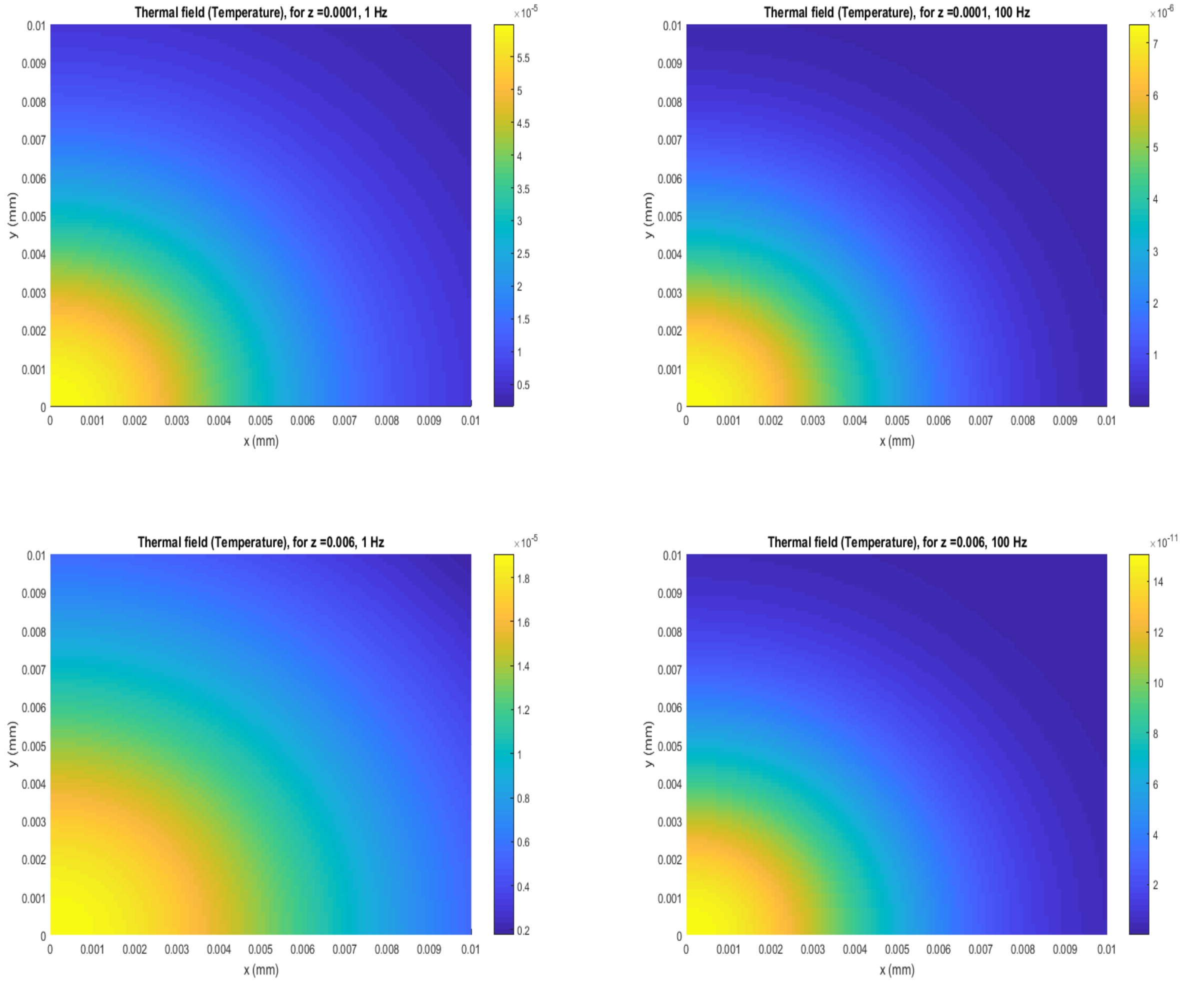
Thermal field (Temperature), for z =0.0001, 1 Hz

Thermal field (Temperature), for z =0.0001, 100 Hz

Thermal field (Temperature), for z =0.006, 1 Hz

Thermal field (Temperature), for z =0.006, 100 Hz

Figure 83 - Analytical frequency domain temperature distribution in finite medium: top surface (top), bottom surface (bottom); at 1 Hz (left) and at 100 Hz (right).

The time domain solution is found inverting the frequency domain solution: due to computational limitations the thermal field evolution is observed up to 1s (Figure 84). Errors show up in the front surface due to time discretization issues.

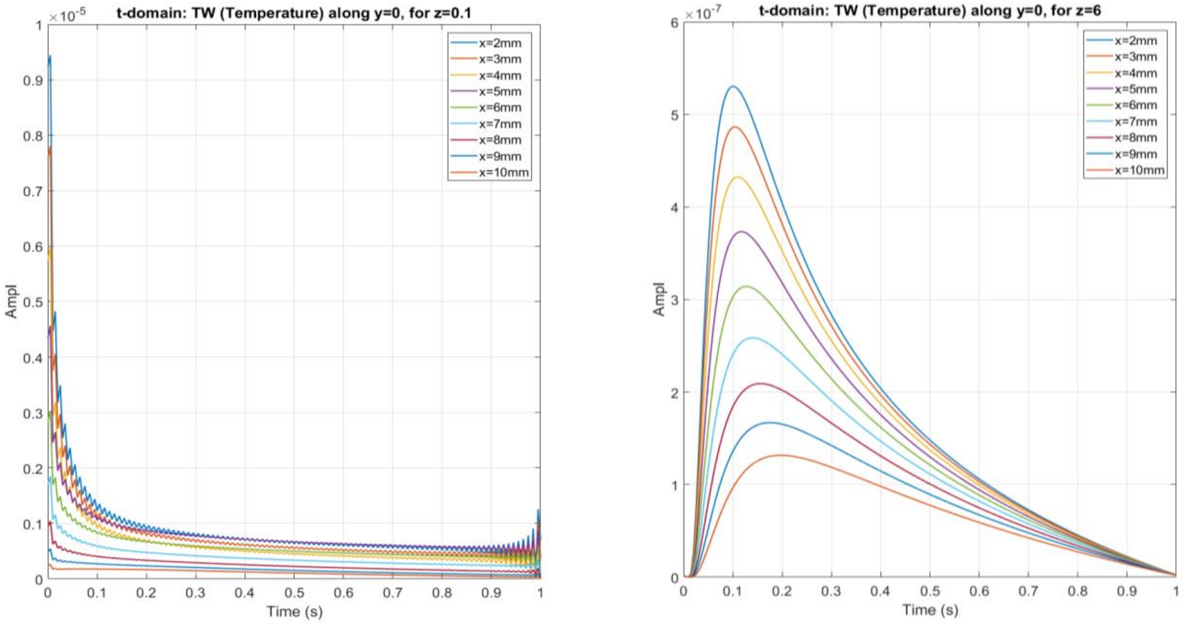

Figure 84 - Analytical time domain temperature distribution in finite medium: top surface (left), bottom surface (right), at y=0 and for varying distances x from the source x=0

The above analytical formulation offered insights on heat propagation interpreted as a thermal diffusing wave and has been used in both passive and active IR thermographic approaches. The semi-infinite medium problem can be related to cases where the diffusion is observed in the depth dimension and/or the diffusion has not yet reached the backwall, since the thickness is greater than the one needed to provide “reflections”. The plate as bounded by two surfaces is used when visualizing heat propagation as thermal guided waves and/or when the presence of a defective surface acts as a reflector within the thickness of the plate. The results provide hints on the possibility of performing material characterization and defect detection, if a thermal GF is retrieved. Numerical simulations, using a commercial software, have been implemented to model cases with more complex geometries, materials (i.e. inhomogeneous thermal properties, defects, …) and to observe heat diffusion in longer time scales.

Moreover, the above-mentioned TW field solutions of heat propagation can be used for a passive approach of IR thermography. The theoretical feasibility of passive Green's function extraction in thermal fields is here discussed.

3.2.2 Passive extraction of thermal Green's function

Cross-correlation of diffuse fields to retrieve GFs has been demonstrated for elastic, dissipative and electromagnetic waves (Snieder et al., 2009; Snieder et al., 2007; Lobkis and Weaver, 2001; Kuperman, 2008) and widely used in many applications as seismology (Snieder, 2004; Waapenar et al., 2006; Sabra et al., 2005), oceanography (Sabra et al., 2005) and structural health monitoring (Tippman et al., 2015; Sabra et al., 2008; Lanza di Scalea et al., 2018a). This is possible because the time-averaged cross-correlation operation suppresses the incoherent part of the response between the two points, and builds up the coherent part which corresponds to the ballistic and antiballistic response (Green's function) between the two receiving points. The approach relies on the fluctuation-dissipation theorem, as discussed by Callen and Welton in 1951 and by Callen and Greene in 1952. This fundamental energy theorem states that a thermodynamic system in equilibrium is related to macroscopic irreversible processes in the same way as generalized fluctuating forces relate to a characterizing dissipative parameter, intrinsic of the system itself:

$$\langle \xi^2 \rangle = -\frac{2\mathrm{k}}{\pi} \int_{-\infty}^{\infty} \frac{\sigma_s(\omega) d\omega}{\omega^2}$$

3.1-17

where $\xi^2$is the mean spectral density of the spontaneous fluctuations, σ_s is the conductance and k is a constant.

This means that the random fluctuations in a system, acquired passively, contain information about the system within the dissipative parameter, that, if extracted, could be then imaged and/or used for NDE or characterization.

The retrieval of the latter could be achieved in terms of GF extraction. For the diffusion equation, following (Snieder, 2006), we can write:

$$i\omega u_{A/B} + \nabla \cdot \left(D \nabla u_{A/B}\right) = -q_{A/B}$$

$$-i\omega u_{A/B}{}^{*} + \nabla \cdot \left(D \nabla u_{A/B}{}^{*}\right) = -q_{A/B}{}^{*}$$

3.1-18

where $u_{A/B}$ is the solution at point A or B for the forces $q_{A/B}$ and D is the diffusion constant. The second equation is about the time reversal form, expressed by the conjugate solution $u_{A/B}{}^{*}$ in frequency domain. The convolution theorem, in frequency domain, states that:

$$\int (u_A q_B - u_B q_A) dV = 0$$

3.1-19

This brings the important consequence of reciprocity, where the GF at point A due to a source at point B equals the GF at point B given by a source at A:

$$G(r_B, r_A) = G(r_A, r_B)$$

3.1-20

Also, the correlation theorem states that:

$$\int (u_A q_B{}^{*} - u_B{}^{*} q_A) dV = 2i\omega \int u_A u_B{}^{*} dV$$

3.1-21

The latter, combined to reciprocity, leads to:

$$G(r_A, r_B, \omega) - G^{*}(r_A, r_B, \omega) = 2i\omega \int G(r_A, r, \omega) G^{*}(r_B, r, \omega) dV$$

3.1-22

Which means that the superposition of the GF between point A and B and its time reversed counterpart are related to the derivative of the convolution of the two.

For random and impulsive sources (uncorrelated) (Snieder, 2008):

$$\langle q(r_1, \omega) q^{*}(r_2, \omega) \rangle = \delta(r_1 \text{-} r_2) |q(\omega)|^2$$

3.1-23

And

$$u(r) = \int G(r, r_0) q(r_0) dV_0$$

3.1-24

Using these equations into the previously obtained eq. (**3.1-22**), we have:

$$G(r_A, r_B, \omega) - G^*(r_A, r_B, \omega)|q(\omega)|^2 = 2i\omega \, \langle u_A(r_A, \omega) u_B^* \, (r_B, \omega)\rangle$$

3.1-25

and

$$G(r_A, r_B, t) - G(r_A, r_B, -t) * C_q = -2\frac{d}{dt}\langle u_A(r_A, t) u_B(r_B, t)\rangle$$

3.1-26

in frequency and time domain, respectively. Equations (**3.1-25**) and (**3.1-26**) state that the GF solution between point A and B, multiplied by the power spectrum of the sources, is proportional to the time derivative of the frequency domain convolution (or time domain cross-correlation) of the fields at point A and B. The thermal Green's Function between two locations can be reconstructed by the cross-correlation of random thermal field fluctuations, recorded at those two locations.

Particular attention has to be placed on the temporal and spatial averaging of the recorded signals and cross-correlated results. Also, the diffusive state of the field needs to be such that it allows for the coherent paths only to emerge from the cross-correlations and any other random path to be averaged out.

The inverse scattering theorem has also been investigated from a theoretical point of view and understood in a thermal and defect detection perspective. Interpreting the defect as a scatterer, the superposition of the direct and backscattered fields is related to the auto-correlation of the field at the source:

$$G(\boldsymbol{r}_0, \boldsymbol{r}_0) - G^*(\boldsymbol{r}_0, \boldsymbol{r}_0) = \frac{1}{|S(\omega)|^2}\langle |u(\boldsymbol{r}_0, \boldsymbol{r}_0)|^2\rangle$$

3.1-27

A schematic of the concept is represented below and has been observed in simulations:

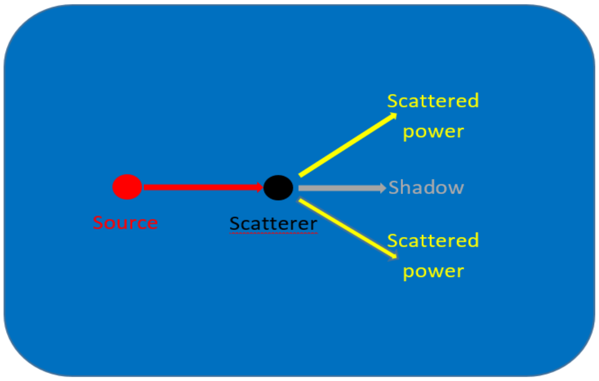

Figure 85 - Schematic of inverse scattering principle

Applying the above-mentioned theoretical conclusions to a thermal environment, the thermal signature of the path between two points can be extracted from the correlation of the temperature time histories of the points, due to the natural thermal exchanges occurring in the structure, when interpreting the fluctuations as given by random Dirac sources (Figure 86).

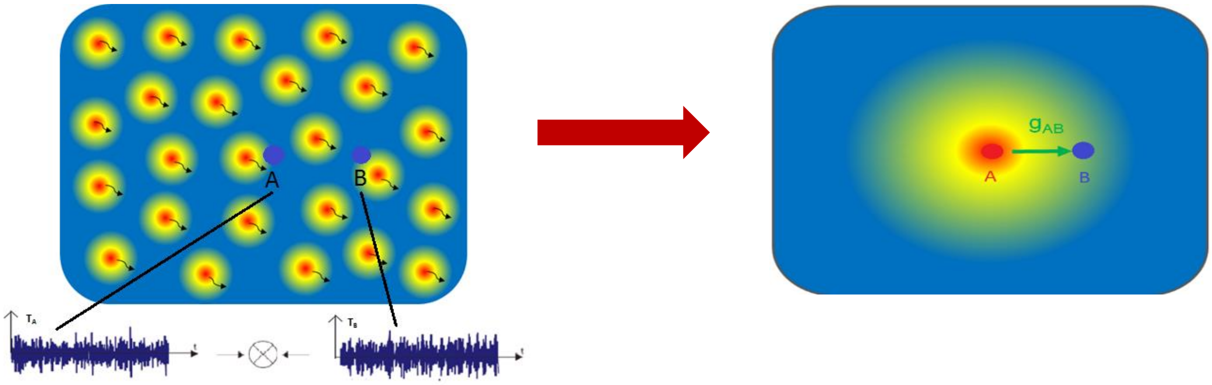

Figure 86 - Passive reconstruction of Green's function: application to thermal waves.

This is because the energy in the volume of interest is related to the energy radiated through the surface and the one loss through the volume. The thermal properties and the presence of defects would interact with the propagating heat and result in the retrieved transfer function.

The passive thermal Green's function retrieval could not be observed through experiments and it remains an open question. This could be due to hardware limitations posed by the sensitivity (or Noise

Equivalent Temperature Difference, NETD) of current IR thermocameras. Another reason could be the necessity of stronger diffused sources, that could not be observed/reproduced in a laboratory environment. Whether the thermal vibrations of atoms are able to generate thermal transients at the macroscopic level to be reconstructed passively, remains an interesting aspect to be further investigated.

3.3 Numerical Investigation

3.3.1 Active thermal Green's Function

Finite element simulations have been performed to understand the conductive heat transfer into plate-like specimens. An Aluminum plate of 2mm thickness has been modeled in LS-Dyna. An impulsive heat source excites the thermal field and heat propagation is observed in Figure 87, mapping temperature.

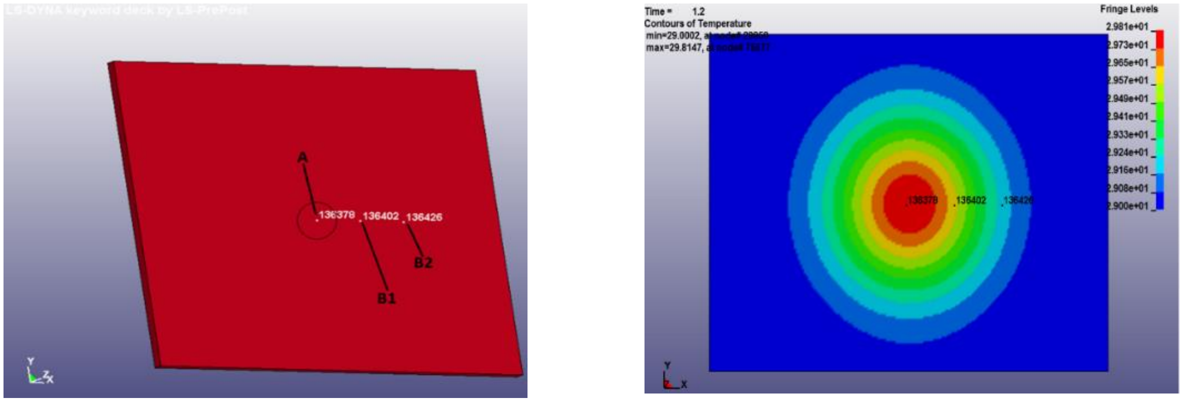

Figure 87 - FEM Heat propagation in pristine Aluminum plate: geometry (left), heat wave propagation as Temperature (right)

Structural defects of different types have been simulated to understand the heat interaction with them and their effect on the thermal wave as it encounters a geometrical or diffusivity mismatch (Figure 88):

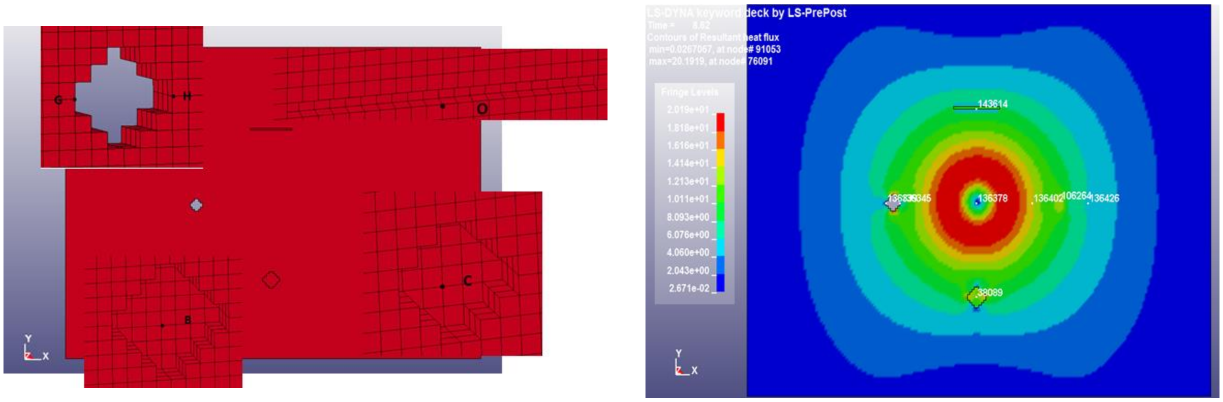

Figure 88 - FEM Heat propagation and defect interaction in Aluminum plate: geometry (left), heat wave propagation as Heat flux (right)

It can be noted in Figure 88 how the defects cause clear discontinuities in the heat flux distribution, including shadowed areas and virtual heat sources. Analogies with optical and acoustic scattering can be observed and exploited, as mentioned in the previous section. Different heat sources distributions and intensities have been simulated in this study.

Moreover, the scale of the problem and the FEM simulated model have been investigated: the fluctuations magnitude has to be related to a certain scale of time and space output, governed by the thermal parameters. The dimensions and duration of the simulation have to be tuned accordingly.

For an impulsive heat source in the center of a plate, the 1D heat propagation has been considered. A through hole has been placed on one side of the source and temperature responses have been recorded on both sides, at different positions at distances from 2.5 mm to 17.5 mm (Figure 89).

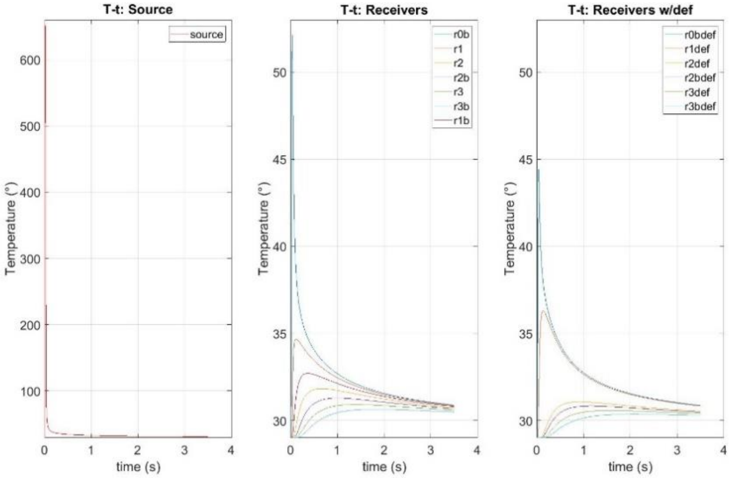

Figure 89 - FEM temperature response: at source (left), at receivers on pristine side (center), at receivers on defective side (right).

The temperature distribution is affected by the presence of the defect according to the inverse scattering principle: the receivers before the defect keep a higher temperature at later times of propagation since the heat is blocked by the hole and is “reflecting” back; the receivers after the defect have a lower temperature since the hole “shadows” the heat.

Cross-correlations have been performed to retrieve the thermal Green’s function between the heat source and the recording nodes (Figure 90 and Figure 91).

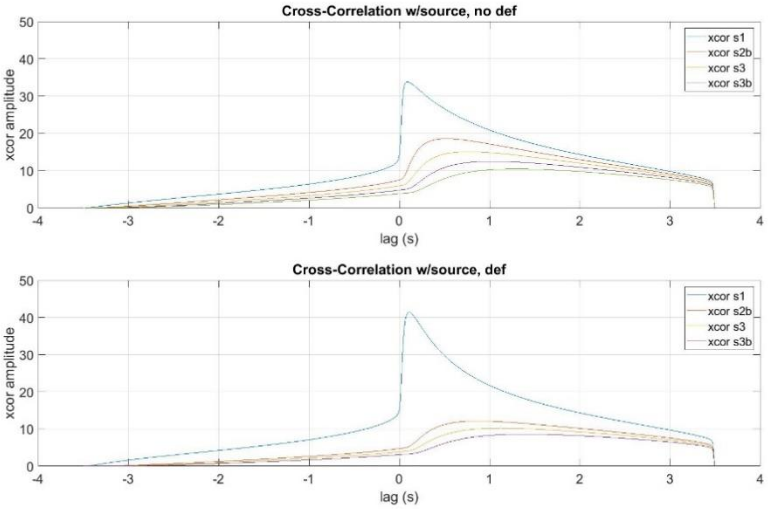

Figure 90 - Cross-correlation of FEM temperature time histories: (top) between source and receivers on pristine side, (bottom) between source and receivers on defective side.

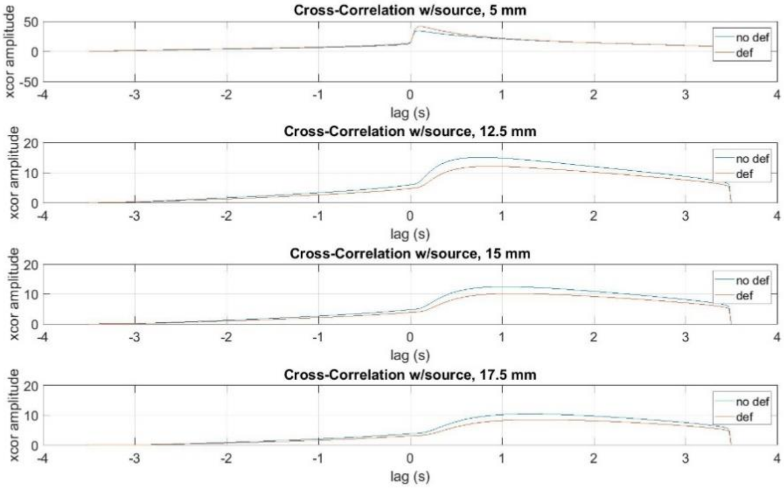

Figure 91 - Cross-correlation of FEM temperature time histories: (top to bottom) increasing distance from source, between source and receivers on pristine side (blue), between source and receivers on defective side (red).

A dissipative thermal wave can be observed as the cross-correlations are plotted for nodes located further away from the source. Also, differences can be noted for the same distance in the pristine and defect case, confirming that the Green’s function retrieval can be exploited for defect detection.

In an NDE perspective, the maximum value and the lag of the peak of each cross- correlation have been extracted for the pristine and defective side (see Figure 92):

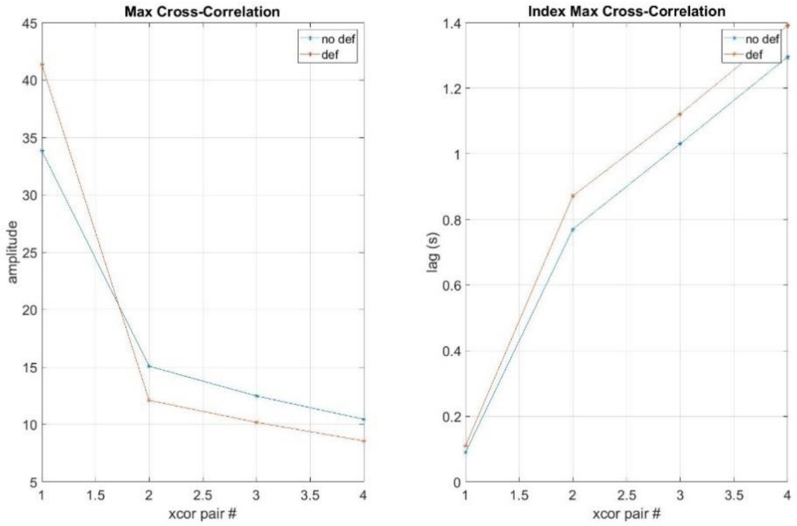

Figure 92 - Cross-correlation of FEM temperature time histories: (left) peak value, (right) lag of peak, for pairs of increasing distance from source, between source and receivers on pristine side (blue), between source and receivers on defective side (red).

Lag, signal processing variables as results in terms of dissipation rate and amplitude have been investigated to extract the associated Green's function. Ideally cross-correlations could be performed between any pair of available nodes in the FEM model (pixel in a real thermographic image) to map meaningful features extracted from the retrieved "active thermal GFs". In a real experimental scenario, no active source would be needed but the natural thermal fluctuations, stimulated by environmental/operational conditions, would serve as thousands of the above simulated cases, arranged as a diffuse field.

3.3.2 Spatial discontinuity of Thermal Guided Waves

The observations related to heat propagation and defect interaction of the cases presented above, combined to the theoretical considerations about heat conduction equations and scattering theorems, suggested an additional interpretation of thermal waves and their potential in NDE.

Recalling eq. (3.1-5) and its hyperbolic nature, we can notice that the temperature spatial distribution is driven by the temperature gradient in time. Due to the asymmetry in time for this kind of process, which distinguish it from the propagation of elastic waves, we can exploit the reciprocity in space. Spatial symmetries and deviations from it can be emphasized by temperature derivatives in space: at every instant in time, a spatial derivative can be calculated to retrieve the heat flux propagating in that direction. This approach would emphasize the presence of material or geometrical discontinuities that alter the normal heat flow, scattering or trapping heat. Moreover, following Li et al., 2000, a linear impulsive source could help enhancing the above-mentioned effect, guiding the heat wave and its interaction with the discontinuities into the plate-like specimen.

The investigation of thermal guided waves (TGWs) propagation is modeled in LS-Dyna, for an Aluminum plate (100x100x6 mm), mesh size = 2mm, with a linear source at the center of the top surface of dx=2mm and dy= 40mm. The heat pulse has a duration of 0.01s and the propagation is observed for 5s. Figure 93 shows the propagation for the pristine plate in terms of temperature and heat flux: the propagation is guided uniformly within the plate and evolves symmetrically, with respect to the source. This is also confirmed by the heat map of the heat flux in the three decomposed directions.

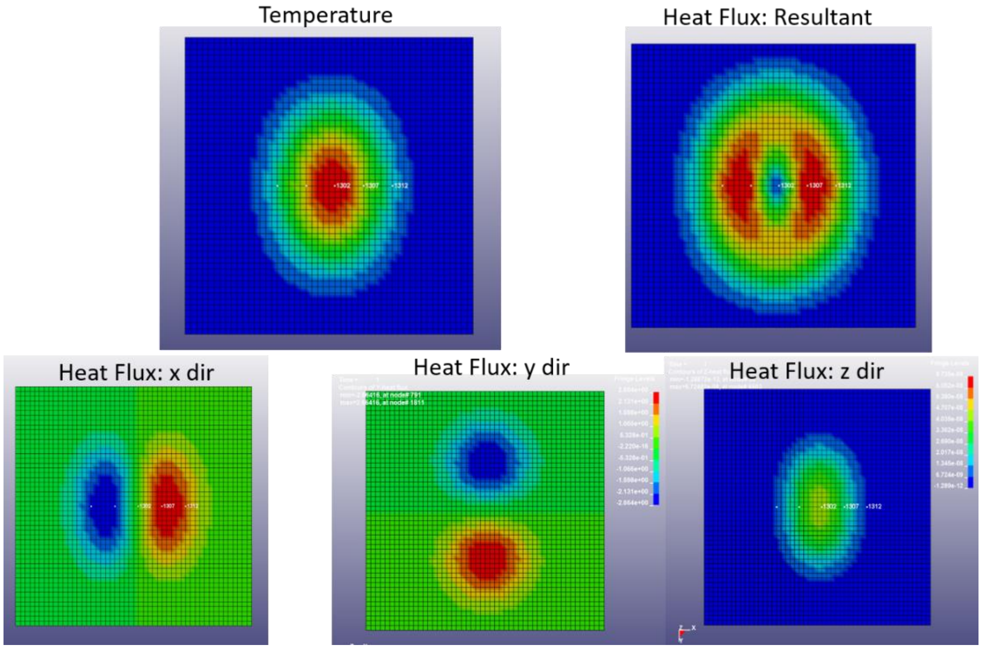

Figure 93 - TGW in FEM pristine Aluminum plate

When introducing defects in the plate as a slit (2x10x2 mm) to simulate a crack, or a reduction in thickness (8x8x4 mm), to simulate corrosion, the diffusion is affected and symmetry is broken. The effect is noticeable in the temperature maps, but is much stronger in the heat flux, where the defect scatters heat and acts as a secondary heat source.

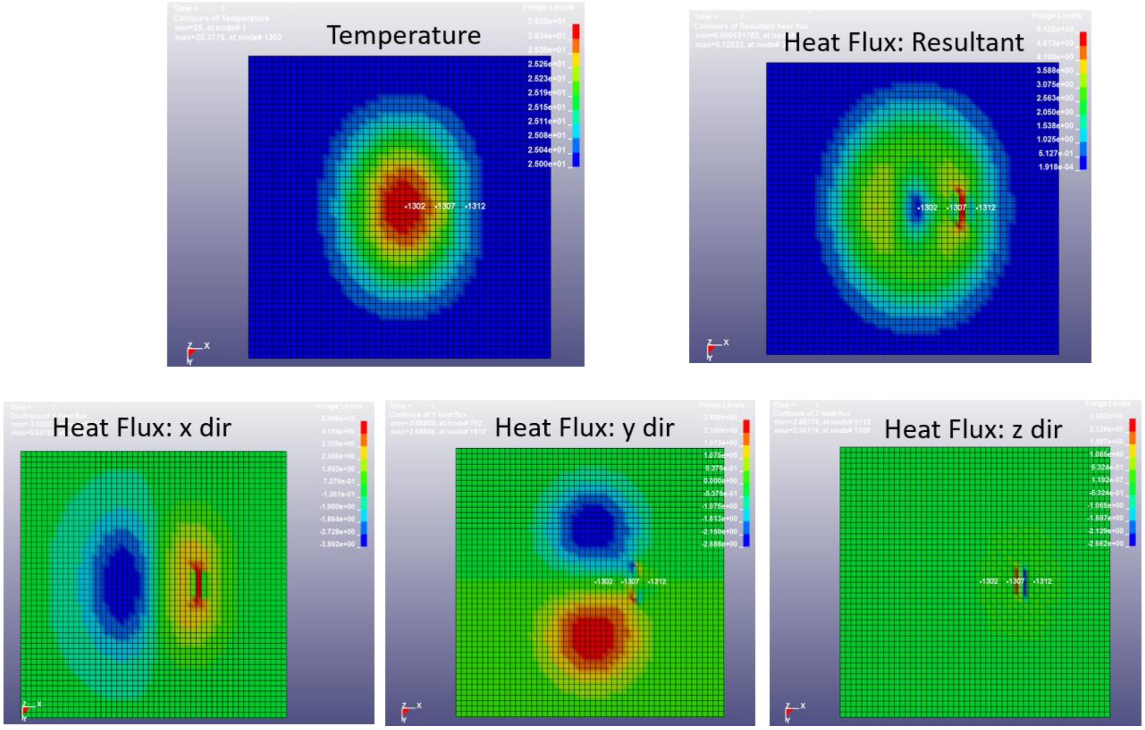

Figure 94 - TGW in FEM Aluminum plate with slit

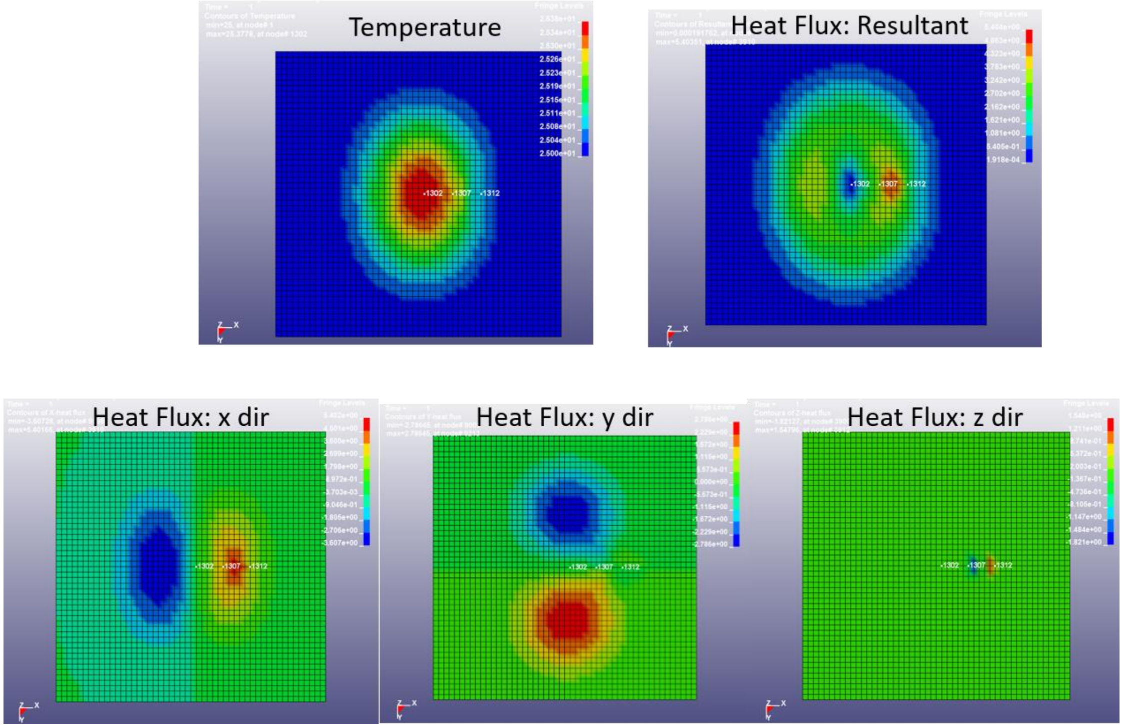

Figure 95 - TGW in FEM Aluminum plate with corrosion

Both defects shadow heat in the x direction and slow the symmetrical evolution of heat in the later portion of the plate. Heat is trapped within the defect leading to local effects in all directions (Figure 94 and Figure 95).

Temperature and heat flux time histories have been extracted every mm along the x direction, at the top surface of the plate: the solid lines represent the pristine area of the plate on the left side of the source, while the dashed ones represent the defective side. The blue and yellow curves represent an early instant, while the red and purple curves a later one. Monitoring temperature along a horizontal line on the surface of the plate, the primary and secondary scatterings lead to a slight increase before and slight decrease after the defect (Figure 96 and Figure 97 top left). This effect is slightly noticeable in the temperature plots but is well emphasized in the heat flux, dominated by the heat flux in the x direction, due to the nature of the linear source.

In a real application, one could only measure temperature and both the defect detection and imaging performance would be reduced by the very low contrast. Using Fourier's law:

$$\boldsymbol{q} = -k\nabla T$$

one could image the spatial derivative of temperature to have a measure of the heat flux, at every instant, and emphasize the discontinuities within the diffusion process. The validation and beneficial effect of this technique are shown in the top right plots of Figure 96 and Figure 97, where the discontinuity in correspondence of the defect location is very well noticeable and the value itself of the function is exactly matching the heat flux, as extracted and plotted in the bottom right plot.

Experimental tests are needed to validate this approach and perform subsurface imaging with TGWs.

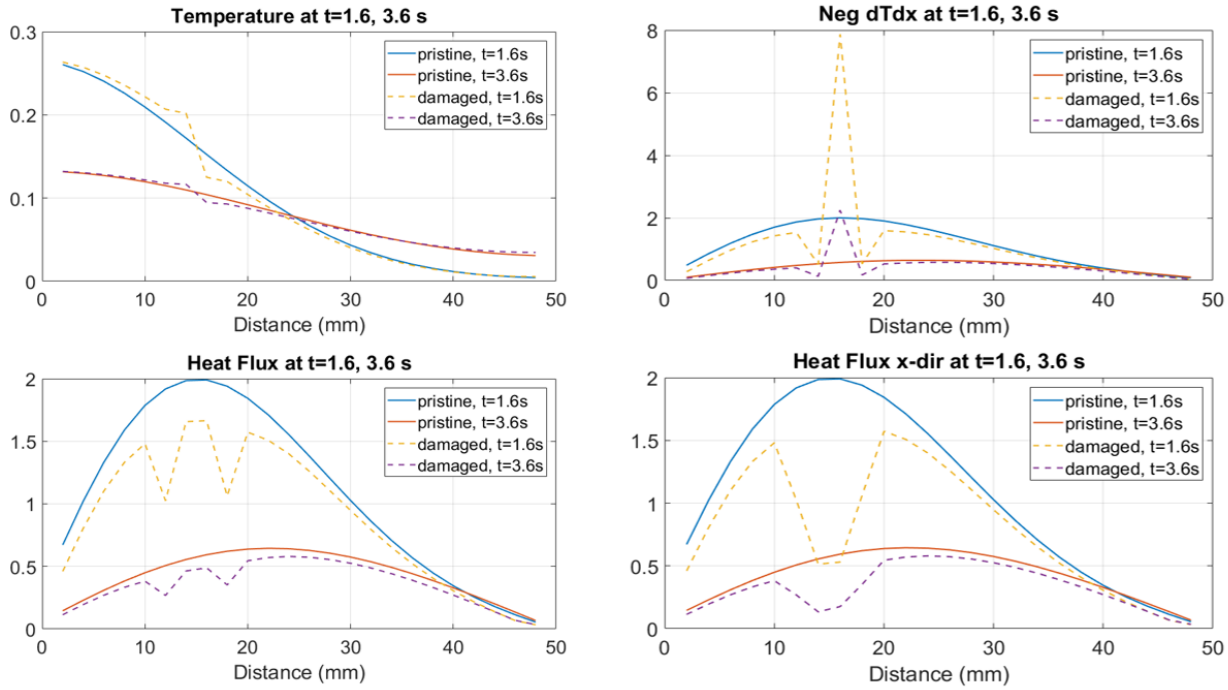

Figure 96 - FEM Slit in Aluminum plate, time histories along x: temperature (top left), spatial derivative of temperature (top right), heat resultant (bottom left), heat x dir (bottom right)

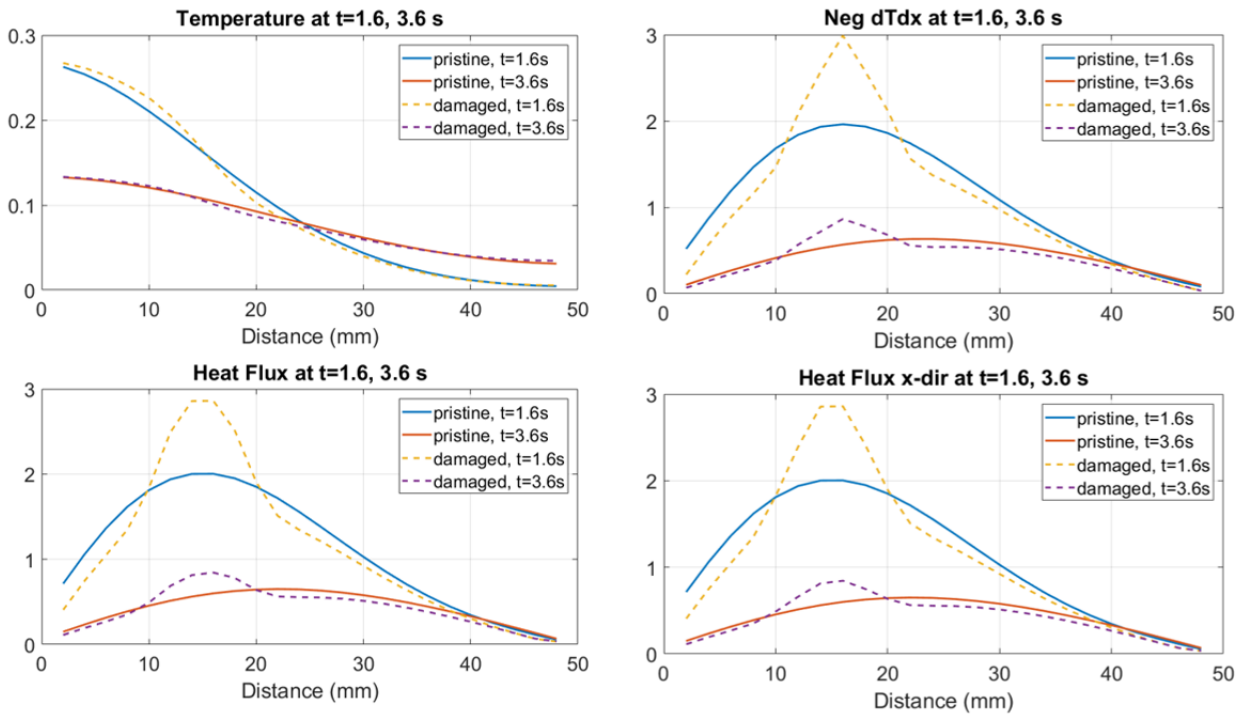

Figure 97 - FEM Corrosion in Aluminum plate, time histories along x: temperature (top left), spatial derivative of temperature (top right), heat resultant (bottom left), heat x dir (bottom right)

3.4 Application: Composite Aerospace panels

Although many techniques and applications are available, as well reviewed by Meola, Carlomagno 2003, especially after exploiting the available temperature-time histories (Vavilov, 1992), in the literature, IR thermography has been widely used for aerospace inspection, because, beside the above-mentioned advantages, the thin character of aircrafts makes them great candidates for this technique. Baleagas et al. (1987) applied pulsed PTR to CFRP, Favro et al. (1992) proposed a real time thermal wave tomographic method in graphite-epoxy structural components subjected to impact damage and more recently Usamentiaga et al. (2013) proposed the automatic detection of such damage in thin CFRP composites. Servais et al. (2008) used it to inspect aerospace composite discontinuities for the characterization of their manufacturing and maintenance using phase information, after several works in the same field. Ibarra-

Castanedo et al. (2007) reviewed the assessment of aerospace structures by pulsed thermography, used in combination of different processing approaches.

Among the reviewed methods, exploiting the wave nature of heat propagation, as heat diffusing in 3D into the structure and reflecting from the backwall and/or defects, we use the Thermal Signal Reconstruction (TSR) technique, as developed by Shepard (2004), to perform NDE on the same composite panels, used in the Elastic waves section. The TSR relies on the two following equations:

$$\Delta T(t) = \frac{Q}{e\sqrt{\pi t}}$$

3.4-1

$$\Delta T(t) = \frac{Q}{e\sqrt{\pi t}}\left(1 + 2\sum_{n=1}^{\infty} e^{-\frac{(nL)^2}{\alpha t}}\right)$$

3.4-2

for a semi-infinite and finite medium respectively, which are basically the time domain version of equations (**3.1-14** and 3.1-16), where ΔT is the temperature evolution in time, normalized by the initial temperature and e is the effusivity ($e = \sqrt{k\rho c}$). Visualizing the temperature distribution in a logarithmic scale, it is possible to simplify the time-temperature relation and to appreciate the effect of the geometry in the propagation. From eq. (3.4-1), we can write:

$$\ln\bigl(\Delta T(t)\bigr) = \ln(K) - \frac{1}{2}\ln(t)$$

3.4-3

here K is a constant.

It can be noticed how the logarithm of temperature decays linearly with time. For a finite medium (i.e. a plate), we account for the multiple reflection within the surfaces: the decay decreases with time, as the number of reflections within the plate increases. Figure 98top shows the trends for the semi-infinite (green), finite plate (black). Rearranging the terms to solve for the temperature, the above equations become:

$$\mathrm{T(t)} = \exp(a_0 + a_1 \ln(t) + \ldots + a_n \ln(t)^n)$$

3.4-4

Hence, the temperature evolution in time can be expressed by a polynomial function. This simplifies the temperature-time relationship both in the theoretical and in the experimental scenario. In fact, the large amount of data, which constitutes one of the disadvantages of thermography, can now be reduced to a simpler function, where only n+1 constants need to be stored. Moreover, the polynomial can be better exploited mathematically, due to its smooth trend. The time derivative allows to appreciate the deviation from a “regular” cooling history, showing the presence of defects within the depth of the plate (Figure 98 left, center). A positive slope represents the reflection from a wall and the arrival of the maximum provides information on the depth of the latter, since temperature plateaus (i.e. maximum temperature increase after cooling, since heat cannot be created).

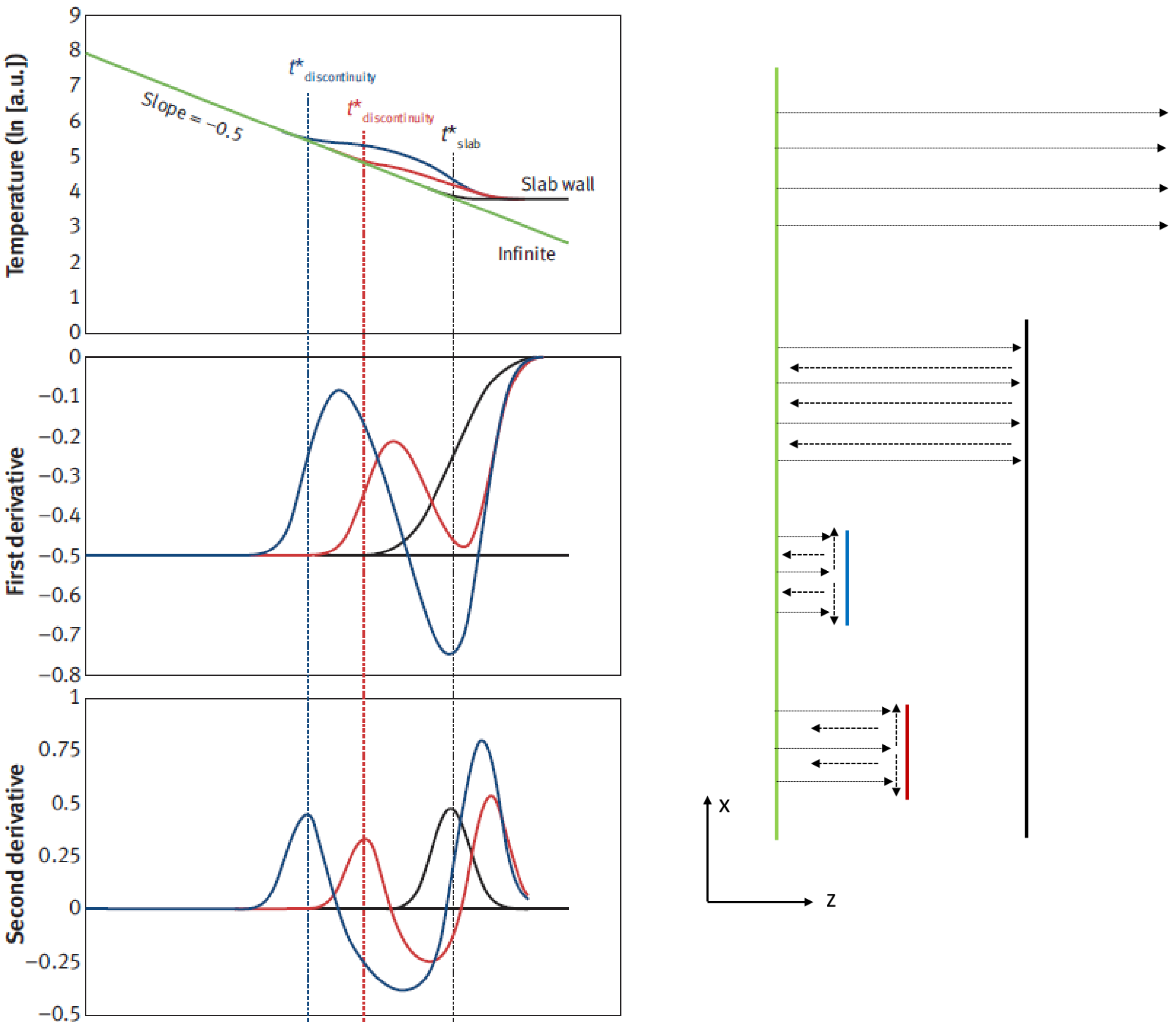

Figure 98 - TSR representative 1D plots (left, Shepard and Lhota, 2014): logarithmic Temperature (top); 1st time derivative (center); 2nd time derivative (bottom); Scheme of specimen corresponding to the TSR 1D plots (right).

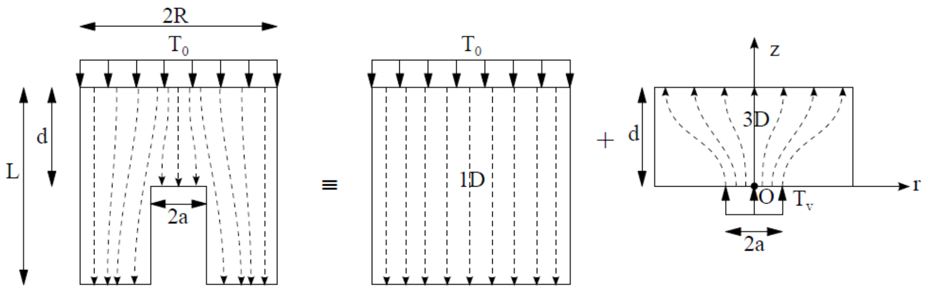

Figure 99 - 3D Heat diffusion in a defective specimen: virtual heat source interpretation (Manohar, 2015)

As discussed in Manohar (2013; Manohar et al., 2015) and in the previous theoretical section, the temperature evolution in a defective portion of a specimen can be viewed as the summation of two contributions: a diffusion of heat through the depth and reflections, and consequent decrease in cooling, after hitting a discontinuity.

This latter scattering effect, as pictured in Figure 99, can also be seen as if the defect traps heat above its reflective surface and becomes a secondary heat source itself, initiating a secondary 3D diffusion process. The more localized and "discontinuous" the defect, the more the "trap and release" effect is evident. To capture this phenomenon, and enhance defect detection and visualization, a second time derivative can be performed on the polynomial. The change in the rate of cooling is here emphasized: the maximum represents the flex point in the cooling, hence the reflection from the discontinuity, while the minimum represents the later highest cooling, hence the 3D diffusion due to the localized defect (Figure 99bottom). To be noted, the absence of defects within the medium should be demonstrated by a positive second derivative, since no secondary cooling should occur. The time of arrival of the maximum of the second derivative (also known as saturation or break time) is related to the depth L of the reflective wall and diffusivity as:

$$t_{sat} = \frac{L^2}{\pi\alpha}$$

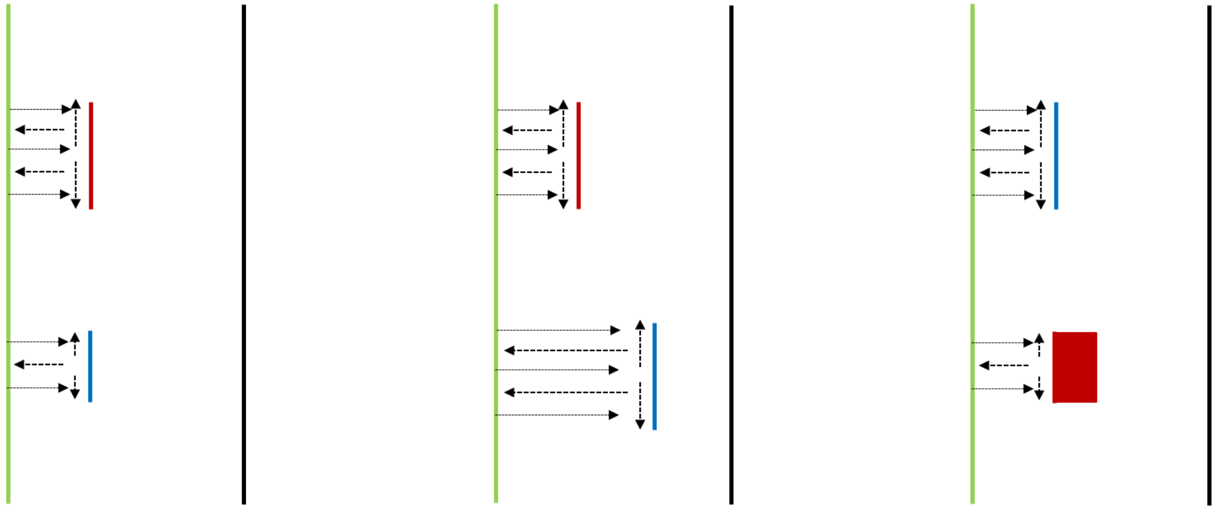

Figure 100 - Secondary cooling dependence on defect aspect ratio

The defect type itself influences the secondary cooling effect, hence the second derivative, both in magnitude and time of positive and negative peak arrival (Shepherd, Frendberg, 2014). Different consideration on the defect aspect ratio, defined as diameter/depth of the defect must be done to interpret the results correctly.

Figure 100 reports three different cases of variations in defect in-plane size (diameter, in-plane extension), depth (distance from the front surface) and thickness (transverse discontinuity size). The first case (Figure 100 left) compares two defects at the same depth but with different in-plane extensions: the red defect will have a stronger and longer secondary cooling, since the lateral diffusion will take longer to dissipate. The second case (Figure 100 center) considers the depth of the defect: the closer to the primary heat source, the greater the amount of heat to be reflected and hence diffused as a secondary source. A minimum aspect ratio is needed, above which detection can be performed. In the third case, a more "localized" defect is compared to a thin one, as an insert or delamination (Figure 100 right): the greater discontinuity in the thickness direction, the greater the mismatch in diffusivity, hence the stronger the trap and release effect. Flat inserts, disbonds and delaminations are harder to detect with respect to flat bottom holes, inclusions and cracking.

The combination of the TSR and the virtual heat source will be applied in this work to detect and study defects in aerospace panels.

The same composite panels (

Table 8), manufactured under the NASA project described in the previous chapter and impacted with different energy levels on the stringer cap and flange, have been tested for an independent IR thermography damage survey.

Two flash lamps (detail flash lamps) provided the excitation and a FLIR A320 Thermocamera (320x240, 30 Hz) recorded the temperature evolution for 120s, including the time of excitation, to capture the entire cooling transient, in a "reflection mode".

The results are presented as 2D maps, at specific time instants, optimized according to 1D time plots. The three 1D time plots (temperature, 1st derivative, 2nd derivative) use the TSR method, implemented in a Matlab routine. Representative cases are shown below.

For the 1D time plots, five pixels have been chosen to represent the skin (blue and cyan), the flange (green), the cap (black) and the defect (red) behavior. In all the raw temperature plots, it is not possible to recognize a noticeable difference in the cooling trend: pixels corresponding to the same component of the panel (as two skin pixels) have an apparent different temperature response, mostly non uniformities in heating are emphasized and only a major plateau effect can be appreciated, demonstrating the plate-like character of the specimen.

The 1st time derivative plot allows to distinguish the different thicknesses, showing a very similar trend in the cooling rate of components of the same thickness (two skin pixels and cap) and a different time at which equilibrium is reached (1st derivative approaches 0) for the skin versus flange corresponding pixels. The cap shows the same cooling trend as the skin pixel, but with a lower cooling rate and slight shift in the plateau time: this could be due to geometrical effects of the cap that could draw heat propagation into the sides and add heat diffusion dynamics, delaying equilibrium. Even if the recording time was set to 120s, the TSR approach reduces the effective observable time, in particular as the degree of the derivative increases. Often the saturation time for thicker components (as the flange) cannot be observed or is affected by reconstruction errors.

Looking at the 2nd time derivative plots, the skin reaches a maximum at around 6s, almost 4 times earlier as the flange, agreeing with the saturation time relation with the depth L, given the same material diffusivity. Cooling trends differences are minimized to enhance the initiation or change in the diffusion

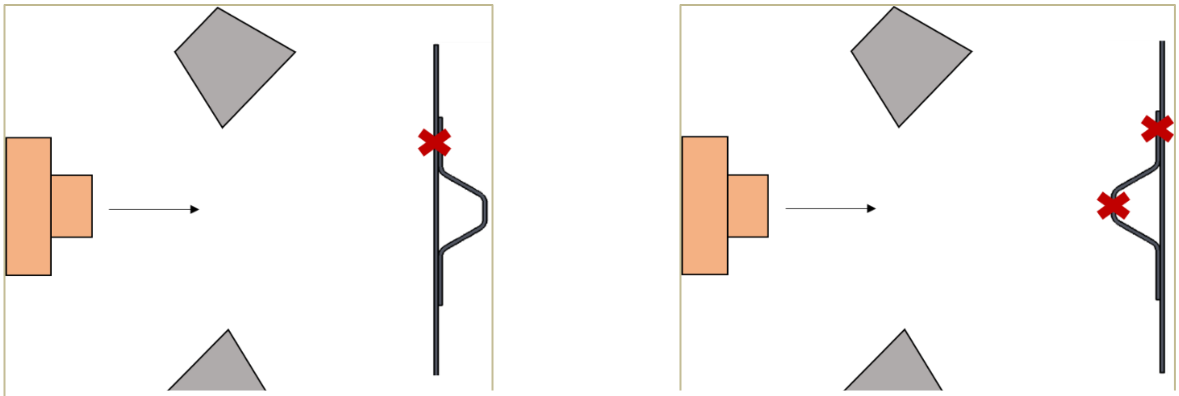

Figure 101 - Thermographic test on composite panels: skin side mode (left), stringer side mode (right)

events only. Defects can be appreciated as they show a unique signature, usually different from the other components, while being closer to the flange (for the flange impacts) since they are mainly affecting the latter.

Figure 102 shows a 90J impacted flange specimen, when inspected from the “skin side”: the top 2D plot shows the raw temperature, where only heat non uniformities in the excitation and surface emissivity differences can be noticed. In the 1st derivative 2D (central) plot, the flange shows as a darker region with respect to the skin, due to its more negative cooling rate driven by the doubled thickness. A skirt shaped damage can be recognized within the flange, with a larger edge on the exterior flange side, since the delamination involves the whole flange to skin bond, but extends more in-plane as it moves further away from the stiffener. The 2nd derivative 2D plot (bottom) reduces the differences in the diffusion process (uniform plot) and is shown at two instants: the earlier one enhances the localized skin defect while the later shows again the skirt shaped delamination and the increased severity further away from the stiffener.

Another test has been performed on the same flange impacted specimen, when inspecting the “stringer side” (Figure 103 and Figure 104): although such modality would not take place in an in-situ inspection, it can still be performed for NDE to have a full field subsurface defect map and to infer additional insights on defect formation.

The 1st derivative 2D plot, at early instants, still shows the geometrical features of the stringer, because of the different scattering from the edges and non-perpendicular surfaces; the different cooling trend can be already observed at the damage location. Flange and skin show different behavior as time evolves and the skirt shaped damage emerges, with the higher severity cooling dynamics around the impact location, due to the “stair” delamination mode. The 2nd derivative 2D plots enhance thickness differences (uniform skin-thick vs flange-thick components) and emphasize the 3D “trap and release” effect due to the localized secondary diffusion process. The top of the cap itself manifests a second cooling, due to the geometrical confinement of heat (Figure 104 top right) and the defect extending to the flange can be clearly located. Moreover, closer to the hat, the defect shows an opposite simultaneous trend, maybe due to the evolution of the delamination in multiple plies of different orientation. At later instants, the opposite trend is instead observed for locations closer to the hat with respect to further away from it: the trap and release effect occurs within the damage, probably due to the different levels (number and depth) of the plies involvement ("stair mode"). Both the 1st and 2nd derivatives show a high severity damage on the stringer flange that was not emerging in the "skin mode" inspection: the damage shows clear and localized, involving different plies within the flange, the disbond at the 16th ply emerges later, since it is deeper in the specimen and shows wider at the edges, merging with the skin.

As for a comparison of the severity of the damage due to a different impact energy, the 2nd derivative plots from the "stringer-side" inspection are reported (Figure 105). Slightly different instants have been chosen, as differences peak at slightly different times. The 70J case shows a less localized damaged, less plies involvement and smaller in-plane extent. The delamination is more contained within the flange itself and stays more superficial.

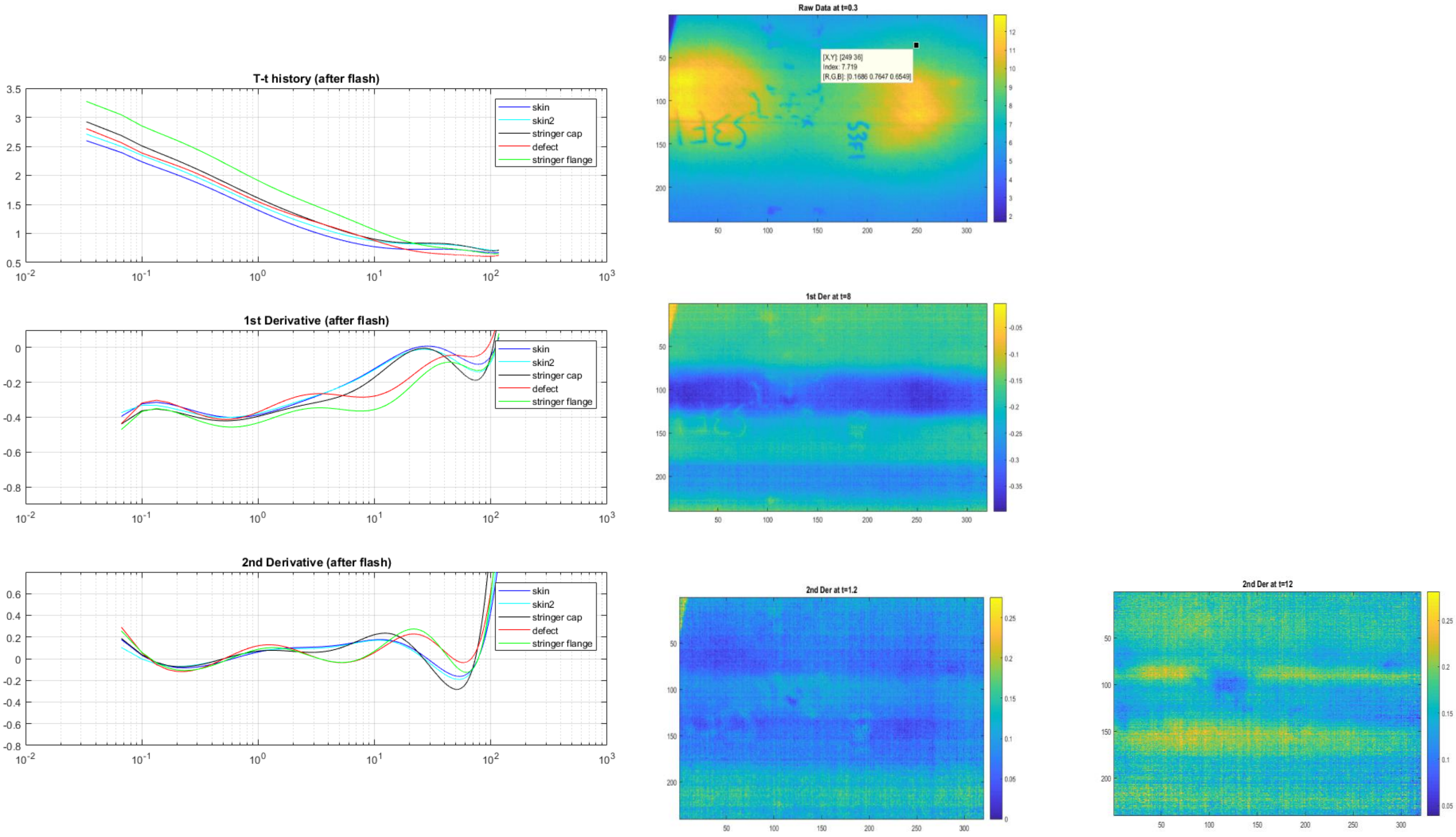

Figure 102 - TSR Thermogrpahy test: Flange 90J impact. 1D plots (left); 2D maps (right) raw Temperature (top), 1st derivative (center), 2nd derivative (bottom) at two time instants

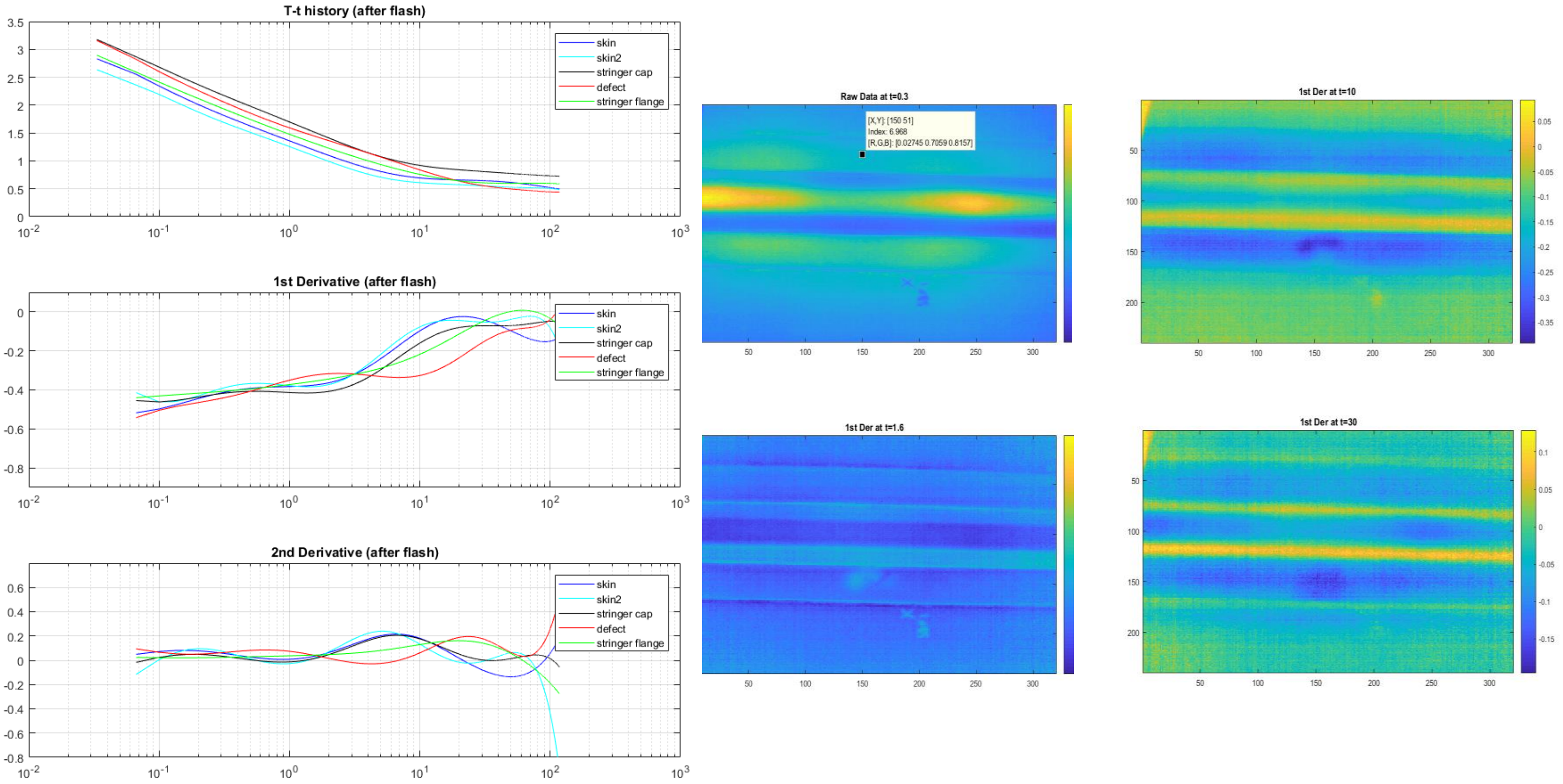

Figure 103 - TSR Thermogrpahy test: Flange 90J impact, "stringer side". 1D plots (left); 2D maps (right) raw Temperature (top left), 1st derivative early instant (bottom left), 1st derivative middle instant (top right), 1st derivative later instant (bottom right)

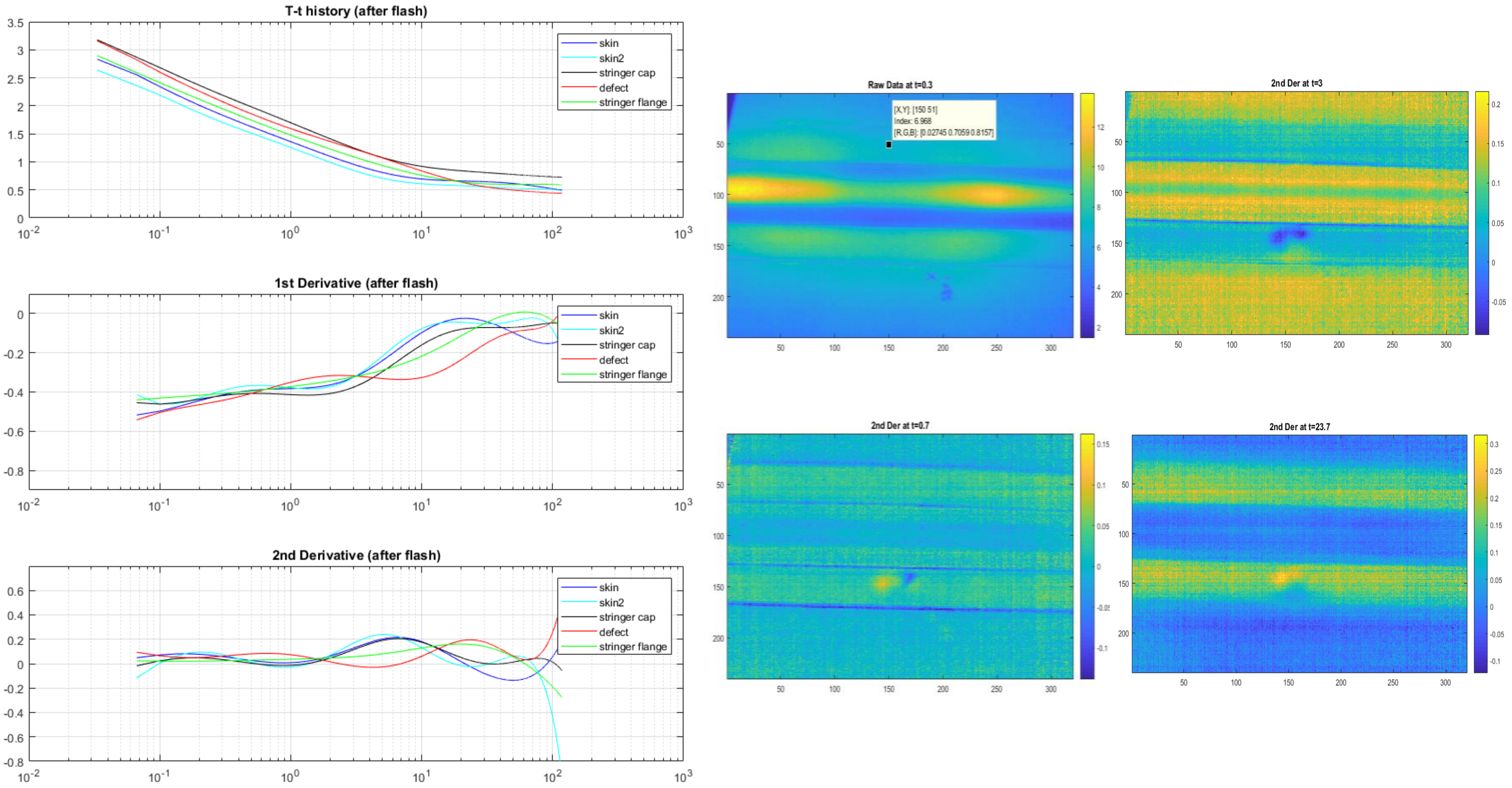

Figure 104 - TSR Thermogrpahy test: Flange 90J impact, "stringer side". 1D plots (left); 2D maps (right) raw Temperature (top left), 2nd derivative early instant (bottom left), 2nd derivative middle instant (top right), 2nd derivative later instant (bottom right)

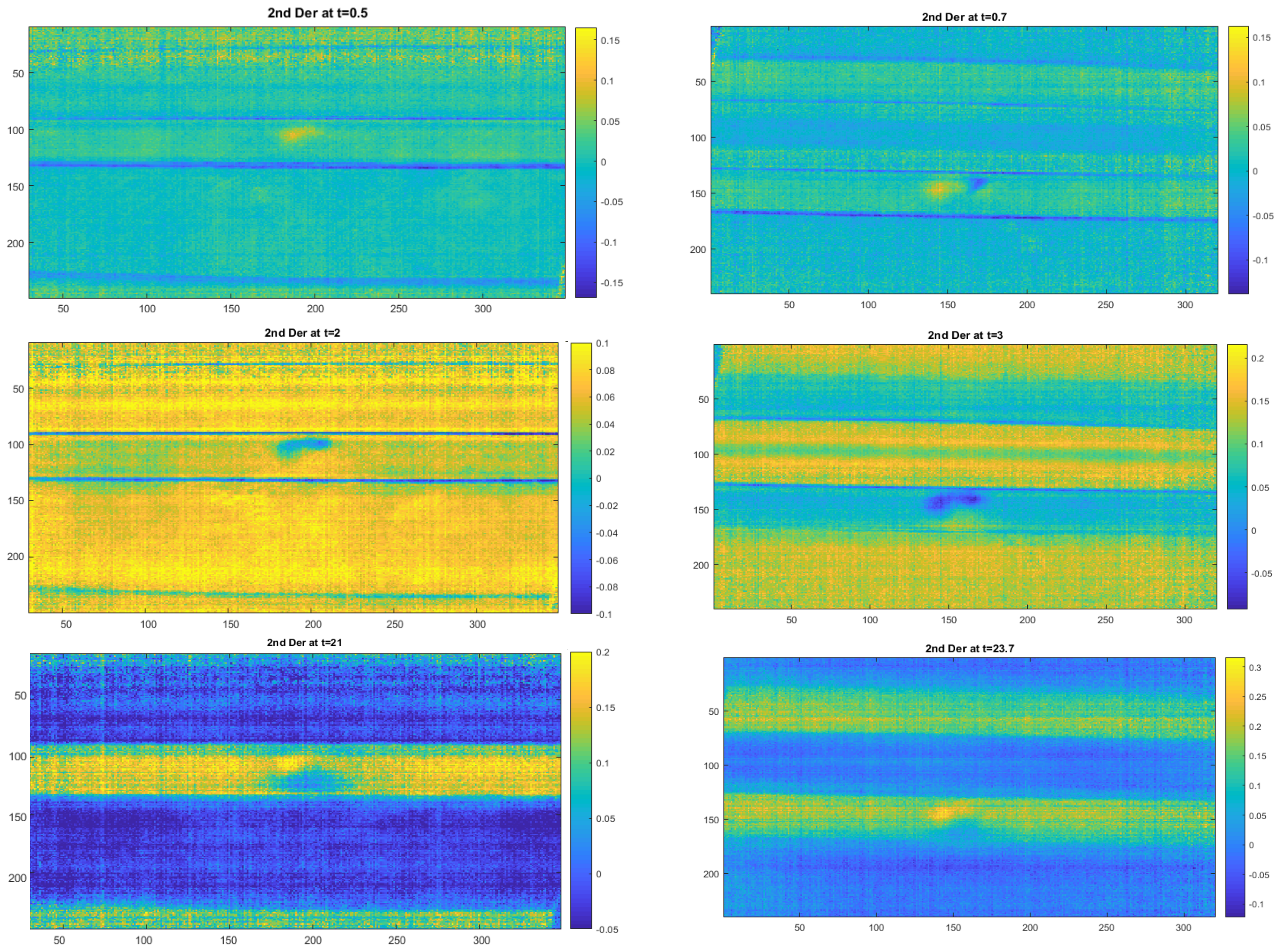

Figure 105 - TSR Thermogrpahy test comparison: Flange 70J (left) vs 90J (right) impact, "stringer side". 2D maps of 2nd derivative:early (top), middle (center), later (bottom) instants

Figure 106 and Figure 107 report the IR thermographic tests performed on the cap impacts, from the “stringer-side” inspection mode. As the 2D plots show, the TSR approach eliminates both the irregularities in the heat excitation and the surface emissivity (e.g. marks from the UT A-scan and writings). The 1st derivative allows the detection of the damage on the top of the stringer hat and the visualization of a superficial central type of defect and a deeper and wider delamination type of defect. The delamination on the top of the hat extends along the longitudinal dimension of the stringer, starting from a thinner central area, corresponding to the impact location. It looks like the laminate propagated the damage to the sides, opening up plies into multiple delaminations. The 2nd derivative 2D plots confirm this damage formation assumption, especially in the later instants, where a cross-shaped damage, involving multiple and deeper layers emerges very well. The earlier instants emphasize the more superficial damage and the diagonally opposite secondary cooling trend, suggesting a stair case damage mode progression, due to the lay-up.

The comparison among the 30J, 50J and 70J cap impact damages is shown in Figure 108. The 2nd derivative 2D maps enhance the defect initiation and progression thanks to the trap and release effect of this very localized damaged. The trend of the impact is exactly the same, demonstrating the same kind of defect, but the severity increases with the impact energy. In particular, the damage extends more along the cap and on the sides and local cracking increases (middle and bottom plots). At a very early time, the virtual heat source effect is very strong and it increases with the severity of the damage: the diagonal asymmetry confirms the augmented cracking and staircase damage progression.

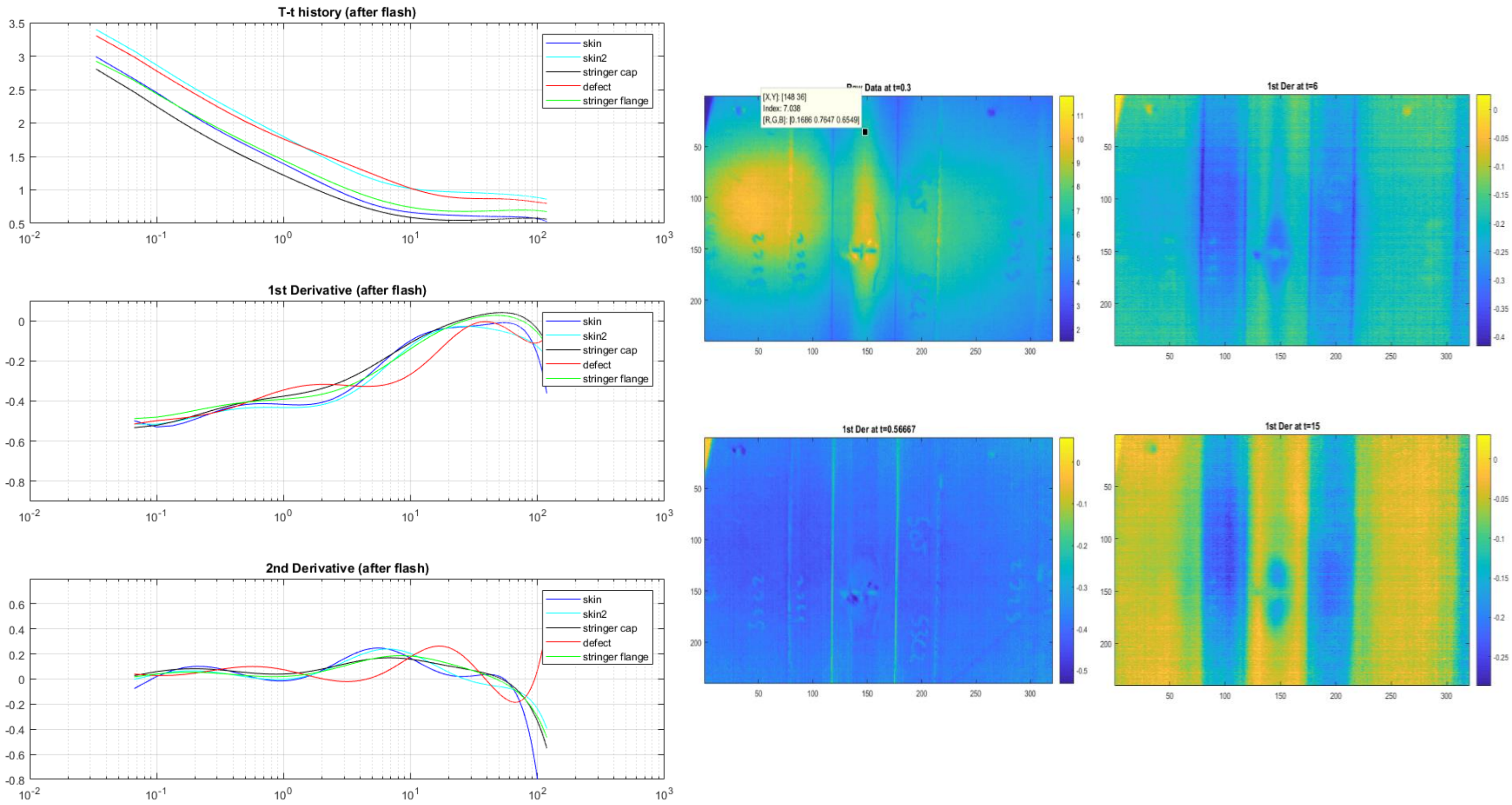

Figure 106 - TSR Thermogrpahy test: Cap 50J impact, "stringer side". 1D plots (left); 2D maps (right) raw Temperature (top left), 1st derivative early instant (bottom left), 1st derivative middle instant (top right), 1st derivative later instant (bottom right)

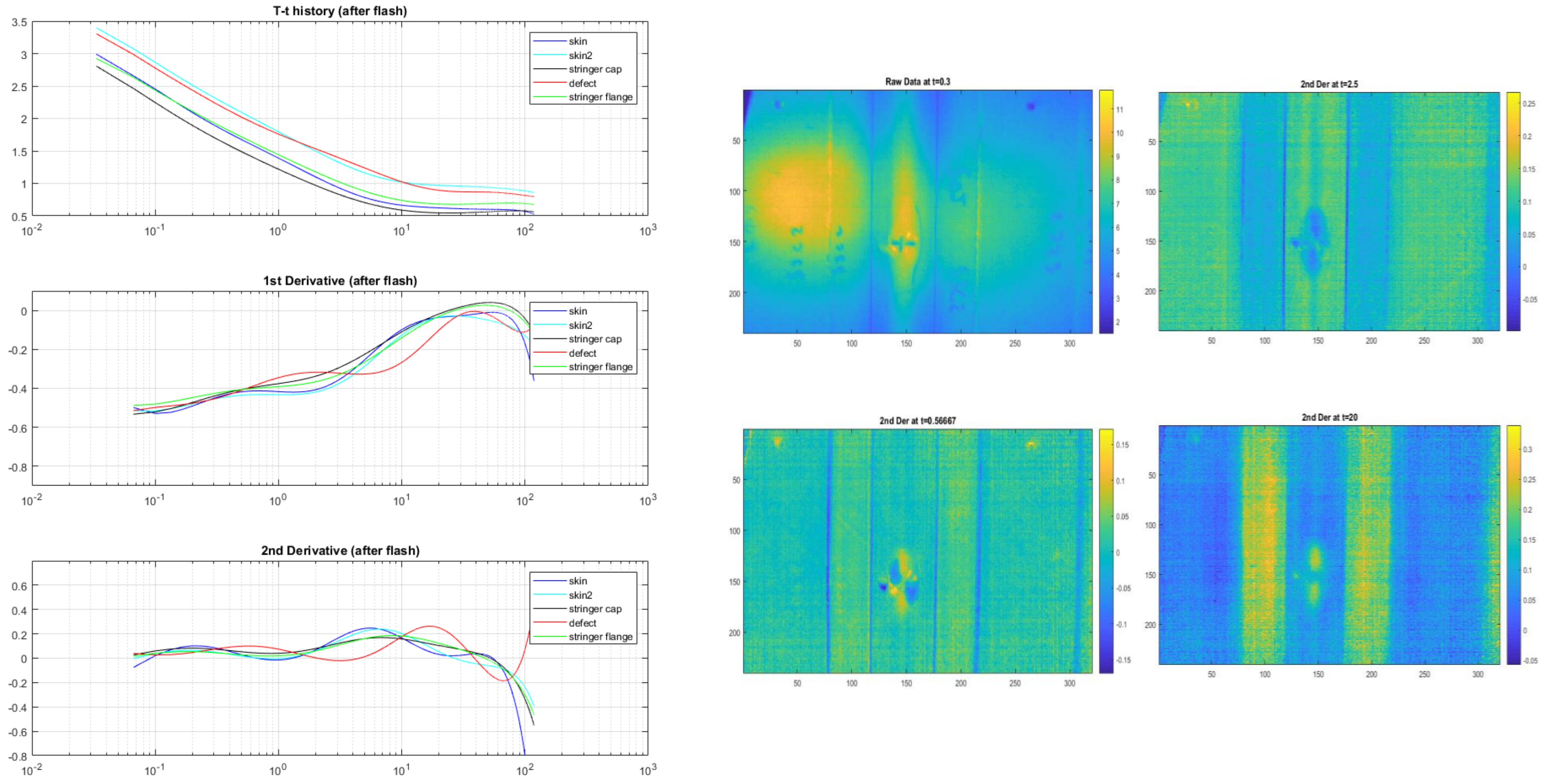

Figure 107 - TSR Thermogrpahy test: Cap 50J impact, "stringer side". 1D plots (left); 2D maps (right) raw Temperature (top left), 2nd derivative early instant (bottom left), 2nd derivative middle instant (top right), 2nd derivative later instant (bottom right)

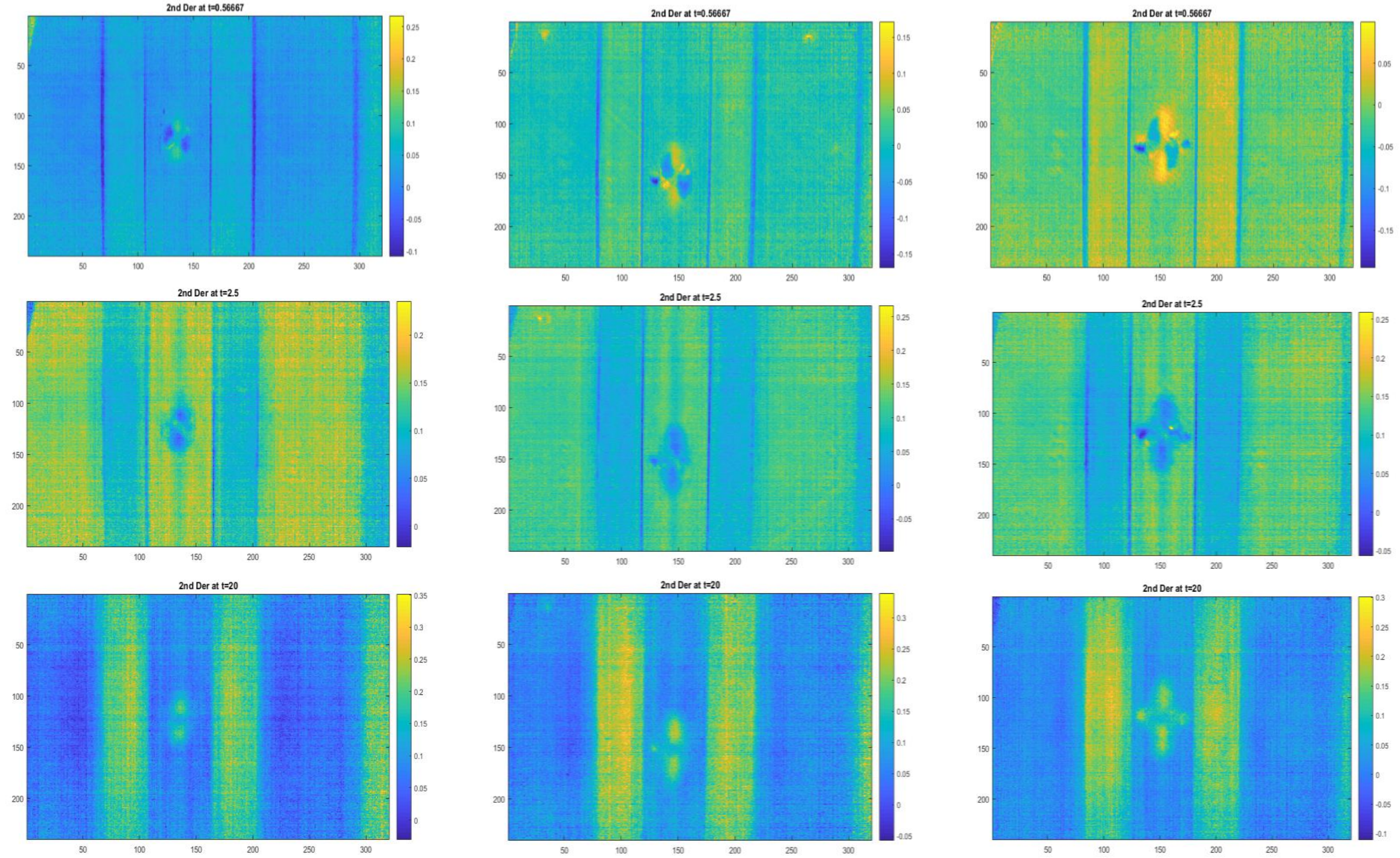

Figure 108 - TSR Thermogrpahy test comparison: Cap 30J (left) vs 50J (center) vs 70J (right) impact, "stringer side". 2D maps of 2nd derivative:early (top), middle (center), later (bottom) instants

ACKNOWLEDGEMENTS

Chapter 3, Section 3.4, in part, is currently being prepared for submission for publication of the material. Capriotti, Margherita; Ellison, Andrew; Kim, Hyungsuk E.; Lanza di Scalea, Francesco; Kim, Hyonny. The dissertation author was the primary investigator and author of this material.

Chapter 4

Comparison of UGW inspection of composite aerospace structures with UT and CT datasets

4.1 Introduction

The characterization of damage in structures is often a tradeoff between the complexity of the inspection set-up and the depth of penetration/resolution/sensitivity of the technique. The choice of the NDE approach to be employed is usually the result of a balance between several factors as difficulty and time of inspection, cost, accessibility, portability, performance and safety. Moreover, the desired level of inspection itself needs to be considered (i.e. damage detection only, damage localization, damage characterization, imaging, microscopic imaging). Hence, the different NDE techniques do not have to be exclusive, but can be employed at different stages and integrated to validate assumptions and offer additional information about the status of the specimen and/or damage.

UGWs inspection embodies advantageous traits offering simplicity of implementation and interpretation, wide-area coverage, low-cost together with a high probability of detection and acceptable resolution, in particular for the inspection of large aerospace structures. Moreover, the development of UGW techniques may be able to characterize not only the presence of damage but also distinguish the type and severity of the latter, while maintaining rapid deployment.

To this end, a comparative study of multiple levels of NDE fidelity has been conducted on impacted composite panels. The developed SIDO UGW scanning prototypes, both in their non-contact and hybrid approaches, have been compared to submerged C-scan ultrasonic testing (UT), X-ray Computed Tomography (CT) and IR Thermography. Specifically, the comparison may allow enhanced interpretation of the UGW results as: the distinction between cap versus flange impact damage, the detection of skin damage versus disbond as separate damage modes (for the flange impact type) and the detection of the severity of the delaminations (for the cap impact type). Also, the enabled interpretation of specific waveform features and their relation to specific damage types could be used to enhance and/or tailor the damage detection performance (i.e. improved feature extraction/selection to input in a MOA) and to improve the design of the tests (i.e. excitation/reception mode, most sensitive frequency-mode combination, scan resolution, scan penetration, etc.).

In particular, the UGWs results is being compared to the UT inspection for the Flange type damage and with the CT scans for the Cap type damage. The conclusions drawn for both damage types can be also compared to the discussion presented in Section 3.4 about the thermographic inspection.

4.2 UGW features sensitivity to impact damage modes

The same SIDO UGW prototype, presented in Section 2.3.4, was used to scan Panel A and Panel B, with the flange and cap type impact damages, respectively, in their entirety, to better simulate a real inspection scenario. UT and CT inspection have been performed in a later stage, after the panels were cut into single stringers. A more detailed scheme of the impacted panels is shown in Figure 109.

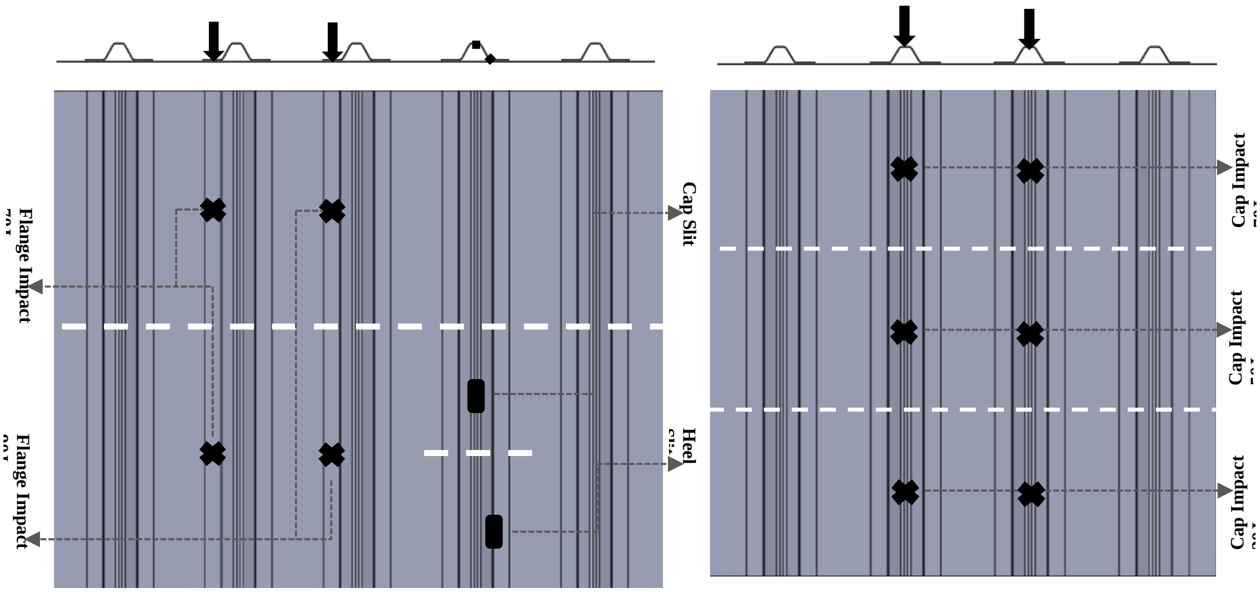

Figure 109 - Scheme of damaged panels: Panel A(left) and Panel B (right).

The collected waveforms have been gathered and organized in a database, according to their location along the longitudinal dimension of the stringer and centered around the impact location, so that they could be later compared with the other techniques. The waveforms have been gated as follows (Figure 110), prior feature extraction, for the hybrid (left) and non-contact (right) extracted transfer function:

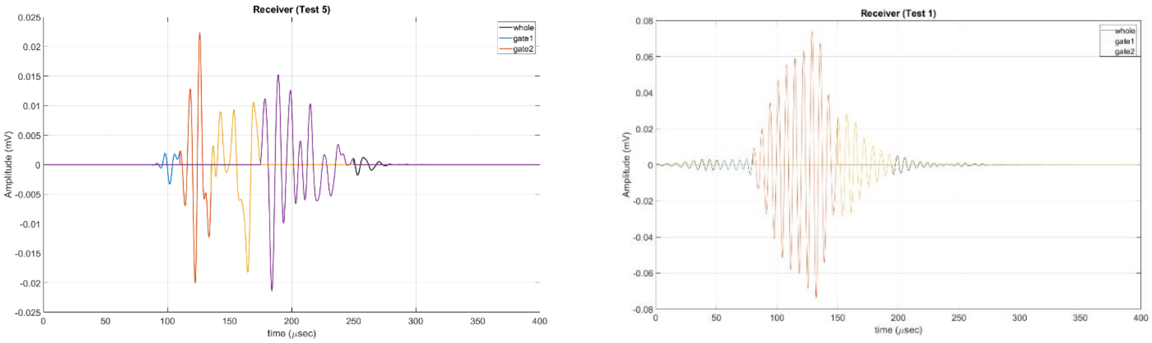

Figure 110 - TF extracted from UGW scan inspection on Panel A with gated wavemodes: hybrid (left) and non-contact (right) prototype.

The main A0 skin mode dominates the signal in both configurations and is plotted in red. The later portion of the signal, highlighted in yellow, contains higher order modes, either interacting with the flanges and travelling into the stringer. The coda of the signal, in purple, contains reflections from the boundaries and other stringers. The earlier mode, in blue, in the hybrid configuration could be the A1 mode, mostly due to the double thickness of the flanges.

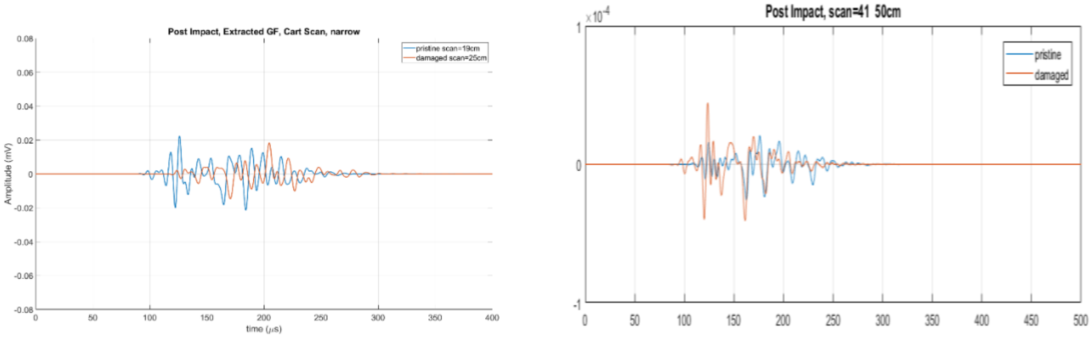

Figure 111 - Typical waveforms of pristine (blue) and defective (red) locations for flange damage (left) and cap damage (right).

From such waveforms and for each mode (or combination of modes), energy-based features (namely RMS, maximum value of the FFT, area under the FFT) and phase-based features (namely time of arrival of the maximum peak, dominant frequency, skewness) have been extracted, to capture the main differences caused by the wave interacting with the defects. Figure 111 (left) reports a representative transfer function waveform from a pristine location, in blue, versus a flange impacted one, in red. Figure 111 (right) is instead representative of a cap impact location. It can be noticed how the flange impact damage absorbs energy, mostly in the early modes, related to the skin and flange; for the cap impact instead, less energy penetrates the stringer, due to the presence of defects in the cap, and contributes to an amplitude increase (with respect to a pristine condition) in both the flange and skin anti-symmetric modes.

We report below the results for a representative case of flange impact, on Panel A, stringer 3: Figure 113, Figure 112, Figure 114, Figure 115 and Figure 116 plot the normalized features versus the location along the stringers in each plot. Each plot belongs to features extracted for different gates and combination of gates, from the earlier to the later modes within the waveform. The energy features have been plotted together since they qualitatively capture the same trend in the signal (red for RMS, green for the peak of FFT and yellow for the area under the FFT), while the skewness has been selected as the most representative phase-related feature (pink).

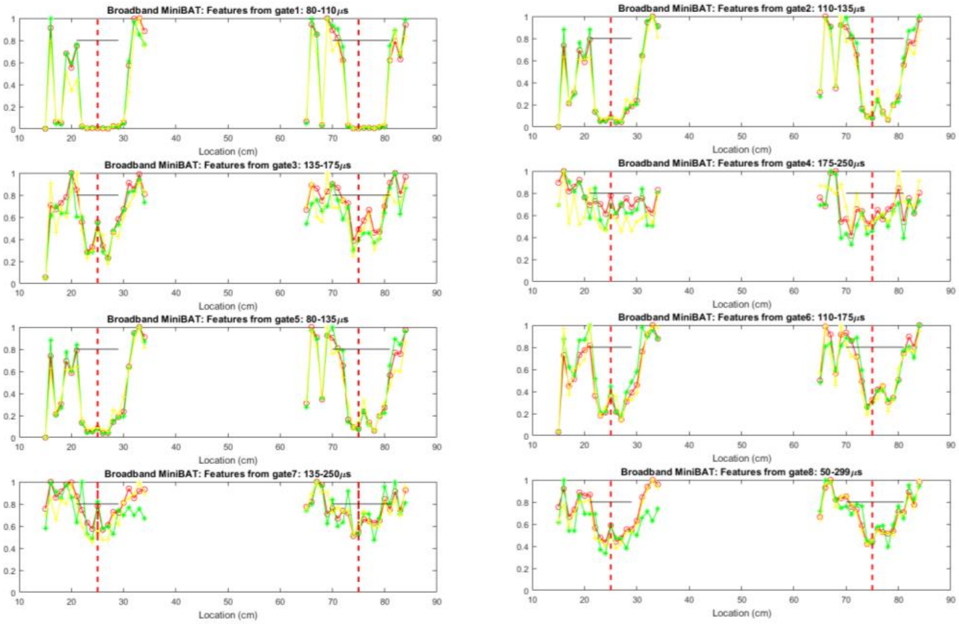

Figure 113 - Energy based features versus location for 90J flange impacted stringer, hybrid prototype: RMS (red), area under FFT (yellow), maximum peak in FFT (green). From top left to bottom right: gate1, gate2, gate3, gate4, gate1+gate2, gate2+gate3, gate3+gate4, entire signal.

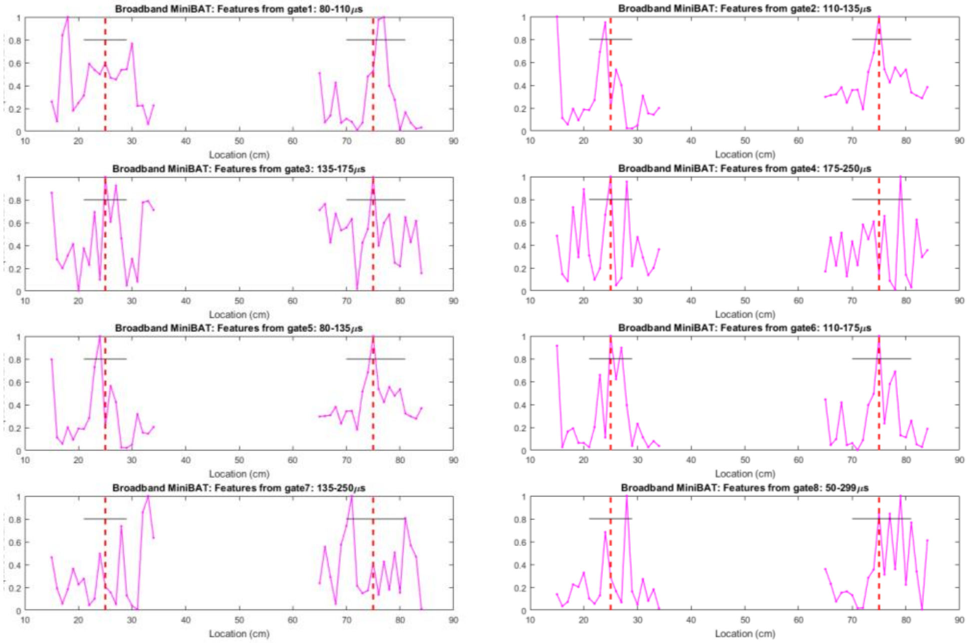

Figure 112 - Phase based features versus location for 90J flange impacted stringer, hybrid prototype: skewness (pink). From top left to bottom right: gate1, gate2, gate3, gate4, gate1+gate2, gate2+gate3, gate3+gate4, entire signal.

The energy-related plot confirm absorption for the entire extension of the damage, in particular for the first two modes (Figure 113). The third gate is also showing the same trend but with less sensitivity. The skewness instead peaks in correspondence of the center of the damage (Figure 112): the dispersion of the guided wave is mostly affected in the earlier modes and where the defect is highly altering the overall thickness of the specimen. Moreover, the severity of damage can be inferred from a quantitative analysis of the features. Figure 114 shows the results from the non-contact scanning prototype: the left plot reports the 90J flange impact, where up to 60-80% of the energy of the dominating wavemode is absorbed. For the 70J flange impact, on the right, the energy is absorbed up to 50-70%.

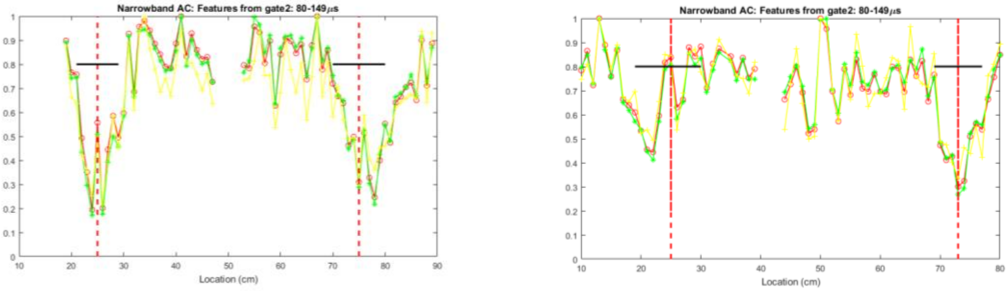

Figure 114 - Energy based features extracted from 90J (left) and 70J (right) flange impacted stringer, non-contact prototype.

For the cap impact on Panel B, stringer 3, hybrid scanning prototype, again the first wavemodes capture the presence of the damage, the A0 in particular, being the most highly penetrating mode. In this damage type though, the energy transmission is enhanced by the defect, with respect to the pristine condition (Figure 115).

The skewness is less robust in detecting the center of the impact (Figure 116): this could be due to the dispersion effect being less accentuated when the defect is deeper in the structure or when this kind of damage does not really cause a thickness change within the skin and flange, hence is not dramatically affecting the velocity of the wave and the presence of early higher order modes.

The above considerations, both in the energy and dispersion content, can help distinguish the damage type.

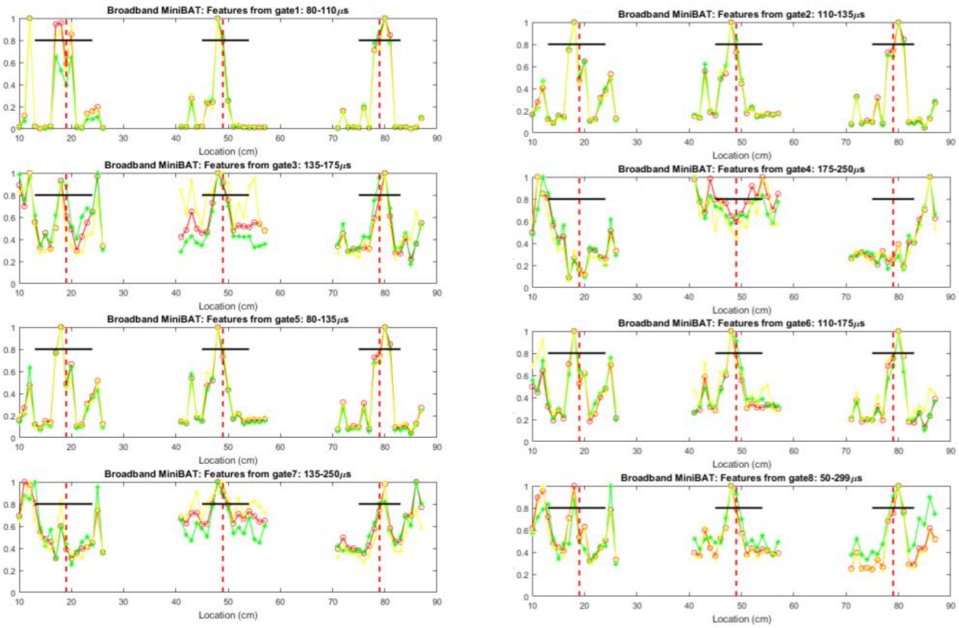

Figure 115 - Energy based features versus location for cap impacted stringer, hybrid prototype: RMS (red), area under FFT (yellow), maximum peak in FFT (green). From top left to bottom right: gate1, gate2, gate3, gate4, gate1+gate2, gate2+gate3, gate3+gate4, entire signal.

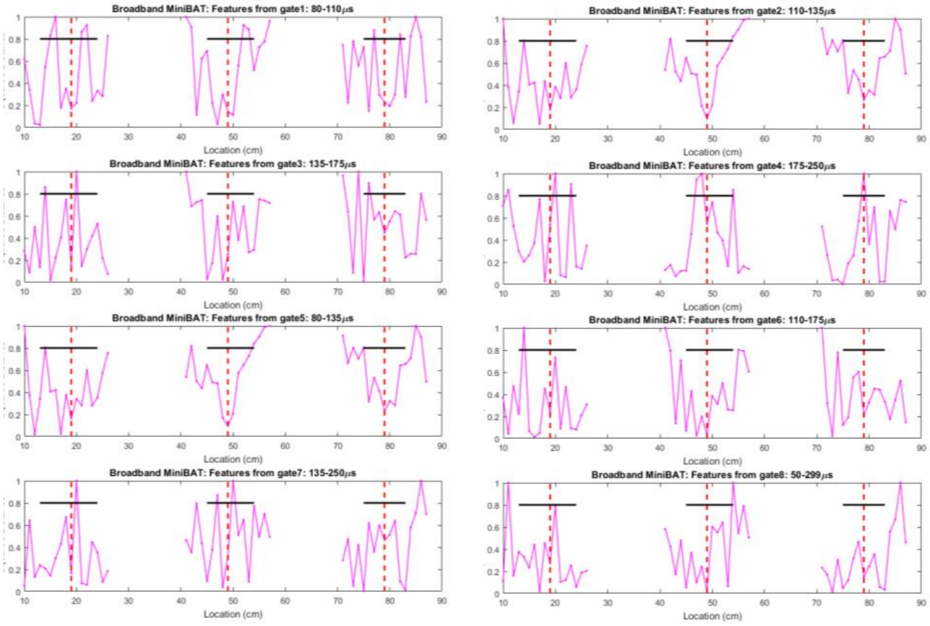

Figure 116 - Phase based features versus location for cap impacted stringer, hybrid prototype: Skewness (pink). From top left to bottom right: gate1, gate2, gate3, gate4, gate1+gate2, gate2+gate3, gate3+gate4, entire signal.

4.3 Correlation for quantitative damage characterization

To quantitatively capture and differentiate damage severity, type and mode (skin damage versus disbond versus crack/delamination dominated mode) and move beyond damage detection with UGWs, a correlation analysis has been implemented. The damaged locations have been inspected with higher resolution techniques that provided the "ground truth" of the defect, in terms of depth, lateral extension, number and level of plies involved. This information has been quantified at every cm, to be compared to the UGW scans. The flange type damages have been compared with the UT scans, where four damage modes have been identified (Figure 118): skin damage (red), disbond (green), flange (blue) and undamaged (white).

A normalized cross-correlation has been performed and the maximum value within 3cm around the impact center is extracted for all the features and wavemodes, to capture their sensitivity to specific damage modes. A positive correlation of the feature with the defect mode establishes an enhanced transmission, while a negative correlation shows absorption due to the defect; vice versa with respect to the undamaged mode. Also, the lag value can be used to provide information about misalignment in the cart inspection, skewness of the wave propagation and/or beam spreading effects.

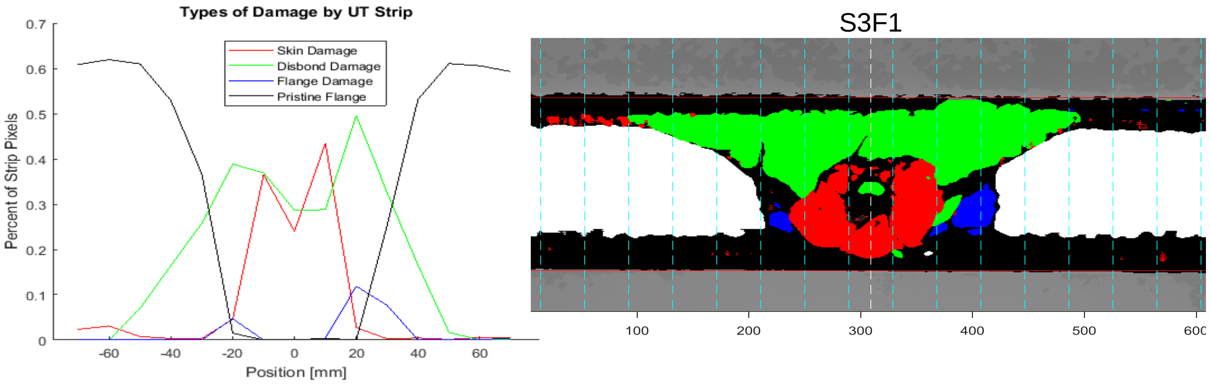

Figure 118 - UT on 90J flange impact damage: extracted pixel count (left), time of flight segmented map (right) versus location. Skin damage (red), disbond (green), flange damage (blue), undamaged flange (white), undamaged skin (black).

For the sake of brevity, representative results are shown in Figure 117, for the 90J flange impact, reporting the highest correlations extracted for each damage mode:

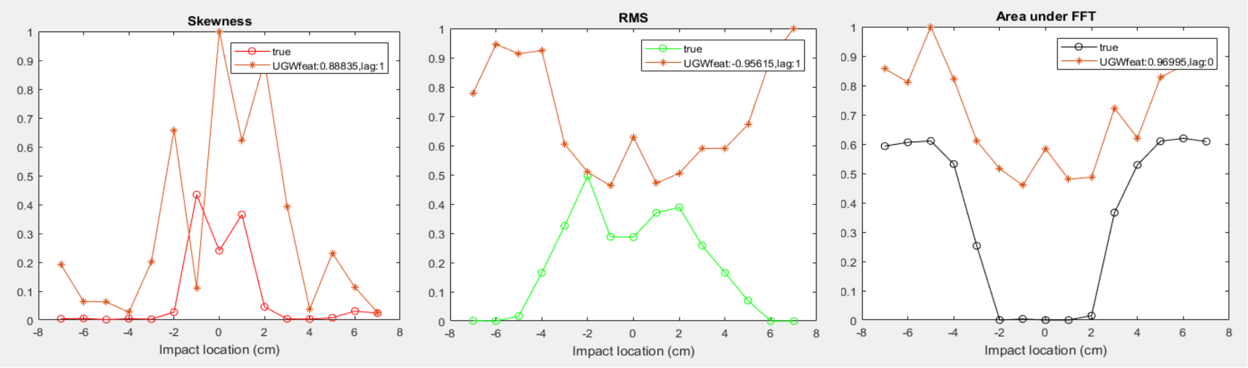

Figure 117 - Correlation analyses between UGW extracted feature (red) and UT extracted feature: skin damage (left), disbond (center) and undamaged flange (right).

The skin damage correlates best with the skewness, extracted from the sixth gate. This confirms the effect of the change in thickness and most superficial skin alteration to the dispersion of the wave. The disbond is best captured by the RMS of the entire waveform: the damage affects multiple modes and components, and confirms the absorption cause by the disbond since the correlation is negative. The area under the FFT for the central and later part of the signal correlates up to 0.97 with the undamaged shape. This means that the extension of the damage manifests itself in the waveform, both in the energy and frequency content, and can be captured and estimated. Moreover, the feature extracted from most of the gates correlate negatively with the disbond, while they correlate positively with the undamaged, confirming the energy absorption behavior.

These results quantitatively provide information about the damage, enabling damage characterization with UGW, and suggest the most sensitive features and gates to select in the previous mentioned MOA, to obtain the best performance in the detection of specific damage modes and improve the ROC curves.

Finally, the three flange damage modes, detected with the UT and UGW techniques, confirm the IR thermography results, where skin, disbond and flange related delaminations where manifesting at different instants, hence involving differently oriented plies and at different depths.

Ongoing and future work will confirm the above- mentioned conclusions on several specimen and damage cases, and will provide more details about the extent and morphology of the damage from the UT and CT data and correlation analyses with UGW and IR thermography.

ACKNOWLEDGEMENTS

Chapter 4, in full, is currently being prepared for submission for publication of the material. Capriotti, Margherita; Ellison, Andrew; Kim, Hyungsuk E.; Lanza di Scalea, Francesco; Kim, Hyonny. The dissertation author was the primary investigator and author of this material.

Chapter 5

Overall Conclusions and Future Recommendations

In this dissertation, two major NDE techniques have been discussed: elastic ultrasonic waves, particularly ultrasonic guided waves (UGWs), and Infrared Thermography, where heat diffusion is used in its interpretation as thermal waves. Both UGWs and IR Thermography have been applied to large composite aerospace panels representative of modern commercial aircraft construction.

The theoretical investigation of the techniques provided a better understanding of the effect of material properties and geometry on the wave propagation and enabled wave manipulation and exploitation of specific features, depending on the wave interaction with the structural defects of interest in stiffened composite aircraft panels.

The numerical analyses aimed at the modeling of relevant case studies, as plate-like geometries and multi-layered materials, in a pristine and defective status. The numerical results provided an accurate and efficient tool to aid the design of experimental inspection strategy, as well as to interpret the recorded data.

Different experimental set-ups have been experimentally tested and iterated on representative aircraft composite panels in the laboratory.

5.2 Elastic wave techniques

This dissertation has addressed the problem of scattering of multimode and dispersive elastic UGWs. Among other applications, this topic is of great interest to ultrasonic guided-wave NDT or SHM of structural components where defects are detected by recording transmission or reflection scattering of a generated incoming wave mode. Predictions of these scattering patterns for a given defect can allow to select optimum mode-frequency combinations for the incoming mode, and/or to identify the type of defect being detected by a specific scattering observation.

For general cases that are complex in terms of either geometry or material properties (or both), this problem requires a numerical solution.

A unified Global – Local (GL) approach has been presented here, exploiting the computational efficiency of the Semi-Analytical Finite Element (SAFE) technique for a cross-sectional discretization of the "global" portion, coupled with a full Finite Element discretization of the "local" portion containing the scatterer. Compared to previous GL studies, this contribution adds: (a) a general and consistent formulation for the evaluation of the nodal tractions at the global-local boundaries; (b) the implementation of a robust mode tracking control, based on B-orthogonality, for the automatic selection of incoming and scattered modes; (c) the possibility to model a wide frequency range also including higher-order modes; (d) the automatic inclusion of an energy balance check in the results; and (e) the unification of SAFE and FE in a stand-alone numerical Matlab code that is readily extendable to more general cases (e.g. independent treatment of the two global regions, explicitly given theoretical formulation such as consistent nodal forces at the boundaries, or extension to 3D cases).

The proposed GL algorithm was applied to a composite skin-to-stringer assembly typical of commercial aircraft construction. Various relevant defects were modelled, and scattering spectra were obtained for guided-wave frequencies as high as 500 kHz under incoming flexural (A0-type) or axial (S0-type) modes that are typically employed as excitations in guided-wave testing of these components. The results reveal quite interesting transmission spectra, same-mode or mode converted, that are peculiar to each of the defects considered. These predictions can be extremely useful to guide and interpret guided-wave inspection tests conducted on these components. The case study considered was a 2D (plain strain) analysis that is quite applicable to a scanning-type guided-wave system of the type utilized by Capriotti et al. (2017). An extension to a 3D scattering case for internal flaws in railroad tracks using this algorithm has also been studied by the authors. High group velocity and excitable modes were chosen as incoming modes to probe a pristine and defective model of track. Results have been presented in terms of energy scattered from transverse head defects of different sizes. Mesh refinement, local region length and number of modes included in the analysis have also been considered.

The results shown for the skin-to-stringer case study and railroad tracks only apply to the specific geometry and material properties considered. However, the cross-sectional mode shapes mostly control the partition of energy between the incoming mode and the scattered modes. Consequently, some scalability of the results to components of different thicknesses can be qualitatively predicted on the basis of the well-known invariance of the guided-wave cross-sectional mode shapes with the <frequency × thickness> product (Rose 2014). In other words, for the same mode shape to be generated, frequency and thickness must be inversely proportional. As a result, for example, specific frequency values of interest in the scattering spectra predicted for a given thickness of the skin could be scaled to a different skin thickness, provided that the <frequency × thickness> product is the same. The model has considered elastic waves with no viscoelastic damping. Damping could be included by considering complex stiffness matrices in the analysis resulting in complex wavenumbers as discussed, for example, by Bartoli et al. (2006). A forced solution, that includes the reproduction of typical experimental excitation and reception set-ups (distances, narrow/broadband signals, area of influence of the sensor) and time-domain responses has also been implemented and is currently being studied for a variety of geometries, damage types and applications.

This research proposes a rapid NDE technique for the detection of structural defects in composite aircraft structures subjected to ground service equipment (GSE) impacts. The approach taken utilizes the waveguide geometry of the structure by means of ultrasonic guided waves. Two laboratory prototypes for line scanning were developed, one using contact PZT transducers with a differential approach and one using non-contact (air-coupled) transducers in a pitch–catch approach. The inspection utilizes a statistical outlier analysis that compensates each measurement for the normal (baseline) variation during a scan, thereby increasing the POD (true detections) and decreasing the PFA (false positive). Tests conducted on previously impacted test panels representative of commercial aircraft construction indicated an excellent detection performance (in terms of POD vs. PFA tradeoffs) for skin and stringer defects. A perfect detection for these defects was actually obtained by the non-contact system once both skin wave modes and stringer wave modes were combined in the statistical feature vector.

The defects tested in this study were limited to the panel skin and stringers. Defects located in the deeper structure, specifically shear ties and C-frames, were not targeted, because the frequencies used were found to be too high to penetrate these regions. Ongoing work is aimed at testing lower UGW frequencies in an effort to penetrate into the C-frames to provide comprehensive coverage of the structure.

A transfer function approach for ultrasonic guided-wave testing is also presented for damage detection purposes. The method is based on a single-input-dual-output (SIDO) scheme that minimizes the effects of the transducers' response and the transducers-to-structure coupling effects compared to a traditional single-input-single-output (SISO) guided-wave testing. For example, the SIDO method enables the use of excitation sources with unknown spectra (e.g. non-instrumented impactors). By utilizing a deconvolution operation, the SIDO approach additionally brings out the coherent wave paths between the two receivers and minimizes the incoherent contributions. These performances are particularly relevant to scanning systems where the acoustic transduction can be variable.

This method, combined with a statistical Outlier Analysis, was utilized to design two scanning systems applied to the rapid inspection of representative composite aircraft panels subjected to various types of impact-caused damage. The two systems explore, respectively, the narrow/high frequency range (~110-210 kHz) offered by non-contact air-coupled piezocomposite transducers and the broad/low frequency range (~ 40-270 kHz) offered by the combination of an ultralight impactor and air-coupled capacitive transducers. The results show how stringer flange impacts affect the skin and the skin-to-stringer interface, generally producing a decrease in wave transmission strength that is detectable by the high frequency wave content excited by both the air-coupled system and the hybrid system. Stringer cap impacts, instead, generally produce an increase in wave transmission strength (through decreased acoustic leakage) that mostly affects the low frequency and high magnitude wave content that are excited by the hybrid system.

The prototypes discussed here are early-stage laboratory systems that do not include automatic data processing of the scan. Ongoing work is aimed at adding an encoder to track the position of the inspection head, implementing automatic signal processing to generate the scan output in quasi-real time and automating the mini impactor excitation modality for the hybrid prototype.

Follow-up work should be devoted to more detailed analyses on the ultrasonic wave interaction with each of these defects. For the impact locations, this will require knowledge of the precise extent and morphology of the damage that will be obtained from X-ray computed tomography and/or ultrasonic C-scan of the test panels. This future study will also refine the selection of damage-sensitive features and of the time gates imposed on the reconstructed transfer function for the Outlier Analysis scans.

5.3 Thermal wave techniques

Heat propagation as a diffusion phenomenon has been investigated in terms of thermal wave propagation. The solution proposed here is the formulation of the thermal field (Temperature) by the use of Green's functions. The method has been chosen to exploit the analogies and dissimilarities with travelling elastic waves, so as to visualize the defects as secondary heat sources and to manipulate the equations in frequency domain, using convolution and correlation theorems, similarly to what done with elastic waves

The passive retrieval of a thermal Green's function by cross-correlation of diffuse fields has been demonstrated theoretically. Although the feasibility is supported by the theoretical formulation and the experimental availability of a large database of temperature time histories, output by infrared 2D detectors, hardware limitations prevented the extraction of a thermal transfer function. The validity of the theoretical idea also needs to be further investigated in terms of scale, specifically distances between the Green's function path, magnitude of the temperature fluctuations, time duration of the diffusion and frequency of the oscillations. Enormous differences arise when observing heat diffusion at the macroscale, as the thermal field recorded by a thermocamera, and at the nanoscale, where atomic vibrations and interactions govern the heat transport.

Such limitations, also characterized by the lack of time invariance in the diffusion process, suggested the exploitation of spatial symmetries. Numerical studies have been performed on plate-like structures for metals of different diffusivities. The interaction of heat with the defects and the alteration of the heat flow has been captured with the use of spatial derivatives. The method enhances the detection of discontinuities and can be interpreted as the visualization of the heat trapped/shadowed by the defect. The implementation of such method in time could also provide the extraction of a heat propagation speed, related to the diffusivity, offering quantitative structural characterization by IR thermographic measurements, and could be experimentally applied following the grid method (Grediac et al., 2016). Further numerical and experimental studies have been started in this direction.

Finally, the Thermographic Signal Reconstruction (TSR) method combined to the virtual heat source concept have been applied to composite aerospace structures, with different damage type. The technique allowed the elimination of surface emissivity and heating non-uniformities and enhanced the detection and distinction of skin damage, disbond, flange and cap damage. The time derivatives enable quantitative defect detection, in terms of depth, type and orientation of the involved plies. This information is being currently validated through the comparison with UT and CT scans.

REFERENCES

Ahmad, Z. A. B., Vivar-Perez, J. M., Gabbert, U., 2013. Semi-analytical finite element method for modeling of lamb wave propagation. *CEAS Aeronautical Journal*, *4*(1), 21-33.

Alleyne, D.; Cawley, P., 1992. The interaction of Lamb waves with defects. *IEEE Trans. Ultrason. Ferroelectr. Freq. Control*, 39, 381–397.

Alleyne, D.N. and Cawley, P., 1990, December. A 2-dimensional Fourier transform method for the quantitative measurement of Lamb modes. In *Ultrasonics Symposium*, 1990. Proceedings., IEEE 1990 (pp. 1143-1146). IEEE.

Almond, D.P. and Lau, S.K., 1994. Defect sizing by transient thermography. I. An analytical treatment. *Journal of Physics* D: Applied Physics, 27(5), p.1063.

Al-Nassar, Y. N., Datta, S. K., Shah, A. H., 1991. Scattering of Lamb waves by a normal rectangular strip weldment. *Ultrasonics*, *29*(2), 125-132.

Ashby, M.F. and Cebon, D., 1993. Materials selection in mechanical design. *Le Journal de Physique* IV, 3(C7), pp.C7-1.

Baleagas, D., Deom, A., Boscher, D., Gardette, G., 1987. NDT of carbon-epoxy composites by a pulsed photothermal method and transposition to stimulated infrared thermography. Qualite Revue Pratique de Controle Industriel, No. 147, pp. 58–63.

Banerjee S, Ricci F, Monaco E, Lecce L and Mal AK (2007) Autonomous impact damage monitoring in stiffened composite panel. *Journal of Intelligent Material Systems and Structures* 18(6): 623-633.

Barnett V and Lewis T (1994) *Outliers in Statistical Data*. New York, Wiley.

Bartoli, I., Lanza di Scalea, F., Fateh, M., Viola, E., 2005. Modeling guided wave propagation with application to the long range defect detection in railroad tracks. *NDT&E International*, 38, 325-334.

Bartoli, I., Marzani, A., di Scalea, F. L., Viola, E., 2006. Modeling wave propagation in damped waveguides of arbitrary cross-section. *Journal of Sound and Vibration*, *295*(3-5), 685-707.

Bartoli, I., 2007. Structural health monitoring by ultrasonic guided waves. PhD dissertation, UC San Diego, CA, USA.

Broggini, F. and Snieder, R., 2012. Connection of scattering principles: A visual and mathematical tour. *European Journal of Physics*, 33(3), p.593.

Callen, H.B. and Welton, T.A., 1951. Irreversibility and generalized noise. *Physical Review*, 83(1), p.34.

Callen, H.B. and Greene, R.F., 1952. On a theorem of irreversible thermodynamics. *Physical Review*, 86(5), p.702.

Caprino, G., 1983. On the prediction of residual strength for notched laminates. *Journal of Materials Science*, 18(8), pp.2269-2273.

Capriotti, M., Kim, H. E., Lanza di Scalea, F., Kim, H., 2017. Non-Destructive inspection of impact damage in composite aircraft panels by ultrasonic guided waves and statistical processing. *Materials*, *10*(6), 1-12.

Carslaw, H.S. and Jaeger, J.C., 1959. Conduction of heat in solids. Oxford: Clarendon Press, 1959, 2nd ed.

Castaings, M., Le Clezio, E., Hosten, B., 2002. Modal decomposition method for modeling the interaction of Lamb waves with cracks. *The Journal of the Acoustical Society of America*, *112*(6), 2567-2582.

Cawley P., The rapid non-destructive inspection of large composite structures. *Composites* 1994, Volume 25, 351-357.

Chang, Z., Mal, A. K., 1995. A global-local method for wave propagation across a lap joint. *ASME Applied Mechanics Division Publications AMD, 204,* 1-1.

Chang, Z., Mal, A.,1999. Scattering of Lamb waves from a rivet hole with edge cracks. *Mechanics of materials*, *31*(3), 197-204.

Chong SY, Victor JJ and Todd MD (2017) Full-field ultrasonic inspection for a composite sandwich plate skin-core debonding detection using laser-based ultrasonics. In: *Health Monitoring of Structural and Biological Systems 2017*, Portland, US, 10170, 1017007. International Society for Optics and Photonics.

Cole, K.D., Beck, J.V., Haji-Sheikh, A. and Litkouhi, B., 2010. Heat conduction using Green's functions. Taylor & Francis.

Croxford A, Wilcox P, Drinkwater B and Konstandtinidis G (2007) Strategies for guided-wave structural health monitoring. In: *Proceedings of the Royal Society of London A: Mathematical, Physical and Engineering Sciences*, 463(2087), 2961-2981. The Royal Society.

Datta, S. K., Ju, T. H., Shah, A. H., 1992. Scattering of an impact wave by a crack in a composite plate. *Journal of Applied Mechanics*, *59*(3), 596-603.

Datta, S. K., Shah, A. H., Bratton, R. L., Chakraborty, T., 1988. Wave propagation in laminated composite plates. *The Journal of the Acoustical Society of America*, *83*(6), 2020-2026.

DeFrancisci, G.K., 2013. High Energy Wide Area Blunt Impact on Composite Aircraft Structures. Ph.D. Dissertation, Advanced Composites and Aerospace Laboratory, University of California, San Diego, CA, USA.

di Scalea, F.L. and McNamara, J., 2004. Measuring high-frequency wave propagation in railroad tracks by joint time–frequency analysis. *Journal of Sound and Vibration*, 273(3), pp.637-651.

di Scalea, F.L., Bonomo, M. and Tuzzeo, D., 2001. Ultrasonic guided wave inspection of bonded lap joints: noncontact method and photoelastic visualization. *Research in Nondestructive Evaluation*, 13(3), pp.153-171.

Dong, S.B., Goetschel, D.B., 1982. Edge effects in laminated composite plates. *Journal of Applied Mechanics*, 49, 129-135.

Duroux A, Sabra KG, Ayers J and Ruzzene M (2010) Extracting guided waves from cross-correlations of elastic diffuse fields: Applications to remote structural health monitoring. *Journal of the Acoustical*

Society of America, 127(1), 204–215.

Farrar CR and James GH (1997) System identification from ambient vibration measurements on a bridge. *Journal of Sound and Vibration*, 205(1), 1–18.

Favro, L.D., Han, X., Ouyang, Z., Sun, G., Sui, H. and Thomas, R.L., 2000. Infrared imaging of defects heated by a sonic pulse. Review of scientific instruments, 71(6), pp.2418-2421.

Favro, L.D., Jin, H.J., Wang, Y.X., Ahmed, T., Wang, X., Kuo, P.K. and Thomas, R.L., 1992. IR thermal wave tomographic studies of structural composites. In Review of Progress in Quantitative Nondestructive Evaluation (pp. 447-451). Springer, Boston, MA.

Federal Aviation Administration, Composite Aircraft Structure, *Advisory Circular*, 2009, No: 20-107(B).

Galán, J. M., Abascal, R., 2002. Numerical simulation of Lamb wave scattering in semi‐ infinite plates. *International Journal for Numerical Methods in Engineering*, *53*(5), 1145-1173.

Galán, J. M., Abascal, R., 2005. Boundary element solution for the bidimensional scattering of guided waves in laminated plates. *Computers & structures*, *83*(10-11), 740-757.

Gershenson, M., US Secretary of Navy, 2000. Synthetic aperture processing for diffusion-equation-based target detection. U.S. Patent 6,147,636.

Gholizadeh S., A review of non-destructive testing methods of composite materials, *Procedia Structural Integrity*, 2016, Volume 1, 50-57.

Giurgiutiu V (2015) *Structural Health Monitoring of Aerospace Composites*, Elsevier Science.

Giurgiutiu V., Piezoelectric wafer active sensors for structural health monitoring of composites structures using tuned guided waves. *Journal of Engineering Materials and Technology* 2011, Volume 133, 0410121-0410126.

Giurgiutiu V., Soutis C., Enhanced composites integrity through structural health monitoring, Applied *Composite Materials* 2012, Volume 19, 813-829.

Goetschel, D. B., Dong, S. B., Muki, R., 1982. A global local finite element analysis of axisymmetric scattering of elastic waves. *Journal of Applied Mechanics*, *49*(4), 816-820.

Grediac, M., Sur, F., & Blaysat, B. (2016). The Grid Method for In‐ plane Displacement and Strain Measurement: A Review and Analysis. Strain, 52(3), 205-243.

Grinzato, E., Bison, P.G., Bressan, C. and Mazzoldi, A., 1998. NDE of frescoes by infrared thermography and lateral heating. In Eurotherm Seminar (Vol. 60, pp. 64-67).

Guo, N., Cawley, P., 1993. The interaction of Lamb waves with delaminations in composite laminates. *The Journal of the Acoustical Society of America*, *94*(4), 2240-2246.

Haider, M. F., Bhuiyan, M. Y., Poddar, B., Lin, B., Giurgiutiu, V., 2018. Analytical and experimental investigation of the interaction of Lamb waves in a stiffened aluminum plate with a horizontal crack at the root of the stiffener. *Journal of Sound and Vibration*, *431*, 212-225.

Hayashi, T., Song, W. J., Rose, J. L., 2003. Guided wave dispersion curves for a bar with an arbitrary cross-section, a rod and rail example. *Ultrasonics*, *41*(3), 175-183.

He J., Yuan FG (2015) Damage identification for composite structures using a cross-correlation reverse-time migration technique. *Structural Health Monitoring*, 14(6), 558-570.

Hudson T, Hou T, Grimsley B and Yuan FG (2015) Detection of CFRP composite manufacturing defects using a guided wave approach, *NASA report* NF1676L-19900.

Ibarra-Castanedo, C., Genest, M., Servais, P., Maldague, X.P. and Bendada, A., 2007. Qualitative and quantitative assessment of aerospace structures by pulsed thermography. *Nondestructive Testing and Evaluation*, 22(2-3), pp.199-215.

Ihn JB and Chang FK (2008) Pitch-catch Active Sensing Methods in Structural Health Monitoring for Aircraft Structures. *Structural Health Monitoring*, 7(1), 15-19.

Ilcewicz L., 2010. FAA Composite Safety Administration and Certification Initiatives. JAMS Conference.

Ilcewicz L., High Energy Wide Area Blunt Impact (HEWABI) as related to Safety and Certification. Composite Transport DT & Maintenance Workshop, September, 2015, Quebec, CA.

Jones, R.M., 2014. Mechanics of composite materials. CRC press.

Kaiplavil, S. and Mandelis, A., 2011. Highly depth-resolved chirped pulse photothermal radar for bone diagnostics. *Review of Scientific Instruments*, 82(7), p.074906.

Kaiplavil, S. and Mandelis, A., 2012, February. Bone-demineralization diagnosis in a bone-tissue-skin matrix using the pulsed-chirped photothermal radar. In Photonic Therapeutics and Diagnostics VIII (Vol. 8207, p. 82076L). International Society for Optics and Photonics.

Kaiplavil, S. and Mandelis, A., 2014. Truncated-correlation photothermal coherence tomography: “crisp” imaging breaking through the diffusion resolution and depth barriers,”. *Nature Photon*.

Karim, M. R., Awal, M. A., Kundu, T., 1992. Elastic wave scattering by cracks and inclusions in plates: in-plane case. *International Journal of Solids and Structures*, *29*(19), 2355-2367.

Karim, M. R., Kundu, T., 1988. Transient surface response of layered isotropic and anisotropic half-spaces with interface cracks: SH case. *International Journal of Fracture*, 37, 245-262.

Karim, M. R., Kundu, T., Desai, C. S., 1989. Detection of delamination cracks in layered fiber-reinforced composite plates. *Journal of Pressure Vessel Technology*, 3,165-171.

Karunasena, W. M., Liew, K. M., Kitipornchai, S., 1995. Hybrid analysis of Lamb wave reflection by a crack at the fixed edge of a composite plate. *Computer methods in applied mechanics and engineering*, *125*(1-4), 221-233.

Kessler SK., Spearing S.M., Soutis C., Damage detection in composite materials using Lamb wave method. *Smart Materials and Structures* 2002, Volume 11, 269-278.

Kim H., DeFrancisci G.K., Chen Z.M., Ground Vehicle Blunt Impact Damage Formation to Composite Aircraft Structures, *Advanced Composite Materials* 2014, Volume 23, 53-71.

Kuperman W., 2008. Correlation of randomly excited diffusive fields., notes.

Kuperman W., 2016. Diffusor Matrices, notes.

Lanza di Scalea F, Sternini S and Liang AY (2018b) Robust passive reconstruction of dynamic transfer function in dual-output systems. *Journal of the Acoustical Society of America*, 143(2), 1019-1028.

Lanza di Scalea F, Zhu X, Capriotti M, Liang AY, Mariani S and Sternini S (2018a) Passive extraction of dynamic transfer function from arbitrary ambient excitations: Application to high-speed rail inspection from wheel generated waves. *Journal of Nondestructive Evaluation Diagnostics Prognosis Engineering Systems*, 1(1), 011005.

Lau, S.K., Almond, D.P. and Milne, J.M., 1991. A quantitative analysis of pulsed video thermography. *Ndt & E International*, 24(4), pp.195-202.

Li, T., Almond, D. P., Rees, D. A. S. (2011). Crack imaging by scanning laser-line thermography and laser-spot thermography. *Measurement Science and Technology*, 22(3), 035701.

Lobkis, O.I., Weaver, R.L., 2001. On the emergence of the Green's function in the correlations of a diffuse field. *The Journal of the Acoustical Society of America*, 110(6), pp.3011-3017.

Lopez, F., Ibarra-Castanedo, C., Maldague, X. and Nicolau, V.D., 2014. Pulsed thermography signal processing techniques based on the 1D solution of the heat equation applied to the inspection of laminated composites. *Materials Evaluation*, 72(1).

Loveday, P. W., Long, C. S., 2007. Time domain simulation of piezoelectric excitation of guided waves in rails using waveguide finite elements. *Sensors and Smart Structures Technologies for Civil, Mechanical, and Aerospace Systems*, 6529, 65290.

Lowe M. J. S. 1992. Plate waves for the NDT of diffusion bonded Titanium. PhD Thesis, Imperial College, London.

Lowe MJS, Neau G and Deschamps M (2004) Properties of guided waves in composite plates, and implications for NDE. In: AIP Conference Proceedings, *Review of Quantitative Nondestructive Evaluation Vol. 23*, (ed DO Thompson and DE Chimenti), 700(1), 214–221, AIP.

Mal A., Ricci F., Samajder H., Baid H., *NDE of Composite Structures using Ultrasonic Guided Waves, Health Monitoring of Structural and Biological Systems, Proc. of SPIE 2013*, Volume 8695.

Mal, A., Chang, Z., 2000. A semi- numerical method for elastic wave scattering calculations. *Geophysical Journal International*, *143*(2), 328-334.

Mandelis A., Thermophotonic radar and thermal coherence tomographies. In Proc. VIIth International Workshop on Advances in Signal Processing for Non Destructive Evaluation of Materials (ASPNDE) (pp. 3-4).

Mandelis, A., 2013. Diffusion-wave fields: mathematical methods and Green functions. Springer Science & Business Media.

Manohar A., 2012. Quantitative nondestructive testing using infrared thermography. PhD Thesis. UC San Diego.

Mariani S., Nguyen T., Phillips R., Kijanka P., Lanza di Scalea F., Staszewski W., Fateh, M., Carr, G., Non-Contact Air-Coupled Ultrasonic Guided Wave Inspection of Rails. *Structural Health Monitoring International Journal, Special Issue on Noncontact Measurement Technologies* 2014, Vol.12, 539-548.

Mariani, S., 2015 Non-Contact Ultrasonic Guided Wave Inspection of Rails: Next Generation Approach. Ph.D. Dissertation, NDE & SHM Laboratory, University of California, San Diego, CA, USA.

Marín, E., 2010. Characteristic dimensions for heat transfer. Latin-American Journal of Physics Education, 4(1), pp.56-60.

Marín, E., Marín-Antuña, J. and Díaz-Arencibia, P., 2002. On the wave treatment of the conduction of heat in photothermal experiments with solids. *European journal of physics*, 23(5), p.523.

Marzani, A., 2008. Time–transient response for ultrasonic guided waves propagating in damped cylinders. *International Journal of Solids and Structures*, 45(25-26), pp.6347-6368.

Marzani, A., Viola, E., Bartoli, I., Lanza di Scalea, F., Rizzo, P., 2008. A Semi-analytical Finite Element Formulation for modeling stress wave propagation in axisymmetric damped waveguides. *Journal of Sound and Vibration*, 318(3), 488-505.

Matt, H., Bartoli, I., Lanza di Scalea, F., 2005. Ultrasonic guided wave monitoring of composite wing skin-to-spar bonded joints in aerospace structures. *Journal of the Acoustical Society of America*, 118(4), 2240-2252.

Meola, C., Carlomagno, G.M., 2004. Recent advances in the use of infrared thermography. *Measurement science and technology*, 15(9), p.R27.

Michaels JE and Michaels TE (2005) Detection of structural damage from the local temporal coherence of diffuse ultrasonic signals. *IEEE Transactions on Ultrasonics, Ferroelectrics and Frequency Control*, 52(10), 1769–1782.

Morse, P.M. and Feshbach, H., 1954. Methods of theoretical physics. *American Journal of Physics*, 22(6), pp.410-413.

Morse, P.M. and Feshbach, H., 2010. Methods of theoretical physics, Vol. II.

Murat B, Khalili P and Fromme P (2016) Scattering of guided waves at delaminations in composite plates. *Journal of the Acoustical Society of America*, 139(6), 3044-3052.

Nicolaides, L. and Mandelis, A., 2000. Novel dental dynamic depth profilometric imaging using simultaneous frequency-domain infrared photothermal radiometry and laser luminescence. *Journal of biomedical optics*, 5(1), pp.31-40.

Nucera, C., White, S., Chen, Z.M., Kim, H. and Lanza di Scalea, F., 2015. Impact monitoring in stiffened composite aerospace panels by wave propagation. *Structural Health Monitoring*, 14(6), pp.547-557.

Oswald-Tranta, B. and Shepard, S.M., 2013, May. Comparison of pulse phase and thermographic signal reconstruction processing methods. In *Thermosense: Thermal Infrared Applications* XXXV (Vol. 8705, p. 87050S). International Society for Optics and Photonics.

Ozisik, M.N. and Tzou, D.Y., 1994. On the wave theory in heat conduction. *Journal of Heat Transfer*, 116(3), pp.526-535.

Pickering, S.G. and Almond, D.P., 2007. An evaluation of the performance of an uncooled microbolometer array infrared camera for transient thermography NDE. *Nondestructive Testing and Evaluation*, 22(2-3), pp.63-70.

Poddar, B. and Giurgiutiu, V., 2016a. Complex modes expansion with vector projection using power flow to simulate Lamb waves scattering from horizontal cracks and disbonds. *The Journal of the Acoustical Society of America*, 140(3), 2123-2133.

Poddar, B. and Giurgiutiu, V., 2016b. Scattering of Lamb waves from a discontinuity: an improved analytical approach. *Wave Motion*, 65, 79-91.

Raghavan A and Cesnik CE (2007) Review of guided-wave structural health monitoring. *The Shock and Vibration Digest*, 39, 91-114.

Rattanawangcharoen, N., Zhuang, W., Shah, A. H., Datta, S. K., 1997. Axisymmetric guided waves in jointed laminated cylinders. *ASCE Journal of Engineering Mechanics*, *123*(10), 1020-1026.

Ricci, F., Monaco, E., Maio, L., Boffa, N.D. and Mal, A.K., 2016. Guided waves in a stiffened composite laminate with a delamination. *Structural Health Monitoring*, 15(3), pp.351-358.

Riegert G., Pfleiderer K., Gerhard H., Solodov I. and Busse G., Modern methods of NDT for inspection of aerospace structures., *ECNDT*, Berlin, Germany, 2006.
Rizzo P, Sorrivi E, Lanza di Scalea F and Viola E (2007) Wavelet-based Outlier Analysis for Guided Wave Structural Monitoring: Application to Multi-wire Strands. *Journal of Sound and Vibration*, 307(1-2), 52-68.

Roche, J.M., Leroy, F.H. and Balageas, D.L., 2014. Images of thermographic signal reconstruction coefficients: a simple way for rapid and efficient detection of discontinuities. *Materials evaluation*, 72(1).

Rose, J.L., 2004. Ultrasonic Waves in Solid Media; Cambridge University Press: Cambridge, UK.
Roth PR (1971) Effective measurements using digital signal analysis. *IEEE Spectrum*, 8(4), 62–70.

Sabra, K.G., Roux, P. and Kuperman, W.A., 2005. Emergence rate of the time-domain Green’s function from the ambient noise cross-correlation function. *The Journal of the Acoustical Society of America*, 118(6), pp.3524-3531.

Sabra, K.G., Gerstoft, P., Roux, P., Kuperman, W.A. and Fehler, M.C., 2005. Extracting time-domain Green's function estimates from ambient seismic noise. *Geophysical Research Letters*, 32(3).

Sabra KG, Srivastava A, Lanza di Scalea F, Bartoli I, Rizzo P and Conti S (2008) Structural health monitoring by extraction of coherent guided waves from diffuse fields. *Journal of the Acoustical Society of America,* 123(1), EL8–EL13.

Sabra KG, Winkel ES, Bourgoyne DA, Elbing BR, Ceccio SL, Perlin M and Dowling DR (2007) Using cross correlations of turbulent flow induced ambient vibrations to estimate the structural impulse response. Application to structural health monitoring. *Journal of the Acoustical Society of America*, 121(4), 1987–1995.

Salas K and Cesnik CE (2009) Guided wave structural health monitoring using CLoVER transducers in composite materials. *Smart Materials and Structures*, 19(1), 015014.

Salvermoser J, Hadziioannou C and Stahler SC (2015) Structural monitoring of a highway bridge using passive noise recordings from street traffic. *Journal of the Acoustical Society of America*, 138(6), 3864–3872.

Schnars U., Heinrich R., Applications of NDT Methods on Composite Structures in Aerospace Industry, *Conference on damage in composite materials*, Stuttgart, Germany, 2006, pp. 1-8.

Servais, P., Gerlach, N., Habermehl, J., Ibarra-Castanedo, C. and Maldague, X., 2008. Characterization of manufacturing and maintenance of aerospace composite discontinuities using infrared thermography. *Materials Evaluation*, 66(9).

Shepard, S. and Frendberg, M., 2014. Thermographic detection and characterization of flaws in composite materials. *Materials Evaluation*, 72(7).

Shepard, S. and Lhota, J.R., 2014. Thermography: More Than a Pretty Picture. *Materials Evaluation*, 72(1).

Shepard, S.M., 2007, October. Flash thermography of aerospace composites. In IV Conferencia Panamericana de END Buenos Aires (Vol. 7).

Shepard, S.M., Thermal Wave Imaging Inc, 2004. System for generating thermographic images using thermographic signal reconstruction. U.S. Patent 6,751,342.

Siakavellas N., 2012. Detection of radial cracks at fastener holes by either eddy current or line heating stimulated thermography. *Emerging Technologies in Non Destructive Testing*, 483-488.

Snieder, R., 2004. Extracting the Green's function from the correlation of coda waves: A derivation based on stationary phase. *Physical Review E*, 69(4), p.046610.

Snieder, R. and Safak, E., 2006. Extracting the building response using seismic interferometry: Theory and application to the Millikan Library in Pasadena, California. *Bulletin of the Seismological Society of America*, 96(2), pp.586-598.

Snieder, R., 2006. Retrieving the Green's function of the diffusion equation from the response to a random forcing. *Physical Review* E, 74(4), p.046620.

Snieder, R., 2007. Extracting the Green's function of attenuating heterogeneous acoustic media from uncorrelated waves. *The Journal of the Acoustical Society of America*, 121(5), pp.2637-2643.

Snieder, R., Sánchez-Sesma, F.J. and Wapenaar, K., 2009. Field fluctuations, imaging with backscattered waves, a generalized energy theorem, and the optical theorem. *SIAM Journal on Imaging Sciences*, 2(2), pp.763-776.

Snieder, R., Slob, E. and Wapenaar, K., 2010. Lagrangian Green's function extraction, with applications to potential fields, diffusion and acoustic waves. *New Journal of Physics*, 12(6), p.063013.

Snieder, R., Wapenaar, K. and Wegler, U., 2007. Unified Green's function retrieval by cross-correlation; connection with energy principles. *Physical Review* E, 75(3), p.036103.

Sohn H, Dutta D, Yang J, Park H, Desimio M, Olson S and Swenson E (2011) Delamination detection in composites through guided wave field image processing. *Composites Science and technology*, 71(9), 1250-1256.

Srivastava, A. and Lanza di Scalea, F., 2010. Quantitative structural health monitoring by ultrasonic guided waves. *ASCE Journal of Engineering Mechanics*, *136*(8), 937-944.

Staszewski, W., Boller, C., Tomlinson, G. R., 2004. *Health monitoring of aerospace structures: smart sensor technologies and signal processing*. John Wiley & Sons.

Tabatabaei, N. and Mandelis, A., 2009. Thermal-wave radar: A novel subsurface imaging modality with extended depth-resolution dynamic range. *Review of Scientific Instruments*, 80(3), p.034902.

Tabatabaei, N. and Mandelis, A., 2011. Thermal coherence tomography using match filter binary phase coded diffusion waves. *Physical review letters*, 107(16), p.165901.

Tabatabaei, N., Mandelis, A. and Amaechi, B.T., 2011. Thermophotonic radar imaging: An emissivity-normalized modality with advantages over phase lock-in thermography. *Applied Physics Letters*, 98(16), p.163706.

Tang, B., & Henneke, E. G. I. I. (1989). Lamb-wave monitoring of axial stiffness reduction of laminated composite plates. *Mater. Eval*., 47(8), 928-934.

Tian J, Gabbert U, Berger H and Su X (2004) Lamb wave interaction with delaminations in CFRP laminates. *Computers Materials & Continua*, *1*(4), 327-336.

Tippmann JD and Lanza di Scalea F (2015) Passive-only damage detection by reciprocity of Green's functions reconstructed from diffuse acoustic fields with application to wind turbine blades. *Journal of Intelligent Material Systems and Structures*, 26(10), 1251–1258.

Tippmann JD and Lanza di Scalea F (2016) Passive-only defect detection and imaging in composites using diffuse fields. In: *Mechanics of Composite and Multi-functional Materials, Volume 7*, 67-72. Springer, Cham.

Tippmann JD, Zhu X and Lanza di Scalea F (2015) Application of damage detection methods using passive reconstruction of impulse response functions. *Philos. Trans. R. Soc. A*, 373(2035), 20140070.

Tretout H., David D., Thevenot F., Review of advanced NDT methods for composites aerospace structures, *Proc. Int. Symp. On Advanced Materials for Lightweight Structures*, Noordwijk., The Netherlands, 1994, pp.624-634.

Tuzzeo D., Lanza di Scalea F., Noncontact air-coupled guided wave ultrasonics for detection of thinning defects in aluminum plates. *Journal of Research in Nondestructive Evaluation* 2001, Volume 13, 61-77.

Usamentiaga, R., Venegas, P., Guerediaga, J., Vega, L. and López, I., 2013. Automatic detection of impact damage in carbon fiber composites using active thermography. *Infrared Physics & Technology*, 58, pp.36-46.

Varis, J., Rantala, J. and Hartikainen, J., 1994. A numerical study on the effects of line heating in layered anisotropic carbon fiber composites. *Research in Nondestructive Evaluation*, 6(2), pp.69-83.

Vavilov, V., 1992, July. Thermal non destructive testing: short history and state-of-art. In QIRT (Vol. 92, pp. 1992-028).

Vavilov, V.P. and Maldague, X.P., 1992, April. Dynamic thermal tomography: new promise in the IR thermography of solids. In Thermosense XIV: An Intl Conf on Thermal Sensing and Imaging Diagnostic Applications (Vol. 1682, pp. 194-207). International Society for Optics and Photonics.

Wapenaar, K. and Fokkema, J., 2006. Green's function representations for seismic interferometry. *Geophysics*, 71(4), pp.SI33-SI46.

Wang L., Yuan F.G., Group Velocity and characteristic wave curves of Lamb waves in composites: Modeling and experiments. *Composites Science and Technology* 2007, Volume 67, 1370-1384.

Worden K, Pierce SG, Manson G, Philp WR, Staszewski W and Culshaw B (2000) Detection of defects in composite plates using Lamb waves and novelty detection. *International Journal of System Science*, 31(11), 1397–1409.

Worden, K., Manson, G. and Fieller, N.R., 2000. Damage detection using outlier analysis. *Journal of Sound and Vibration*, 229(3), pp.647-667.

Zhou, W. J., Ichchou, M. N., 2011. Wave scattering by local defect in structural waveguide through wave finite element method. *Structural Health Monitoring*, *10*(4), 335-349.